MONASH University

Atomically Engineered Electronic Two-Dimensional Organic Nanostructures

Dhaneesh Kumar Gopalakrishnan

B.Sc., University of British Columbia (2016)

Supervisors:

Dr. Agustin Schiffrin

Dr. Jack Hellerstedt

A thesis submitted for the degree of

Doctor of Philosophy

At Monash University

School of Physics and Astronomy

February 2021

Copyright Notice

Abstract

Present-day electronics are fast approaching fundamental limits of size and speed based on their material composition and mode of operation. Two-dimensional (2D) materials—because of their reduced dimensionality—can host a variety of novel quantum effects which, when exploited, can overcome these limits. Incorporating these 2D materials for next-generation electronics will rely on precise structuring at the nanoscale. Owing to their tunability and self-assembly capability, organic molecules as building nanounits allow for the bottom-up on-surface precise synthesis of 2D materials with tailored structural, electronic, and magnetic properties. The on-surface self-assembly of 2D organic nanostructures rely on the interplay between substrate-mediated and intermolecular interactions. These interactions affect the structural and electronic properties of the self-assemblies, making their understanding crucial.

Here, I considered self-assembled 2D organic nanostructures on different substrates. These organic nanostructures are comprised of 9,10-dicyanoanthracene (DCA) molecules whose cyano-functional groups allow for versatile in-plane molecular-molecular interactions via hydrogen- or metal-ligand bonding. 2D DCA-based organic nanostructure have also been predicted to host novel quantum phenomena such as topologically protected electronic states and strong electron-electron interactions. Using scanning tunnelling microscopy (STM), scanning tunnelling spectroscopy (STS) and non-contact atomic force microscopy (nc-AFM) techniques, I studied the structural and electronic properties of self-assembled 2D DCA-based systems for a variety of intermolecular and substrate-mediated interactions.

On a noble metal Ag(111) surface, I demonstrated the synthesis of a self-assembled 2D DCA molecular film. The charge state of the molecules within the film can be altered, depending on its adsorption site, by an STM-tip-induced electric field. Limited molecule-substrate interactions resulted in an effective tunnelling barrier between DCA and Ag(111) that enabled electric-field-induced population of the lowest unoccupied molecular orbital (LUMO), i.e., charging of the molecule. Subtle site-dependent variation of the DCA adsorption height translates into a significant spatial modulation of the LUMO energy, effective molecule-surface tunnelling barrier and, consequently, likelihood of charging of the molecules. The weak molecule-substrate interactions is further corroborated by a nearly free-like dispersion behaviour, measured via Fourier-transformed (FT) STS, for electrons at the interface between the DCA film and the underlying Ag(111) substrate. These results are important in the consideration and design of electrically addressable organic quantum dots at the nanoscale.

I further demonstrated the synthesis of a 2D metal-organic framework (MOF) where the DCA molecules form a kagome arrangement via coordination with copper atoms on

Ag(111). Using STS, I observed the Kondo effect at the Cu and DCA sites within the MOF, signalling the screening of local magnetic moments by the underlying Ag(111) conduction electrons. Facilitated by weak molecule-substrate interactions, corroborating density functional theory and mean-field Hubbard calculations (performed by collaborators) show that these moments resulted from strong electron-electron interactions within the MOF. This is the first time that the effect of strong electron-electron interactions in a 2D molecular film is observed directly. This can have important implications for the design of 2D organic materials where controllable electron-electron interactions lead to tuneable electronic quantum phase transitions.

Finally, I demonstrated the self-assembly of a 2D DCA molecular film on an insulating hBN monolayer grown on Cu(111), whose molecular arrangement is similar to DCA/Ag(111), indicative of weak molecule-substrate interactions. The LUMO energies for the molecules were found to be much higher than those on Ag(111) due to the absence of metal screening by the underlying hBN substrate. Similar to DCA/Ag(111), we further found significant spatial modulation of the DCA LUMO energies which, by means of vacuum alignment, followed the known spatial modulation of the hBN/Cu(111) surface work function. This presents serious implications for the use of thin insulators as means to electronically decouple organic nanofilms from the underlying substrate support.

Overall, this thesis highlights the tailoring of the electronic properties of on-surface 2D organic self-assemblies (e.g., strong electron correlations, field-induced charging of molecules) by means of different intermolecular (e.g., hydrogen-bonding, metal-ligand bonding) and substrate-mediated (e.g., metal screening, surface work modulation, metal-molecule potential barrier) interactions. This paves the way for the rational design of 2D organic nanostructures with tailored electronic and structural properties for next-generation electronics.

Declaration

I hereby declare that this thesis contains no material which has been accepted for the award of any other degree or diploma at any university or equivalent institution and that, to the best of my knowledge and belief, this thesis contains no material previously published or written by another person, except where due reference is made in the text of the thesis.

This thesis includes one original paper published in a peer reviewed journal. The core theme of the thesis is atomically engineered electronic two-dimensional organic nanostructures. The ideas, development and writing up of all the papers in the thesis were the principal responsibility of myself, the student, working within the School of Physics and Astronomy under the supervision of Dr. Agustin Schiffrin.

The inclusion of co-authors reflects the fact that the work came from active collaboration between researchers and acknowledges input into team-based research.

In the case of Chapter 3, my contribution to the work involved the following:

Thesis Chapter	**Publication Title**	**Status**	**student contribution**	**Co-author name(s). Nature and % of Co-author's contribution**	**Co-author(s), Monash student Y/N**
3	Electric Field Control of Molecular Charge State in a Single-Component 2D Organic Nanoarray	Published	65%. Concept and collecting data and writing first draft	1) Cornelius Krull, assisted in measurements manuscript, provided input for manuscript 5% 2)Yuefeng Yin, performed theoretical computations manuscript, provided input for manuscript 10% 3) Nikhil Medhekar: provided input for manuscript, 5% 4)Agustin Schiffrin: assisted in concept, provided input for manuscript, 15%	No

I have renumbered sections of submitted or published papers to generate a consistent presentation within the thesis.

Student name: Dhaneesh Kumar Gopalakrishnan

Student signature: _____ **Date:** 26th Feb. 2021

I hereby certify that the above declaration correctly reflects the nature and extent of the student's and co-authors' contributions to this work. In instances where I am not the responsible author, I have consulted with the responsible author to agree on the respective contributions of the authors.

Main Supervisor name: Agustin Schiffrin

Main Supervisor signature: _____ **Date:** 26th Feb 2021

Publications During Enrolment

1. **Kumar, D.**; Krull, C.; Yin, Y.; Medhekar, N. V.; Schiffrin, A. Electric Field Control of Molecular Charge State in a Single-Component 2d Organic Nanoarray. *ACS Nano* **2019**, *13* (10), 11882–11890
2. Krull, C.; Castelli, M.; Hapala, P.; **Kumar, D.**; Tadich, A.; Capsoni, M.; Edmonds, M. T.; Hellerstedt, J.; Burke, S. A.; Jelinek, P. Iron-Based Trinuclear Metal-Organic Nanostructures on a Surface with Local Charge Accumulation. *Nat. Commun.* **2018**, *9* (1), 1–7

In Preparation:

1. **Kumar, D.**; Hellerstedt, J.; Field, B.; Lowe, B.; Yin, Y.; Medhekar, N. V.; Schiffrin, A. Kondo Effect in a 2D Kagome Metal-organic Framework on a Metal.
2. **Kumar, D.**; Hellerstedt, J.; Lowe, B.; Schiffrin, A. Hydrogen-bonded Molecular Self-assembly on hBN/Cu(111).
3. **Kumar, D.**; Hendy, M.; Hellerstedt, J.; Hewes, J.; Kolomoisky, S.; Krull, C.; Schiffrin, A. Electronic Energy Landscape of a Weakly-interacting Molecular Film on a Surface.
4. Lowe, B.; Hellerstedt, J.; **Kumar, D.**; Schiffrin, A. On-surface Gold-aryl Covalent Bonding via Selective C-H Activation at Room Temperature.

Acknowledgements

"No man is an Island, entire of itself" is a phrase from John Donne's *Devotions upon Emergent Occasions* that fondly comes to mind as I write this. It continues to remind me that my work, as presented in this dissertation, would not have been achievable if it were not for the abundance of help, be it scientific, professional, or personal, that I have received from others. This page is dedicated to them.

First and foremost, I would like to extend my gratitude to my PhD supervisor, Dr. Agustin Schiffrin, for his guidance and advice throughout all my years as a PhD student. He has been an endless repository of scientific knowledge that I strive to be one day. His insights and approach to scientific problems have been instrumental in overcoming the challenges that I have faced in my research. His approach to these problems is something I will be sure to make full use of in the future and if anyone knows him well enough, this approach often begins with the phrase "if I were an electron …". I would like to further thank Dr. Cornelius Krull, who has been instrumental in my training on using Ned Kelly (the nickname of our SPM set-up) during the first two years of my PhD. Sharing in our joint frustrations for LabView has made some of my time as a PhD student memorable. I also thank Dr. Jack Hellerstedt for his assistance and guidance in a lot of the experiments that I have performed during the second half of my PhD. I also thank him for showing me the benefit of a bravado attitude to science; it pays off … sometimes.

I would like to thank Dr. Yuefeng Yin, Mr. Bernard Field and Dr. Nikihil Medhekar for providing theoretical results to complement my experimental findings. Their help was important in the formation of a coherent interpretation of some of the experimental findings presented in this dissertation. This clearly underscores the importance of collaboration in the scientific enterprise. I also thank Prof. Kris Helmerson, Dr. Alexis Bishop, Dr. Mark Edmonds, and Dr. Anton Tadich, who were all on my PhD advisory panel and whose positive feedback on my progress in my PhD was a great source of encouragement. I extend my appreciation for the Surface NanoPhysics group at Monash for fostering such an incredibly positive and encouraging environment.

To my friends in Melbourne, Li Jane, Alex K., Alex L., Steph, Li Ann, Yan Chi, Jimmy, Aswin, and many others, thank you for making Melbourne a home away from home. To Afiq and Evan, despite the vast ocean separating us, our continuing friendship has been a bountiful source of motivation in doing what I do. To my extended family, I thank you all for your encouragements. To my parents, Amma and Appa, who have been encouraging and supporting me from young to pursue whatever makes me happy, even if it means being a physicist rather

than a physician, I am deeply thankful for the both of you for being such wonderful and loving parents. I certainly cannot forget my partner, Jern-lyn, who, throughout my PhD, has lovingly and wholeheartedly supported me through my many ups and downs. I cannot express a deep enough gratitude for dealing with my quirks and for taking time to understand what I do. For this, I love you. Finally, to my grandfather, retired police officer Sgt. Major S. Kesavan, Tata, I thank you for your continued blessings and for your unrelenting support for what I do. I hope I have made you proud.

List of Figures

Figure 1.1: Top-down vs bottom-up approaches to nanofabrication. 2
Figure 1.2: Self-assembly of organic nanostructures on surfaces. 4
Figure 1.3: Experimental and theoretical results for 2D MOFs based on DCA molecules. 6
Figure 2.1: Bottom-up synthesis of 3D organic nanostructures via self-assembly. 12
Figure 2.2: Supramolecular engineering in two dimensions. 13
Figure 2.3: Schematic atomic structure of DCA_3Cu_2 metal-organic framework. 15
Figure 2.4: Molecular-beam epitaxy (MBE) schematic. 16
Figure 2.5: Overview of structural and electronic properties of Ag(111) and Cu(111) surfaces. 17
Figure 2.6: Solutions to Schrödinger equation for an electron in a 1D semi-periodic potential. 18
Figure 2.7: hBN/Cu(111) overview. 20
Figure 2.8: Schematic overview of a scanning tunnelling microscope. 23
Figure 2.9: Constant-current scanning mode vs constant-height scanning mode. 24
Figure 2.10: Schematic of quantum tunnelling as predicted by the Schrödinger equation. 25
Figure 2.11: Schematic approach to Bardeen tunnelling mechanism. 26
Figure 2.12: Tip-sample geometry used in the Tersoff-Hamann model. 28
Figure 2.13: Overview of systems that have been imaged via STM. 31
Figure 2.14: A still frame from the movie "*A Boy and His Atom*" [164]. 32
Figure 2.15: CO tip-functionalisation via STM vertical manipulation. 33
Figure 2.16: Elastic vs Inelastic tunnelling spectroscopy mechanism. 35
Figure 2.17: Overview of the Fourier-transform scanning tunnelling spectroscopy technique. 39
Figure 2.18: STM and STS measurements of various hydrogen-substituted molecules on Au(111). 41
Figure 2.19: STS measurements of a molecules on a metallic surface vs on an insulator. 42
Figure 2.20: Schematic overview of an atomic force microscope (AFM). 43
Figure 2.21: Typical Lennard-Jones potential curve describing intermolecular forces between two molecules. 44
Figure 2.22: Schematic overview of qPlus sensor design and operation in nc-AFM. 45
Figure 2.23: Force spectroscopy curves with a bare metallic vs passivated tip. 47
Figure 2.24: Nc-AFM imaging with a metallic tip vs passivated tip. 49
Figure 2.25: Overview of the measurement of the contact potential difference in an STM junction. 50

Figure 2.26: Measurement of local contact potential difference (LCPD) via Kelvin probe force microscopy. 51
Figure 2.27: Overview of LT-SPM at New Horizons Research Centre, Monash University, Australia. 53
Figure 2.28: Overview of STM head and cryostat. 54
Figure 2.29: Overview of translational manipulator for the LT-SPM set-up 56
Figure 3.1: STM and nc-AFM imaging of DCA submonolayers on Ag(111). 59
Figure 3.2: FT-STM and apparent height measurements of DCA/Ag(111). 60
Figure 3.3: Variation of DCA/Ag(111) molecular adsorption height measured via nc-AFM. 62
Figure 3.4: DFT-calculated energetically favourable adsorption geometries of DCA on Ag(111). 63
Figure 3.5: Point STS and dI/dV mapping measurements on DCA monolayer on Ag(111). 64
Figure 3.6: STM imaging showing direct topographic correlation between the DCA LUMO and the DCA negatively charged state. 65
Figure 3.7: $V^*(z)$ and $V_{LUMO}(z)$ measurements and the double barrier tunnelling junction (DBTJ) model. 67
Figure 3.8: Variations in zero-field LUMO energy due to screening by underlying metal and surrounding molecules. 71
Figure 3.9: Lateral Coulomb repulsion in DCA monolayer on Ag(111). 74
Figure 3.10: STM and STS measurements on DCA dimers. 75
Figure 3.11: KPFM measurements on DCA monolayer on Ag(111). 77
Figure 4.1: Evolution of Ag(111) Shockley surface state across DCA domain boundary and formation of DCA/Ag(111) interface state. 80
Figure 4.2: One-dimensional potential model for graphene adsorbed on an Ag(111) surface. 82
Figure 4.3: Interface state energy shift, ΔE_{IS} as a function of graphene adsorption height, d_C, on a metal. 83
Figure 4.4: dI/dV STS mapping of a defect-filled DCA/Ag(111) submonolayer. 86
Figure 4.5: FT-STS measurements of defect-filled DCA/Ag(111) submonolayer. 88
Figure 4.6: DCA/Ag(111) interface potential landscape and band structure calculations. 92
Figure 5.1: Structural and electronic overview for a 2D kagome lattice. 96
Figure 5.2: STM and nc-AFM overview of DCA_3Cu_2 kagome on Ag(111). 98
Figure 5.3: STM & nc-AFM imaging of DCA_3Cu_2 kagome structures on Ag(111) and Cu(111). 100
Figure 5.4: Cu atoms next-nearest-neighbour distance in DCA_3Cu_2 MOFs on Ag(111) & Cu(111). 101
Figure 5.5: Registration of DCA_3Cu_2 on Ag(111) and Cu(111). 103

Figure 5.6: Apparent and real adsorption height difference between Cu_A and Cu_B atoms in DCA_3Cu_2/Ag(111). 104
Figure 5.7: STS characterisation of DCA_3Cu_2 kagome MOF on Ag(111)..... 106
Figure 5.8: LDOS simulation for DCA_3Cu_2/Ag(111) via Electron Plane Wave Expansion (EPWE) modelling..... 108
Figure 5.9: Temperature-dependent near-Fermi dI/dV STS data for DCA_3Cu_2/Ag(111) kagome MOF..... 110
Figure 5.10: Temperature dependence of ZBP width: evidence of the Kondo effect..... 113
Figure 5.11: DFT-calculated vibrational modes of a single Cu_2DCA molecular complex in the gas phase..... 116
Figure 5.12: DFT-calculated band structures for DCA_3Cu_2 kagome on Ag(111) and free-standing..... 117
Figure 5.13: DFT+U calculated magnetic moment and spin density for DCA_3Cu_2/Ag(111) MOF..... 119
Figure 5.14: Local magnetic moment and spin density for DCA_3Cu_2 calculated via MFH modelling. 121
Figure 5.15: Schematic summarising the emergence of local magnetic moments as a result of electron-electron interactions and their subsequent Kondo screening in DCA_3Cu_2/Ag(111). 122
Figure 6.1: STM overview of a self-assembled molecular submonolayer comprised of hydrogen-bonded dicyanoanthracene (DCA) molecules on hBN/Cu(111). 129
Figure 6.2: STM imaging at DCA/hBN film boundary. 131
Figure 6.3: $\mathrm{d}I/\mathrm{d}V$ STS measurements on DCA/hBN/Cu(111) and on hBN/Cu(111)..... 132
Figure 6.4: Spatial modulation of DCA LUMO and hBN CBM energies..... 135
Figure A.1: Different DCA monolayer domains on Ag(111)..... 164
Figure A.2: V^* measurements for different molecules along a_1 in a DCA monolayer..... 165
Figure A.3: Topography contribution to constant height dI/dV maps. 166
Figure A.4: Determination of V_{LUMO} and tip-sample distance in Chapter 3. 167
Figure B.1: Dispersion, E(k), plots along DCA/Ag(111) high-symmetry directions. 169
Figure C.1: Differential conductance measurements at the DCA molecular centre with various tips..... 178
Figure C.2: Differential conductance measurements along high-symmetry lines for the DCA_3Cu_2 kagome structure. 179
Figure C.3: dI/dV STS maps obtained at energies corresponding to side peaks observed in dI/dV data at high symmetry locations in DCA_3Cu_2/Ag(111). 180
Figure C.4: Tip-sample distance-dependent dI/dV STS data at the high symmetry locations within the DCA_3Cu_2/Ag(111) MOF. 181

Figure C.5: Extracted HWHM of ZBP in dI/dV data without and with thermal smearing considered. 182
Figure C.6: ZBP spatial dependence measurements. 183
Figure C.7: DFT calculated band structure for freestanding DCA_3Cu_2 and DCA_3Cu_2/Ag(111) kagome structure with and without U. 185
Figure C.8: DFT calculated band structure for DCA_3Cu_2/Ag(111) and DCA_3Cu_2/Cu(111) kagome. 185
Figure C.9: MOF-substrate calculated charge transfer as function of MOF-substrate separation. 186
Figure C.10: Band structures for DCA_3Cu_2 on Ag(111) and Cu(111) as a function of vertical displacement from the respective substrates. 188
Figure C.11: DFT+U local magnetic moment calculation for DCA_3Cu_2 kagome structure in gas phase, on Ag(111) and on Cu(111). 189
Figure C.12: Magnetic phase diagram calculated via DFT+U and MFH modelling for the DCA_3Cu_2 kagome structure. 190
Figure C.13: Spin densities as calculated by the MFH model for selected values of U_{MFH} and electron filling, n. 192
Figure C.14: Effect of disorder on the magnetic properties of DCA_3Cu_2 via MFH modelling. 194
Figure D.1: STM imaging of different self-assembled DCA domains on hBN/Cu(111). 195

List of Tables

Table 2.1: Overview of basic interactions in supramolecular engineering at a surface. 14
Table 3.1: Adsorption height differences between DCA molecules measured via nc-AFM. .. 62
Table 5.1: ZBP fit results for dI/dV STS data for DCA_3Cu_2/Ag(111) kagome MOF. 114
Table B.1: RMSE for fits to experimentally measured DCA/Ag(111) interface state dispersion. 170

List of Abbreviations

2DEG	Two-Dimensional Electron Gas
AFM	Atomic Force Microscopy
ARPES	Angle-resolved Photoemission Spectroscopy
BZ	Brillouin Zone
CO	Carbon Monoxide
COF	Covalent Organic Framework
CPD	Contact Potential Difference
DCA	9,10-dicyanoanthracene
DFT	Density Functional Theory
DOS	Density of States
EPWE	Electron Plane Wave Expansion
FCC	Face Centred Cubic
FM	Ferromagnetic
FT	Fourier Transform
FT-STS	Fourier Transformed Scanning Tunnelling Spectroscopy
FWHM	Full Width at Half Maximum
hBN	Hexagonal Boron Nitride
HOMO	Highest Occupied Molecular Orbital
HWHM	Half Width at Half Maximum
IS	Interface State
KPFM	Kelvin Probe Force Microscopy
LCPD	Local Contact Potential Difference
LDOS	Local Density of States
LT-SPM	Low-temperature Scanning Probe Microscopy
LUMO	Lowest Unoccupied Molecular Orbital
MBE	Molecular Beam Epitaxy
MFH	Mean-field Hubbard
ML	Monolayer
MOF	Metal Organic Framework
MP	Multi-pass
Nc-AFM	Non-contact Atomic Force Microscopy
PDOS	Projected Density of States
PIN	Pinned Phase
QD	Quantum Dot

RMSE	Root-mean-square Error
SDW	Spin Density Wave
SS	Surface State
STM	Scanning Tunnelling Microscopy
STS	Scanning Tunnelling Spectroscopy
TB	Tight Binding
UC	Unit Cell
UHV	Ultrahigh Vacuum
VB	Valence Band
ZBP	Zero-bias Peak

Table of Contents

Copyright Notice ..... **i**
Abstract ..... **iii**
Declaration ..... **v**
Publications During Enrolment ..... **vii**
Acknowledgements ..... **ix**
List of Figures ..... **xi**
List of Tables ..... **xv**
List of Abbreviations ..... **xvii**
Table of Contents ..... **xix**
Chapter 1: Introduction **1**
1.1 Future of Electronics: Top-down vs Bottom-up 1
1.2 Organic Molecules as Building Blocks 2
1.3 Self-assembled 2D Organic Nanostructures: Progress and Challenges 3
1.4 Thesis Objective and Scope 5
Chapter 2: Experimental Overview **11**
2.1 Organic Nanomaterial Growth Techniques 11
2.1.1 On-surface supramolecular chemistry *11*
2.1.2 Molecular-beam epitaxy *15*
2.1.3 Structural and electronic properties of substrates *17*
2.1.4 Substrate preparation details *21*
2.1.5 Sample preparation details *22*
2.2 Scanning Tunnelling Microscopy 23
2.2.1 Operating principle *23*
2.2.2 Quantum tunnelling *24*
2.2.3 Bardeen Transfer Hamiltonian theory *26*
2.2.4 Tersoff-Hamann model *28*
2.2.5 WKB approach to tunnelling *30*
2.2.6 State-of-the-art STM imaging *30*
2.2.7 Atomic-scale manipulation *32*
2.3 Scanning Tunnelling Spectroscopy 34
2.3.1 Elastic tunnelling differential conductance spectroscopy *34*
2.3.2 Inelastic tunnelling differential conductance spectroscopy *34*
2.3.3 dI/dV STS acquisition modes *36*
2.3.4 dI/dV STS maps *37*
2.3.5 Fourier-transform STS *39*
2.3.6 State-of-the-art dI/dV STS *40*
2.4 Non-contact Atomic Force Microscopy 42
2.4.1 Operating principle *43*
2.4.2 Force spectroscopy *46*
2.4.3 Nc-AFM imaging *48*
2.4.4 Kelvin probe force microscopy *49*
2.4.5 State-of-the-art nc-AFM *52*
2.5 Details of Experimental Set-up 52
2.5.1 Overview of low-temperature scanning probe microscopy set-up *52*

2.5.2 STM head and cryostat *53*
2.5.3 STM and nc-AFM tips *55*
2.5.4 STM and nc-AFM calibration *55*
2.5.5 Sample preparation tools *55*
Chapter 3: Electric Field Control of Molecular Charge State in DCA/Ag(111) Nanoarray **57**
3.1 Overview 57
3.2 Structural Characterisation of DCA Monolayer on Ag(111) 58
3.2.1 STM and nc-AFM structural characterisation *58*
3.2.2 DFT-calculated adsorption height *62*
3.3 STS Characterisation of DCA Monolayer on Ag(111) 63
3.4 Electric-field-induced Ag(111)-to-DCA Electron Transfer 65
3.5 *z*-dependent STS Measurements and DBTJ Model 66
3.6 Molecular Screening Environment 70
3.7 Dielectric constant for DCA monolayer on Ag(111) 72
3.8 Charging Hindrance: Lateral Coulomb Repulsion 73
3.9 Formation of DCA Dimers at Low Substrate Temperature 75
3.10 KPFM Measurements on DCA monolayer on Ag(111) 76
3.11 Summary 77
Chapter 4: Dispersion of DCA/Ag(111) Interface State **79**
4.1 Overview 79
4.2 Formation of 2DEG at DCA/Ag(111) Interface 79
4.3 Energy Dispersion of Interface State Measured via FT-STS 84
4.4 Molecular Potential Landscape at DCA/Ag(111) Interface 91
4.5 Summary 93
Chapter 5: Strongly Correlated Electrons in 2D DCA_3Cu_2 Kagome Metal-Organic Framework on Ag(111) **95**
5.1 Overview 95
5.2 Structural Characterisation of DCA_3Cu_2 Kagome on Ag(111) 97
5.2.1 STM and nc-AFM overview of DCA_3Cu_2 kagome on Ag(111) *97*
5.2.2 Structural disorder in DCA_3Cu_2/Ag(111) *99*
5.2.3 Origin of Cu contrast in STM and nc-AFM imaging of DCA_3Cu_2/Ag(111) *103*
5.3 STS Characterisation of DCA_3Cu_2 Kagome on Ag(111) 105
5.4 Nature of ZBP and Near-Fermi Features in d*I*/d*V* STS Data 109
5.4.1 Temperature-dependent dI/dV data and fitting overview *109*
5.4.2 Temperature dependence for ZBPs in dI/dV STS data *112*
5.4.3 Temperature dependence for satellite peaks in dI/dV STS data *114*
5.4.4 DCA vibrational modes *115*
5.5 Origin of Local Magnetic Moments within DCA_3Cu_2/Ag(111) 117
5.5.1 DFT+U calculations for DCA_3Cu_2/Ag(111) kagome MOF *117*
5.5.2 Mean-field Hubbard model calculations for the DCA_3Cu_2 kagome MOF *120*
5.6 Estimation of Interaction Energies for DCA_3Cu_2/Ag(111) MOF 123
5.6.1 Kondo exchange interaction energy *123*
5.6.2 Interspin exchange interaction energy *123*
5.7 Summary 125
Chapter 6: Self-Assembled DCA Monolayers on hBN/Cu(111) **127**
6.1 Overview 127
6.2 STM Characterisation of DCA/hBN/Cu(111) 128

6.3 STS Characterisation of DCA/hBN/Cu(111) 131
6.4 Modulation of DCA LUMO by hBN/Cu(111) Work Function 134
6.5 Summary 137
Chapter 7: Conclusions and Outlook 139
Bibliography 145
Appendix A: DCA Monolayers on Ag(111) 163
A.1 Theoretical Methods 163
A.2 DCA/Ag(111) Domains and Superstructure Periodicity 163
A.3 d*I*/d*V* STS measurements for molecules M_0 to M_{39} (negative bias range) 164
A.4 Topography Contribution to Constant Height d*I*/d*V* maps 165
A.5 Determination of V_{LUMO} and tip-sample distance 166
Appendix B: DCA/Ag(111) Interface State Dispersion 169
B.1 Interface State Dispersion Along High-Symmetry Directions 169
B.2 RMSE Calculations for Evaluating Dispersion Fits 169
B.3 Band Structure Calculation 171
Appendix C: DCA_3Cu_2 Kagome MOF on Ag(111) 173
C.1 Theoretical Methods 173
C.2 Subtle Satellite Peaks in d*I*/d*V* STS Data 178
C.3 d*I*/d*V* STS Measurements along High-symmetry Lines 179
C.4 Near-Fermi d*I*/d*V* Maps 180
C.5 Tip-sample Distance-dependent d*I*/d*V* STS Measurements 180
C.6 Thermal Smearing in Temperature-dependent d*I*/d*V* STS Data 182
C.7 Spatial-dependent d*I*/d*V* STS Data 183
C.8 Band Structure Calculations 184
C.9 MOF-substrate Charge Transfer 186
C.10 Magnetic Moment and Spin Density Calculations 188
C.11 Effect of Structural Disorder in DCA_3Cu_2/Ag(111) 193
C.12 Estimation of Exchange Interaction Energy, J_{ex} 194
Appendix D: DCA Monolayers on hBN/Cu(111) 195
D.1 Different Moiré Superstructures for DCA/hBN/Cu(111) 195

Chapter 1
Introduction

1.1 Future of Electronics: Top-down vs Bottom-up

Electronics are ubiquitous in our daily lives and form the bedrock of our modern technological advances. Inherently, electronics rely on the control of charge flow, i.e., current. A transistor is a device that enables such control. Since the development of the transistor in 1947 [1], the field of conventional electronics have seen unprecedented improvements in speed and efficiency, both of which can be attributed to the exponential progress in device miniaturisation [2]. These improvements are to meet a seemingly insatiable demand for a more technologically driven society. This could, for example, be in the form of needing to perform complex computations more quickly or being able to store data in even smaller devices. In any case, these improvements are not without limit, as current electronic components, e.g., transistors, are limited in how small they can be made since quantum effects become a considerable challenge to overcome at the nanoscale [3, 4]. Furthermore, the intrinsic non-zero resistance of these devices inevitably leads to a significant loss of energy which is dissipated via heat i.e., Joule Heating [5]. This introduces a severe limitation on the absolute efficiency that conventional electronics can attain.

Next-generation electronic architectures have been proposed to overcome these limitations. These include, but are not limited to, the use of quantum dots (QD)—atom-like objects with externally tuneable discrete electronic states—as single-electron transistors [6], the incorporation of newly discovered class of matter with dissipation-less charge transport, i.e., topological insulators [7], and the manipulation and use of strongly correlated matter where electron-electron interactions are dominant [8]. While the fabrication of conventional electronic components has greatly benefitted from processes that make big structures smaller, i.e., "top-down" approaches (e.g., electron-beam writing [9], advanced lithography techniques [10]; see **Figure 1.1**), these next-generation electronics require precise structuring at the nanoscale that is not offered by these top-down approaches [11, 12]. A viable alternative would be to employ a so-called "bottom-up" approach to the nanofabrication of these next-generation electronic components [13] (see **Figure 1.1**). This entails the growth of functional components from smaller building blocks (atoms, molecules, or both) in a controlled and predictable manner.

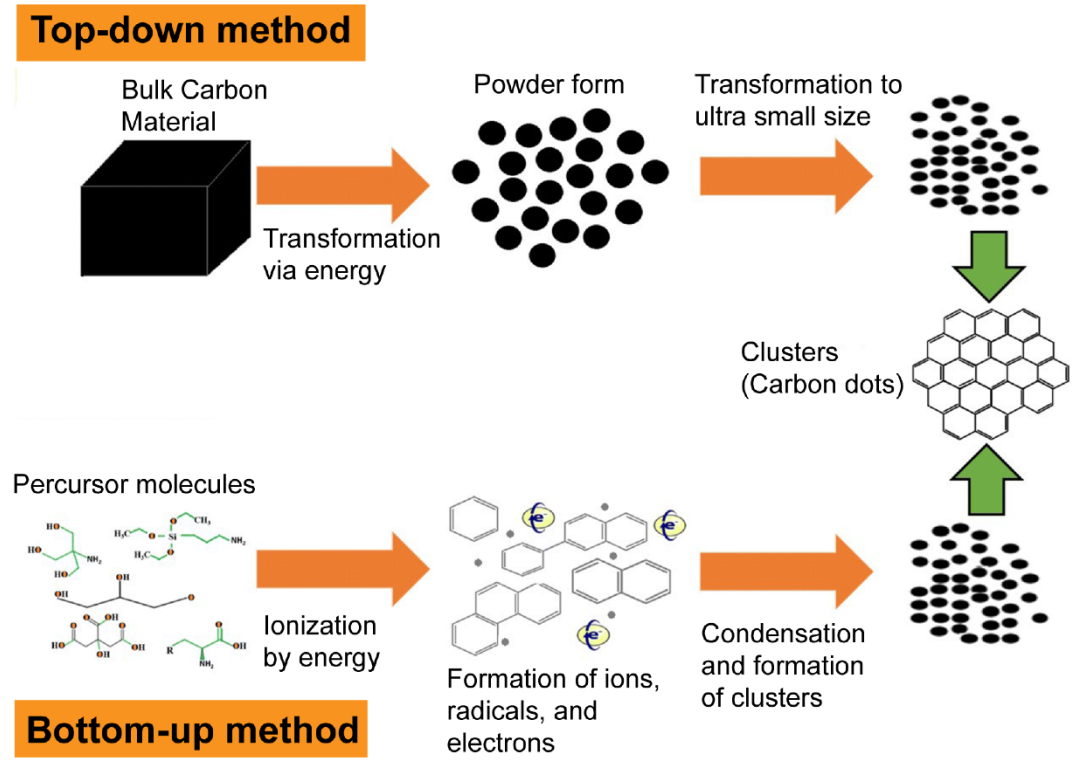

Figure 1.1: Top-down vs bottom-up approaches to nanofabrication. The schematic shows two different routes to the fabrication of functional nanostructures, which in this case is represented by Carbon dots. Top-down methods involve reducing bulk material, e.g., by mechanical grinding, to smaller fragments until desired functionalities are achieved. Bottom-up methods involve growing desired functional materials from even smaller units, e.g., from individual molecules. This schematic is reproduced from ref. [14] under a Creative Commons Attribution 4.0 International License.

1.2 Organic Molecules as Building Blocks

Carbon-containing molecules, i.e., organic molecules, represent a promising class of materials as building blocks within the bottom-up approach [15]. Generally, these molecules, which are semiconducting, have low manufacturing costs and are easy to fabricate from precursor components thanks to the vast expertise offered by the field of organic chemistry. Furthermore, these molecules tend to have a reduced environmental impact compared to inorganic molecules [16, 17]. These properties, in addition to their small size and weight, stability, and mechanical properties [18], make organic molecules suitable for a more sustainable and cheaper route to the manufacturing of functional components.

More crucially, the interactions between organic molecules can lead to the self-assembly of larger and more complex superstructures [15, 18], making these molecules ideal building blocks within the context of the bottom-up approach to nanofabrication of functional components. Molecular self-assembly is a key concept in supramolecular chemistry—which is a field in chemistry that concerns weaker and reversible non-covalent interactions between molecular species [19]. Via well-established techniques of supramolecular chemistry, exploiting the self-assembly process through these intermolecular interactions (which include

hydrogen bonding, van der Waals forces, π-π interactions, and metal coordination [15]) has allowed for a vast array of different applications such as organic solar cells [20], organic light emitting diodes (OLEDs) [21, 22], gas-sensors [23], and organic field-effect transistors (OFETs) [24].

Typically, these intermolecular interactions can be tuned (and therefore affect the self-assembly process) thanks to the tailorability of organic molecules i.e., the synthesis of organic molecules with selected physical and chemical properties, functional groups, and symmetries [25–27]. Metal atoms can be further introduced in the self-assembly process to facilitate metal-ligand coordination and/or to provide active sites for catalytic processes [28, 29], to establish a mechanism for light absorption [30] or to introduce localized magnetic moments [31–33]. Altogether, these factors allow for a rationally designed nanostructure with the desired structural, electronic, optical, or magnetic properties.

1.3 Self-assembled 2D Organic Nanostructures: Progress and Challenges

The techniques of supramolecular chemistry, originally applied for the synthesis of 3D nanostructures in solution, have been extended to on-surface synthesis leading to formations of 2D (or even 1D) self-assembled surface-supported organic nanostructures [25–27]. These low-dimensional (2D, 1D or even 0D) materials are systems in which electronic state wavefunctions are confined in one dimension for 2D materials, in two dimensions for 1D materials, or in all three spatial dimensions for 0D materials. For these materials, these spatial confinements can give rise to quantum size effects which can significantly alter their electronic properties as compared to their bulk (3D) counterparts. Graphene, a 2D material, is quintessential of this where, unlike in 3D graphite, the delocalised π electrons behave like massless Dirac electrons [34] and where electron mobilities are remarkably high [35]. The surfaces on which these 2D organic nanostructures are synthesised on, via self-assembly, act as a form of support for these systems. Additionally, these surface supports can play an important role such as that of an electrode in the case of applications for electronic or optoelectronic devices [36].

Within this scheme of self-assembly on surfaces, molecules (and/or metal adatoms) are adsorbed onto a substrate where they can, via an interplay of adsorbate-adsorbate and adsorbate-substrate interactions, self-assemble to form ordered nanostructures (see **Figure 1.2**). This growth process, when influenced by temperature, flux and composition of adsorbates, and by choice of substrate can lead to a variety of different self-assembled nanostructures [25–27]. Therefore, this on-surface synthesis process offers an additional benefit of steering the self-assembly process of 2D organic nanostructures.

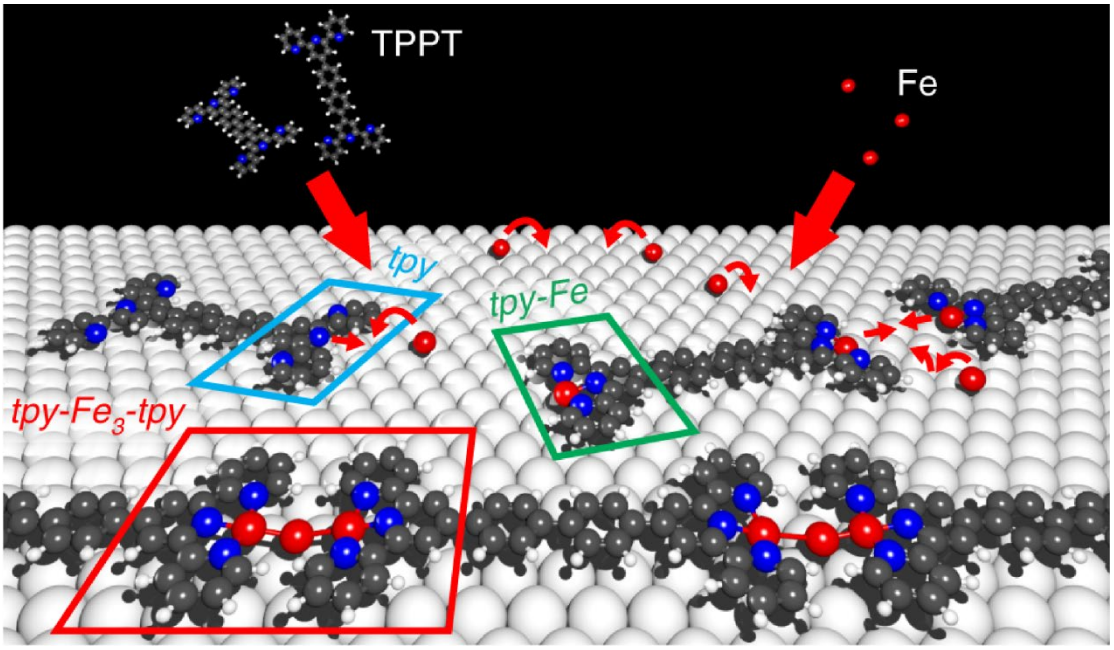

Figure 1.2: Self-assembly of organic nanostructures on surfaces. Schematic showing the self-assembly of a 1D organic nanostructure after the co-deposition of terpyridine-phenyl-phenyl-terpyridine (TPPT) molecules and Fe atoms onto a surface. Diffusion of TPPT molecules and Fe atoms on the surface enables the metal-ligand coordination between the Fe atoms and the terpyridine (*tpy*; blue square) groups of the TPPT molecules to form a 1D metal-organic chain. The linkages between TPPT molecules in this 1D chain is given by the *tpy*-Fe_3-*tpy* bond (red square). This schematic was adapted from ref. [37] under a Creative Commons Attribution 4.0 International License.

In recent years, this approach has been successful at synthesising a variety of 2D organic nanostructures ranging from the synthesis of closed-pack structures with square [38, 39], rectangular [40] and monoclinic lattice [41] structures to the synthesis of porous organic systems with well-known honeycomb lattice structures [42, 43] or even the more exotic Kagome lattice structure [44]. The transition from a single-walled to a double-walled organic nanoporous structure has been demonstrated after a change of a molecular species' functional group [45]. 2D organic self-assemblies based on molecular species possessing a variety of functional groups [46–49] has been shown. 2D organic nanostructures resulting from metal-ligand coordination, i.e., metal-organic frameworks (MOFs), have also been demonstrated via on-surface self-assembly with the metallic species in these 2D MOFs having two- [50, 51], three- [52, 53] and even four-fold [54, 55] coordination geometries.

The potential functionalities of these self-assembled 2D organic nanostructure have been demonstrated as well. Organic assemblies comprised of multi-molecular species, where one molecular species acts as donor molecules (donates electrons away) and another species acts as acceptor molecules (accepts electrons), have been synthesised [56]. It has been shown that the charge state of these molecules can be controlled via external electric fields. The manipulation of charge in these systems—at the single electron level and with nanoscale precision—allows for various potential applications [57], e.g., nanoelectronics, memory

storage, classical and quantum computing [58], and light-emitting devices [59]. As another example, 2D organic self-assemblies where the molecular units possess localized magnetic moments have also been synthesised [31, 33]. The resulting arrangement of magnetic moments would be important for applications in spintronics [60].

Alongside these experimental successes, there have been many theoretical predictions of 2D π-extended organic systems hosting useful electronic properties. These include predictions of 2D MOFs hosting topologically protected electronic states [61–63], strongly correlated electrons [64], flat electronic bands [65], and superconducting phases [66]. While these properties are found in inorganic systems, they have yet to be demonstrated experimentally for 2D organic nanostructures. These theoretical predictions often concern 2D organic systems in their free-standing configuration, i.e., without the substrate present, whereas on-surface synthesis via self-assembly exploits interactions between molecules *and* interactions between molecules and the underlying substrate. In the case of the latter, the strength of interactions can vary from strong (chemisorption) to very weak (physisorption) molecule-substrate interactions [26, 67]. Desired molecular properties can be modified or even removed altogether due to these interactions. Understanding what effects these interactions (molecule-molecule and substrate-mediated) can have on the morphology, electronic, and magnetic properties of adsorbed molecules remain a key challenge in the bottom-up on-surface synthesis of functional 2D organic nanostructures.

1.4 Thesis Objective and Scope

The challenges outlined in the previous section prompt a further understanding of the physics and chemistry that happens at the nanoscale with regards to molecular self-assemblies on surfaces. To this end, my research efforts as presented in this thesis have been directed at studying 2D self-assembled organic nanostructures on surfaces and identifying the impact of the substrate and the molecular-molecular interactions on the structural and electronic properties of the 2D self-assemblies. The work here would further pave the way for rationally designed organic nanostructures on surfaces with desired structural, optical, electronic, or magnetic functionalities.

The focus of my thesis is on a single kind of organic molecule, namely 9,10-dicyanoanthracene (DCA). This aromatic, mirror-symmetric molecule hosts two reactive cyano-functional groups as seen in **Figure 1.3**a. The aromaticity of the molecule ensures a flat adsorption configuration on surfaces. This facilitates in-plane intermolecular interactions via the DCA cyano-functional groups through hydrogen bonding with neighbouring molecules. These cyano-functional groups can also coordinate, via the nitrogen lone electron pair, with different transition metals (e.g., Cu [68, 69], Fe [70], Co [52, 71, 72], Au [68, 73]) to form in-

plane metal-ligand bonds. Depending on the choice of transition metals, two- [74, 75], three- [68, 71, 72], and even four-fold [70, 76] coordination geometries are possible. This versatility in intermolecular interactions, aided by the DCA molecules' small size, can lead to the formation of different 2D DCA-based organic nanostructures. Furthermore, the inclusion of metal adatoms in these structures permits the ability to tune parameters such spin-orbit coupling strengths [63], to introduce catalytic active sites [28, 29], to introduce magnetic moments [31–33], or to allow for light absorption [30] within these structures. Coupled with the simple structure of the DCA molecule, surface-supported 2D organic nanostructures comprising DCA molecules are model systems to investigate. Here, I present my study on the impact of the local nanoscale environment on the properties of 2D organic nano-assemblies consisting of DCA molecules. Changes in the local environment are reflected in the choice of substrates and difference in molecular coordination (i.e., inclusion of metallic adatoms in the self-assembly process). Low-dimensional DCA-based self-assemblies, so far, have been synthesised on a variety of surfaces [52, 53, 73, 77, 78] (see **Figures 1.3**d,e). Furthermore, theoretical predictions of 2D MOFs involving DCA molecules [63, 64, 79, 80] (see **Figures 1.3**b,c) with interesting electronic properties have been put forward. These past experimental and theoretical works serve as useful references and/or comparisons to my findings.

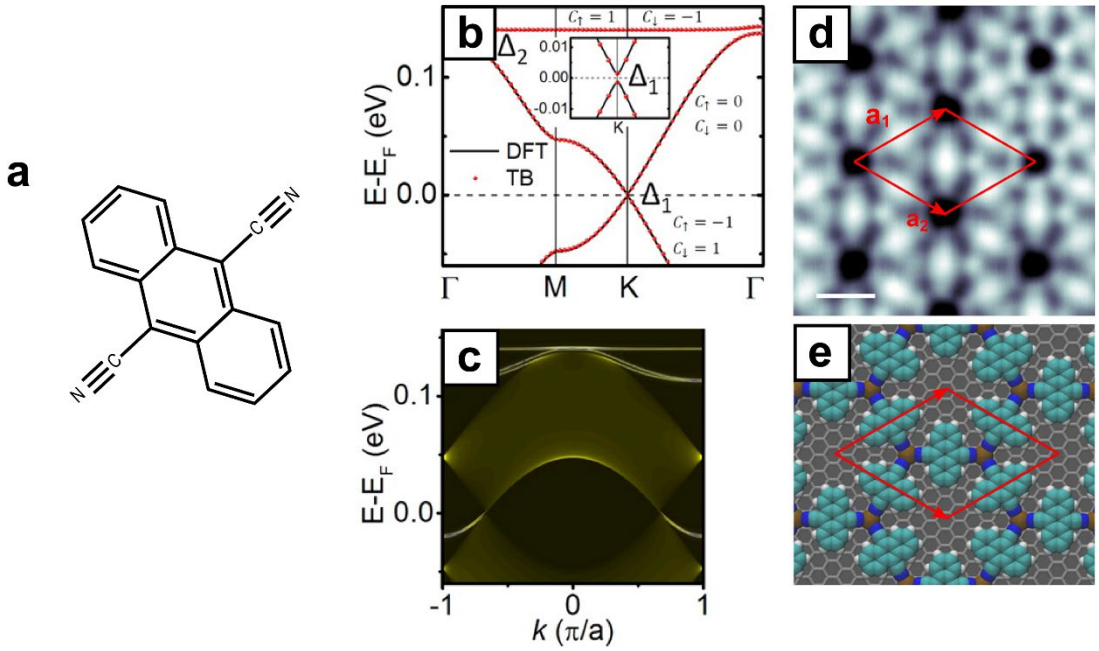

Figure 1.3: Experimental and theoretical results for 2D MOFs based on DCA molecules. (a) chemical structure of a 9,10-dicyanoanthracene (DCA) molecule. (b)-(c) show theoretically calculated electronic band structures for a 2D metal-organic kagome framework resulting from coordination between DCA molecules and Cu atoms. The band structures show a presence of flat band and a band gap at the Dirac point. Within this band gap, there exists topologically protected edges states. (d) STM imaging of a 2D MOF kagome framework resulting coordination between DCA molecules and Co atoms on Graphene/Ir(111). Scale bar is 1 nm. (e) Structural schematic for the 2D MOF seen in (d). (b)-(c) were adapted with permission from ref. [63]. Copyright (2016) American Chemical Society. (d)-(e) were adapted with permission from ref. [52]. Copyright (2018). American Chemical Society.

Two important aspects of the work presented here include the following: (i) growth, and (ii) characterisation of the self-assembled 2D organic nanostructures. Chapter 2 presents an overview and theoretical description of the growth techniques used in this work. Here, I will highlight the sample preparation details for the various self-assemblies presented throughout this thesis. Concurrent to the advances in on-surface synthesis of low-dimensional organic self-assemblies is the advances in surface-sensitive probing techniques such as scanning probe microscopy. In this chapter, I will further present such techniques employed to characterise the structural and electronic properties of the self-assembled surface-supported organic nanostructures. More specifically, I will introduce imaging techniques such as scanning tunnelling microscopy (STM) and non-contact atomic force microscopy (nc-AFM) that enables the structural characterisation of on-surface structures with atomic resolution. Complementary techniques such as scanning tunnelling spectroscopy (STS) which enables electronic characterisation of the on-surface system with sub-nano precision is introduced here as well. To afford such precision, these characterisation efforts (STM, nc-AFM and STS measurements) were performed in a highly controlled environment e.g., in ultrahigh vacuum (UHV) conditions and at low temperatures (~5 K). These controls are also introduced here.

Having introduced the growth and characterisation techniques that I have employed as part of this work, I then present the results in Chapter 3 on self-assembled 2D organic array of molecules comprising only hydrogen-bonded DCA molecules on a noble metal surface, Ag(111). This substrate choice is motivated by: (i) its chemical inertness; (ii) the Ag(111) hexagonal surface symmetry to optimise for the synthesis of three-fold coordination structure e.g., DCA_3Cu_2 MOF structure [63]; and (iii) established self-assembly protocols on noble metal surfaces. In this chapter, I present an extensive characterisation of the structural and electronic properties of the DCA molecules within the molecular self-assembly. We find that these molecules exhibit electric field-controlled spatially periodic charging on the metal surface, i.e., the charge state of DCA can be altered (between neutral and negative), depending on its adsorption site, by the local electric field induced by the scanning tunnelling microscope tip. We rationalise this phenomenon with the weak interactions between the DCA molecule and the underlying Ag(111) surface. Comparisons with the on-surface DCA dimers on Ag(111) suggests that the full participation of the DCA cyano-functional groups in the 2D organic array mitigates strong bonding with the underlying surface, resulting in weak metal-molecule interactions. These results are important in the consideration and design of electrically addressable organic quantum dots at the nanoscale and have been published [81].

In Chapter 4, I present results complementary to the results presented in the previous chapter. The Ag(111) surface hosts a 2D electron gas-like state which results naturally from the break in crystal translational symmetry at the surface [82]. This so-called surface state has been

studied extensively and has a well-known energy onset and dispersion [83]. Here, I present results showing a 2D electron gas-like state at the interface between the self-assembled DCA molecular array and Ag(111). This interface state is derived from an upshift in the energy of the Ag(111) surface state. In this chapter, I show by means of STS or more precisely, Fourier-transformed STS (FT-STS), the energy dispersion of this interface state. We find subtle deviations from a free electron-like dispersion at high energies particularly for electron wavevectors close to satisfying the Bragg condition [84]. Deviations in the free electron-like dispersion behaviour at the organic-metal interface can translate to significant alteration of the electronic properties of 2D organic nanostructures at energies where these deviations are detected.

In Chapter 5, I present results of a self-assembled 2D MOF on Ag(111) as a direct result of metal-ligand coordination between DCA molecules and Cu atoms co-adsorbed onto Ag(111). We find that the resulting MOF is ordered according to a kagome crystal structure—where the DCA molecules are arranged in corner-sharing equilateral triangles as predicted in ref. [63]. Using temperature-dependent STS measurements, we reveal Kondo screening [31, 85, 86] by the underlying metal surface conduction electrons, of magnetic moments localized at Cu and DCA locations within the MOF. Through complementary theoretical considerations, we rationalize the (indirect) observation of local magnetic moments as a result of strong correlations between the kagome MOF electrons [85]. The results in this chapter reveals the first direct experimental demonstration of strongly correlated electrons in an atomically thin 2D metal-organic framework. This can have crucial implications for correlated electron electronics based on organic materials.

The results presented in Chapters 3, 4 and 5 are all regarding organic nanostructures synthesised on noble metal surfaces where on-surface synthesis of 2D organic nanostructures via self-assembly is well-established. It is desirable to perform on-surface synthesis of these structures on insulating substrates where these substrates can act as decoupling layers to preserve the intrinsic electronic characteristics of molecular adsorbates [87, 88]. However, synthesis of these structures via self-assembly on insulating substrates remain limited [55, 89–95]. In Chapter 6, I present results on self-assembled 2D DCA molecular films on an ultrathin insulating hexagonal boron nitride (hBN) monolayer grown on Cu(111). Most significantly, we find that the modulation in the work function of hBN/Cu(111) results in the modulation of the energy of the DCA lowest unoccupied molecular orbital (LUMO) adsorbed on hBN/Cu(111). Here, while thin insulating layers are efficient for electronic decoupling between adsorbates and the underlying metal (i.e., negligible metal-molecule interactions), spatial variations of the substrate work function can severely affect the adsorbate's energy level alignment. This has

important ramifications in the electronic functionality of the organic self-assembly on these insulating layers and must be considered.

Finally, I summarise the results presented in this work in Chapter 7. I further provide an outlook of how these findings relate to the overarching research goals outlined in this chapter. I also discuss future possible experiments to further extend my findings.

Chapter 2
Experimental Overview

The study of 2D organic self-assemblies on surfaces necessitates the growth and characterisation of these systems. In this chapter, I describe the growth and characterisation techniques that I have employed throughout this dissertation. I begin by discussing the growth techniques (section 2.1), namely, molecular self-assembly via on-surface supramolecular chemistry. Here, I provide specific details on sample preparation which includes preparation of the substrate upon which these 2D organic nanostructures are grown. Following this, I describe the characterisation techniques used to study these self-assemblies. These include surface-sensitive techniques such as scanning tunnelling microscopy (STM; section 2.2), scanning tunnelling spectroscopy (STS; section 2.3) and non-contact atomic force microscopy (nc-AFM; section 2.4). Altogether, these growth and characterisation techniques were carried using the state-of-the-art low-temperature scanning probe microscope (LT-SPM), located at the New Horizons Research Centre (Monash University, Australia). Details of this set-up is provided in section 2.5.

2.1 Organic Nanomaterial Growth Techniques

2.1.1 On-surface supramolecular chemistry

Supramolecular chemistry—the development of which led to the awarding of the 1987 Nobel Prize in Chemistry to Donald J. Cram, Jean-Marie Lehn and Charles J. Pedersen [19]—focuses on reversible noncovalent interactions between organic species. These noncovalent interactions include, but are not limited to, hydrogen bonding, van der Waals interactions, π-π interactions and electrostatic interactions [96]. Interactions such as metal-ligand coordination are also considered provided their bonding strengths are not too large [96]. Techniques of supramolecular chemistry can be used to direct the molecular recognition and subsequently self-assembly capabilities of individual organic species to form, in-solution and from the bottom-up, a wide variety of 3D organic nanostructures. This is shown schematically in **Figure 2.1**. Over the past few decades, 3D organic nanostructures synthesised via molecular self-assembly have seen applications in sensing [97], molecular machines [98], catalysis [98, 99], green chemistry [100–102].

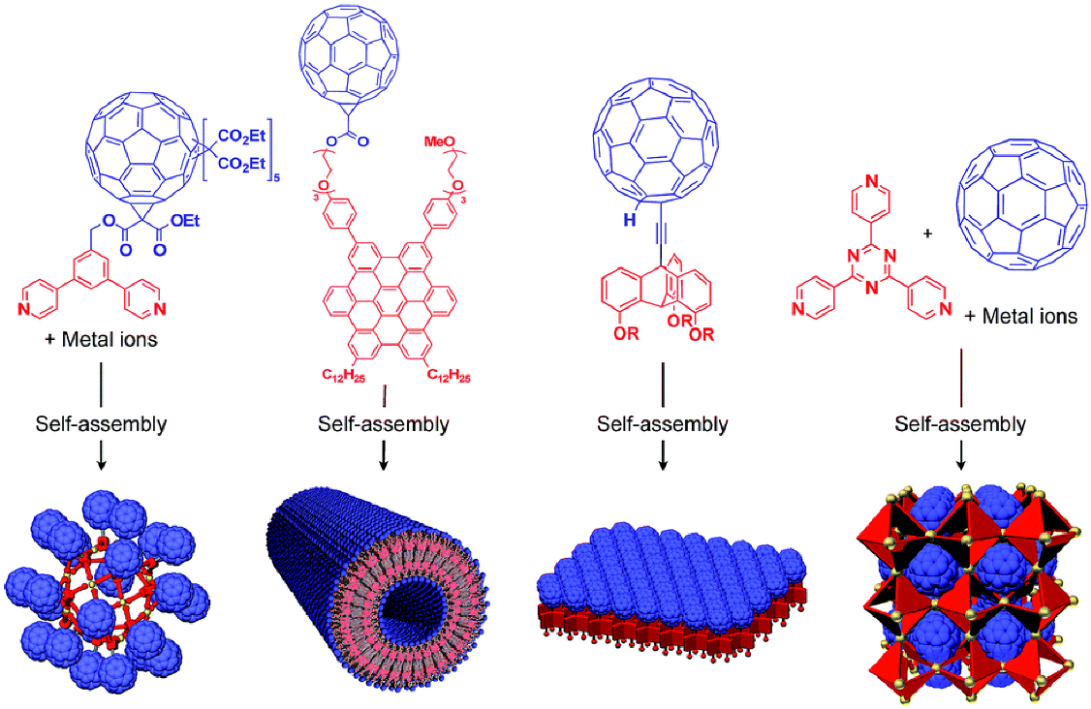

Figure 2.1: Bottom-up synthesis of 3D organic nanostructures via self-assembly. Tailoring the individual organic building nanounits (top) can direct the molecular recognition and self-assembly of these molecules to form different 3D organic nanostructures (bottom). This figure was adapted from ref. [103] under a Creative Commons Attribution 3.0 Unported License (CC BY 3.0).

Although originally developed for in-solution synthesis of extended organic structures, techniques of supramolecular chemistry have been expanded to on-surface synthesis of low-dimensional organic assemblies. Methods for synthesising these structures include but are not limited to spin-coating [104], the Langmuir-Blodgett method [105, 106], and molecular beam epitaxy (MBE) [107]. Spin-coating and Langmuir-Blodgett methods are excellent at synthesising thin organic films at surfaces. However, with spin-coating, these organic films are typically limited to colloidal particles [108] and polymers [109]. Langmuir-Blodgett method, on the other hand, is limited to amphiphilic molecules and most recently nanoparticles [105, 110]. MBE does not share these limitations and offers the capability of growing structures with multi-organic species and precise nano-structuring [107]. In this dissertation, I employed MBE for the on-surface self-assembly of low-dimensional organic nanostructures.

Schematically (see **Figure 2.2**), this involves exposing a surface to a molecular beam (subsection 2.1.2) by which these molecular building blocks, i.e., tectons are then adsorbed onto the surface. By means of direct lateral interactions between tectons (which include hydrogen bonding, metal-ligand coordination, electrostatic forces and van der Waals forces) and substrate-mediated interactions, these tectons can self-organize into larger extended organic assemblies. However, supramolecular engineering of this form is only possible through a balancing act of these (lateral and substrate-mediated) interactions. More precisely, these tectons must be enabled to fully explore the potential landscape of the different noncovalent

structures that can be formed at the surface interface and therefore form a thermodynamically favourable structure. Near such a thermodynamic equilibrium, the molecular self-assembly process via non-covalent interactions can take place. Self-corrections, facilitated by the reversibility of non-covalent bonds (compared to the irreversibility of covalent bonds), near this equilibrium further corrects for defects in the assembly process [26]. The non-covalent nature of interactions within the self-assembled structure, however, translates to a weaker stability at elevated temperatures (beyond room temperature) compared to covalently bonded structures. This is a necessary trade-off given the versatility in the synthesis of organic nanostructures via non-covalent self-assembly.

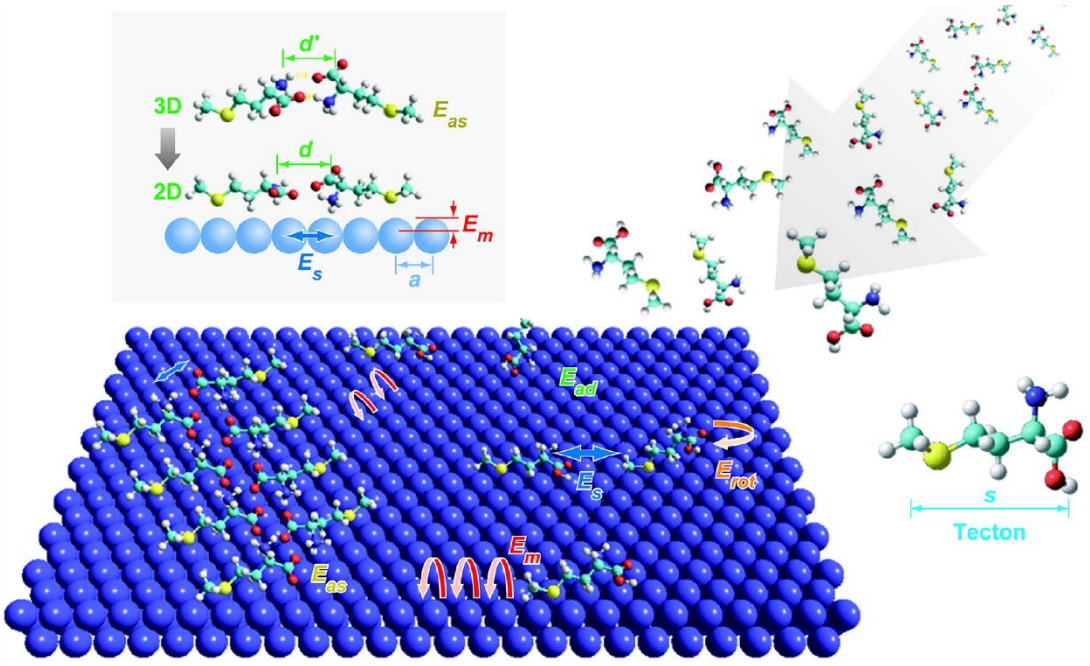

Figure 2.2: Supramolecular engineering in two dimensions. Molecular building blocks known as tectons are deposited onto a 2D atomic lattice where they can self-assemble to form on-surface organic nanostructures. The self-assembly process depends crucially on the adsorption energies, E_{ad}, migration barriers, E_m, rotational barriers, E_{rot}, substrate-mediated interaction energies, E_s, and direct lateral interaction energies, E_{as}, of the tectons. Substrate choice and symmetry can further affect non-covalent interactions between tectons (inset; atomic lattice periodicity given by a) characterised by a different bonding length, d, between tectons when on a surface than in gas-phase, d'. Figure republished with permission of Annual Reviews, Inc., from ref. [26]; permission conveyed through Copyright Clearance Center, Inc.

Modifications and therefore control of the different non-covalent interactions can be done via internal and external controls. Internal controls include the tailoring of these tectons to have the appropriate physical (e.g., size, and weight) and chemical properties (e.g., functional groups). External controls include substrate temperature, deposition flux of these tectons onto the surface, F, and choice of substrate. These controls altogether modify adsorption energies, E_{ad}, migration barrier, E_m, 2D rotation barrier, E_{rot}, surface diffusion rates, D, substrate-mediated interaction energies, E_s, and direct lateral energies, E_{as} of these tectons. For example,

modification of the diffusion rate-to-deposition flux ratio, D/F, can lead to either a kinetic driven (small D/F) synthesis of an on-surface nanostructure or a thermodynamically driven one (large D/F) [25].

Precise nanostructuring, on the other hand, would mean exploiting the selective and directional bonding character offered by these direct lateral interactions such as hydrogen bonding and metal-ligand interactions. Tailoring the tectons to have the right physical (e.g., shape and symmetry) and chemical properties (e.g., functional groups) are also to be considered in this case. Introduction of transition metal adatoms as co-adsorbates onto the surface enables metal-ligand coordination. Achieving the desired coordination structure in this case depends on the choice of the introduced metallic species, in addition to the shape, symmetry and functional groups of the tectons. These choices need to be made in consideration of their impact on the self-assembly process as outlined in the previous paragraph. **Table 2.1** provides an overview of the different interactions and their respective energies and effective ranges relevant to the on-surface synthesis of organic nanostructures via supramolecular chemistry.

	Energy range	**Distance**	**Character**
Adsorption	$E_{ad} \approx 0.5 - 10$ eV	$\approx 1.5 - 3$ Å	Directional, site selective
Surface migration	$E_m \approx 0.05 - 3$ eV	$\approx 2.5 - 4$ Å	1D/2D
Rotational motion	$E_{rot} \sim \dim(E_m)$	s	2D
Indirect substrate mediated	$E_s \approx 0.001 - 0.1$ eV	a to nanometre range	Oscillatory
Reconstruction mediated	$E_s \sim 1$ eV	Short	Covalent
van der Waals	$E_{as} \approx 0.02 - 0.1$ eV	< 10 Å	Nonselective
Hydrogen bonding	$E_{as} \approx 0.05 - 0.7$ eV	$\approx 1.5 - 3.5$ Å	Selective, directional
Electrostatic ionic	$E_{as} \approx 0.05 - 2.5$ eV	Long range	Nonselective
Metal-ligand interactions	$E_{as} \approx 0.5 - 2$ eV	$\approx 1.5 - 2.5$ Å	Selective, directional

Table 2.1: Overview of basic interactions in supramolecular engineering at a surface. The table provides the energies/barriers, typical relevant distances and character of interactions that should be considered during on-surface supramolecular engineering of nanostructures. Here, s and a refers to the tecton length and substrate lattice constant as seen in **Figure 2.2**. Table republished with permission of Annual Reviews, Inc., from ref. [26]; permission conveyed through Copyright Clearance Center, Inc.

In the context of this dissertation, I have focused on studying molecular self-assemblies involving the aromatic DCA molecules as tectons (see **Figure 2.2**). The relatively small size of this molecule would mean lower migration barriers, enabling effective surface diffusion and hence exploration of the local environment. Flat adsorption configurations, where the plane spanned by the carbon rings lie parallel to the surface, are typical of aromatic molecules on surfaces as this minimizes the adsorption energies for these molecules [111]. The flat adsorption configuration further enables precise nanostructuring of organic self-assemblies via the DCA

chemically reactive cyano-functional groups and therefore confining interactions (and nanostructure formation) to two dimensions. The DCA cyano-functional groups allows for interactions with many different transition metal atoms [52, 74, 112] via the nitrogen atoms' lone electron pairs, i.e., metal-ligand coordination. This, therefore, allows for the realisation of a variety of 2D DCA-based metal-organic nanostructures depending on the choice of transition metal adatom. The promotion of metal-ligand coordination within the self-assembled organic nanostructure can be accomplished with the co-adsorption of these transition metal adatoms alongside the DCA molecules on a surface, as was done in Chapter 5 with the co-adsorption of Cu atoms and DCA molecules on a metallic substrate.

The choice of Cu atoms as coordination centres is motivated by prediction of a stable 2D MOF formation comprising of DCA-Cu three-fold metal-ligand coordination (see **Figure 2.2**) [63] and ready coordination with cyano-functional groups [53, 68, 113].

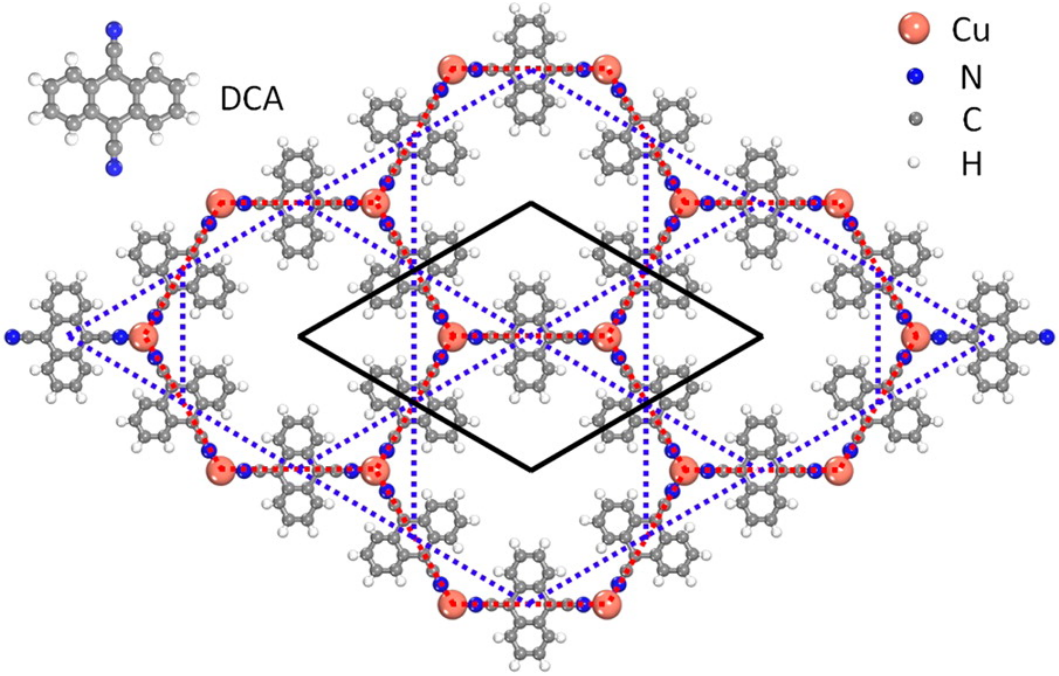

Figure 2.3: Schematic atomic structure of DCA_3Cu_2 metal-organic framework. The coordination between the DCA molecules and the Cu atoms forms a combined honeycomb-kagome lattice where the red dashed lines outline the honeycomb lattice by the Cu atoms and the blue dashed lines outline the kagome lattice by the DCA molecules. The black lines represent the unit cell of the DCA_3Cu_2 structure. The top left inset shows the DCA molecule. Figure was republished with permission from ref. [63]. Copyright (2016) American Chemical Society.

2.1.2 Molecular-beam epitaxy

The utility of on-surface synthesis of organic nanostructures via molecular self-assembly rely on the delivery of tectons to the surface in a controllable manner. For this, I used protocols of molecular-beam epitaxy [107]. This involves the sublimation and deposition of organic and/or metal evaporants under ultra-high vacuum (UHV) conditions (~10^{-10} mbar) onto a well-defined

and atomically clean surface. Thermal evaporation of these evaporants can be done by simply heating the sources in an effusion cell—a crucible with a small orifice—to a point where they slowly sublime out the cell opening (see **Figure 2.4**). Sublimation under UHV conditions is necessary as to ensure a long mean free path (> 1 km) of the tectons coming out of the effusion cells [114]. The long mean free path translates to a severely reduced probability of tecton-tecton interactions during flight towards the surface. This ensures the arrival of individual tectons on the surface as opposed to a cluster of tectons. As previously mentioned, control of the deposition flux is important in the on-surface synthesis process. This is achieved by controlling the (tecton) source temperature. Higher (lower) temperatures lead to higher (lower) deposition flux. The source-to-sample distance also affects the molecular beam-sample cross section and needs to be taken into consideration (see **Figure 2.4**).

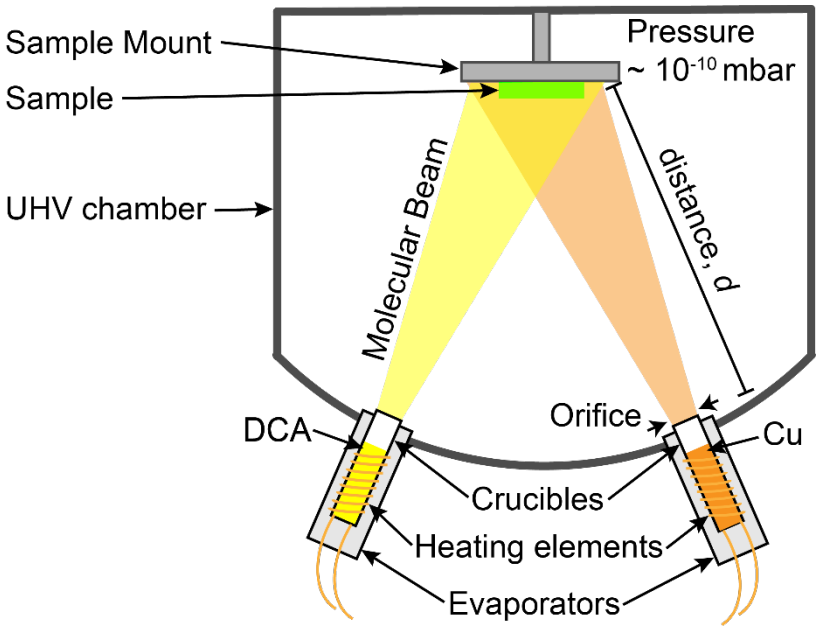

Figure 2.4: Molecular-beam epitaxy (MBE) schematic. MBE is typically carried out in a UHV chamber where low pressures can be achieved, which is necessary for a long mean free path for the molecules/atoms. The evaporants, here DCA and Cu, are heated in separated crucibles until they sublime. The resulting molecular beams exiting through the crucible orifices are directed towards the sample where DCA molecules and Cu atoms are adsorbed.

It is important to note that this method is restricted by the sublimation of the molecules from the solid phase to gas phase in UHV. This is not feasible for molecules with much larger molecular weights. The increased molecular weight increases the sublimation temperatures for these molecules—temperatures at which these molecules fragment. Recent developments using electrospray deposition circumvents this problem allowing for the deposition of larger, extended, and more intricate molecules onto a substrate [115, 116].

2.1.3 Structural and electronic properties of substrates

Throughout this dissertation, I have considered growth of 2D organic nanostructures on three different substrates: Ag(111); Cu(111); and hBN/Cu(111). Here I review their structural and electronic properties.

Ag(111) and Cu(111)

Ag(111) and Cu(111) are noble metal surfaces; their relatively inert surfaces promotes non-covalent substrate-adsorbate interactions, perfect for on-surface self-assembly of organic nanostructure. There are well established protocols for preparing these surfaces such that they are atomically flat over > 1 μm^2 areas (see subsection 2.1.4). On-surface synthesis of organic nanostructures on these surfaces via self-assembly has been widely demonstrated [113, 117–119]. Both bulk Ag and Cu have face-centred cubic (FCC) crystal structures. Taking a cut along the (111) plane naturally results in a surface lattice structure for both Ag(111) and Cu(111) that is hexagonal (also known as a triangular lattice) as seen in **Figures 2.5**a,b.

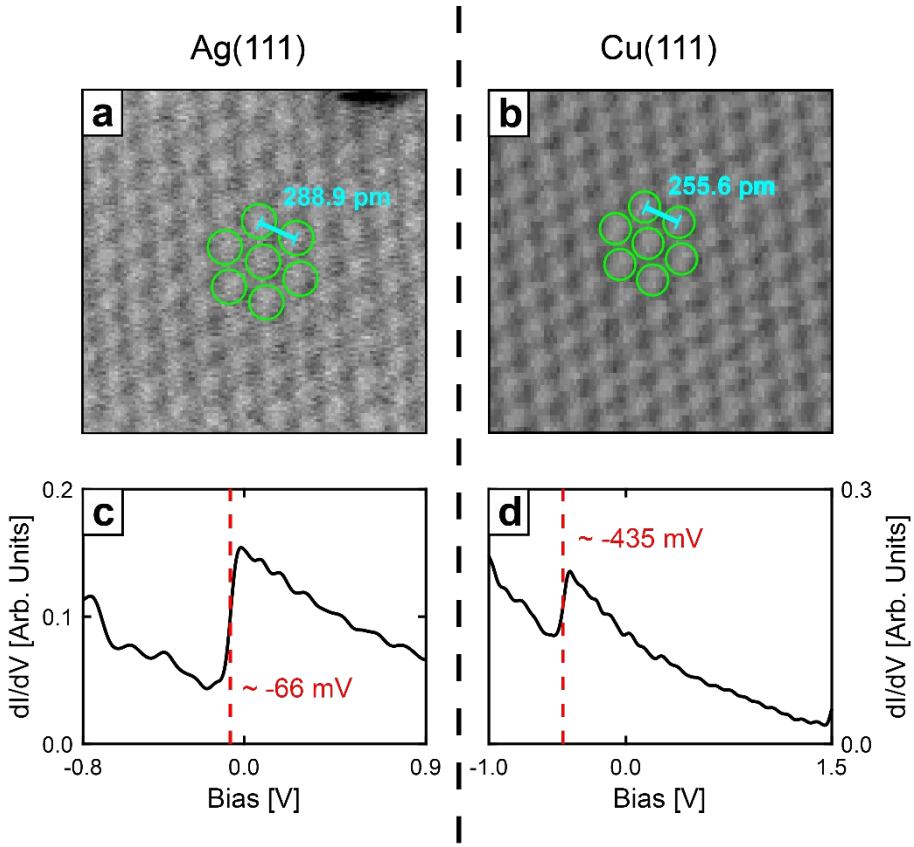

Figure 2.5: Overview of structural and electronic properties of Ag(111) and Cu(111) surfaces. (a)-(b) Atomically-resolved nc-AFM images of an (a) Ag(111) surface and a (b) Cu(111) surface. The subtle but brighter features seen in the images are the surface atoms as imaged by nc-AFM. These atoms form the basis of a hexagonal surface lattice structure (green circles) with a lattice constant of 288.9 pm and 255.6 pm for Ag(111) and Cu(111), respectively. (c)-(d) Differential conductance (dI/dV), as measured by STS, representative of the LDOS, on (c) Ag(111) surface and (d) Cu(111) surface. Both curves show a step-like feature indicative of a Shockley surface state for both surfaces with onset energies of -66 meV and -435 meV for Ag(111) and Cu(111), respectively.

Using the bulk lattice constants for Ag and Cu ($a_{\mathrm{bulk}} = 408.53$ pm and 361.49 pm [120], respectively), the surface lattice constants, a_{surf}, for Ag(111) and Cu(111) are 288.9 pm and 255.6 pm, respectively ($a_{\mathrm{surf}} = a_{\mathrm{bulk}}/\sqrt{2}$). The surfaces' hexagonal symmetry is preferable for the growth of structures that are of a similar symmetry such as the proposed DCA_3Cu_2 MOF. Electronically, both Ag(111) and Cu(111) are similar in that they are both metals (electrically conducting) and, more remarkably, they both host a two-dimensional electron gas-like state at their surfaces. These states, known as Shockley surface states [82], appear in the local density of states (LDOS), measured via scanning tunnelling spectroscopy (STS; see section 2.3) on these surfaces, as step-like features with specific onset energies: –66 meV for Ag(111) [83] and –435 meV for Cu(111) [121] (see **Figures 2.5**c,d).

These Shockley surface states are a consequence of the break in translational symmetry in the system, i.e., at the surface termination of materials. Generally, solving the Schrödinger equation for an electron in an infinitely periodic potential yields solutions that are itself periodic. This is a well-known consequence of Bloch's Theorem [84] where these solutions, the wavefunctions, are known as Bloch states. Applied to real materials such as bulk Ag and Cu where the periodic potential represents that of the atomic lattice, these Bloch states represent the "bulk-states" of the material (see **Figure 2.6**a).

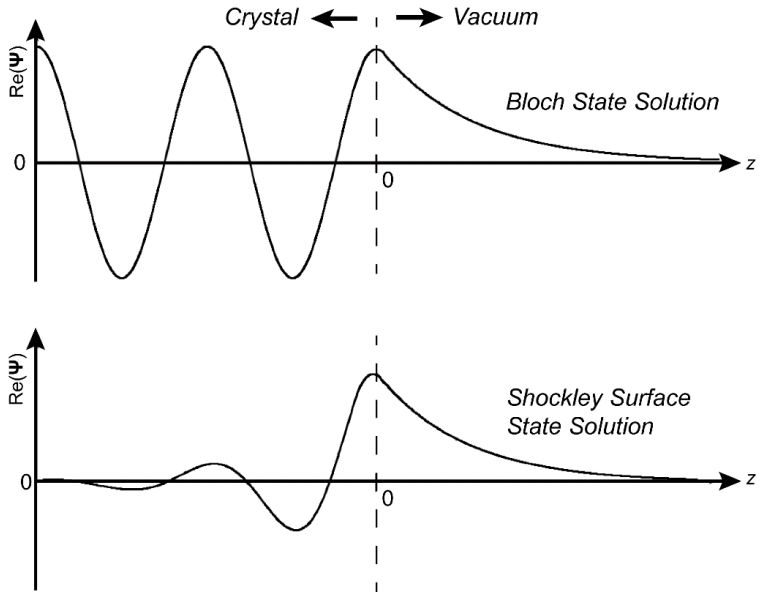

Figure 2.6: Solutions to Schrödinger equation for an electron in a 1D semi-periodic potential. The top plot shows (the real part of) the Bloch state solution which is representative of "bulk" electronic states in real metals. The bottom plot shows (the real part of) the Shockley surface state solution which is an electronic state that is localised at the surface termination of real metals. The dashed line separates the crystal region (left) from the vacuum region (right).

Realistically, these materials are not infinitely extending and have surface terminations. Factoring these terminations (break in translational symmetry) and applying the nearly-free electron approximation, valid for metals, in the solving of Schrodinger equation yields, in

addition to Bloch states, quasi 2D electron states that are localised at the surface terminations (i.e., states that exponentially decays away from the surface) called Shockley surface states (see **Figure 2.6**b). These solutions exist on surfaces whose projected band structure exhibits a band gap. For FCC metals, such as Ag and Cu, such gaps exist at the (111) surfaces. These features in the electronic structure of both Ag(111) and Cu(111) are helpful in the characterisation of the surface (e.g., in how clean it is) and of the STM tip.

hBN/Cu(111)

Translating the synthesis of 2D organic nanostructures onto functional substrates constitutes an important step for electronic device implementation. For example, functional substrates such as insulating substrates can act as dielectric spacers between a gate and a molecular overlayer as in the design of organic field-effect transistors [122]. To date, on-surface self-assembly of low-dimensional organic nanostructures on insulating substrate remains limited and warrants further study [55, 89–95]. For this reason, I considered ultrathin hexagonal boron nitride (hBN) as surface support for the growth of 2D organic nanostructures. hBN is a bulk insulator with a measured band gap of ~ 5.9 eV [123]. It has a layered structure like graphite where in each layer, boron and nitrogen atoms are covalently bonded in a honeycomb-like lattice (see **Figure 2.7**a). As for Ag(111) and Cu(111), the hBN hexagonal symmetry is preferable for the growth of structures that are of a similar symmetry such as the proposed DCA_3Cu_2 MOF.

A single layer of this material can be grown on metallic supports such as Cu(111) (see subsection 2.1.4). The growth of organic nanostructures on ultrathin hBN/Cu(111) is favourable in this work as it allows for the characterisation of the system via scanning probe microscopy (see section 2.2) whereas this is not possible for organic nanostructures on bulk hBN. hBN/Cu(111) has a lattice constant of 2.488 ± 0.016 Å [124, 125] which is very similar to that of Cu(111). Further, hBN has flat configuration on Cu(111) with a measured structural corrugation on the order of 30–70 pm [126]. Despite this almost perfect flatness, hBN shows a modulation in its local work function on Cu(111). This modulation depends on how the hBN overlayer is oriented with respect to the underlying Cu(111). The lattice mismatch between these two structures results in an observable electronic Moiré pattern in STM imaging (see **Figures 2.7**b,c). The bright (pore) regions seen in **Figure 2.7**c correspond to a region where nitrogen atoms in the hBN monolayer lie directly above the Cu atoms (in the substrate below). This in contrast to the darker (wire) regions where the nitrogen atoms do not lie directly above the Cu atoms [87]. The pore regions are regions of lower work functions than that of the wire regions. Different hBN domains with different Moiré periodicity, λ, and therefore modulations in work function are possible (see **Figure 2.7**d).

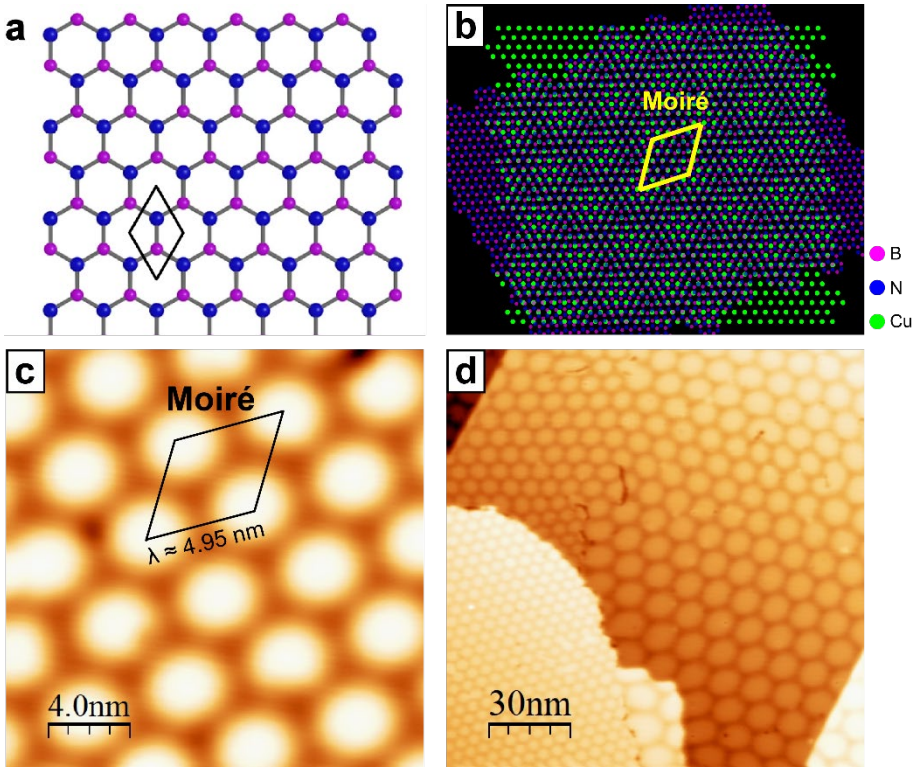

Figure 2.7: hBN/Cu(111) overview. (a) schematic of hBN monolayer structure with a lattice constant of 2.488 ± 0.016 Å (see parallelogram). The blue and magenta atoms represent nitrogen and boron atoms, respectively. (b) Schematic indicating the formation of a Moiré pattern with a unit cell periodicity indicated by the parallelogram (yellow). The Moiré pattern forms as a direct result of the lattice mismatch between the hBN layer (nitrogen and boron atoms represented by blue and magenta circles) and the underlying Cu(111) surface (Cu atoms represented by green circles). (c) STM image of a hBN monolayer domain on Cu(111) with $V_b = 4$ V, $I_t = 100$ pA showing a Moiré pattern with a periodicity, $\lambda \approx 4.95$ pm. The bright regions correspond to regions of lower surface work function compared to the darker regions in the image. (d) STM image of a larger area of hBN/Cu(111) ($V_b = 4$ V, $I_t = 100$ pA) showing multiple hBN domains on Cu(111) characterised by the different Moiré patterns observed. The STM images in (c)-(d) were provided courtesy of Mr. Benjamin Lowe.

With the Moiré periodicity, λ, the relative angle between the hBN and Cu(111), θ, can be determined according to [127]:

$$\theta = \cos^{-1}\left(1 - \left[\frac{\left(\frac{(1+\delta)a}{\lambda}\right)^2 - \delta^2}{2(1+\delta)}\right]\right) \qquad \text{(Eq. 2.1)}$$

where δ represents the relative size difference between the hBN and Cu(111) lattice which is 2% and a represents the hBN lattice constant. Likewise, the modulation in work function, ΔW, has been empirically determined to follow the following expression [128]:

$$\Delta W = 0.024 \cdot \lambda \text{ eV} \qquad \text{(Eq. 2.2)}$$

2.1.4 Substrate preparation details

The preparation of atomically clean surfaces is crucial for any on-surface growths of 2D organic nanostructures. Here, I describe the standard protocols used to prepare the surfaces used throughout this dissertation.

Ag(111) and Cu(111)

The preparation of Ag(111) and Cu(111) follow identical protocols. For each of these substrates, two sputter-anneal cycles were performed (in UHV) to achieve atomically clean surfaces. A sputter-anneal cycle consists of Ar^+ ion sputtering of the surface followed by an annealing of the surface.

Ar^+ ion sputtering involves the bombardment of the metallic surfaces with high energy Ar^+ ions to mechanically remove adsorbates or impurities from the substrate's surface. Ar^+ ions can be generated by introducing argon gas to an ion source: a high applied electric field between the anode and cathodes of the ion source (1–1.5 keV) ionises the argon gas producing Ar^+ ions which are then accelerated from the anode towards the exit aperture of the ion source (cathode) and finally toward the metallic surfaces. A sputter current on the sample of ~12 μA at an angle of incidence of 90° relative to the substrate's surface is maintained for approximately 7 minutes. The sputter current on the sample is increased or decreased by similarly increasing or decreasing the argon gas partial pressure in the UHV chamber (The target sputter current can also be achieved by adjusting the emission current between the anode and cathode). For the LT-SPM set-up used in this dissertation (see section 2.5), this partial pressure is $\sim 10^{-5}$ mbar. This procedure of Ar^+ ion sputtering, while effective at removing surface contaminants, leaves the surface highly corrugated.

Annealing the metal surfaces at 500°C (below their respective melting points) enables the surface atoms of the substrates to diffuse, facilitating an atomically flat surface reconstruction. Slow cooling to room temperature at the end of the annealing procedure ensures large terrace formations and minimises step-bunching on these surfaces.

hBN/Cu(111)

The synthesis of monolayer hBN on Cu(111) is well-established [92, 95, 129, 130]. The synthesis process first involves preparing a clean and atomically-flat Cu(111) surface using the protocols described above. After this, the Cu(111) substrate is heated to and maintained at a temperature of 920°C (just below the Cu(111) melting point) and subsequently exposing it to a partial atmosphere of borazine ($B_3H_6N_3$). The heated Cu(111) surface catalyses the formation of hBN from the adsorbed precursor borazine molecules. Once a monolayer of hBN is formed, the synthesis process self-terminates as all of the Cu(111) surface is covered by the hBN monolayer. Within our LT-SPM set-up (see section 2.5), a borazine partial pressure of $\sim 10^{-6}$

mbar is introduced into the UHV chamber and exposed to the heated Cu(111) surface for approximately 30 minutes to achieve a full hBN monolayer growth on the Cu(111) surface.

2.1.5 Sample preparation details

Here, I provide the details for synthesising the on-surface organic nano-assemblies presented in this dissertation. In all cases, a clean substrate refers to a substrate that has been prepared using the protocols described in subsection 2.1.4. The base pressure during molecular and/or metal depositions is kept below 5×10^{-10} mbar.

In Chapter 3 and Chapter 4, I present results on self-assembled 2D DCA submonolayers on Ag(111). These were synthesised in UHV by deposition of DCA molecules (> 95% purity) from the gas phase onto a clean Ag(111) surface held at room temperature. The DCA molecules were sublimed at 373 K resulting in a deposition rate of ~ 150 nm^2/s. The surface coverage of the DCA submonolayers is controlled by the deposition time. Additionally, in Chapter 3, I present results on self-assembled DCA dimers on Ag(111). These follow a similar synthesis protocol as described above, however, with the Ag(111) surface held at ~5 K and with a much lower deposition rate of ~0.08 nm^2/s.

In Chapter 5, I present results on self-assembled 2D MOFs comprised of DCA molecules and Cu atoms on Ag(111). These were synthesised in UHV by depositing DCA molecules (>95% purity) and Cu atoms (>99.99% purity) from the gas phase onto a clean Ag(111) surface. Two different MOF sample preparation procedures were considered: (i) co-deposition of DCA and Cu onto Ag(111) held at room temperature; and (ii) sequential deposition of DCA [with near full surface coverage of DCA on Ag(111)] followed by Cu onto Ag(111) held at ~100 K. Procedure (i) yields less than 10% MOF surface coverage, with a high coverage of DCA-only self-assembled domains. Procedure (ii) yields more than 60% MOF surface coverage. For both procedures, DCA was sublimed at 393 K and Cu at 1253 K with a deposition time between 1-2 minutes for DCA and Cu. In Chapter 5, I also present results on 2D MOFs comprised of DCA molecules and Cu atoms on Cu(111). These were synthesised in UHV by depositing DCA molecules (>95% purity) from the gas phase onto a clean Cu(111) surface held at room temperature. DCA was sublimed at 393 K with a deposition time of 2.5 minutes. This yields ~100% MOF surface coverage on Cu(111) where the Cu atoms are provided by the Cu(111) substrate itself.

Finally, in Chapter 6, I present results on self-assembled 2D DCA submonolayers on hBN/Cu(111). These were synthesised in UHV by deposition of DCA molecules (>95% purity) onto a clean hBN/Cu(111) held at room temperature. DCA was sublimed at 373 K with resulting deposition rate of ~150 nm^2/s. The surface coverage of the DCA submonolayers on hBN/Cu(111) is controlled by the deposition time.

2.2 Scanning Tunnelling Microscopy

There are many surface-sensitive techniques that are available to characterise 2D materials. One that stands out is scanning tunnelling microscopy (STM). STM is a powerful technique that allows us to attain a real-space map of the electronic structure and morphology of 2D materials with atomic resolution [131]. In principle, STM allows us to "see" the nanoscale world of individual atoms and molecules. This is done by measuring the current between an atomically sharp tip and the 2D sample of interest when tip and sample are several ångströms of distance apart. The development of STM has rightly led to the award of the 1986 Nobel Prize in Physics to the inventors of STM: G. Binnig and H. Rohrer [132]. Here, I provide a brief review on how STM works and its applications.

2.2.1 Operating principle

STM involves bringing an atomically sharp tip in proximity, on the order of several ångströms, to a (conducting) sample of interest (see **Figure 2.8**). When a bias voltage, V_b, is applied between the tip and the sample, a tunnelling current, I_t, is established between them. This tunnelling current is a consequence of electron tunnelling through the separation barrier at this STM junction when a bias is applied. External circuitries enable the amplification and subsequent processing and display of the measured tunnelling current. These also enable the precise lateral and vertical control of the tip's movement over the sample by an appropriate control of applied voltages to the piezoelectric actuators connected to the STM tip.

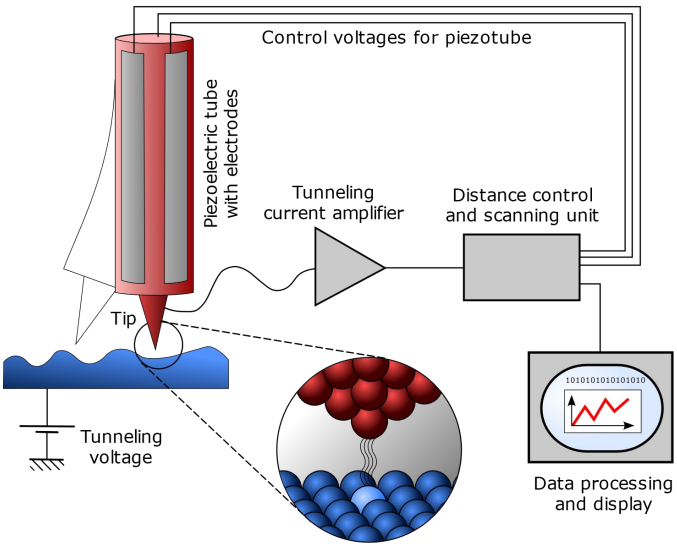

Figure 2.8: Schematic overview of a scanning tunnelling microscope. At the STM junction, a tip is brought in proximity to a sample where a tunnelling current is established when a bias is applied to the sample. External electronics allow for the amplification, processing and displaying of the tunnelling current. The position of the STM tip relative to the sample is controlled by means of piezoelectric actuators connected to the tip. The figure was republished courtesy of M. Schmid and G. Pietrzak [133] under a Creative Commons Attribution ShareAlike 2.0 Austria License.

Scanning the tip and recording the measured tunnelling current over a region of interest of the sample can result in a raster image of said region. These raster images of the sample can be obtained via two main scanning modes (see **Figure 2.9**): (i) constant-current scanning mode; and (ii) constant-height scanning mode. In constant-current mode, the tip-height, z, on a specific point on the sample is adjusted until a specified tunnelling current between the tip and sample is established. The choice of bias voltage in the STM junction, V_b, further affects the tip-height at which the specified tunnelling current, I_t, is established. Together, these parameters, V_b and I_t are called the tunnelling set point. As the tip scans across a region on the sample, a feedback loop is employed to continuously stabilise the tip-height such that a constant tunnelling current is maintained. In this case, variations in the tip-height, to maintain a constant tunnelling current, is recorded. The resulting raster image using this constant-current scanning mode is called a constant-current STM image where the observable is changes in the apparent height of the sample. In constant-height scanning mode, the tip-height at a reference point on the sample is fixed according to a specified tunnelling set point. The feedback loop is opened, and the tip is scanned over a region of interest on the sample. Throughout this operation, the tip is maintained at a constant height while variations in the tunnelling current is recorded. The resulting raster image is known as a constant-height STM image. Here the observable is changes in the tunnelling current.

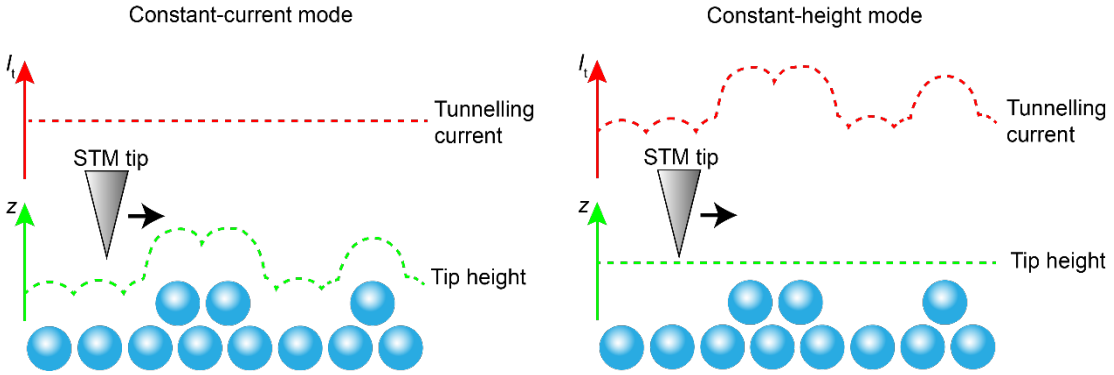

Figure 2.9: Constant-current scanning mode vs constant-height scanning mode. In constant-current STM scanning mode (left), the tip-height is continuously adjusted, by means of a feedback-loop, such that a constant tunnelling current is maintained as the tip is scanned across the sample. The recorded tip-height measures the topography of the sample. In constant-height STM scanning mode (right), the tip-height is kept fixed as the tip is scanned across the sample. The recorded tunnelling current gives a measure of the topography of the sample.

2.2.2 Quantum tunnelling

The essential Physics principle that STM operates on is quantum tunnelling. This same principle that enables the nuclear fusion of Hydrogen atoms into heavier Helium is the necessary ingredient that we need to peer into the world of atoms. According to quantum mechanics, when an electron encounters a potential barrier with a finite width, where the electron energy is less than the barrier height, there is a small but non-zero probability that

electron can appear on the other side of that barrier. In contrast to the classical world, we say that the electron has "tunnelled" through the barrier.

To demonstrate this quantitatively, we solve the time-independent Schrödinger equation for a simple 1D model representing this situation (see **Figure 2.10**):

$$\left(\frac{-\hbar^2}{2m_e}\frac{d^2}{dz^2} + V(z)\right)\Psi = E\Psi \qquad \text{(Eq. 2.3)}$$

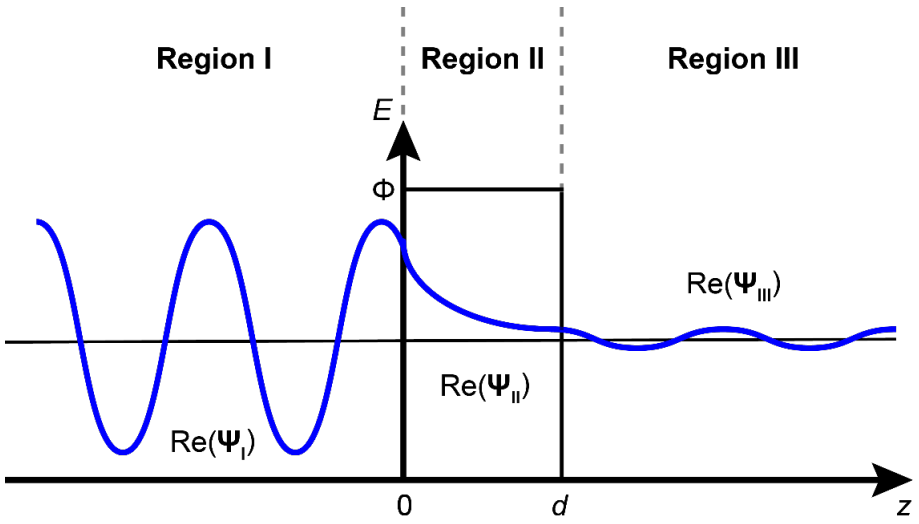

Figure 2.10: Schematic of quantum tunnelling as predicted by the Schrödinger equation. The figure shows the real part of a wavefunction for an electron with energy, E_0, when it encounters a potential barrier (from the left) of height, $\Phi > E_0$, and width, d. In the potential barrier (region II), the electron wavefunction decays exponentially to a severely decayed sinusoidal wavefunction right of the barrier (region III). In this region III, $|\Psi_{III}|^2 > 0$ indicating that there is a small probability that an electron can tunnel from the left side of the barrier to the right side of the barrier.

Here, we consider the specific situation of an electron with energy, E_0, encountering a potential barrier (from the left) with height, Φ, and width, d. We then solve for the electron wavefunctions in the regions I (left of the barrier), II (in the barrier) and III (right of the barrier) as indicated. For each of these regions, the wavefunctions are of the following forms:

$$\Psi_1 = e^{ikz} + A \cdot e^{-ikz}$$
$$\Psi_2 = B \cdot e^{i\kappa z} + C \cdot e^{-i\kappa z}$$
$$\Psi_3 = D \cdot e^{ikz}$$

$$\text{with } k = \frac{\sqrt{2m_e E_0}}{\hbar} \text{ and } \kappa = \frac{\sqrt{2m_e(\Phi - E_0)}}{\hbar}$$

where m_e is the electron mass and $\hbar$ is Planck's constant. Ensuring the continuity of the electron wavefunction and its derivative in z allows us to determine the coefficients (A, B, C, D) [134].

The probability that an electron tunnels through the potential barrier is then given by the transmission coefficient, T:

$$T = \frac{|\Psi_1|^2}{|\Psi_3|^2} = \frac{A^2}{D^2} = \left[\left(\frac{k^2+\kappa^2}{2k\kappa}\right)^2 \sinh(\kappa d)\right]^{-1} \qquad \text{(Eq. 2.4)}$$

We can simplify the above expression by assuming that barrier potential is high compared to the energy of the electrons, $\Phi \gg E_0$, that is, $\kappa d \gg 1$, to obtain:

$$T \approx \frac{16k^2\kappa^2}{(k^2+\kappa^2)^2} \cdot e^{-2\kappa d} \qquad \text{(Eq. 2.5)}$$

This tells us that the tunnelling probability depends exponentially on the barrier width, d. This particular trait is inherited by a more formal quantitative modelling of the STM tunnelling junction and is responsible for the kind of spatial resolution that is offered by STM.

2.2.3 Bardeen Transfer Hamiltonian theory

In 1961, John Bardeen introduced a transfer Hamiltonian approach to rationalize observations of tunnelling of electrons between superconductors that are separated by thin oxide barriers [135]. His approach is instrumental in laying down the basic theory for vacuum tunnelling necessary the development of a working STM. A metal-insulator-metal junction can be modelled by a simple 1D model where there is a non-zero potential barrier separating the left and right regions of zero potential (see **Figure 2.11**).

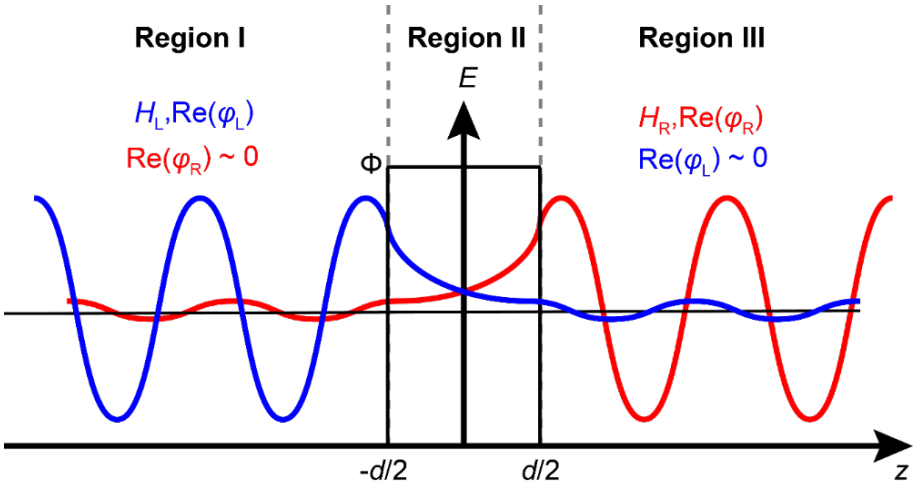

Figure 2.11: Schematic approach to Bardeen tunnelling mechanism. The Hamiltonian for the system can be made to be separable i.e., $H = H_L + H_R$ where H_L is defined over regions I and II and H_R is defined over regions II and III. This is possible since the $H_L \cdot H_R \sim 0$ in region II where the solutions to the H_L, $H_R[\varphi_L(\text{blue}), \varphi_R(\text{red})]$ decays exponentially in the potential barrier to near-zero. When these solutions are analytically continued to the other side of the barrier, we see that the overlap between the wavefunctions is negligible. Fermi's Golden Rule can then be used to evaluate the probability of an electron tunnelling from a state in the region I to a state in region III and vice versa.

The full Hamiltonian of the junction can be written as a combination of three terms:

$$H = H_L + H_R + H_T \qquad \text{(Eq. 2.6)}$$

with:

$$H_L = \frac{-\hbar^2}{2m_e}\frac{\mathrm{d}^2}{\mathrm{d}z^2} + V_L(z), \qquad z \in (\text{Region I} \cup \text{Region II})$$

$$H_R = \frac{-\hbar^2}{2m_e}\frac{\mathrm{d}^2}{\mathrm{d}z^2} + V_R(z), \qquad z \in (\text{Region II} \cup \text{Region III})$$

H_T in Eq. 2.6 represents the (unknown) transfer Hamiltonian for the system. Bardeen's key insight was that the Hamiltonian is separable to a first approximation. To see this, we note that the wavefunction solutions to H_L and H_R separately fall exponentially to near-zero in the potential barrier (blue and red curves, respectively in **Figure 2.11**) and that the overlap of their wavefunctions on either side of the potential barrier is insignificant, i.e., $\varphi_L \cdot \varphi_R \approx 0$ in regions I and regions III, respectively. With this, to a first approximation, we can set $H_T = 0$ in Eq. 2.6. Using Fermi's Golden Rule, we can then evaluate the probability of an electron tunnelling from a state $\varphi_{L,\mu}$ in region I (left) to a state $\varphi_{R,\nu}$ in region III (right), $P_{\mu\nu}$:

$$P_{\mu\nu} = \left(\frac{2\pi}{\hbar}\right)\left|M_{\mu\nu}\right|^2 \delta(E_{R,\nu} - E_{L,\mu}) \qquad \text{(Eq. 2.7)}$$

Here, $E_{L,\mu}$ and $E_{R,\nu}$ are the energies of the states $\varphi_{L,\mu}$ and $\varphi_{R,\nu}$, respectively. $M_{\mu\nu}$ is given by the following expression:

$$M_{\mu\nu} = \left\langle \varphi_{R,\nu} \middle| H \middle| \varphi_{L,\mu} \right\rangle \qquad \text{(Eq. 2.8)}$$

With the new modified Hamiltonian, $H = H_L + H_R$, $M_{\mu\nu}$ can be written as:

$$M_{\mu\nu} = \frac{\hbar^2}{2m_e}\left(\varphi_{L,\mu}\frac{\partial \varphi^*_{R,\nu}}{\partial z} - \varphi^*_{R,\nu}\frac{\varphi_{L,\mu}}{\partial z}\right)\Bigg|_{z=a} \qquad \text{(Eq. 2.9)}$$

where a is point in between regions I and III. The results so far do not depend on the details of potential barrier as long as the overlap of the wavefunctions in the regions on either side of the barrier is negligible. Eq. 2.9 can be generalised to three dimensions:

$$M_{\mu\nu} = \frac{\hbar^2}{2m_e}\int_{S_{LR}} \varphi_{L,\mu}\nabla\varphi^*_{R,\nu} - \varphi^*_{R,\nu}\nabla\varphi_{L,\mu}\, dS \qquad \text{(Eq. 2.10)}$$

where the integral is evaluated over a surface, S_{LR}, separating regions on either side of the potential barrier.

Here, the key take-away is that the calculation of $M_{\mu\nu}$ and therefore the tunnelling probability (hence the tunnelling current) requires the knowledge of only the wavefunctions of the separated left and right regions and not the full system Hamiltonian in Eq. 2.6 nor the full system wavefunction. Using this approach, the tunnelling current between a metallic tip and a conducting sample separated by a tunnelling barrier can be written as:

$$I_t = \frac{2\pi e}{\hbar}\sum_{\mu,\nu} f(E_\mu)\left(1 - f(E_\nu + eV_\mathrm{b})\right)\left|M_{\mu,\nu}\right|^2 \delta(E_\nu - E_\mu) \qquad \text{(Eq. 2.11)}$$

where e is the electron charge, $f(E)$ is the Fermi-Dirac distribution, and V_b is the applied tunnelling bias between the tip and sample.

2.2.4 Tersoff-Hamann model

A more realistic theoretical description of an STM junction was provided by Tersoff and Hamann [136, 137]. They considered an STM junction as seen in **Figure 2.12**. The geometry of the tip apex is assumed to be spherical with a radius, R, and centred at $\mathbf{r}_0$. The tip apex is further assumed to be separated from the sample by a distance d.

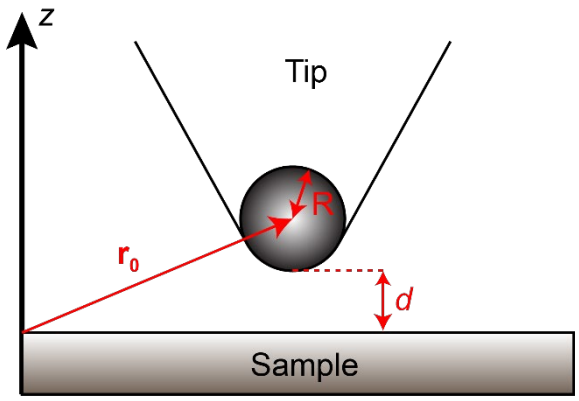

Figure 2.12: Tip-sample geometry used in the Tersoff-Hamann model. Tersoff-Hamann model makes use of a simplified model geometry to approximate the tip wavefunction. Here, the tip apex, centred at $\mathbf{r}_0$, is assumed to be spherical with a radius, R, and separated from the surface of the sample by a distance, d.

Following their treatment of this problem, we make several assumptions. We assume low temperatures and voltages, $eV_\mathrm{b} \ll \Phi$ (barrier height). Under these conditions, $f(E)\sim 1$ for $E < E_F$ (Fermi level) and 0 otherwise. Then Eq. 2.11 can be simplified to:

$$I_t = \frac{2\pi}{\hbar} e^2 V_\mathrm{b} \sum_{\mu,\nu} \left|M_{\mu,\nu}\right|^2 \delta(E_\mu - E_F)\delta(E_\nu - E_F) \qquad \text{(Eq. 2.12)}$$

Here, the label μ and ν labels the sample and tip, respectively. We further assume the wavefunctions for both the sample and the tip. For the sample we consider wavefunctions of the form:

$$\Psi_\nu = \frac{1}{\sqrt{\Omega_S}} \sum_{\mathbf{G}} a_{\mathbf{G}} \exp\left(-\sqrt{\kappa^2 + \left|\boldsymbol{k}_\parallel + \boldsymbol{G}\right|^2} z\right) \exp(i[\boldsymbol{k}_\parallel + \boldsymbol{G}] \cdot \mathbf{x}) \qquad \text{(Eq. 2.13)}$$

here, $\kappa = \sqrt{2m\Phi}/\hbar$, Ω_S is the normalization volume of the sample, $a_{\mathbf{G}}$ are Fourier coefficients, $\mathbf{G}$ is the reciprocal lattice vector for the sample, and $\boldsymbol{k}_\parallel$ is a surface Bloch wavevector. The direction z is orthogonal to the surface of the sample while $\mathbf{x}$ spans the plane parallel to the sample's surface. These wavefunctions are constructed in a way that satisfies Bloch's Theorem in $\mathbf{x}$ (second exponential term in Eq. 2.13) and decays exponentially into the vacuum perpendicular to the surface, parallel to z (first exponential term in Eq. 2.13). Due to the proposed geometry of the tip apex, we model the wavefunction of the spherical tip apex with a spherical *s*-wave wavefunction:

$$\Psi_\mu = \frac{1}{\sqrt{\Omega_T}} \kappa R e^{\kappa R} \frac{1}{\kappa|\mathbf{r} - \mathbf{r}_0|} e^{-\kappa|\mathbf{r}-\mathbf{r}_0|} \qquad \text{(Eq. 2.14)}$$

where Ω_T is the normalization volume of the tip apex. With these assumptions, the tunnelling matrix elements, $M_{\mu\nu}$ can be calculated:

$$M_{\mu\nu} = \frac{4\pi\hbar^2}{2m_e} \frac{1}{\sqrt{\Omega_T}} R e^{\kappa R} \Psi_\nu(\mathbf{r}_0) \qquad \text{(Eq. 2.15)}$$

With this, the tunnelling current can then be calculated:

$$I_t = 32 \frac{\pi^3}{\hbar\kappa^4} e^2 V_\mathrm{b} \Phi^2 R^2 e^{2\kappa R} \frac{1}{\Omega_T} \sum_{\mu,\nu} |\Psi_\nu(\mathbf{r}_0)|^2 \delta(E_\mu - E_F) \delta(E_\nu - E_F) \qquad \text{(Eq. 2.16)}$$

Local density of states (LDOS) for the tip and the surface are defined as follows:

$$\rho_\mathrm{tip}(E) = \frac{1}{\Omega_T} \sum_{\mu} \delta(E_\mu - E) \qquad \text{(Eq. 2.17)}$$

$$\rho_\mathrm{surface}(E, \mathbf{r}_0) = \sum_{\nu} |\Psi_\nu(\mathbf{r}_0)|^2 \delta(E_\nu - E) \qquad \text{(Eq. 2.18)}$$

Leading to a final expression for the tunnelling current:

$$I_t \propto V_\mathrm{b} \rho_\mathrm{tip}(E_F) \rho_\mathrm{surface}(E_F, \mathbf{r}_0) \qquad \text{(Eq. 2.19)}$$

This treatment shows that the tunnelling current, therefore, measures the local density of states (LDOS) of the sample at the Fermi energy at the tip location, $\mathbf{r}_0$, above the surface of the sample.

2.2.5 WKB approach to tunnelling

The tunnelling current as defined by Eq. 2.19 is restricted to tunnelling bias voltages close to the Fermi level. Selloni et al [138] generalized the expression of the tunnelling current to larger bias windows using the semi-classical Wentzel-Kramers-Brillouin (WKB) approach:

$$I_{\mathrm{t}}(V_{\mathrm{b}}) \propto \int_{E_F}^{E_F+eV_{\mathrm{b}}} \rho_S(E_F + eV_{\mathrm{b}} + \varepsilon)\rho_T(E_F + \varepsilon)T(eV_{\mathrm{b}}, z, \varepsilon)\, d\varepsilon \qquad \text{(Eq. 2.20)}$$

with:

$$T(eV_{\mathrm{b}}, z, \varepsilon) = \exp\left(-\frac{2m_e}{\hbar^2}\sqrt{\Phi_S + \Phi_T + eV_b - 2\varepsilon z}\right) \qquad \text{(Eq. 2.21)}$$

Here, $T(eV_{\mathrm{b}}, z, \varepsilon)$ is the transmission function and is related to the tunnelling matrix element, $M_{\mu\nu}$. Φ_S and Φ_T are the work functions for the surface and the tip, respectively. The exponential term in the transmission function shows an acute sensitivity in z. That is, the tunnelling current is most significantly dominated by the part of the tip that is closest to the sample's surface e.g., a single atom at the tip apex. This gives significant lateral resolution, i.e., atomic resolution when it comes to measuring variations in the tunnelling current between the tip and the sample. Furthermore, the tunnelling current contains information regarding the LDOS of both the tip and the sample. Typically, the STM tip material is chosen such that the LDOS of the tip is relatively unremarkable (e.g., constant). This ensures that STM imaging is not heavily influenced by the electronic structure of the tip but instead by the electronic structure of the sample. On that note, STM imaging does not probe the topography of the system but rather its electronic structure. Despite this, in many cases, the electronic structure does follow the topography of the system since the electron density of atoms and molecules closely hugs the structure of said atoms and molecules.

2.2.6 State-of-the-art STM imaging

Advancements in engineering controls such as piezoelectronic actuators (to control the movement of the tip in x-y-z space), external electronics (e.g., for signal amplification, feedback control, data processing and data display), vibration controls, vacuum technologies, and cryogenics has enabled the exploitation of STM as an almost universal technique to image and to characterise the world at the nanoscale. To-date, STM has been used to image a variety

of metallic surfaces and even semiconducting surfaces such as Si [139–141]. Adsorbates on these surfaces such as atoms [142–144], individual molecules [31, 145–147] and molecular assemblies [148–151], similarly, have been imaged via STM (see **Figure 2.13**). STM has even been extended to image ultrathin layers of insulating materials. Typically, these materials are grown on metallic surfaces as to facilitate electron conduction between the substrate (through the ultrathin insulating materials) and the STM tip. The utility in this is that the electronic properties of the adsorbates can be effectively decoupled from the underlying metallic substrate, i.e., this minimises hybridisation and destruction of the intrinsic adsorbate electronic states. Adsorbates on these surface-supported ultrathin insulators such as MgO [152–154], CuO [155, 156], hBN [55, 91, 92, 94] and NaCl [157–159] has been imaged via STM (see **Figure 2.13**). These examples are by no means exhaustive and only sample a small subset of systems studied via STM.

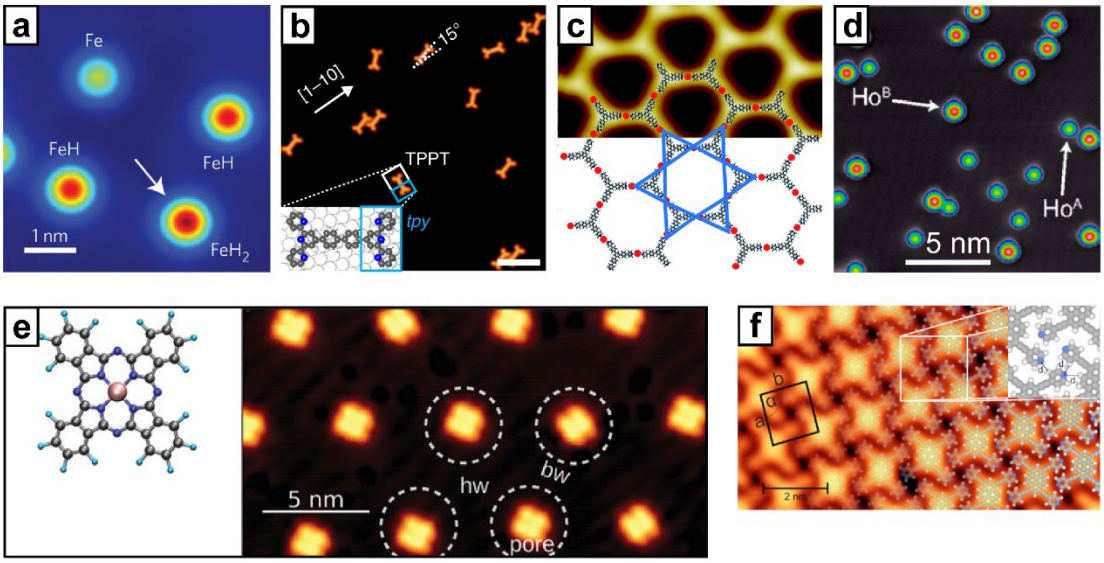

Figure 2.13: Overview of systems that have been imaged via STM. (a) Constant-current STM imaging of Fe and Fe-H complexes adsorbed on Pt(111). (b) Constant-current STM imaging of terpyridine-phenyl-phenyl-terpyridine (TPPT) molecules adsorbed on Ag(111). Scale bar: 5 nm (c) Constant-current STM imaging of a self-assembled metal-organic framework comprised of 1,3,5-trispyridiylbenzene (TPyB) molecules coordinated with Cu atoms (red dots). (d) Constant-current STM imaging of holmium (Ho) atoms adsorbed on a monolayer of MgO grown on Ag(100). Here two different adsorption configurations for the Ho atoms are possible (Ho^A and Ho^B). (e) Left: fluorinated cobalt phthalocyanine ($F_{16}CoPc$) chemical structure; right: constant-current STM imaging of $F_{16}CoPc$ molecules adsorbed on ultrathin hBN grown on Cu(111). (f) Constant-current STM imaging of a self-assembled molecular film comprised of 1,3,6,8-tetrakis(pyridine-4-ylethynyl)pyrene on ultrathin hBN grown on Cu(111). (a) was adapted from ref. [160] by permission from Copyright Clearance Centre: Springer Nature, Nature Nanotechnology, copyright (2017). (b), (e), and (f) were adapted from refs. [37], [94], and [95], respectively under a Creative Commons Attribution 4.0 International License. (c) was adapted from ref. [161] with permission from the Royal Society of Chemistry. (d) was reprinted with permission from ref. [154]; copyright (2017) by the American Physical Society.

2.2.7 Atomic-scale manipulation

Lateral manipulation

Precise control of the STM tip movement has enabled the use of the STM tip in manipulating the lateral position of adsorbates on a surface. By positioning the STM tip in extreme proximity to an adsorbate, attractive or repulsive tip-adsorbate interactions can be activated. The STM tip motion can then be used to pull or push these adsorbates, depending on the nature of the tip-adsorbate interactions, from their previous location on a surface to a new one. This method has found uses such as arranging adatoms or molecules on the surface in a specified geometry. On metal surfaces with a Shockley surface state, the arrangement of the atoms/molecules can lead to phenomena such as quantum corrals [162] or lead to band-engineering [163]. This method has also been used to form the famous "world's smallest movie" [164] (see **Figure 2.14**).

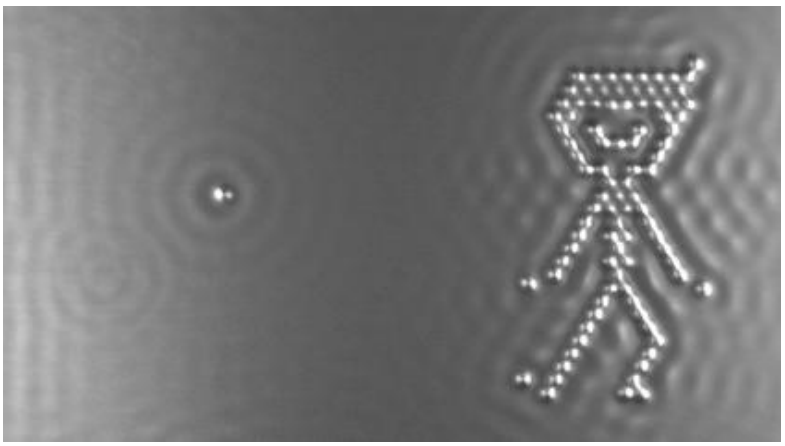

Figure 2.14: A still frame from the movie "*A Boy and His Atom*" [164]**.** Each frame was taken by STM imaging after positioning CO molecules on a Cu(111) surface in a specified arrangement by means of STM tip lateral manipulation. Here, the collection of CO molecules on the right is the "*Boy*" and the lone CO molecule on the left is his "*Atom*". The figure is reprinted under a fair-use policy.

Vertical manipulation

In addition to lateral manipulation of adsorbates on surfaces, the STM tip can be used to displace adsorbates directly off a surface via vertical manipulation. This technique has been used extensively to increase the spatial resolution of an STM tip and in particular an nc-AFM tip (see section 2.4) by means of picking up adsorbates such as CO [165–167], Xe [168], NO [169] and CuO [170] at the tip apex.

In this dissertation, I have used vertical manipulation via STM to create CO-functionalised STM and nc-AFM tips (see section 2.4). Protocols for CO tip-functionalisation is well-established: CO is adsorbed onto Ag(111) by introducing residual CO gas (partial pressure of $\sim 5 \times 10^{-8}$ mbar) for a short duration (~3 seconds; in units of Langmuirs, this is ~0.113 L) into the UHV chamber housing the STM head. The short duration ensures that the Ag(111) surface is not saturated with CO molecules. **Figure 2.15**a shows an STM image of an

Ag(111) surface after introducing CO molecules into the UHV chamber. The STM tip is then positioned above a CO molecule at a tip height defined by the tunnelling set point, $I_t = 25$ pA, $V_b = 20$ mV. The STM tip is then brought closer to the CO molecule until an abrupt change in the tunnelling current is detected. This typically happens at a height ~400 pm below the set point. The positioning of the CO molecule at the tip apex is crucial as to avoid unnecessary imaging artefacts. This can be assessed by imaging another CO molecule with the newly acquired CO functionalised tip. If this procedure is done correctly, STM imaging of another CO molecule would yield a bright protrusion that is perfectly centred at an imaged CO molecule (see **Figure 2.15**b). If not, the CO molecule can be dropped from the tip apex by a series of rapid tunnelling bias changes (pulses). The procedure, i.e., picking up a CO molecule, is then repeated until the desired outcome is achieved. In some cases, the tip apex morphology is not conducive to the desired positioning of the CO molecule at the tip apex. When this happens, the tip is reconditioned prior to picking up a CO molecule (see subsection 2.5.3). This procedure is similar for picking up CO molecules off a Cu(111) surface. The CO molecule at the tip apex is positioned such that the carbon atom is attached to the tip and the oxygen atom is away from the tip [171] (see **Figure 2.15**c).

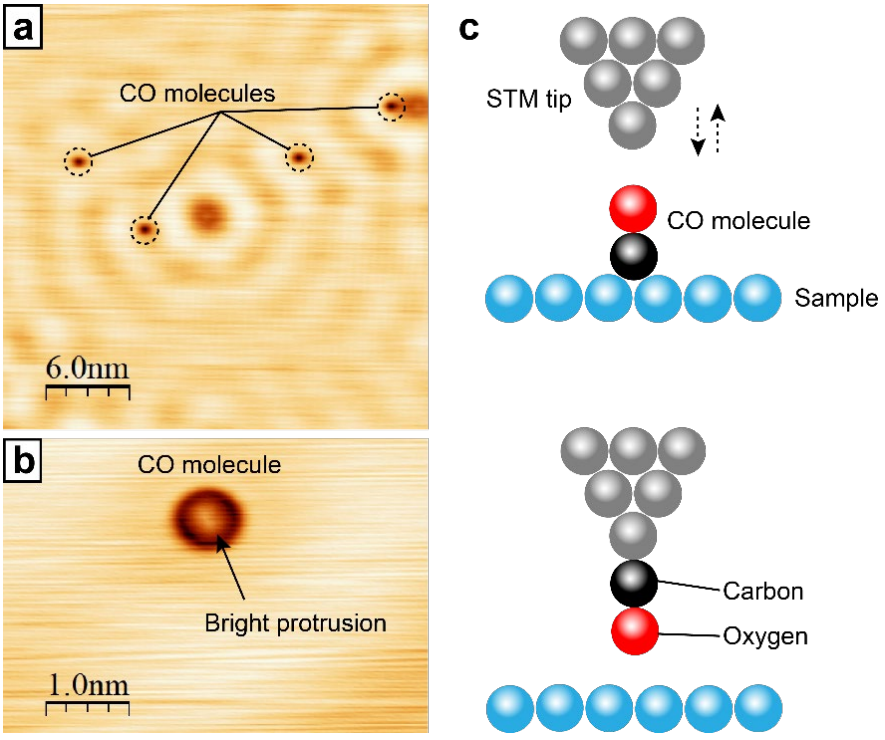

Figure 2.15: CO tip-functionalisation via STM vertical manipulation. (a) Constant-current STM image of an Ag(111) surface after deposition of CO molecules. The CO molecules appear as dark circular features in STM imaging. (b) Constant-current STM imaging of a CO molecule with a tip functionalised with a CO molecule. If the CO molecule sits perfectly at the tip apex, a bright protrusion is seen centred at the imaged CO molecule. (c) Schematic of the CO tip functionalisation. The tip is moved closer to a CO molecule adsorbed onto the surface until the CO molecule is transferred to the tip apex. Once this happens, the carbon atom of the CO molecule is attached to the tip apex and the oxygen atom of the CO molecule sits closer to the surface of the sample.

2.3 Scanning Tunnelling Spectroscopy

Scanning tunnelling spectroscopy (STS) is an extension of the STM technique. Complementary to STM, STS is used to extract information regarding the electronic properties of samples of interest. While STM measures the tunnelling current, STS measures the derivative of the tunnelling current. STS has been used to provide a real-space mapping of electronic states of materials with exquisite resolution. Here, I discuss the working principle of STS and how I have used this technique throughout this dissertation.

2.3.1 Elastic tunnelling differential conductance spectroscopy

Taking the result of the Tersoff-Hamann model for the tunnelling current Eq. 2.19 and differentiating it with respect to the tunnelling bias voltage, V_b, we find that the differential conductance is proportional to the LDOS of both the tip and of the sample:

$$\frac{\mathrm{d}I_\mathrm{t}}{\mathrm{d}V_\mathrm{b}} \propto \rho_T(E_F)\rho_S(E_F, \mathbf{r}_0) \qquad \text{(Eq. 2.22)}$$

When the LDOS of the tip is known or unremarkable (e.g., constant in energy), the differential conductance provides a measure of the LDOS of the sample. This result is not only limited to the results of the Tersoff-Hamman model. In fact, from Eq. 2.20, taking the derivative yields:

$$\frac{\mathrm{d}I_\mathrm{t}}{\mathrm{d}V_\mathrm{b}} \propto e\rho_S(eV_\mathrm{b})T(eV_\mathrm{b}, z, \varepsilon) + e\int_0^{eV_\mathrm{b}} \rho_S(\varepsilon)\frac{\mathrm{d}T(eV_\mathrm{b}, z, \varepsilon)}{\mathrm{d}V_\mathrm{b}}d\varepsilon \qquad \text{(Eq. 2.23)}$$

For small bias voltages, we assume that the transmission function is roughly constant in that energy range. Then, we get:

$$\frac{\mathrm{d}I_\mathrm{t}}{\mathrm{d}V_\mathrm{b}} \propto e\rho_S(eV_\mathrm{b}) \qquad \text{(Eq. 2.24)}$$

Here, the differential conductance, $\mathrm{d}I_\mathrm{t}/\mathrm{d}V_\mathrm{b}$, directly measures the electronic structure of the sample via its LDOS. For larger tunnelling biases, the normalised differential conductance, $(\mathrm{d}I_\mathrm{t}/\mathrm{d}V_\mathrm{b})/(I_\mathrm{t}/V_\mathrm{b})$ is a more appropriate measure of the LDOS of the sample [172]. These expressions for the differential conductance (as a measure for the sample LDOS) are valid for when there is no loss in energy during the tunnelling process, i.e., when the tunnelling is *elastic*. Throughout this dissertation, the terms $\mathrm{d}I_\mathrm{t}/\mathrm{d}V_\mathrm{b}$ and $\mathrm{d}I/\mathrm{d}V$ are used interchangeably to mean the differential conductance.

2.3.2 Inelastic tunnelling differential conductance spectroscopy

In some cases, for example when tunnelling through molecules, electrons can couple to internal degrees of freedom such as molecular vibrational modes [173–175] and spin excitations [31,

176]. Once an electron has sufficient energy to couple to these different internal modes, a new tunnelling channel is opened. That is, in addition to direct tunnelling from tip to adsorbate or vice versa, there is an additional tunnelling channel whereby electrons can tunnel between the tip and adsorbate via coupling to these internal modes. In the case of off-resonant inelastic tunnelling, these processes manifest themselves as a symmetric step function in $\mathrm{d}I_\mathrm{t}/\mathrm{d}V_\mathrm{b}$ measurements (see **Figure 2.16**b).

Inelastic tunnelling can also take place during resonant tunnelling through an electronic state of an adsorbate. When the lifetime of such an electronic state is long enough, coupling to internal modes such as molecular vibrational modes are possible. On-resonant inelastic tunnelling is typical on decoupled molecular systems (e.g., molecules on insulators) [89]. For these systems, vibronic excitations during the tunnelling process appear as satellite peaks in the $\mathrm{d}I_\mathrm{t}/\mathrm{d}V_\mathrm{b}$ signal at multiples of the energy of the vibrational mode above the molecular resonances (see **Figure 2.16**c).

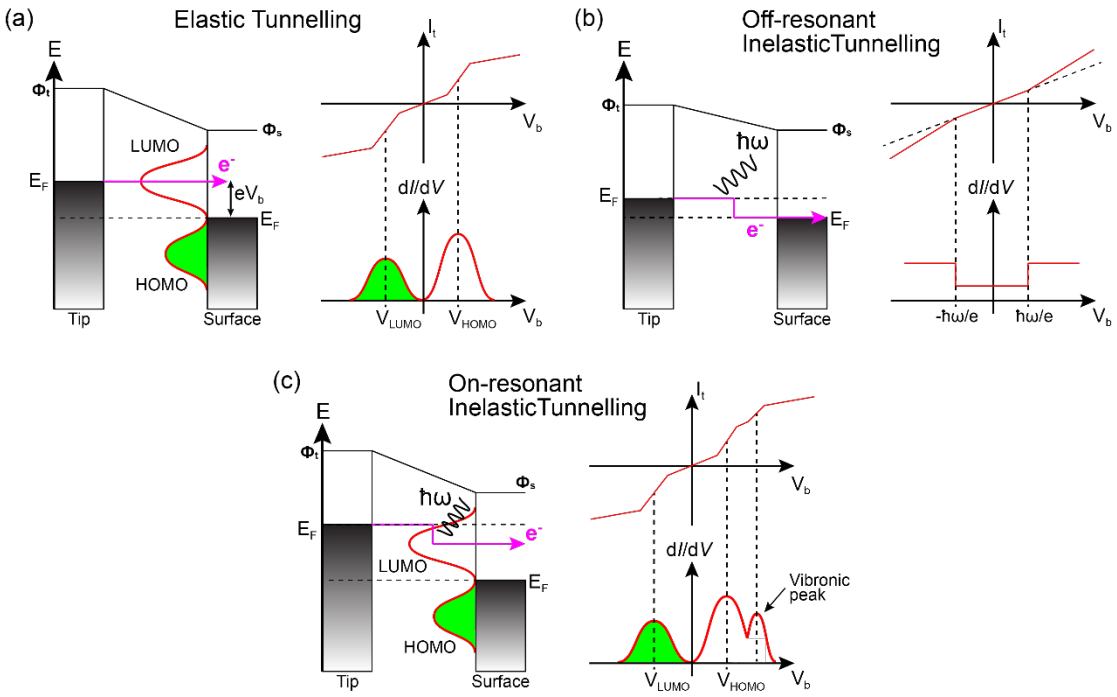

Figure 2.16: Elastic vs Inelastic tunnelling spectroscopy mechanism. (a) Energy level diagram showing elastic tunnelling through a molecule at a positive bias eV_b. Here Φ_t and Φ_s are the work functions of the tip and the sample, respectively. Electrons tunnel from the tip into the sample probing the unoccupied states of the molecule, i.e., lowest unoccupied molecular orbital (LUMO). $\mathrm{d}I/\mathrm{d}V$ curve shows the position of the molecular states in energy. (b) Off-resonant inelastic tunnelling: at sufficiently high energy ($V_\mathrm{b} = \hbar\omega/\mathrm{e}$), electrons tunnelling from the tip can excite a vibrational mode of the molecule. This opens an additional tunnelling channel resulting in an increase in conductance at that energy. This appears as symmetric steps in $\mathrm{d}I/\mathrm{d}V$ measurements. (c) On-resonant inelastic tunnelling: electrons tunnelling through a molecular state can couple to the vibrational modes of the molecule. These vibronic excitations appear as satellite peaks to the LUMO peak in $\mathrm{d}I/\mathrm{d}V$ measurements.

2.3.3 dI/dV STS acquisition modes

Numerical dI/dV

Measuring the differential conductance, $\mathrm{d}I/\mathrm{d}V$, signal can be done by first measuring the current signal, I_t, while continuously sweeping the bias voltage, V_b, at a fixed tip location and at a fixed tip-sample separation. Numerically differentiating the obtained I-V curve yields the desired $\mathrm{d}I/\mathrm{d}V$ signal. This technique of $\mathrm{d}I/\mathrm{d}V$ acquisition is suitable for obtaining signal over small bias ranges where multiple I-V can be obtained in quick succession which are then averaged to increase signal-to-noise ratio (SNR).

Lock-in technique

An alternative way to measure the $\mathrm{d}I/\mathrm{d}V$ signal can be done via a lock-in technique. This involves adding a small sinusoidal bias modulation to the tunnelling bias voltage, $V_{b,0}$:

$$V_b(\tau) = V_{b,0} + V_A \sin(2\pi f \tau) \qquad \text{(Eq. 2.25)}$$

where V_A and f is the amplitude and frequency of the bias modulation, respectively. The resulting bias, $V_b(\tau)$, causes a response in the measured tunnelling current, $I_\mathrm{t}(V_\mathrm{b}(\tau))$. This tunnelling current is then fed into a lock-in amplifier where the signal is mixed (multiplied) with the n^{th} harmonic of the modulating signal with a signal phase offset, $\delta\phi$, and passed through a low-pass filter. The low pass filter essentially averages the signal over a given time, T. The resulting output signal is the nth order demodulated signal, S_n:

$$S_n = \frac{1}{T}\int_0^T \sin(2\pi n f \tau + \delta\phi)\, I_\mathrm{t}(V_\mathrm{b}(\tau))\, d\tau \qquad \text{(Eq. 2.26)}$$

When T is made sufficiently large, the averaging process removes all time-dependent components. Taylor expansion of the $I_\mathrm{t}(V_\mathrm{b}(\tau))$ and taking the limit for $T \to \infty$, yields for the 1$^{\mathrm{st}}$ order demodulated signal, S_1:

$$S_1 = \frac{V_A}{2}\cos(\delta\phi)\left.\frac{\mathrm{d}I_\mathrm{t}(V_\mathrm{b}(\tau))}{\mathrm{d}V_\mathrm{b}(\tau)}\right|_{V_{\mathrm{b,o}}} \qquad \text{(Eq. 2.27)}$$

By adjusting the reference phase such that $\delta\phi = 0$, S_1 is then directly proportional to $\mathrm{d}I_\mathrm{t}/\mathrm{d}V_\mathrm{b}$.

This technique poses several advantages in acquiring $\mathrm{d}I/\mathrm{d}V$ signals. First, this technique is highly effective at removing unwanted frequency components (noise) far from the reference frequency, f. Further, from Eq. 2.27, we note that the signal is proportional to V_A. Freedom in choosing both parameters, f and V_A, can yield a drastic increase in the SNR compared to numerically acquired $\mathrm{d}I/\mathrm{d}V$ signals. Further, this technique has a better dynamic bias range, i.e., it is not restricted to small bias ranges. Despite these advantages, this technique has several drawbacks. Firstly, higher V_A results in greater smearing of the features observed in

the $\mathrm{d}I/\mathrm{d}V$ signal, i.e., the energy resolution of the measurement is decreased by $\sim 2V_A$. Therefore, a judicious choice of V_A must be made to ensure a large a SNR but not too large as to obscure any interesting features in the $\mathrm{d}I/\mathrm{d}V$ signal. Secondly, acquisition of $\mathrm{d}I/\mathrm{d}V$ signals via this lock-in technique is generally more time-consuming compared to numerically acquired $\mathrm{d}I/\mathrm{d}V$ signals. This is because a reliable output of S_1 relies on a large time integration, T. Typically, T is picked to be 3–5 times the time constant, τ_{LP}, of the low-pass filter to be effective. τ_{LP} is related to the cut-off frequency, f_{LP}, of the low-pass filter by $\tau_{LP} = 1/(2\pi f_{LP})$. The cut-off frequency, f_{LP}, of the low-pass filter can be tuned to a desired value. Here, therefore, is a trade-off between SNR and acquisition time: a low f_{LP} means a longer acquisition time but high SNR, whereas a high f_{LP} means a shorter acquisition time but low SNR. This trade-off must be further considered with other factors such as thermal drift, tip height stabilisation, etc. Where this technique is used in this dissertation, the relevant parameters used in the acquiring the $\mathrm{d}I/\mathrm{d}V$ signal are quoted.

2.3.4 d*I*/d*V* STS maps

We can extend $\mathrm{d}I/\mathrm{d}V$ measurements at a single point on a surface of a sample to an entire defined area of the surface. This enables a direct visualisation of the LDOS of the sample as a function of lateral spatial coordinates, x and y: $\rho_S(x, y)$. This, therefore, provides a picture of the spatial extent of interesting electronic states at the surface. There are two main ways by which we can obtain measurements of $\mathrm{d}I/\mathrm{d}V(x, y)$: (i) $\mathrm{d}I/\mathrm{d}V$ STS grids; or (ii) $\mathrm{d}I/\mathrm{d}V$ STS mapping. Both methods have been used as a part of this work. Their descriptions are presented below.

dI/dV STS grids

This method involves defining an (x, y)-grid over an area of interest on the surface. At each (x, y) location within this grid, the STM tip is positioned at some defined tip-sample separation and then a measurement of differential conductance as a function of bias, $\mathrm{d}I/\mathrm{d}V(V_\mathrm{b})$, is made (either via numerical differentiation of I-V curves or via the lock-in technique). Once this procedure is completed, a measurement of the differential conductance as function of spatial location, x, y and of the tunnelling bias, V_b, i.e., $\mathrm{d}I/\mathrm{d}V(V_\mathrm{b}, x, y)$, is obtained. Post-processing of this three-dimensional data array can then be performed. In particular, one can take a cut of the $\mathrm{d}I/\mathrm{d}V(V_\mathrm{b}, x, y)$ measurement at a particular bias, V_0, which gives a measure of the LDOS of the surface at that bias, V_0. With this data acquisition method, several considerations must be made such as grid resolution, bias resolution, acquisition time, drift correction and tip-sample distance.

The consideration of the tip-sample distance is of particular importance especially when performing measurements on systems where large variations in sample topography is

present. Large variations in the topography can make interpretation of $\mathrm{d}I/\mathrm{d}V(V_\mathrm{b}, x, y)$ difficult due to the convolution of topography with electronic state contributions to the $\mathrm{d}I/\mathrm{d}V$ signal. $\mathrm{d}I/\mathrm{d}V$ STS measurements at each (x, y) location within the grid can be taken at a fixed tip-sample separation (relative to a single point on the surface). This is known as a constant-height $\mathrm{d}I/\mathrm{d}V$ STS grid. Alternatively, the $\mathrm{d}I/\mathrm{d}V$ STS measurements at each (x, y) location within the grid can be taken at a tip-sample separation defined by a tunnelling set-point leading to a constant-current $\mathrm{d}I/\mathrm{d}V$ STS grid measurement. The application of either kind of measurement (and at what tunnelling set point) depends on the system and on how best to reduce topographic influence on the obtained $\mathrm{d}I/\mathrm{d}V$ data.

Constant-current/constant-height dI/dV STS mapping

Contrary to $\mathrm{d}I/\mathrm{d}V$ STS grids, $\mathrm{d}I/\mathrm{d}V$ STS mapping is performed analogously to performing STM imaging of a sample of interest. During a raster STM scan of the sample, at a specific bias, we simultaneously measure the differential conductance, $\mathrm{d}I/\mathrm{d}V$ by the lock-in technique, i.e., we record the 1st order demodulation of the tunnelling current response to a small bias modulation in the tunnelling bias. This provides a simultaneous recording of STM and $\mathrm{d}I/\mathrm{d}V$ data. This allows for a direct comparison between topographic and electronic information at a specific bias. Like STM imaging, $\mathrm{d}I/\mathrm{d}V$ STS mapping can be performed in constant-height mode or in constant-current mode (see subsection 2.2.1). Necessarily however, this method includes topographic and electronic contributions to the $\mathrm{d}I/\mathrm{d}V$ signal.

Multipass dI/dV STS mapping

A more complicated procedure to potentially minimise variations of $\mathrm{d}I/\mathrm{d}V$ due to variations in topography of the sample is to use a multipass (MP) approach. This approach consists of: first, (i) acquiring a constant-current STM topographic profile along a scanning line (with a defined current and bias set point); then, (ii) recording the $\mathrm{d}I/\mathrm{d}V$ with the lock-in technique along the same scanning line while following the same constant-current STM topographic profile as in (i); and finally, (iii) repeating this procedure sequentially for each scanned line of the map.

Grids vs. maps

Choosing to perform a $\mathrm{d}I/\mathrm{d}V$ STS grid or map involves a trade-off between energy resolution and spatial resolution. While a $\mathrm{d}I/\mathrm{d}V$ STS grid provides an excellent visualisation of the evolution of electronic states of a sample as a function of bias, they are limited in spatial resolution. For cryogenic reasons, acquisition times for these grids are typically restricted to ~60 hours (see subsection 2.5.2). This places a restrictive limit on how well-resolved the grid can be in (x, y). $\mathrm{d}I/\mathrm{d}V$ STS maps, on the other hand, are useful to provide well-resolved maps in (x, y) at specific desired biases. Within the same acquisition time limit (~60 hours), however, only a handful maps (depending on the acquisition time per map) can be acquired.

2.3.5 Fourier-transform STS

Knowing the band structure of a material is useful to understanding its electronic properties. For given crystal momentum, $\mathbf{k}$, there are ranges of energy levels, E, for which there are solutions to the Schrödinger equation describing the system. Collectively, these allowed energy levels, $E(\mathbf{k})$, describes the band structure of a material. One notable disadvantage of STS is its apparent lack of access to the dispersion relation (band structure), $E(\mathbf{k})$, of materials of interest. This is because the local density of states at a given location, $\mathbf{r}$, on the surface (as measured by STS) is related to the $\mathbf{k}$-space eigenstates, $\Psi_{\mathbf{k}}(\mathbf{r})$, by:

$$\mathrm{LDOS}(E_0, \mathbf{r}) \propto \sum_{\mathbf{k}} |\Psi_{\mathbf{k}}(\mathbf{r})|^2 \, \delta\big(E_0 - E(\mathbf{k})\big) \qquad \text{(Eq. 2.28)}$$

That is, the LDOS is momentum-integrated and all $\mathbf{k}$-space information is lost. However, Fourier-transform STS (FT-STS), which involves Fourier-transforming real-space $\mathrm{d}I/\mathrm{d}V$ data, can be used to extract useful $\mathbf{k}$-space information under specific circumstances.

For example, FT-STS has been used to study the dispersion relation, $E(\mathbf{k})$, of Shockley surface states of noble metal surfaces such as Ag(111) [83], Cu(111) [177] and Au(111) [178]. Typically, for these systems, adsorbates are introduced as point-like. The surface state electrons scatter off these impurities resulting in circular modulations with specific wavelengths in the surface LDOS as measured using $\mathrm{d}I/\mathrm{d}V$ STS mapping (see **Figure 2.17**a). Taking the Fourier-transform of such a map yields a ring-like feature in reciprocal space (see **Figure 2.17**b).

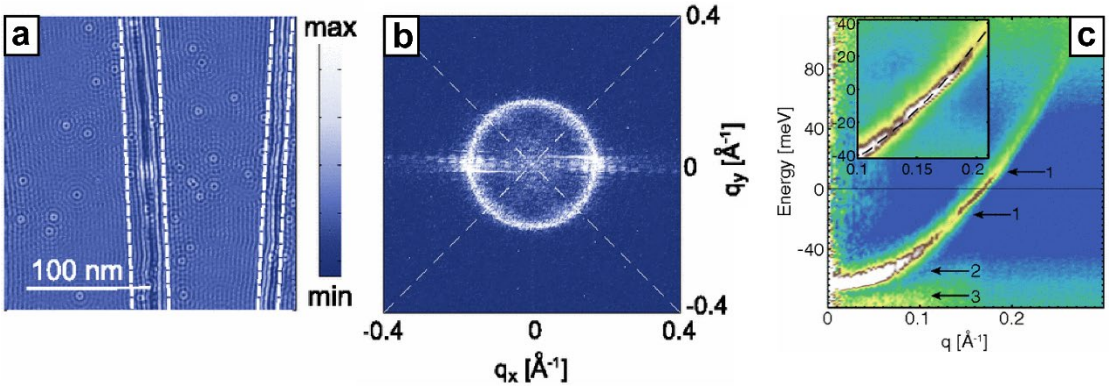

Figure 2.17: Overview of the Fourier-transform scanning tunnelling spectroscopy technique. (a) $\mathrm{d}I/\mathrm{d}V$ STS map taken at $V_\mathrm{b} = 0$ V, of an Ag(111) surface after deposition of CO molecules onto the surface. About each CO molecule, we can observe circular wave-like ripples. (b) Absolute value of the Fourier-transform (power spectrum) of the $\mathrm{d}I/\mathrm{d}V$ map in (a) showing a ring-like feature with radius $\mathbf{q} = 2\mathbf{k_f}$ where $\mathbf{q}$ is the scattering vector. (c) The dispersion, $E(\mathbf{k})$, of the Ag(111) Shockley surface state as measured by FT-STS. This was obtained by taking the Fourier-transform of the $\mathrm{d}I/\mathrm{d}V$ measurements for a range of energies and subsequently plotting the data along a single line cut in $\mathbf{q}$-space. Fitting a parabolic dispersion yields an energy onset, $\mu_0 = 65 \pm 1$ meV and an electron effective mass, $m^*/m_e = 0.41 \pm 0.02$. (a)-(c) were reprinted with permission from ref. [83]. Copyright (2013) by the American Physical Society.

To rationalize this feature, we consider a situation where electrons in a state with initial wavevector $\mathbf{k_i}$, scatter off these impurities. The scattering process sends these electrons to a state with a final wavevector $\mathbf{k_f}$. The scattering vector, $\mathbf{q}$, connects these two states by:

$$\mathbf{q} = \mathbf{k_f} - \mathbf{k_i} \quad \text{(Eq. 2.29)}$$

Assuming that this scattering process is elastic, and that backscattering is dominant ($|\mathbf{k_f}| = |\mathbf{k_i}|$), then:

$$\mathbf{q} = 2\mathbf{k_f} \quad \text{(Eq. 2.30)}$$

That is, we should expect a ring-like feature in $\mathbf{q}$-space (reciprocal space) with radius, $|\mathbf{q}| = 2|\mathbf{k_f}|$. Acquiring FT-STS maps at different energies (either through taking the Fourier transform of $\mathrm{d}I/\mathrm{d}V$ STS maps or a $\mathrm{d}I/\mathrm{d}V$ STS grid) allows for visualisation of the dispersion relation for these Shockley surface states (see **Figure 2.17**c). Fitting these to a parabolic dispersion:

$$\mathrm{E}(\mathbf{k}) = \frac{\hbar^2|\mathbf{k}|^2}{2m^*} + \mu_0 \quad \text{(Eq. 2.31)}$$

yields relevant quantities such as the effective mass of the electron, m^* and the energy onset of the Shockley surface state, μ_0.

In addition to studying the dispersion relations of Shockley surface states on noble metal surfaces, FT-STS has been used to study the band properties of a variety of other systems including graphene [179, 180], superconductors [181–183], topological insulators [184, 185], Weyl semimetals [186, 187], and so on.

2.3.6 State-of-the-art d*I*/d*V* STS

Like STM, STS has been used to study a variety of systems due to its ability to access their electronic properties. For example, **Figure 2.18** shows STM and STS measurements of four different kinds of molecules on a metallic Au(111) surface. $\mathrm{d}I/\mathrm{d}V$ STS measurements on a point on these molecules (see **Figures 2.18**c, f, i, l) show peak-like features corresponding to the molecules' highest occupied molecular orbital (HOMO) and lowest unoccupied molecular orbital (LUMO). $\mathrm{d}I/\mathrm{d}V$ STS mapping at the energies corresponding to the HOMO (see **Figures 2.18**a, d, g, j), and LUMO (see **Figures 2.18**b, e, h, k) states enable a direct visualisation of the spatial extent of these molecular orbitals.

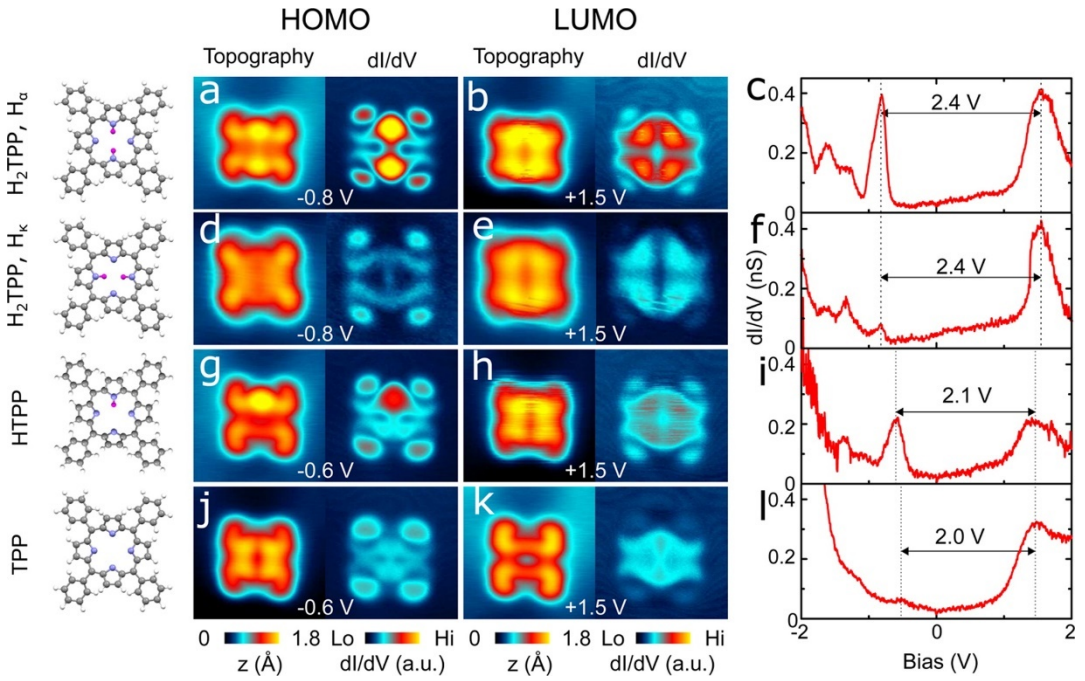

Figure 2.18: STM and STS measurements of various hydrogen-substituted molecules on Au(111). The figure shows STM imaging and $\mathrm{d}I/\mathrm{d}V$ STS mapping of four different molecules at their respective HOMO and LUMO energies. These energies correspond to peaks seen in the point $\mathrm{d}I/\mathrm{d}V$ STS measurements taken at each of the molecules. Reprinted with permission from ref. [188]. Copyright (2016) American Chemical Society.

Metallic surfaces sometimes pose the problem of hybridisation between metallic and adsorbate states, potentially destroying any intrinsic adsorbate electronic properties. Decoupling layers such as hBN, MgO, or NaCl, to name a few, can be introduced to circumvent this issue. To maintain the use of STS, these decoupling layers must be thin enough to allow for electron conduction from the tip to the underlying conducting substrate, through the decoupling layer. This procedure can yield a much more resolved STS map of the molecular orbitals as seen in **Figure 2.19**.

STS is not only limited to studying electronic states and inelastic excitation of internal modes of systems of interest. In some cases, there are features in point $\mathrm{d}I/\mathrm{d}V$ STS measurements, such as sharp dips and sharp peaks at Fermi, that cannot be attributed to any intrinsic electronic state or inelastic tunnelling processes. These features have been linked to changes in the charge states of the molecules [56, 189], the emergence of Majorana modes [190], and even to the emergence of many-body screening of local magnetic moments known as the Kondo effect [86, 175].

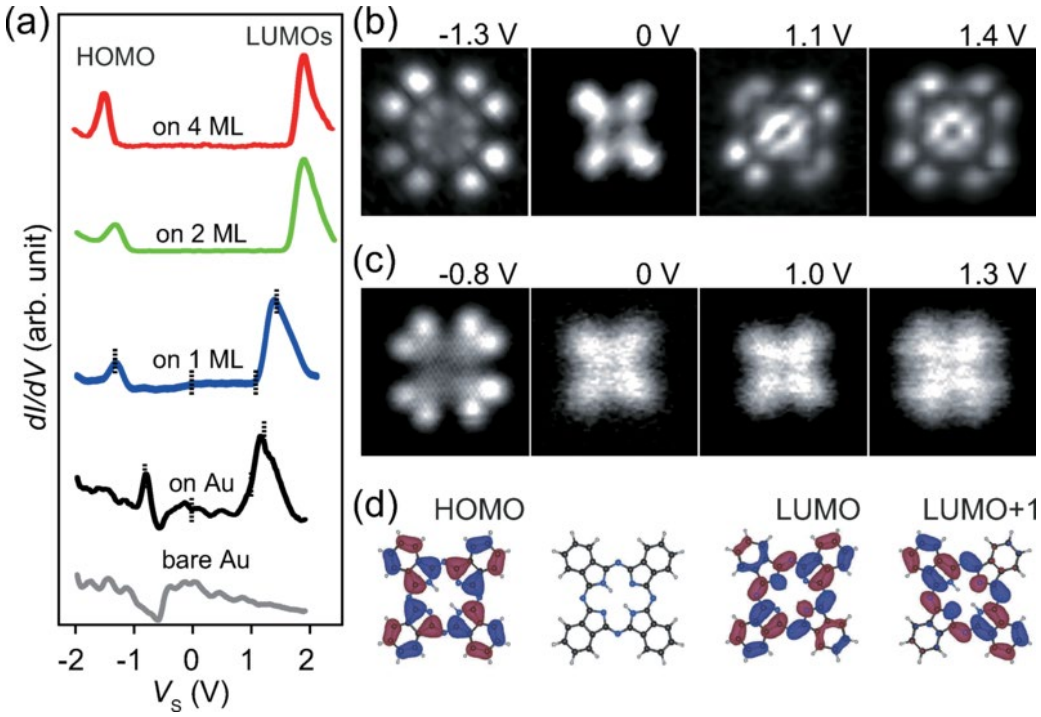

Figure 2.19: STS measurements of a molecules on a metallic surface vs on an insulator. (a) dI/dV STS measurements on a bare Au(111) surface, and on phthalocyanine (H_2Pc) molecules on Au(111), 1 monolayer (ML) of NaCl on Au(111), 2 ML of NaCl on Au(111) and 3 ML on NaCl on Au(111). The peaks associated with the molecular states becomes sharper the more decoupled the molecules are from the metallic surface. (b)-(c) dI/dV STS maps of a H_2Pc molecule on (b) 1 ML NaCl/Au(111) and (c) bare Au(111) surface. The molecular orbitals appear more resolved when probed on the decoupling NaCl layer. (d) Molecular structure of H_2Pc and density functional theory (DFT) calculation results of the spatial distributions of the HOMO, LUMO and LUMO+1 of H_2Pc in the gas phase. The figure was reprinted with permission from ref. [191]. Copyright (2018) by the American Physical Society.

2.4 Non-contact Atomic Force Microscopy

STM and STS techniques have been and still are monumental in characterising materials at the nanoscale. Despite their successes, these techniques are limited only to conductive samples (such that conduction of electrons through the materials can take place) and does not permit characterisation of bulk insulators such as metal oxides. G. Binnig and C. F. Quante developed an atomic force microscope (AFM) as an alternative to STM [192]. AFM works very similarly to STM, where in AFM, a sharp tip, connected to a cantilever, is brought in extreme proximity to the sample of interest. Contrary to STM, AFM measures the forces between the tip and the sample of interest. Variations in the tip-sample forces as the tip is scanned across the sample results in (minute) deflections in the cantilever holding the tip. These deflections can be measured, for example, using a laser (see **Figure 2.20**), resulting in a direct measurement of the forces at the nanoscale. Since this technique does not rely on the conduction of electrons, it is not restricted to only conductive samples and can be used to study insulating samples. This mode of AFM known as static mode AFM, however, is limited in the spatial resolution that it can achieve.

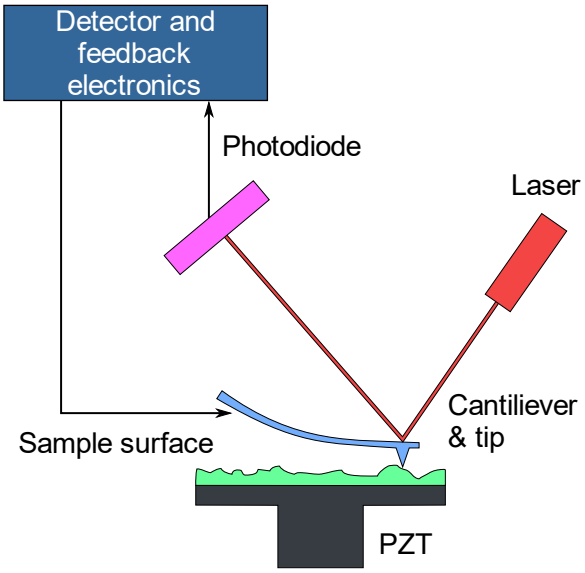

Figure 2.20: Schematic overview of an atomic force microscope (AFM). Differential forces between a sharp tip and the sample causes minute deflections in the cantilever to which the tip is attached to. The deflections in the cantilever causes a laser's reflection off the cantilever to shift and hit different locations on a photodiode as seen in the figure. Changes in where the reflected laser beam hits the photodiode can be correlated with the deflection of the cantilever and thus allow for precise measurements of tip-sample forces.

It was not until the introduction of non-contact atomic force microscopy (nc-AFM) by F. Giessibl [193] that true atomic resolution was achieved. Nc-AFM, also known as dynamic mode AFM, modifies the working principle of static-mode AFM by having the cantilever oscillate as the tip is scanned across the sample. Advancements in the designs and techniques of nc-AFM has enabled the achievement of sub-atomic resolution in the imaging of nanomaterials. This makes nc-AFM unparalleled in real-space resolution in the field of surface science. Here, I provide an overview of the working principle of nc-AFM and the measurements that I have employed in this dissertation using this technique.

2.4.1 Operating principle

Forces at the nanoscale

The operation of nc-AFM relies on measuring the forces present between the tip and the sample. Typically, at the nanoscale, forces such as Pauli repulsion forces dominate at short ranges ($<$ 1 nm) whereas van der Waals forces dominate at longer ranges ($\gg$ 1 nm). An archetypical model of intermolecular interactions (between two molecules) involving these two forces can be represented by the Lennard-Jones potential [194]:

$$V_{LJ} = 4\varepsilon\left[\left(\frac{\sigma}{r}\right)^{12} - \left(\frac{\sigma}{r}\right)^{6}\right] \qquad \text{(Eq. 2.32)}$$

where r is the distance between two molecules and where ε and σ are parameters characterising the interaction potential with the ε relating to the depth of the potential and σ to the size of the

molecules. The r^{-12} term describes the short-range Pauli repulsion between the molecules while the r^{-6} term describes the long-range van der Waals interaction (more precisely, London dispersion interaction) between the molecules. A typical Lennard-Jones potential curve is shown in **Figure 2.21**.

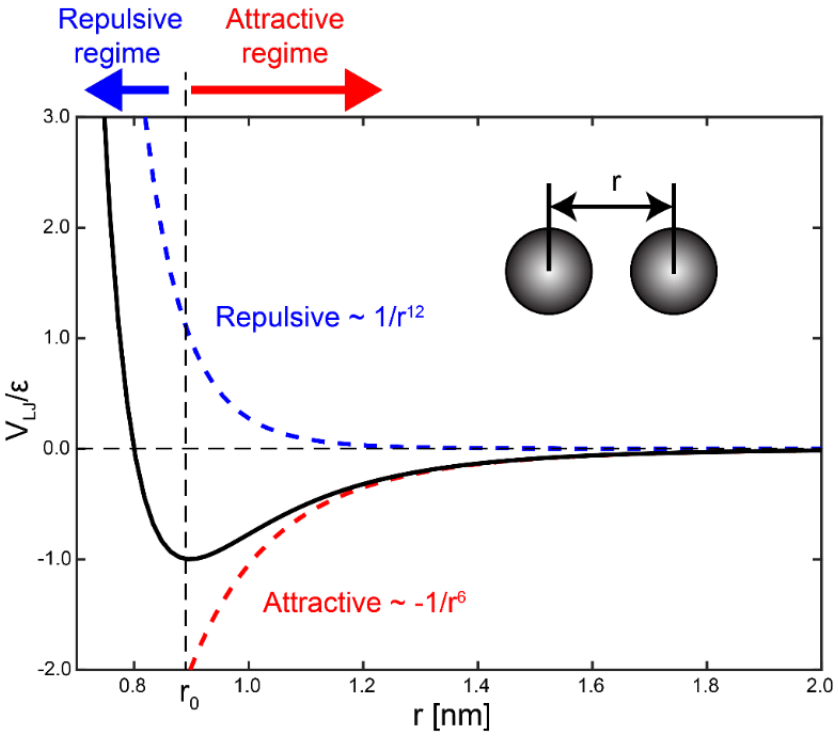

Figure 2.21: Typical Lennard-Jones potential curve describing intermolecular forces between two molecules. The potential curve is described by $V_{LJ}/\varepsilon = 4\left[\left(\frac{\sigma}{r}\right)^{12} - \left(\frac{\sigma}{r}\right)^{6}\right]$ where the r^{-12} term is a repulsive term while the r^{-6} term is an attractive term. Overall, the force between the molecules is repulsive when $r < r_0$ and attractive when $r > r_0$.

Where the gradient of the potential is negative ($r < r_0$), attractive forces dominate whereas where the gradient of the potential is positive ($r > r_0$) repulsive forces dominates. Other interactions that dominate at short ranges can include chemical interactions such as covalent or metallic bonding. At all ranges, however, electrostatic interactions can further contribute. Despite these other possible interactions, the shape of the interaction potential curve is qualitatively well-described by Eq. 2.32, i.e., there is an equilibrium separation, r_0, and that for $r < r_0$, repulsive forces dominate and for $r > r_0$, attractive forces dominate.

Frequency-modulated nc-AFM and frequency shift

As previously mentioned, nc-AFM works by driving the oscillation of a cantilever (with a tip attached at one end) close to resonance. Changes in the force gradient between the tip and the sample of interest causes an instantaneous change in the oscillation of the cantilever either in the amplitude or in the frequency of the oscillation [195, 196].

In this work, I made use of a mode of nc-AFM known as frequency-modulated nc-AFM (henceforth referred to as nc-AFM). Further, a qPlus sensor was used in this work [197], a schematic of which is shown in **Figure 2.22**a. This consists of a quartz tuning fork with one prong of the fork fixed to a support and the other prong left free to oscillate but with a metallic tip glued at one end. A qPlus sensor has a high Q-factor ($\gg 10^4$) and a large spring constant ($k \approx 1800$ N/m). This means that they can operate at small oscillation amplitudes (< 100 pm), increasing sensitivity to short-range forces (where the force gradients are rather steep) and increasing SNR [197]. The design of qPlus sensors is also advantageous because they permit simultaneous STM operation (see **Figure 2.22**a). In the context of frequency-modulated nc-AFM, the free prong of the quartz tuning fork is driven at its resonance frequency, f_0, (see **Figure 2.22**b) and with a constant oscillation amplitude, A. Here, the oscillation amplitude is kept constant via a feedback loop. In the presence of changing interactive forces between the tip and the sample, the resonance frequency is changed: $f = f_0 + \Delta f$. This shift in the resonance frequency, Δf, contains information regarding these interactive forces.

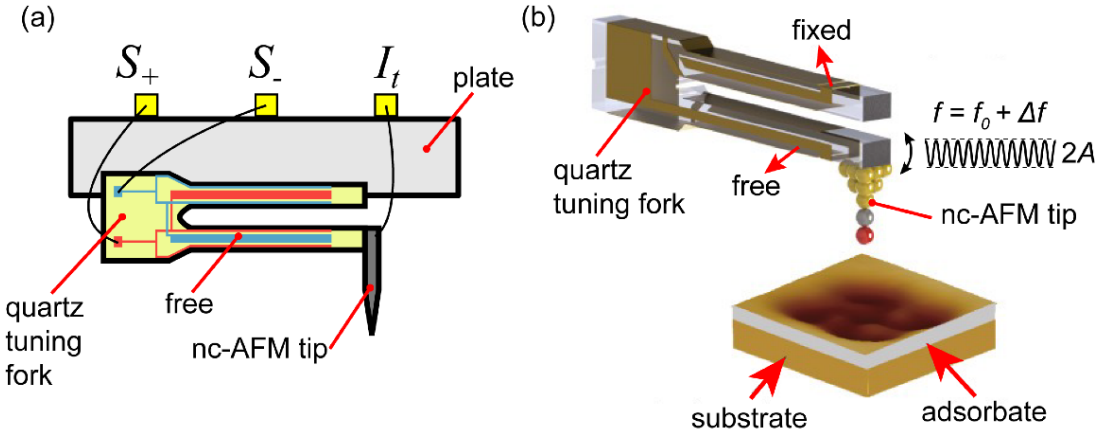

Figure 2.22: Schematic overview of qPlus sensor design and operation in nc-AFM. (a) The figure shows a schematic design of a qPlus sensor which uses a quartz tuning fork where one prong is held in place, connected to a plate and where one prong is left free. A sharp metallic tip is glued to the end of the free prong. Connection terminals allow for the oscillation of the quartz tuning fork (S_+, S_-) and the detection of a tunnelling current between the tip and sample (I_t). (b) In nc-AFM, the qPlus sensor is operated by driving the free prong of the tuning fork at resonance frequency, f, with a peak amplitude, A. Upon changes in the tip-sample forces, by bringing the tip closer to an adsorbate on a surface, the resonance frequency changes by Δf and is measured. (a) was adapted courtesy of Stirling Julian under under an Attribution-ShareAlike 3.0 Unported License. (b) was adapted with permission from ref. [198] under a Creative Commons Attribution 4.0 International License.

To see this, we model the system as a weakly perturbed harmonic oscillator where the unperturbed (classical) Hamiltonian is given by:

$$H_0 = \frac{p^2}{2m^*} + \frac{kq'^2}{2} \qquad \text{(Eq. 2.33)}$$

where $p = m^* \mathrm{d}q'/\mathrm{d}t$, $m^*$is the effective mass of the cantilever, k is the spring constant and q' is the deflection of the tip of the cantilever. Solving for the unperturbed motion of the cantilever gives:

$$q'(t) = A_0 \cos(2\pi f_0 t) \quad \text{(Eq. 2.34)}$$

with, f_0, the resonant frequency given by:

$$f_0 = \frac{1}{2\pi}\sqrt{\frac{k}{m^*}} \quad \text{(Eq. 2.35)}$$

By treating V_{ts}, the tip-sample interaction potential, as a small perturbation to the Hamiltonian in Eq. 2.33, it can be shown that [197]:

$$\Delta f = -\frac{f_0}{kA^2}\langle F_{\mathrm{ts}} q' \rangle \quad \text{(Eq. 2.36)}$$

Where $F_{\mathrm{ts}} = -\partial V_{\mathrm{ts}}/\partial z$, is the force acting between the tip and the sample. The brackets correspond to an averaging over one oscillation cycle of the cantilever. When the force gradient $\partial F_{\mathrm{ts}}/\partial z$ is roughly constant throughout one oscillation cycle of the cantilever, the frequency shift takes on a particularly simple form:

$$\Delta f = -\frac{f_0}{2k}\frac{\partial F_{\mathrm{ts}}}{\partial z} \quad \text{(Eq. 2.37)}$$

The above simplification is valid when we restrict the oscillation amplitude to small values ($A \lesssim 100$ pm). With Eq. 2.37, from the frequency shift, we can only deduce the force gradient but not the (attractive or repulsive) nature of the forces between the tip and sample. A more quantitative approach to this problem has led to an expression where the force between the tip and sample can be calculated directly from the frequency shift [199]:

$$F_{\mathrm{ts}}(z) = 2k\int_z^\infty \left(1 + \frac{A^{\frac{1}{2}}}{8\sqrt{\pi(t-z)}}\right)\Omega(t) - \frac{A^{\frac{3}{2}}}{\sqrt{2(t-z)}}\frac{\mathrm{d}\Omega(t)}{\mathrm{d}t}\mathrm{d}t \quad \text{(Eq. 2.38)}$$

with $\Omega(t) = \Delta f/f_0$.

2.4.2 Force spectroscopy

One of the easiest yet still informative measurements that can be performed via nc-AFM is force spectroscopy. This measurement involves: (i) maintaining the tip over a specific location on the sample; and (ii) measuring the frequency shift as function of tip-sample separation, $\Delta f(z)$. Such a measurement with a qPlus sensor tip yields a force curve such as the one seen in **Figure 2.23**a.

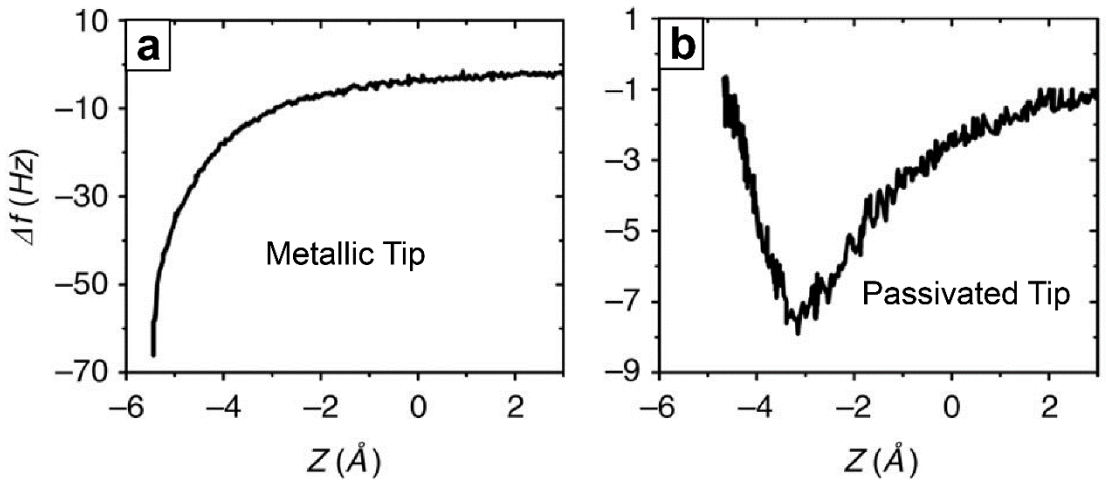

Figure 2.23: Force spectroscopy curves with a bare metallic vs passivated tip. (a) A force spectroscopy curve, $\Delta f(z)$, taken on a H-Si surface, with a bare metallic (reactive) tip. (b) A force spectroscopy curve, $\Delta f(z)$, taken on the same surface in (a) but with a hydrogen-passivated tip. Adapted with permission from ref. [200] under a Creative Commons Attribution 4.0 International License.

Here, observing the expected upturn in the $\Delta f(z)$ curve is not possible with a bare metallic tip as at smaller tip-sample separations, large tip-sample interactions tend to damage both the tip and the sample of interest. To circumvent this issue, protocols to passivate the tip *in-situ* have been established. This includes passivation of the tip through the tip-functionalisation with Xe [168], CuO [170], or even CO [165–167]. Throughout this dissertation, tip-functionalisation has been performed by picking up CO molecules adsorbed onto the surface (see subsection 2.2.7). **Figure 2.23**b shows a typical force curve with a passivated tip. Here, we can clearly observe the upturn in the $\Delta f(z)$ curve. Passivation ensures that at small tip-sample separations, both the tip and the sample remain unperturbed.

Force spectroscopy is useful in identifying regimes in z where interesting interactions are present e.g., where short-range forces are more dominant. This is important when performing nc-AFM imaging (see subsection 2.4.3). Force spectroscopy is also useful in identifying regimes in z where only long-range forces such as electrostatic forces are dominant. This is of particular importance when performing Kelvin probe force microscopy (see subsection 2.4.4). Beyond these reasons, force spectroscopy can be used to measure differences in adsorption heights of adsorbates. This is done by first performing $\Delta f(z)$ measurements on the same species of adsorbates that otherwise occupy different adsorption sites on a surface. It is important to ensure that these measurements are done relative to the same initial tip-sample separation. Having done so, we then determine the tip-sample separation, z_{min}, that corresponds to the minima of these $\Delta f(z)$ curves. The differences between these values, Δz_{min}, gives the approximates difference in adsorption heights for these adsorbates [201].

2.4.3 Nc-AFM imaging

Perhaps most famously, nc-AFM is used to produce bond-resolved images of organic molecules. Nc-AFM imaging of organic nanostructures involves recording the frequency shift, $\Delta f(z)$, as the tip scans across the region of interest, all the while maintaining a constant tip height. A suitable height is determined from performing a force spectroscopy measurement on the organic system. Typically, a tip height is chosen corresponding to a tip-sample separation just below $z_{\min}$ where short-range forces are more dominant allowing for the resolving of chemical bonds in imaging. At such a tip height, a bare metallic nc-AFM tip will induce a large tip-sample interaction that will perturb the tip, organic nanostructure, or both. As outlined in the previous section, tip passivation is used to circumvent this issue. Here, I focus on using CO molecules as a means of tip passivation. CO-passivation has an added effect of enhancing the spatial resolution of nc-AFM imaging leading to the well-known chemical bond-resolved images of organic molecules (see

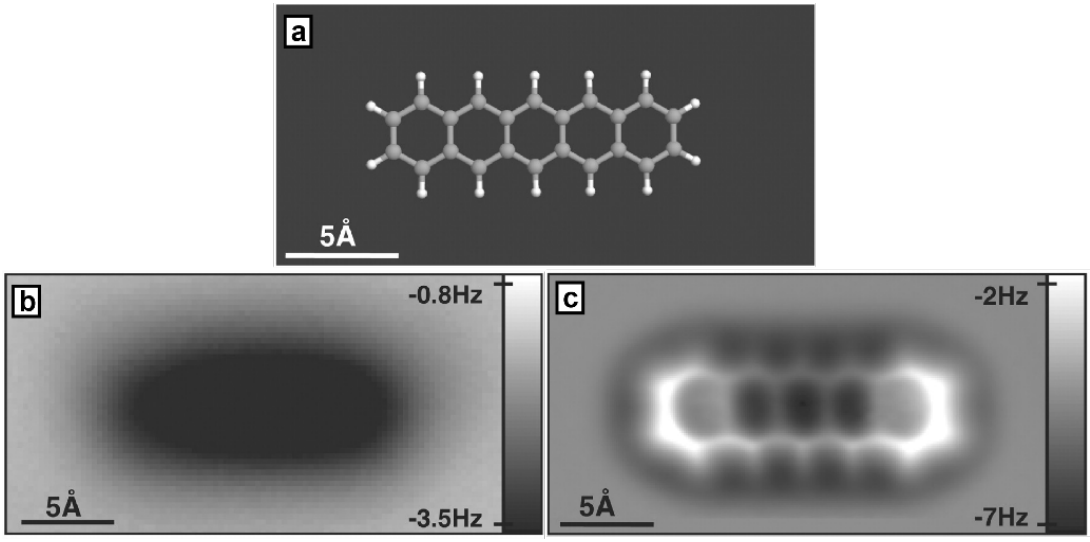

Figure 2.24).

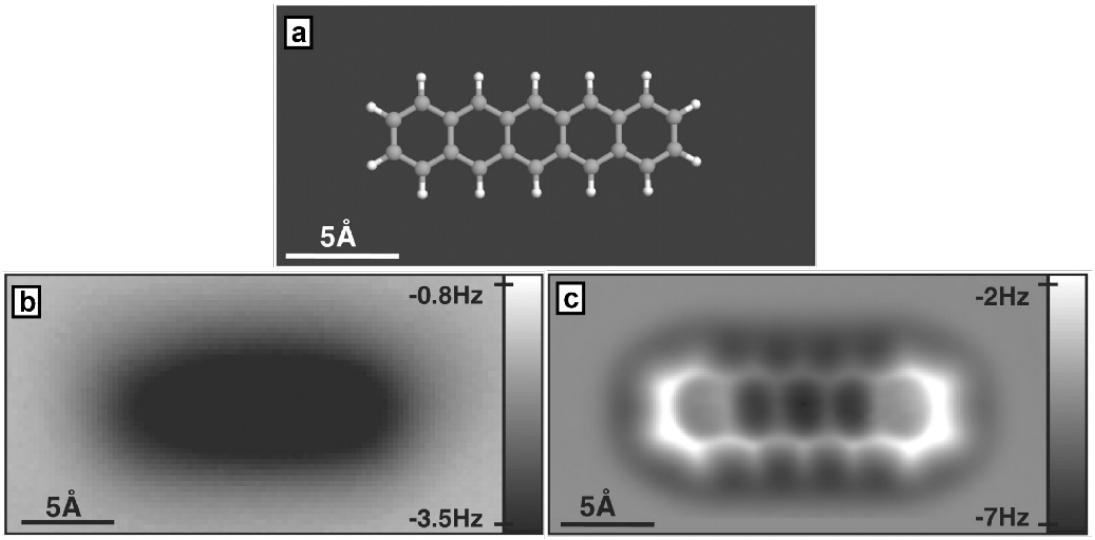

Figure 2.24: Nc-AFM imaging with a metallic tip vs passivated tip. (a) Chemical structure of a pentacene molecule. (b) Constant-height nc-AFM imaging with a bare metallic tip of a pentacene molecule. (c) Constant-height nc-AFM imaging with a CO-passivated tip of a pentacene molecule showing the resolved chemical bonds. The scalebars in b-c show the variation in the shift in resonance frequency, Δf. The figure was adapted from ref. [167] with permission from AAAS.

The enhanced resolution has been attributed to the flexible movement of the CO molecule at the tip apex position [202, 203]. This enhancement in imaging resolution has also been attributed to the localized *p*-orbital extending from the Oxygen atom of the CO molecule toward the sample [170, 204]. The exact origin for the intra-molecular contrast remains inconclusive.

2.4.4 Kelvin probe force microscopy

Bond-resolved imaging as seen in the previous section is enabled thanks to nc-AFM's sensitivity to short-range forces. On the other hand, nc-AFM's sensitivity to long-range forces, in particular electrostatic forces, enables the measurement of local variations in the work function of a surface via Kelvin probe force microscopy (KPFM). Through measurements of the local work function of a surface, one can, for example, directly access the charge distribution of nanostructures on a surface [37] or discriminate between different charge states of an adsorbate [205].

KPFM measurements are performed by measuring the contact potential difference, V_{CPD}, between the nc-AFM tip and the sample of interest. Generally, when a metallic tip and surface are physically far apart (and electrically insulated), they have different work functions and consequently different Fermi levels (see **Figure 2.25**a). The contact potential difference, V_{CPD}, is defined as the difference between these work functions:

$$V_{\mathrm{CPD}} = \frac{(\Phi_s - \Phi_t)}{e} \qquad \text{(Eq. 2.39)}$$

When the tip and sample are brought into electrical contact, electrons flow between them until the Fermi levels for both equilibrate, $E_F^t = E_F^s$, (see **Figure 2.25**b). This transfer of electrons causes the accumulation of net charges in the both the tip and the sample where the metal with the (originally) larger work function developing a negative net charge at its surface and the other with net charge of the same magnitude but opposite in sign. In the context of an STM junction, these opposing charges create an electrostatic field with a force, F_{el}, between them.

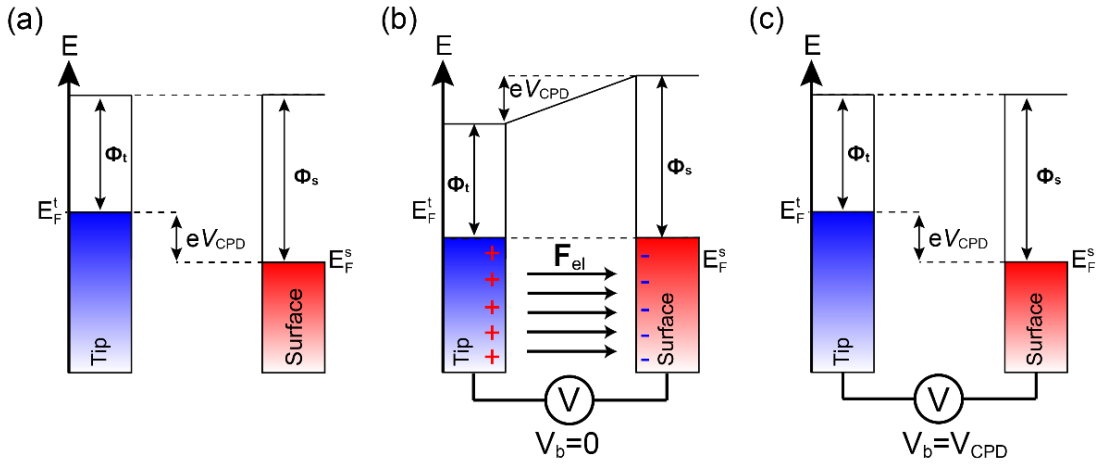

Figure 2.25: Overview of the measurement of the contact potential difference in an STM junction. (a) When the tip and sample are physically and electrically separated, their vacuum levels are aligned. With differing work functions, the tip and sample have different Fermi levels. The difference in their work functions is known as the contact potential difference, eV_{CPD}. (b) When the tip and sample are electrically connected, electrons flow until the Fermi levels both the tip and sample equilibrate. The transfer of electrons results in an electrostatic force, $\mathbf{F}_{el}$, across the STM junction. (c) When tunnelling bias is equal to the contact potential difference, $V_b = V_{CPD}$, the tip and sample become electrically neutral as in (a). This corresponds to a situation where $|\mathbf{F}_{el}| = 0$ in the STM junction which can be measured using nc-AFM.

The contact potential difference, V_{CPD}, can be measured by applying a bias voltage such that electrons are forced to flow between the tip and the sample until they become electrically neutral again. In this case, the electrostatic force between the tip and sample is null, i.e., $|\mathbf{F}_{el}| = 0$. In this situation, the applied bias voltage is equal to the contact potential difference, $V_b = V_{CPD}$ (see **Figure 2.25**c). In principle, KPFM via nc-AFM can be used to measure the electrostatic force between the tip and sample and deduce the contact potential difference, V_{CPD}. The lateral spatial resolution of the nc-AFM tip allows for the measurement in the variation surface contact potential difference, i.e., we can measure the *local* contact potential difference (LCPD) rather than the large surface-averaged value of the contact potential difference.

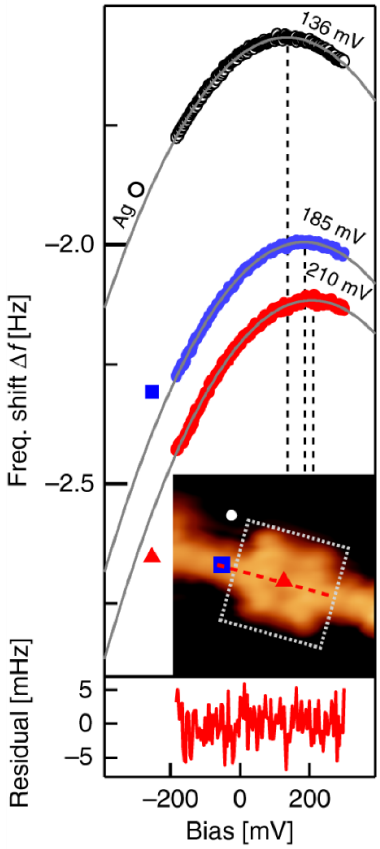

Figure 2.26: Measurement of local contact potential difference (LCPD) via Kelvin probe force microscopy. Here the measurements of $\Delta f(V)$ on the bare metal surface (black circle) and on the organic molecule (blue square and red triangle) yield parabolic curves. Fitting these curves with a parabola allows for the extraction for the maxima for these curves which corresponds to the LCPD at the measurement locations. Differences in the LCPD show differences in charge accumulation at the organic molecule compared to the bare metallic surface. Figure adapted from ref. [37] under a Creative Commons Attribution 4.0 International License.

KPFM measurements are performed by measuring the frequency shift as a function of applied tunnelling bias voltage, $\Delta f(V)$, at a specific location on the sample and at a constant tip height. The choice of tip height is important as we would need to ensure that the only forces sensed by the nc-AFM tip are electrostatic in nature, i.e., this measurement must be performed far enough that other forces, such as Pauli repulsion, are negligible. Force spectroscopy (see subsection 2.4.2) can help determine a suitable tip height (preferably where the force curve is flat). KPFM measurements typically result in $\Delta f(V)$ curves that resemble a parabola such as in **Figure 2.26**. To see why, we model the tip and sample in the STM junction as parallel plate capacitors with a capacitance C and with energy $U_{el} = \frac{1}{2}C(V_{CPD} - V)^2$. The electrostatic force, $|\mathbf{F}_{\mathrm{el}}| = F_{\mathrm{el}}$, in the STM junction is, therefore, according to this model:

$$F_{el}(V,z) = -\nabla U_{el} = -\frac{1}{2}(V_{CPD} - V)^2 \frac{\mathrm{d}C}{\mathrm{d}z} \qquad \text{(Eq. 2.40)}$$

Since $\Delta f \propto \partial F_{\mathrm{el}}/\partial z$ and that that V_{CPD} and V are independent of z, then:

$$\Delta f(V) \propto -\frac{1}{2}(V_{CPD} - V)^2 \qquad \text{(Eq. 2.41)}$$

This explains the parabolic shape of KPFM curves. The accurate determination of the LCPD can then be performed by fitting these KPFM curve with a quadratic function.

2.4.5 State-of-the-art nc-AFM

Nc-AFM represents a versatile tool in the study of low-dimensional materials especially in the study of low-dimensional organic nanostructures. The techniques outlined in the previous subsections enables the characterisation of molecular properties such as the adsorption geometry and conformation of individual molecules on surfaces [201, 206–208], discrimination of bond orders of bonds within organic molecules [209–211], molecular charge states [212, 213], and molecular charge distribution [214, 215]. Nc-AFM is also incredibly useful in molecular identification, particularly, in tracking the reaction process of surface-assisted organic molecular reactions such as in dehydrogenation reactions [216] or Bergman cyclization reactions [217]. Altogether, these make nc-AFM another invaluable tool, alongside STM and STS, for the characterisation of low-dimensional organic nanostructures on surfaces.

2.5 Details of Experimental Set-up

All results and findings presented in this work were performed using a commercially available low-temperature scanning probe microscope (LT-SPM) from Createc Fischer & Co. The LT-SPM used is located at the New Horizons Research Centre at Monash University, Australia. Here, I provide an overview of this experimental set-up and associated tools.

2.5.1 Overview of low-temperature scanning probe microscopy set-up

Figure 2.27 shows an image of the LT-SPM used in this work. The set-up consists of three chambers: (i) an STM chamber; (ii) a preparation chamber; and (iii) a load-lock chamber. These chambers are partitioned from one another by means of an operable gate valve. The STM chamber houses a cryostat cooling the STM head where characterisation of samples of interest are performed. These samples are prepared in the preparation chamber where various sample preparation tools such as source evaporators, a residual gas analyser, and an ion source are located. A translational manipulator is also affixed to this chamber where the substrates are mounted during sample preparation. The STM and preparation chambers are kept under UHV with a pressure of $\sim 1 \times 10^{-10}$ mbar, keeping all operations involving growth and characterisation of samples of interest under UHV conditions. The load-lock chamber is a small volume chamber that enables quick insertion of materials from ambient conditions (outside the chamber) into the preparation chamber and vice versa. The small volume enables quick pumping down of the chamber from ambient pressures necessary for this procedure.

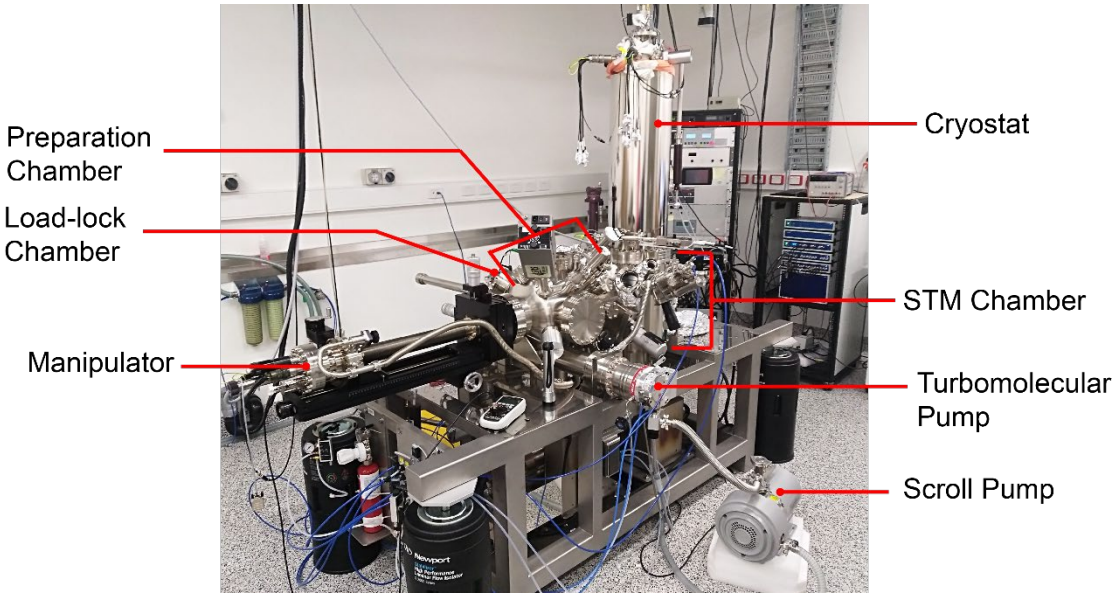

Figure 2.27: Overview of LT-SPM at New Horizons Research Centre, Monash University, Australia. The LT-SPM set-up consists of three main chambers: (i) STM chamber; (ii) preparation chamber; and (iii) load-lock chamber. Pumps allow UHV conditions to be maintained within the chambers. The cryostat can be filled with cryogenic liquids such as liquid helium (lHe) or liquid nitrogen (lN_2) enabling characterisation of samples of interest at ~5 K or at ~80 K, respectively.

Vacuum conditions of the chambers are achieved through a combined action of various pumps such as turbomolecular pumps (with scroll pumps as backing pumps), ion pumps, and titanium sublimation pumps. The cryostat when kept cold with the use of cryogenic liquids, further acts as a kind of cryopump. These pumps, altogether, enable a final pressure in the high 10^{-11} to low 10^{-10} mbar in the STM chamber. Pressures in the chambers of the LT-SPM set-up are monitored using hot-filament ion gauges.

2.5.2 STM head and cryostat

Figure 2.28a shows a schematic drawing of the STM head and cryostat. The cryostat has an inner cylinder that holds cryogenic liquids such as liquid nitrogen (lN_2) or liquid helium (lHe). The choice of cryogenic liquid dictates the operating base temperature for STM/nc-AFM measurements namely ~5 K, ~80 K or room temperature if the inner cylinder is filled with lHe, lN_2, or neither, respectively. The cryostat also has an outer jacket that can be filled with lN_2. This increases the hold time, i.e., the amount of time that it takes for the cryogenic liquid in the inner cylinder, which keeps the instrument cold, to evaporate away. When the inner cylinder and outer jackets are filled with lHe and lN_2, respectively, the hold time is approximately 72 hours. After which, the cryogenic liquids need to be replaced. This places restrictions on any continuous measurements (e.g., $\mathrm{d}I/\mathrm{d}V$ STS grid).

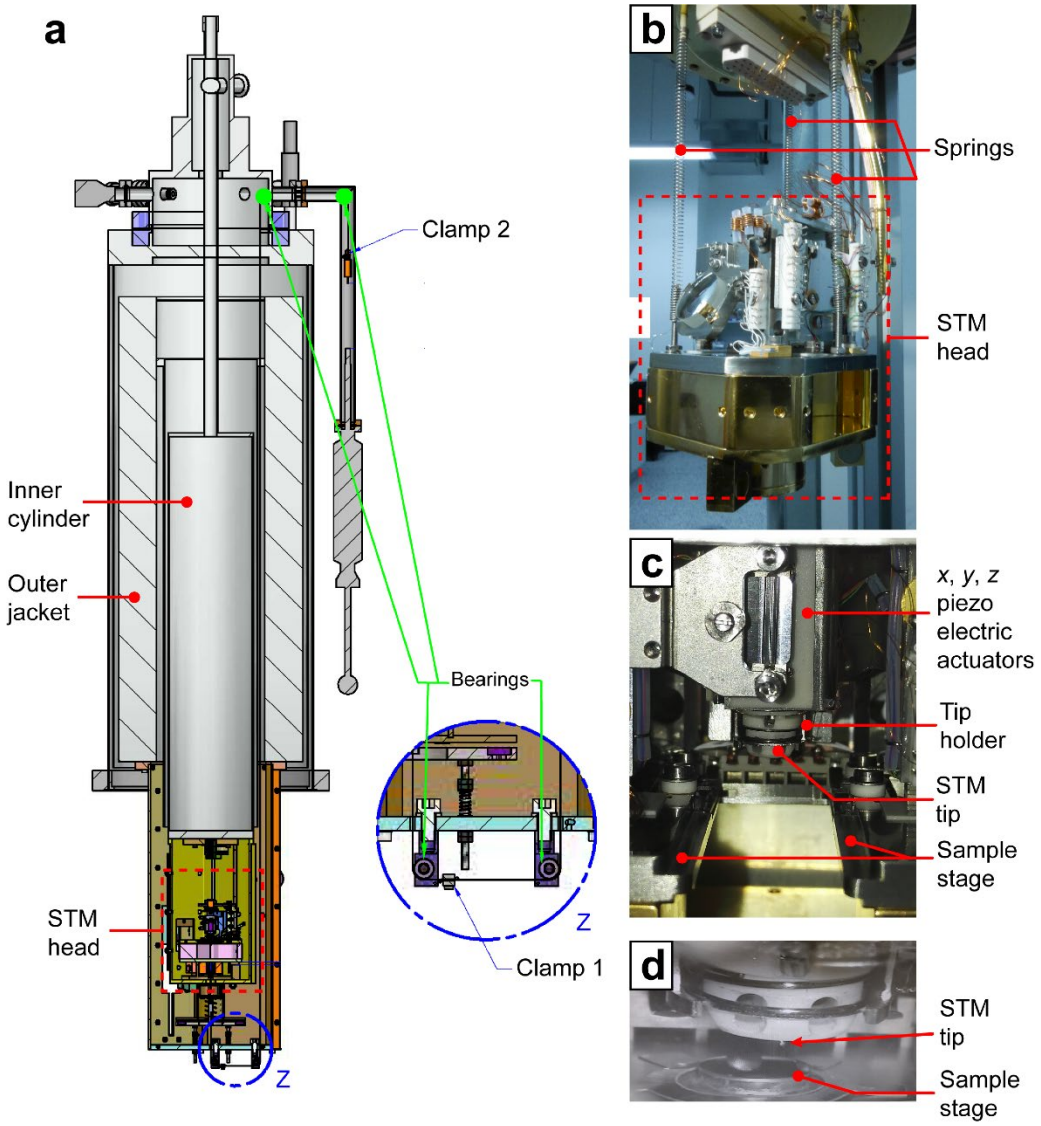

Figure 2.28: Overview of STM head and cryostat. (a) schematic overview of cryostat and STM head located at the bottom of the cryostat. (b) Image of an STM head removed from the STM chamber. When unclamped, the STM head hangs freely off the base of the cryostat by three springs. (c) Image of STM tip/sample stage within the STM head. The movement of the tip is driven by piezoelectric actuators. (d) Image of an STM tip above a sample within the STM tip/sample stage.

The STM head is located directly at the bottom of the cryostat. This ensures efficient cooling of the entire STM head when clamped, i.e., when it is not freely floating. When unclamped, the STM hangs freely from the bottom of the cryostat on three springs (see **Figure 2.28b**). These springs together with a magnetic eddy-current damping system decouples the STM head from external vibrations. In this configuration (unclamped), the STM head maintains thermal contact with the cryostat via a thin Cu wire, enabling cooling of the STM head. The STM head itself is based on a Pan-styled slider type model [218] where piezoelectric actuators move the tip toward a sample and enable lateral movements of the tip across the sample (see **Figures 2.28**c,d). An STM or nc-AFM tip is placed in the tip holder and can be exchanged *in-situ*. A small Zener diode mounted to the baseplate of the STM head can be operated to locally

heat up the STM head. This enables temperature-dependent measurements such as those presented in Chapter 5. Heating up the STM head yields an increased lHe consumption which means a reduced hold time.

2.5.3 STM and nc-AFM tips

Throughout this dissertation, standard home-made Pt/Ir STM tips and commercially available Createc qPlus Pt/Ir sensors were used. The quality of data, e.g., STM and nc-AFM imaging depends strongly on the morphology of the tip apex. Unwanted artefacts in imaging such as doubling (where imaging is doubled) caused by a tip apex morphology where there are two protruding atoms can happen [219]. Blurred imaging due to a blunt tip is also possible. High quality data often involves a sharp tip with a single protruding atom at the tip apex. Tip conditioning can help achieve such a tip *in-situ*. One way of conditioning the tip involves a deliberate indentation of the tip in a bare metallic surface. This procedure leads to a restructuring of the tip apex and is continuously repeated until a desired imaging quality is achieved. Bias pulses—rapid changes in the tunnelling bias voltage—can also help to restructure the tip apex. Alternatively, applying a large enough bias to the tip (100 V) can lead to the emission of electrons from the tip to the sample in high currents. Reversing the polarity results in the bombardment of the tip by electrons emitted from the surface. This procedure, known as field emission, can also assist in progressively restructuring the tip.

2.5.4 STM and nc-AFM calibration

Precise movements of the STM and nc-AFM tips in the x, y, and z directions are ensured by their proper calibration. The lateral movements of the tips (x and y directions) are calibrated by acquiring atomically-resolved images of a bare surface such as Ag(111) where the surface lattice constant is known (see subsection 2.1.3, **Figure 2.5**a). The vertical movement of the tips (z direction) is calibrated by measuring the differences in the apparent heights of different terraces on Ag(111) and comparing them to the known interplanar distance of silver in the [111] direction, $d_{Ag(111)} = 235.86$ pm.

2.5.5 Sample preparation tools

As previously mentioned, samples of interests are prepared in the preparation chamber of the LT-SPM. Details for sample preparation can be found in subsections 0 and 2.1.4. Here, we mention the tools that are required for such preparations: source evaporators from which DCA molecules and Cu atoms can be thermally evaporated from; an ion source for Ar^+ ion sputtering; and leak valves to introduce residual gasses such as Ar (for Ar^+ ion sputtering), CO (for CO tip-functionalisation) and borazine (for hBN/Cu(111) sample preparation). The preparation chamber also houses a translational manipulator where a sample can be mounted on the manipulator head (see **Figure 2.29**).

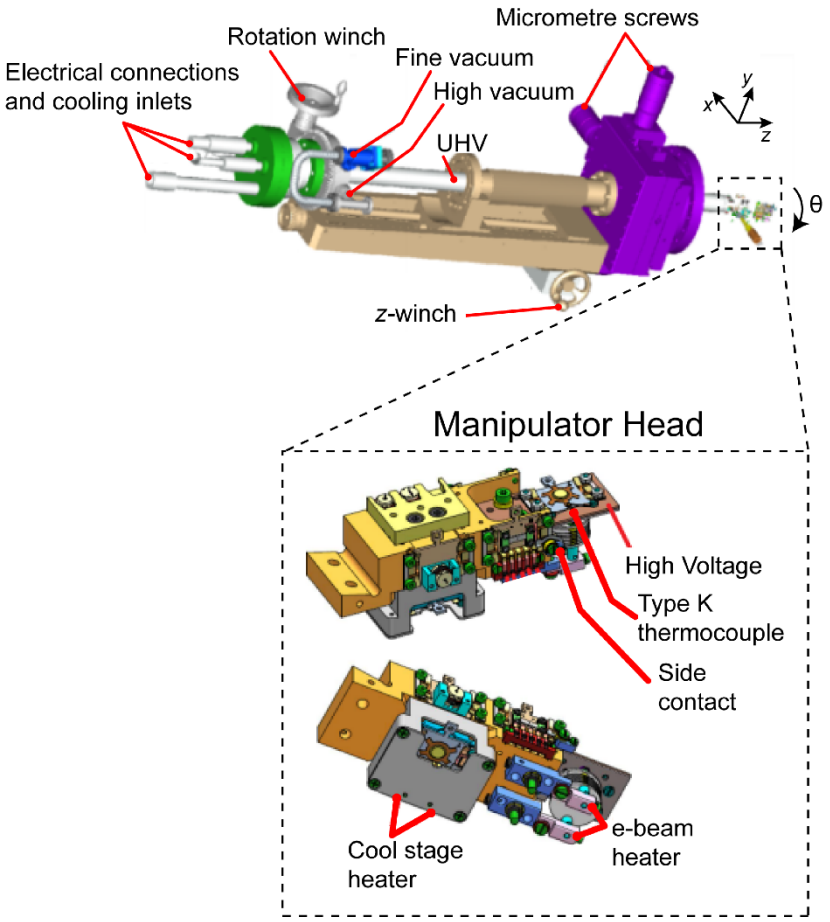

Figure 2.29: Overview of translational manipulator for the LT-SPM set-up. The sample is mounted on at the manipulator head located at the end of the manipulator either at the cool stage or the e-beam stage. The location and the relative orientation of the sample within the preparation chamber is manipulated via the micrometre screw gauges, the *z*-winch, and the rotation winch. Annealing of the sample can be done using the e-beam heater (for high-temperature annealing) or using the cool-stage heater (for low-temperature annealing).

With the manipulator, the position of the sample can be manipulated within the chamber via the micrometre screws (displacement in x and y), the *z*-winch (displacement along z), and the rotation winch (rotation about θ). This allows the sample to be positioned appropriately, for example, for molecular/atomic deposition via MBE or for Ar^+ ion sputtering. Mounting the sample on the E-beam stage allows for annealing of the sample (up to ~1200°C) necessary for cleaning the Ag(111) and Cu(111) substrates and for preparing ultrathin hBN/Cu(111) samples. A cool-stage heater allows for reliably controlled heating of the sample at lower temperatures (< 200°C). The cool stage is also effective at cooling the sample down to ~100 K when the manipulator is fed lN_2 through the cooling inlets.

Chapter 3
Electric Field Control of Molecular Charge State in DCA/Ag(111) Nanoarray

3.1 Overview

DCA molecules are aromatic, mirror-symmetric organic molecules that hosts reactive cyano-functional groups. The cyano-functional groups of these molecules can facilitate a variety of in-plane intermolecular interactions and can therefore facilitate the on-surface formation of variety of different 2D organic nanostructures (see section 1.4 and subsection 2.1.1). This versatility is particularly important in elucidating the impact of different interactions at the nanoscale on the structural and electronic properties of on-surface self-assembled nanostructures. As a first step, I sought to experimentally characterise, using the methods detailed in Chapter 2, the structural and electronic properties of DCA molecules on an Ag(111) surface. This constitutes an important prelude to studying more complicated DCA-based organic nanostructures on surfaces such as the proposed 2D DCA_3Cu_2 kagome metal-organic framework (MOF) [63]. The choice of Ag(111) surface is motivated by the chemically inert nature of the noble metal surface. Ag(111) also does not suffer from surface reconstructions such as those observed in Au(111), i.e., the herringbone surface reconstruction [220, 221]. The (111) face of the Ag metal was chosen for its hexagonal surface lattice structure which is preferable for the growth of structures that are of similar symmetry such as the proposed 2D DCA_3Cu_2 kagome MOF [63].

Here, I present results demonstrating the synthesis of a single-component self-assembled 2D array of DCA molecules that exhibit electric-field-controlled spatially periodic charging on a noble metal surface, Ag(111). I show that the charge state of the DCA molecules can be altered (between neutral and negative), depending on its adsorption site, by the local electric field induced by an STM tip. Here, these molecules act as quantum dots [222, 223] (QD) with controllable integer charge states, where their manipulation of charge—at the single electron level and with nanoscale precision—allows for various potential applications [57], e.g., memory storage [224], classical and quantum computing [225], and light-emitting devices [59]. This level of charge control, via an external electric field, is typically hindered on metallic substrates due to screening of the applied field, pinning of the molecular states to the metal Fermi level, and/or hybridisation between molecular and surface electronic states [226]. By

efficiently decoupling molecule and substrate electronic states—that is, creating an effective potential barrier that separates molecule and surface—it becomes possible to alter the charge state of the molecular adsorbate with an external electric field.

By means of STM and STS, I show that the charging of the DCA molecules on Ag(111) is enabled by an effective tunnelling barrier as a result of limited metal-molecule interactions. Subtle site-dependent variation of the molecular adsorption height as measured by STM and nc-AFM measurements translates into a significant spatial modulation of the molecular polarizability, dielectric constant, and lowest unoccupied molecular orbital (LUMO) energy level alignment, giving rise to a spatially dependent effective molecule-surface tunnelling barrier. Density functional theory calculations, as performed by a collaborator, Dr. Yuefeng Yin, are presented to complement the experimental findings. Dr. Cornelius Krull assisted in performing some of the measurements presented in this chapter. Dr. Cornelius Krull, Dr. Yuefeng Yin, Prof. Nikhil Medhekar and Dr. Agustin Schiffrin, all assisted in the interpretation of the findings here. Unless otherwise stated, all experimental measurements, presented in this chapter were performed at 4.4 K.

Finally, the results presented in this chapter have been published as Kumar, D.; Krull, C.; Yin, Y.; Medhekar, N. V.; Schiffrin, A. Electric Field Control of Molecular Charge State in a Single-Component 2d Organic Nanoarray. *ACS Nano* **2019**, *13* (10), 11882–11890 [81].

3.2 Structural Characterisation of DCA Monolayer on Ag(111)

3.2.1 STM and nc-AFM structural characterisation

Figure 3.1a shows an nc-AFM image (taken with a CO-functionalised tip; see subsection 2.2.7) of DCA molecules within a self-assembled domain after deposition on Ag(111) (see subsection 2.1.5 for sample preparation details). Here, we considered sub-monolayer molecular coverages that resulted in DCA domains larger than 200 × 200 nm^2. The molecules form a 2D monoclinic lattice with unit cell vectors $\mathbf{a_1}$ and $\mathbf{a_2}$ ($\|\mathbf{a_1}\| = 1.20 \pm 0.02$ nm; $\|\mathbf{a_2}\| = 0.99 \pm 0.01$ nm; $\angle(\mathbf{a_1};\mathbf{a_2}) = 53 \pm 1°$). Like other aromatic molecules, DCA adopts a planar adsorption configuration on Ag(111) [227–230]. The molecular axis along the anthracene group (yellow dashed line) follows a 5 ± 1° angle with respect to $\mathbf{a_1}$.The two-fold symmetric cyano groups – with their lone electron pairs – mediate in-plane directional hydrogen-bonding with the neighbouring molecules' extremities of the anthracene group, resulting in non-covalent networking. Such non-covalent 2D molecular self-assembly based on in-plane hydrogen bonding involving cyano-containing molecules is well established [68, 77, 113].

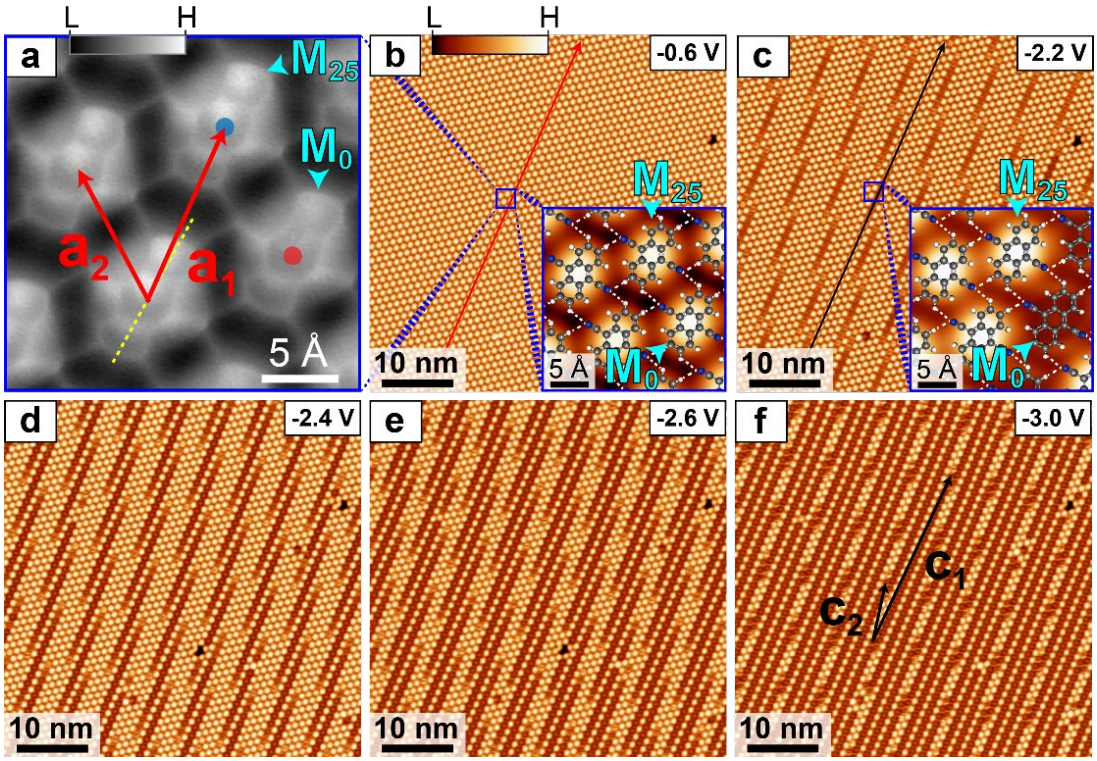

Figure 3.1: STM and nc-AFM imaging of DCA submonolayers on Ag(111). (a) Tip-functionalised nc-AFM image of DCA molecules in a self-assembled monolayer on Ag(111) (tip retracted 20 pm with respect to STM set point V_b = –20 mV, I_t = 200 pA, adjusted on top of molecule centre). Long molecular axis (yellow dashed line) forms a ~5° angle with vector $\mathbf{a_1}$. (b)-(f) Constant-current STM imaging of DCA sub-monolayer on Ag(111) at V_b = –0.6, –2.2, –2.4, –2.6, –3.0 V (I_t = 50 pA). At V_b = –0.6 V, the molecular domain appears homogenous; each bright ellipse is a DCA molecule. As V_b decreases, some molecules are imaged darker, with a smaller apparent height [molecule labelled M_0 in (c) inset; M_{25} indicates molecule with unchanged contrast], defining a periodic superstructure with unit cell vectors $\mathbf{c_1}$ and $\mathbf{c_2}$. The number of these dark molecules increases with increasing absolute value of V_b. Labels M_0 and M_{25} in (a) and in insets of (b) and (c) indicate the same molecules.

The STM image in **Figure 3.1**b shows a larger area of the DCA self-assembly at a bias voltage, V_b = – 0.6 V. Each bright elliptical feature corresponds to a single DCA molecule (inset of **Figure 3.1**b). Like the nc-AFM image in **Figure 3.1**a, the DCA domain appears homogenous. **Figures 3.1**c-f correspond to STM images of the same area at different bias voltages (V_b = – 2.2 V, – 2.4 V, – 2.6 V, – 3.0 V, respectively). We observe that some molecules show a change in contrast, with a significantly smaller apparent height (label 'M_0' in inset of **Figure 3.1**c), that is, with a significantly lower conductance (since a smaller tip-sample distance is required to maintain the same tunnelling current). This change in contrast depends on the applied bias voltage, with more molecules showing a smaller apparent height along $\mathbf{a_1}$ as the absolute value of V_b increases. This change in imaging contrast is reversible; the molecule regains its normal appearance with decreasing absolute value of V_b. The molecules with altered contrast define a periodic superstructure, which, for this specific molecular domain, has unit cell vectors $\boldsymbol{c_1} = 22\mathbf{a_1} - \mathbf{a_2}$ and $\mathbf{c_2} = 6\mathbf{a_1} + 2\mathbf{a_2}$ (**Figure 3.1**f), with $|\mathbf{c_1}| = 26.4 \pm 0.1$ nm, $|\mathbf{c_2}| = 7.5 \pm 0.1$ nm, and $\angle(\mathbf{c_1}; \mathbf{c_2}) = 11 \pm 1°$ (superstructure unit cell area: 37.8 ± 4.0 nm^2).

Here, along $\mathbf{a_1}$, this bias-dependent imaging contrast behaviour repeats after 50 molecules. Along this direction, we labelled the molecules sequentially as 'M_i' (i = 0, …, 49), with 'M_0' corresponding to the molecule that shows a change in contrast at the smallest $|V_b|$.

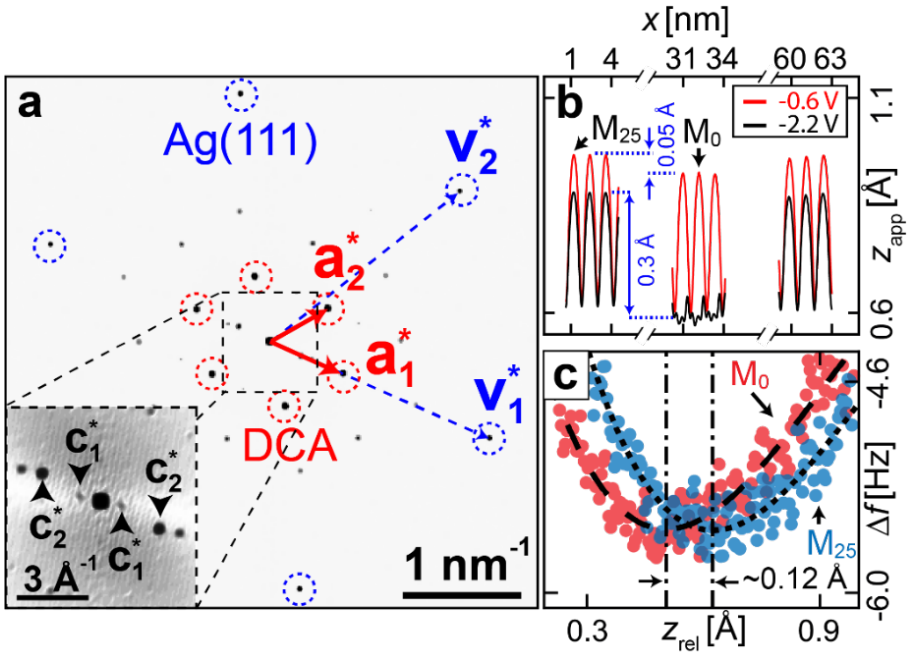

Figure 3.2: FT-STM and apparent height measurements of DCA/Ag(111). (a) Fourier transform (FT; k = 1/wavelength) of STM image in **Figure 3.1**b, superimposed to the FT of an atomically resolved STM image of bare Ag(111). Vectors $\mathbf{v_1^*}$ and $\mathbf{v_2^*}$, $\boldsymbol{a_1^*}$ and $\mathbf{a_2^*}$, and $\mathbf{c_1^*}$ and $\mathbf{c_2^*}$ (indicated by black triangles in inset) define, respectively, unit cells of the reciprocal Ag(111) atomic lattice, of the reciprocal DCA domain lattice, and of the reciprocal superstructure lattice given by small variations of the molecular STM apparent height. These lattices are commensurate with each other. The reciprocal space vectors $\mathbf{c_1^*}$ and $\mathbf{c_2^*}$ correspond to the real space vectors $\mathbf{c_1}$ and $\mathbf{c_2}$ in **Figure 3.1**f. That is, the superstructure in **Figure 3.1**c – f given by bias-dependent altered contrast of DCA is perfectly correlated to the superstructure given by small apparent height variations in **Figure 3.1**b. (b) STM apparent height profiles of a molecular row along $\mathbf{a_1}$ at V_b = – 0.6 V (red arrow in **Figure 3.1**b) and at V_b = – 2.2 V (black arrow in **Figure 3.1**c). At V_b = – 0.6 V, the apparent height of molecule M_0 is 0.05 ± 0.01 Å smaller than that of M_{25}. (c) Nc-AFM (tip functionalised with CO) resonance frequency shift Δf as a function of relative tip-sample distance z_{rel} (z_{rel} = 0 corresponds to STM set point V_b = –20 mV, I_t = 200 pA measured on M_0), measured on M_0 (red) and M_{25} (blue) (see **Figure 3.1**a). The turning point difference of ~0.12 Å confirms that M_0 adsorbs closer to the surface than M_{25}, and that molecule-surface distance depends on adsorption site, consistent with the STM apparent height variations.

Figure 3.2a corresponds to the Fourier Transform (FT) of the STM image in **Figure 3.1**b superimposed on the FT of an atomically resolved STM image of bare Ag(111) (reciprocal lattice unit cell vectors $\mathbf{v_1^*}$and $\mathbf{v_2^*}$). We observe peaks related to the periodicity of the molecular self-assembly (red dashed circles; vectors $\mathbf{a_1^*}$ and $\mathbf{a_2^*}$) as well as lower frequency peaks (black triangles in **Figure 3.2**a inset; vectors $\mathbf{c_1^*}$ and $\mathbf{c_2^*}$). These lower frequency peaks correspond to a subtle real-space long-range modulation of the molecular domain STM apparent height in **Figure 3.1**b. Importantly, the Fourier space vectors $\mathbf{c_1^*}$ and $\mathbf{c_2^*}$ associated with this modulation correspond to the real space vectors $\mathbf{c_1}$ and $\mathbf{c_2}$ associated with the bias-dependent superstructure

in **Figures 3.1**c-e. That is, the molecules (labelled 'M_0') that have a slightly smaller (~0.05 Å) STM apparent height in **Figure 3.1**b (closer to the surface) are those that appear darker in **Figure 3.1**c as the bias voltage V_b is lowered from positive to negative values. This can further be observed in the STM apparent height profiles in **Figure 3.2**b.

From the FT in **Figure 3.2**a, we can deduce that for the molecular domain in **Figures 3.1**b–f:

$$\begin{pmatrix} \mathbf{a_1} \\ \mathbf{a_2} \end{pmatrix} = \begin{bmatrix} 199/50 & 0 \\ 14/25 & 3 \end{bmatrix} \begin{pmatrix} \mathbf{v_1} \\ \mathbf{v_2} \end{pmatrix} \quad \text{(Eq. 3.1)}$$

where $\mathbf{v_1}$ and $\mathbf{v_2}$ define a real-space unit cell of the Ag(111) atomic lattice, and therefore:

$$\begin{pmatrix} \mathbf{c_1} \\ \mathbf{c_2} \end{pmatrix} = \begin{bmatrix} 87 & -3 \\ 25 & 6 \end{bmatrix} \begin{pmatrix} \mathbf{v_1} \\ \mathbf{v_2} \end{pmatrix} \quad \text{(Eq. 3.2)}$$

The DCA self-assembly is commensurate with the noble metal atomic lattice, with the molecular row along $\mathbf{a_1}$ parallel to one of the Ag(111) <1,1,0> crystallographic axes. The superstructure with unit cell vectors $\mathbf{c_1}$ and $\mathbf{c_2}$ is a Moiré structure resulting from the lattice mismatch [231–233] between the molecular domain and Ag(111). Therefore, the change in molecular STM imaging contrast observed at negative biases (**Figures 3.1**c-f) depends on the molecules' adsorption site; two DCA molecules with the exact adsorption site will exhibit the same bias-dependent change in STM imaging contrast. It is important to note that the long range of the STM contrast modulation periodicity along $\mathbf{a_1}$ results in molecular domains where the relationships between vectors $\{\mathbf{c_1}, \mathbf{c_2}\}$ and $\{\mathbf{v_1}, \mathbf{v_2}\}$ vary slightly but remain commensurate (see Appendix A.2).

Measurements of nc-AFM frequency shift, Δf, as a function of tip-molecule distance z above different molecules (using a CO-functionalised tip) allow for the evaluation of the differences in the *real* adsorption heights of different molecules (see subsection 2.4.2), as opposed to differences in the *apparent* heights for the different molecules measured by STM. The differences in the z positions of the $\Delta f(z)$ minima provide an estimate for the differences in actual tip-sample distance (and hence in actual molecule adsorption heights). **Figure 3.2**c shows that the adsorption height of molecule M_0 is ~0.12 Å smaller than that of M_{25}. This was determined after fitting a 3rd order polynomial to the $\Delta f(z)$ data in the vicinity of the minima. Repeating this procedure using different CO-functionalised tips yielded measurements for the difference in adsorption height, Δh_{ads} between molecule M_0 and M_{25} as shown in **Table 3.1**. These measurements give a weighted mean adsorption height difference between molecules M_0 and M_{25}, $\langle \Delta h_{ads} \rangle = 0.08 \pm 0.02$ Å. This corroborates the differences in the apparent heights of the molecules as measured by STM in **Figure 3.2**b.

Datasets	$\Delta h_{ads} = h_{min}^{(25)} - h_{min}^{(0)}$
Tip 1	0.024 Å
Tip 2	0.062 Å
Tip 3	0.117 Å
Tip 4	0.109 Å
Tip 5	0.089 Å

Table 3.1: Adsorption height differences between DCA molecules measured via nc-AFM. Difference in adsorption height, Δh_{ads}, between molecules M_0 ($h_{min}^{(0)}$: z position of $\Delta f(z)$ minimum for M_0) and M_{25} ($h_{min}^{(25)}$), was measured with 5 different CO-functionalised tips. This resulted in a mean adsorption height difference, $\langle \Delta h_{ads} \rangle$ = 0.08 ± 0.02 Å (the uncertainty reported is the standard error of the mean).

This (subtle) variation in the molecules' adsorption heights can also be seen in nc-AFM imaging of the molecular domain (see **Figure 3.3**a). **Figure 3.3**b shows the FT of the nc-AFM image in **Figure 3.3**a. Fourier-space peaks with vectors space peaks with vectors $\mathbf{c_1^*}$ and $\mathbf{c_2^*}$ indicate low-frequency modulation identical to that observed in STM imaging (**Figure 3.2**a).

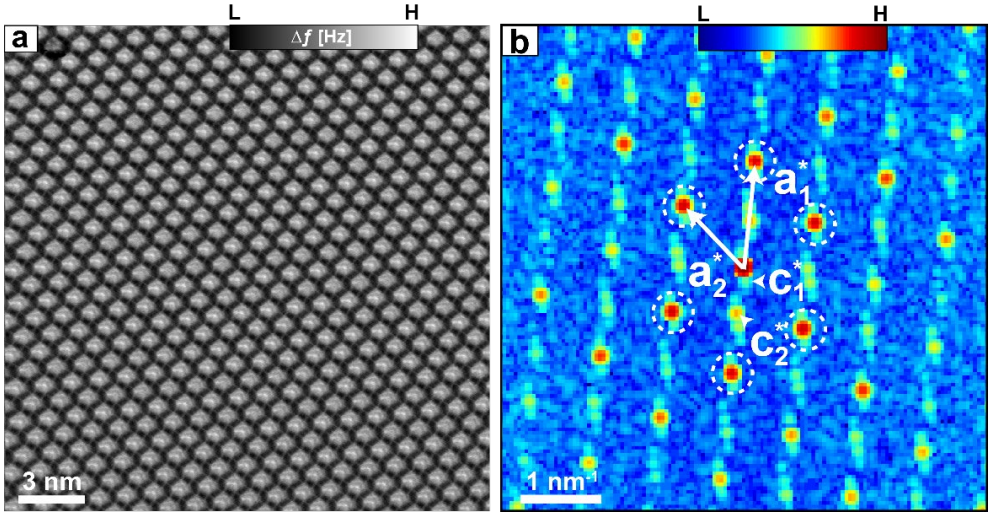

Figure 3.3: Variation of DCA/Ag(111) molecular adsorption height measured via nc-AFM. (a) Constant-height nc-AFM Δf image of DCA/Ag(111) taken with CO-functionalised tip (tip height determined by STM set point V_b = -20 mV, I_t = 200 pA on a DCA molecule; imaging at V_b = 0 V). (b) FT of nc-AFM image in (a) showing peaks with vectors $\mathbf{a_1^*}$ and $\mathbf{a_2^*}$ corresponding to the periodicity of the molecular lattice (dashed circles) and low frequency peaks with vectors $\mathbf{c_1^*}$ and $\mathbf{c_2^*}$ due to the subtle long-range modulation of the molecules' adsorption height (white triangles).

3.2.2 DFT-calculated adsorption height

To understand the varying adsorption heights (as measured by STM and nc-AFM) of the DCA molecules on Ag(111), DFT calculations were performed by collaborator Dr. Yuefeng Yin to determine how the conformation of a single DCA molecule change as a function of its adsorption site on Ag(111). For the DFT computation, we considered three inequivalent initial DCA adsorption sites and allowed the system to relax to a final, energetically favourable, configuration. **Figure 3.4** shows the resulting adsorption heights, with slight variations

depending on the adsorption site. Here, we find variations of the adsorption height of ~0.1 Å. This is consistent with the findings via nc-AFM ($\langle \Delta h_{ads} \rangle = 0.08 \pm 0.02$ Å). With DFT, the average adsorption height was found to be $\langle h_{ads} \rangle \approx 2.86$ Å. Details of the DFT computation can be found in the Appendix A.1.

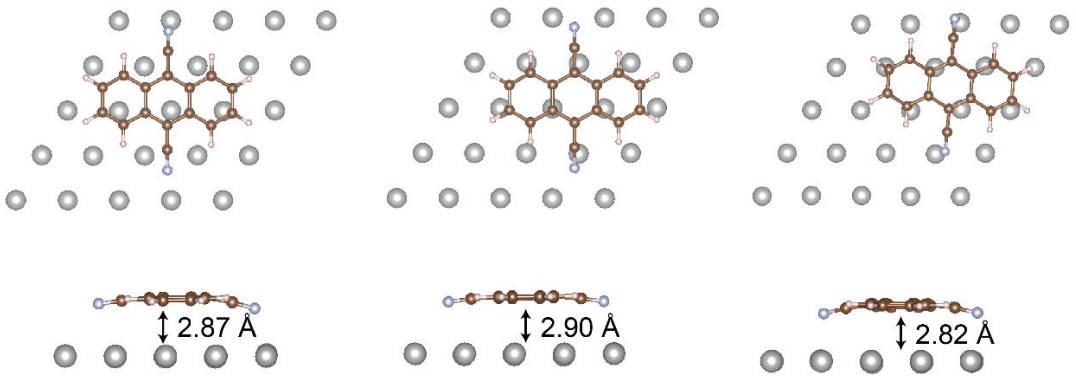

Figure 3.4: DFT-calculated energetically favourable adsorption geometries of DCA on Ag(111). Here we consider three inequivalent initial adsorption sites for single DCA molecules on Ag(111) and then allow the molecules to relax to their final configuration. The shown adsorption heights consist of the average distances between the molecule atoms and the atoms of the Ag surface top layer. The figure is courtesy of Dr. Yuefeng Yin.

3.3 STS Characterisation of DCA Monolayer on Ag(111)

To gain insight into the bias-dependent change in STM imaging contrast (**Figure 3.1**), we performed differential conductance $\mathrm{d}I/\mathrm{d}V$ STS measurements at different locations within a molecular domain (see **Figure 3.5**; note that this is a different domain from that of **Figure 3.1** and **Figure 3.2**). In **Figure 3.5**b, the $\mathrm{d}I/\mathrm{d}V$ spectrum taken on top of molecule M_0 (molecule that changes its STM contrast at negative bias with the smallest absolute value $|V_b|$; e.g., inset **Figure 3.1**c) shows a dip at a voltage $V^* \approx -2.1$ V. This dip in the $\mathrm{d}I/\mathrm{d}V$ STS spectrum is indicative of surface-to-molecule electron transfer and negative charging of the molecule induced by the bias voltage at the STM junction [56]. Note that this is characteristically similar to Coulomb blockade effects observed when tunnelling through quantum dots [234, 235]; sharp changes in the tunnelling conductance are due to an increase in energy required for tunnelling electrons to overcome the Coulomb repulsion and subsequently occupy an already electron-occupied quantum dot. The ring observed in the negative-bias $\mathrm{d}I/\mathrm{d}V$ map in **Figure 3.5**b inset corroborates the charging of the molecule [236–241]. The charging bias onset V^*corresponds to the bias below which the contrast of the molecule changes in STM imaging, with a significant bias-dependent reduction of the apparent height (e.g., dark molecules in **Figures 3.1**c-f). This contrast change is the result of bias-induced negative charging of DCA.

The charging onset V^* depends on the location of the molecule within the molecular domain. Molecule M_0 exhibits the smallest absolute value $|V^*|$; the further a molecule is from

M_0 along $\mathbf{a_1}$, the larger $|V^*|$ is (see Appendix A.3). For example, $V^* \approx -2.23$ V for molecule labelled M_4 along $\mathbf{a_1}$ in **Figure 3.5**a. Within the considered bias voltage window (i.e., for $V_b > -3.2$ V, since $V_b < -3.2$ V tends to damage the molecules in the nanofilm), we did not observe charging for molecules adjacent to M_0 in the next parallel molecular row (for example, molecule M_{29}).

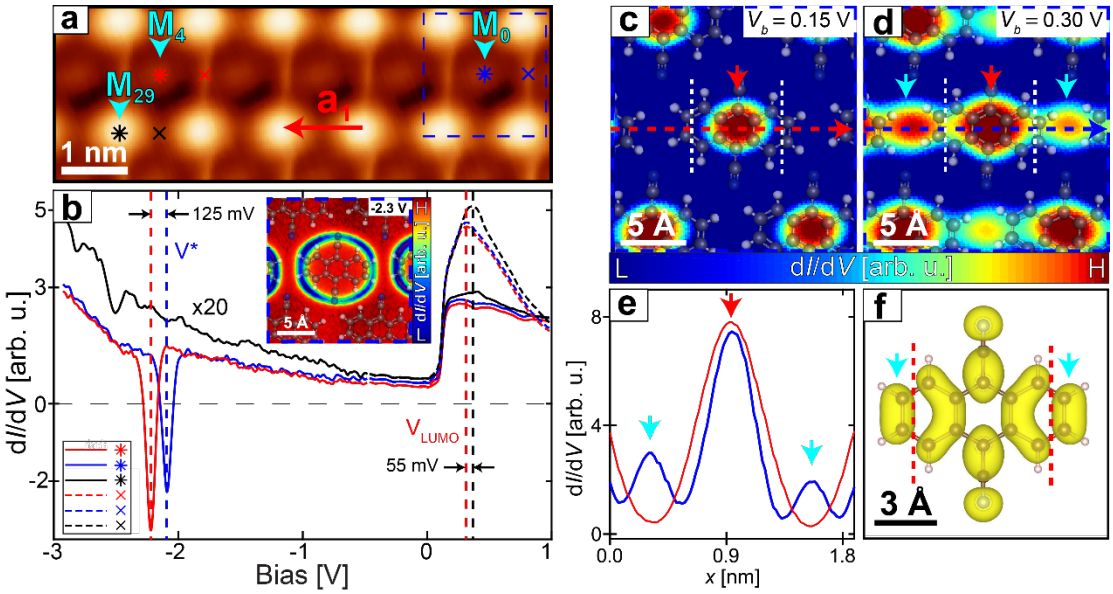

Figure 3.5: Point STS and dI/dV mapping measurements on DCA monolayer on Ag(111). (a) Constant-current STM image of DCA domain (V_b = –2.4 V, I_t = 50 pA). At this bias voltage, molecules M_0 (blue dashed box) to M_5 show altered contrast, with a significantly reduced apparent height (dark imaging). Adjacent molecular row parallel to $\mathbf{a_1}$ shows unaltered apparent height (bright imaging). (b) dI/dV spectra taken at locations indicated in (a) (set point V_b = –0.5 V, I_t = 150 pA). Spectra for dark molecules in (a) show negative differential conductance dip at negative bias voltages V^*, indicative of Coulomb repulsion due to bias-induced negative charging of molecule. Negative voltage part of spectra was scaled by a factor of 20 for clarity. Spectra on top of molecules reveal a step-like feature with an onset at ~120 mV, indicative of a 2D interface state. Spectra in between molecules show a peak at positive bias voltages V_{LUMO}, associated with the lowest unoccupied molecular orbital (LUMO). Inset: constant-height dI/dV map of molecule M_0 in (a), showing charging ring (V_b= –2.3 V; set point of V_b = –0.5 V, I_t= 150 pA on top of molecule). (c) – (d) Constant-height dI/dV maps of molecule M_0 in (a), (V_b = 0.15 V and 0.3 V respectively; tip retracted 50 pm from set point V_b = –20 mV, I_t= 5pA on top of molecule). (e) dI/dV profiles across maps in (c) (red), (d) (blue). Higher intensity at molecule center is due to topography (red arrows). For V_b = 0.3 V, higher intensity at anthracene extremities (cyan arrows) and nodal planes parallel to the axis defined by the cyano groups are characteristic of the LUMO (white dashed line). (f) DFT-calculated LUMO frontier of DCA in gas phase (isosurface level = 8.29 × 10^{-4} e/Å^3). The dI/dV maps in c-d were bias cuts taken from a dI/dV STS grid. dI/dV STS grid was performed by numerically differentiating obtained I-V curves at a fixed tip-sample separation. The dI/dV in the inset of b was obtained with a lock-in technique with a lock-in amplitude and frequency of 7 mV and 1.13 kHz, respectively.

At positive bias voltages, a dI/dV spectrum taken on top of a molecule (**Figure 3.5**b) shows a sharp step-like feature with an onset at ~120 mV. We associate this feature with a 2D electron gas (2DEG) at the molecule-metal interface [56, 242–244]. Investigation of this

interface 2DEG is the subject of Chapter 4. When acquired in between two molecules along $\mathbf{a_1}$, a $\mathrm{d}I/\mathrm{d}V$ spectrum shows—in addition to the 2DEG step-like feature—a peak at an energy which depends on the location within the long-range superstructure; next to molecule M_4, the peak is located at ~0.34 V; next to M_{29}, at ~0.39 V (**Figures 3.5**a,b).

The $\mathrm{d}I/\mathrm{d}V$ maps taken in the vicinity of molecule M_0 at V_b = 0.15 and 0.30 V (**Figures 3.5**c-e) show features centred on the molecules (red arrows) that we attribute to topography (see Appendix A.4). At V_b = 0.30 V, the map shows extra features located at the extremities of the anthracene groups, in between molecules along $\mathbf{a_1}$, associated with the ~335 mV peak (cyan arrows; **Figures 3.5**d,e). The features at the anthracene extremities are reminiscent of the DCA lowest unoccupied molecular orbital (LUMO) with its nodal planes along the cyano-cyano axis [see LUMO of DCA on Ag(111) calculated by density functional theory in **Figure 3.5**f]. We hence associate the $\mathrm{d}I/\mathrm{d}V$ peak at $V_b \approx 335$ mV with the LUMO of the DCA molecule. This is consistent with previous work on DCA adsorbed on graphene/Ir(111) [52].

3.4 Electric-field-induced Ag(111)-to-DCA Electron Transfer

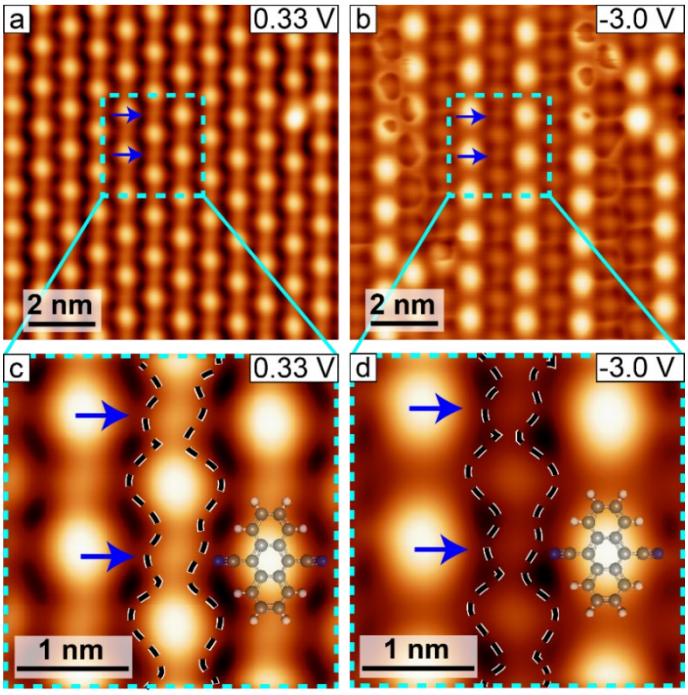

Figure 3.6: STM imaging showing direct topographic correlation between the DCA LUMO and the DCA negatively charged state. (a)-(b) Constant-current STM images of DCA monolayer on Ag(111) (a: V_b = 330 mV, I_t = 4 nA; b: V_b = –3.0 V, I_t = 300 pA). Nodal features (blue arrows) in-between DCA molecules associated with the LUMO can be seen for the neutral (a) and negatively charged species (b). (c)-(d) Zoomed-in STM images of (a) and (b) (cyan dashed square). Black dashed contours outline the same molecular row.

In the previous section, we deduced that charging of DCA at negative bias voltages for $|V_b| > |V^*|$ was the result of an electron transfer from Ag(111) to the LUMO. To further support this,

we consider the following. **Figure 3.6**a shows an STM image of DCA/Ag(111) at a bias voltage V_b = 0.33 V, above the LUMO onset, where DCA is neutral. Features in between the molecule centres, near the anthracene extremities, are characteristic of the LUMO (blue arrows in **Figures 3.6**a,c). At negative bias voltages, for $|V_b| > |V^*|$, STM imaging of negatively charged molecules shows similar intermolecular features at the anthracene extremities (blue arrows in **Figures 3.6**b,d), identical to the neutral DCA LUMO. This similarity between imaging of neutral DCA unoccupied states (positive bias) and of negatively charged DCA occupied states (negative bias), with features characteristic of the LUMO, provides direct evidence that the field-induced charging of DCA is mediated by a population of the LUMO.

3.5 z-dependent STS Measurements and DBTJ Model

To further understand the bias-induced charging of DCA, we performed measurements of V^* and of the energy position, V_{LUMO}, of the LUMO dI/dV peak, as a function of tip-molecule distance z, for different molecules (M_0 to M_{39}; here, the periodicity along $\mathbf{a_1}$ repeats after 39 molecules, that is, $M_0 = M_{39}$ and so on) along $\mathbf{a_1}$ (see **Figure 3.7**a). This was done by acquiring I-V curves on each of these molecules for negative (–0.02 to –3 V) and positive (–0.02 to 0.8 V) bias voltages, at different tip-sample distances z (determined relative to a tunnelling set point V_b= –0.02 V, I_t= 5 pA above M_0). We then calculated $\mathrm{d}I/\mathrm{d}V$ by numerically differentiating the I-V curves and determined V^* at a given z and given molecule as the energy position of the sharp dip at negative biases (**Figure 3.5**b). We determined $V_{\mathrm{LUMO}}(z)$ of the LUMO peak by fitting the $\mathrm{d}I/\mathrm{d}V$ curves at positive biases (see Appendix A.5 for details).

Figure 3.7b shows plots of $V^*(z)$ and $V_{\mathrm{LUMO}}(z)$ for M_0, M_5 and M_9. The absolute value $|V^*|$ of the charging bias voltage increases linearly with increasing z (e.g., $V^* = $ –1.70 V to –2.48 V for $\Delta z = 3.1$ Å, for M_0, that is, 46 % variation,). This linear relationship provides evidence that the negative charging of the molecule is driven by the electric field applied at the STM junction; the slope of $V^*(z)$ defines the gating electric field, F_g, required to charge the molecule (e.g., $F_g = $ –2.48 ± 0.01 V/nm for M_0). The energy position $V_{\mathrm{LUMO}}(z)$ of the LUMO also decreases (slightly) as z is increased (e.g., $V_{\mathrm{LUMO}} = $ 300 to 294 mV for $\Delta z = $1 Å for M_0, that is, 2 % variation). This demonstrates that the molecular orbital energy level is not perfectly pinned to the Fermi level E_F of Ag(111). Similar z-dependent variations of V_{LUMO} have been observed previously, but mostly on thin dielectric films [245].

The observed field-induced charging and z-dependent measured V_{LUMO} of DCA is a strong indication that the interaction between molecule and surface is weak. Indeed, significant interactions would hamper charge localisation [56, 245, 246] and would result in Fermi level pinning of the LUMO. We explain this limited metal-molecule interaction by the flat molecular adsorption, similar to other aromatic molecules [227–230], and by the cyano group lone

electron pairs mainly interacting with adjacent molecules' anthracene groups via in-plane directional hydrogen bonding [68, 113]. The molecule-surface system therefore behaves as if an effective potential barrier existed between DCA and Ag(111), similar to the case of molecules adsorbed on thin insulating film on metals [245]. Importantly, the proximity of the DCA LUMO to the Fermi level is a key factor enabling the field-induced on-metal charging of DCA. This is in contrast to DCA dimers [formed during deposition with Ag(111) held at low temperature] which exhibit charging at significantly larger electric field magnitudes due to a higher LUMO energy and a greater molecule-surface interaction via the cyano-group lone electron pairs (see section 3.9).

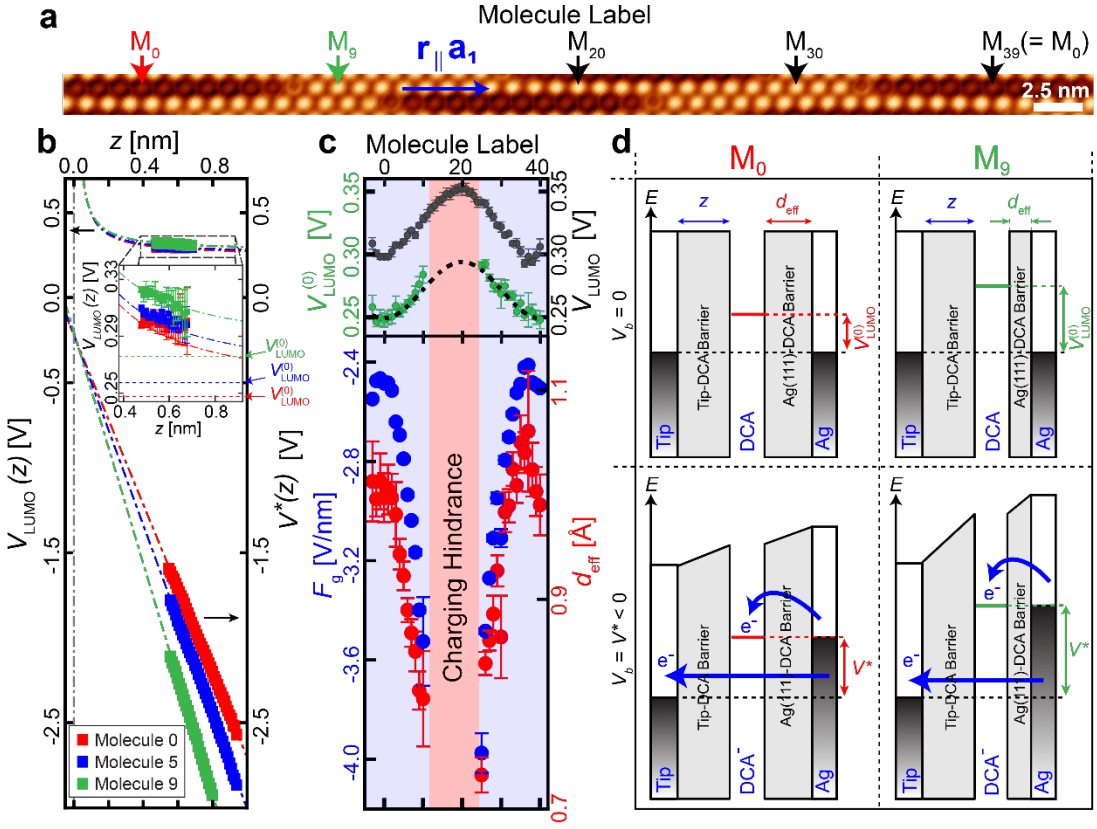

Figure 3.7: $V^*(z)$ and $V_{\mathrm{LUMO}}(z)$ measurements and the double barrier tunnelling junction (DBTJ) model. (a) STM image (V_b = –2.4 V, I_t = 50 pA) of molecular domain where the bias-dependent charging behaviour of DCA along $\mathbf{a_1}$ repeats after 39 molecules. (b) Measurements of V^* (bottom) and V_{LUMO} (top) for molecules M_0, M_5 and M_9 [labelled in (a)] as a function of tip-molecule distance, z. Dashed lines are fits of data based on the DBTJ model (Methods). Inset: zoomed-in plot of $V_{\mathrm{LUMO}}(z)$, asymptotically approaching $V_{\mathrm{LUMO}}^{(0)}$ as $z \to \infty$ (z = 0.58 nm corresponds to STM set point V_b = –20 mV, I_t = 5 pA on top of M_0; actual tip height was derived from DBTJ model fit). (c) Top: variation of V_{LUMO} (black at z = 0.47 nm) and $V_{\mathrm{LUMO}}^{(0)}$ (green) as a function of molecule label. Bottom: gating field, $F_g = dV^*/dz = -V_{\mathrm{LUMO}}^{(0)}/d_{\mathrm{eff}}$, (blue) required to charge each molecule and effective molecule-metal distance, d_{eff} (red). Both $V_{\mathrm{LUMO}}^{(0)}$ and d_{eff} were extracted from DBTJ model fits of $V^*(z)$ and $V_{\mathrm{LUMO}}(z)$ data. For molecules M_{11} to M_{24}, $V^*(z)$ could not be measured (and F_g, $V_{\mathrm{LUMO}}^{(0)}$, d_{eff} could not be extracted) due to Coulomb repulsion effects from neighbouring charged molecules. All error bars are ±1 standard deviation, except for $V^*(z)$ in (b) where they were omitted due to small size. (d) Schematic of DBTJ energy model depicting charging of molecules M_0 and M_9 [red and green arrows in (a)]. Charging bias

onset V^* corresponds to bias voltage V_b at which the substrate's Fermi level and molecule's LUMO align; V^* depends on z, d_{eff} and $V_{LUMO}^{(0)}$. Top: $V_b = 0$. Bottom; $V_b = V^*$.

This allows us to model the STM junction as a double barrier tunnelling junction (DBTJ) [56, 246, 247], where one potential barrier consists of the vacuum between tip and molecule (with a barrier width z), and the other barrier consists of the effective potential barrier between molecule and metal (barrier width d_{eff}; **Figure 3.7**d). Within this model, when a negative bias voltage V_b is applied, the potential across the DCA-Ag(111) barrier drops, that is, the LUMO energy shifts towards E_F. This potential drop and resulting LUMO energy shift depend linearly on the ratio between d_{eff} and total barrier width $(z + d_{eff})$; they are null if $d_{eff}/(z + d_{eff}) = 0$. If the potential drop becomes equal to the intrinsic LUMO energy $V_{LUMO}^{(0)}$ (that is, the LUMO energy with respect to E_F when $V_b = 0$), the LUMO energy V_{LUMO} aligns with E_F, that is, $V_{LUMO} = 0$; an electron can then tunnel through the DCA-Ag(111) barrier and populate the LUMO, resulting in negative charging of the molecule. When molecular charging occurs, $V_b = V^*$. Within this model, the bias voltage at which the molecule charge is given by:

$$V^*(z) = -\frac{V_{LUMO}^{(0)}}{d_{eff}} z - V_{LUMO}^{(0)} \qquad \text{(Eq. 3.3)}$$

with $F_g = -V_{LUMO}^{(0)}/d_{eff}$ [56, 236], and the measured LUMO energy with respect to E_F is given by:

$$V_{LUMO}(z) = V_{LUMO}^{(0)} \frac{d_{eff}}{z} + V_{LUMO}^{(0)} \qquad \text{(Eq. 3.4)}$$

We determined $V_{LUMO}^{(0)}$ and d_{eff} by fitting our measured $V^*(z)$ and $V_{LUMO}(z)$ with Eq. 3.3 and Eq. 3.4, respectively, for molecules M_0 to M_{10} and M_{25} to M_{39} (**Figures 3.7**a,b) as described in the following.

For each molecule, we determined $V_{LUMO}^{(0)}$ and d_{eff} by minimising the following quantity χ:

$$\chi = \sqrt{\chi_1^2 + \chi_2^2} \qquad \text{(Eq. 3.5)}$$

where,

$$\chi_1 = \frac{\sum_i \left(V^*(z_i) - V^*_{\text{Eq(3.3)}} \left(V_{LUMO}^{(0)}, d_{eff}, z_i \right) \right)^2}{\left(\delta V^*(z_i) \right)^2} \qquad \text{(Eq. 3.6)}$$

and:

$$\chi_2 = \frac{\sum_i \left(V_{\mathrm{LUMO}}(z_i) - V_{\mathrm{LUMO}}^{(\mathrm{Eq}(3.4))} \left(V_{\mathrm{LUMO}}^{(0)}, d_{\mathrm{eff}}, z_i \right) \right)^2}{\left(\delta V_{\mathrm{LUMO}}(z_i) \right)^2} \qquad \text{(Eq. 3.7)}$$

The sum is performed over the all the tip heights z_i for which the measurements were performed at. The functions $V_{\mathrm{Eq}(3.3)}^{*}$ and $V_{\mathrm{LUMO}}^{(\mathrm{Eq}(3.4))}$ are given by Eq. 3.3 and Eq. 3.4, respectively, whereas $V^*(z_i)$, $V_{\mathrm{LUMO}}(z_i)$, $\delta V^*(z_i)$, and $\delta V_{\mathrm{LUMO}}(z_i)$ are the measured $V^*(z)$ and $V_{\mathrm{LUMO}}(z)$ for each molecule and their respective uncertainties (at different heights).

Eq. 3.3 and Eq. 3.4 also allows us to estimate the z = 0 reference (same for all molecules; see Appendix A.5). By combining these equations, we obtain:

$$\frac{\partial \log\left(V^*(z)\right)}{\partial z} * \left(\frac{V_{\mathrm{LUMO}}(z)}{V^*(z)} - 1 \right) \Bigg|_{z = z_{\mathrm{setpoint}}} = \frac{1}{z_{\mathrm{setpoint}}} \qquad \text{(Eq. 3.8)}$$

Using the above equation, we estimated that the absolute tip-sample distance corresponding to a tunnelling set point of V_{b} = –0.02 V, I_{t} = 5 pA at the location M_0, z_{setpoint}, is 5.8 ± 0.3 Å (see Appendix A.5).

Note that we did not observe field-induced charging (for V_{b} between ~ -3.2 and 0 V, i.e., for a maximum applied electric field strength of $\sim$4.5 V/nm) and could not retrieve $V_{\mathrm{LUMO}}^{(0)}$ and d_{eff} (and hence F_{g}) for M_{11} to M_{24}, (**Figure 3.7**c); charging of these molecules is hindered due to Coulomb repulsion by adjacent charged molecules, which charge at smaller $|F_{\mathrm{g}}|$ (see section 3.8). It is important to note that, for a given molecule, the same values of $V_{\mathrm{LUMO}}^{(0)}$ and d_{eff} (combined with a general z = 0 reference) result in the best fitting of both $V^*(z)$ and $V_{\mathrm{LUMO}}(z)$. This demonstrates that the DBTJ model provides a good physical description of our system, with reliable retrieval of $V_{\mathrm{LUMO}}^{(0)}$ and d_{eff} for each molecule. Also, it provides compelling evidence that the LUMO is indeed the electronic state involved in the charging via Ag(111)-to-DCA electron transfer.

The retrieved values of $V_{\mathrm{LUMO}}^{(0)}$ and d_{eff} (and hence F_{g}) vary for different molecules (**Figure 3.7**c) following the spatial periodicity of the molecular charging pattern seen in **Figure 3.7**a; that is, $V_{\mathrm{LUMO}}^{(0)}$ and d_{eff} depend on the molecular adsorption site on Ag(111). For example, molecule M_0 exhibits the smallest $V_{\mathrm{LUMO}}^{(0)} \approx 248$ mV and largest $d_{\mathrm{eff}} \approx 1.0$ Å, resulting in the smallest absolute value of the gating field required for charging ($|F_{\mathrm{g}}| \approx 2.48$ V/nm). For comparison, $V_{\mathrm{LUMO}}^{(0)} \approx 276$ mV, $d_{\mathrm{eff}} \approx 0.8$ Å and $|F_{\mathrm{g}}| \approx 3.4$ V/nm for M_9 (**Figure 3.7**c). This spatially periodic variation of the susceptibility of charging for different molecules when

exposed to an applied electric field is what gives rise to the charging superstructure observed in STM images at a given bias voltage (**Figure 3.1**).

3.6 Molecular Screening Environment

What is the physical mechanism behind the adsorption site dependence of $V_{\mathrm{LUMO}}^{(0)}$ and d_{eff}? We explain the variation of $V_{\mathrm{LUMO}}^{(0)}$ by screening effects from the underlying metal, that can stabilise an electron injected to the LUMO via an image charge and increase the molecular electron affinity by a stabilisation energy [248, 249], $\Delta E(d)$:

$$V_{\mathrm{LUMO}}^{(0)}(d) = V_{\mathrm{LUMO}}^{(0)}(\mathrm{d} \to \infty) - \Delta E(d) \qquad \text{(Eq. 3.9)}$$

with:

$$\Delta E(d) = \frac{1}{4\pi\epsilon_0}\frac{e^2}{2d} \qquad \text{(Eq. 3.10)}$$

where d is the molecule-metal distance. Note that this classical approach is justified by the weak DCA-Ag(111) interaction observed and does not include quantum mechanical effects (e.g., hybridisation). Given the small spatially periodic variations of d along $\mathbf{a_1}$ observed in nc-AFM and STM (that is, related to apparent heights measured at small bias absolute values, where molecules are neutral; **Figures 3.2**b,c), we can write:

$$d(n) = d_{\mathrm{min}} + \frac{\Delta d}{2}\left(1 - \cos\left(\frac{2\pi n}{\lambda}\right)\right) \qquad \text{(Eq. 3.11)}$$

where n is the molecular position ($n = 0$ corresponds to M_0) and λ is the observed periodicity of d along $\vec{a}_1$ for a specific molecular domain (here, for **Figure 3.7**a, $\lambda = 39$). By using this expression of $d(n)$ in Eq. 3.11, we fitted our measured $V_{\mathrm{LUMO}}^{(0)}(d(n))$ (**Figure 3.7**c) and determined the parameters d_{min} (minimum molecule-surface distance, corresponding to M_0) and Δd (molecule-surface distance variation between M_0 and M_{20}). This was done by minimising the quantity χ_{d}:

$$\chi_{\mathrm{d}} = \frac{\sum_i \left(V_{\mathrm{LUMO}}^{(0)}(n) - V_{\mathrm{LUMO}}^{(Eq(3.9))}(d_{\mathrm{min}}, \Delta d, n)\right)^2}{\left(\delta V_{\mathrm{LUMO}}^{(0)}(n)\right)^2} \qquad \text{(Eq. 3.12)}$$

With this procedure, we found $d_{\mathrm{min}} \approx 2.8$ Å and $\Delta d \approx 0.1$ Å. **Figure 3.8**a shows experimental data of $V_{\mathrm{LUMO}}^{(0)}$ (blue; reproduced here from **Figure 3.7**c) and best fit according to this model (red), with $d_{\mathrm{min}} \approx 2.8$ Å and $\Delta d \approx 0.1$ Å. These values are consistent with our nc-AFM data ($\langle \Delta \mathrm{h}_{ads} \rangle = 0.08 \pm 0.02$ Å; subsection 3.2.1) and with DFT-based calculations of the DCA adsorption height ($\langle \mathrm{h}_{ads} \rangle \approx 2.85$ Å; subsection 3.2.2).

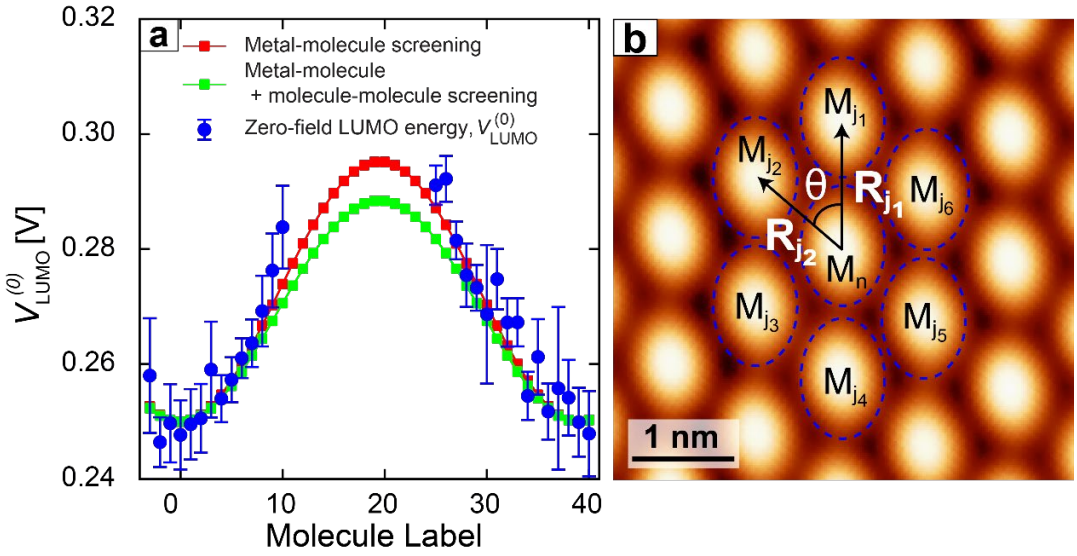

Figure 3.8: Variations in zero-field LUMO energy due to screening by underlying metal and surrounding molecules. (a) Zero-field LUMO energy $V_{\mathrm{LUMO}}^{(0)}$ as a function of molecule label along $\mathbf{a_1}$ in **Figure 3.7**a. Blue circles: experimental data. Red: model fit with screening stabilisation energy provided only by molecule-metal interactions. Green: model fit with screening stabilisation energy provided by molecule-molecule and molecule-metal interactions. (b) Constant-current STM image of DCA molecule M_n (here, $n = 0$) surrounded by six nearest neighbours M_{j_1} ... M_{j_6} on Ag(111) (V_b = –0.02 V, I_t = 50 pA). In our model to calculate in-plane screening due to nearest-neighbour molecule-molecule interactions, we used $\|\mathbf{R_{j_1}}\|$ = 12.3 Å, $\|\mathbf{R_{j_2}}\|$ = 10.8 Å, and θ = 50.2°, as determined by experiment.

We also considered screening effects by the surrounding molecules, which can be polarized laterally (in plane) and further increase the stabilisation energy. Using the *Gaussian* software [250], we calculated the molecular polarizability tensor $\boldsymbol{\alpha}$ of DCA in the gas phase (in CGS units):

$$\boldsymbol{\alpha}(\text{Å}^3) = \begin{pmatrix} \alpha_{xx} & \alpha_{xy} & \alpha_{xz} \\ \alpha_{yx} & \alpha_{yy} & \alpha_{yz} \\ \alpha_{zx} & \alpha_{zy} & \alpha_{zz} \end{pmatrix} = \begin{pmatrix} 41.40 & 0 & 0 \\ 0 & 35.82 & 0 \\ 0 & 0 & 8.17 \end{pmatrix} \qquad \text{(Eq. 3.13)}$$

Where x is along the long molecular axis (anthracene), y is along the cyano-cyano axis and z is perpendicular to the anthracene plane. Screening via classical electrostatic metal-molecule interaction changes the molecular in-plane polarizability α_{xx} and α_{yy} according to [251]:

$$\alpha_{xx,yy}{}' = \frac{\alpha_{xx,yy}}{1 - \frac{k\alpha_{xx,yy}}{(2d)^3}} \qquad \text{(Eq. 3.14)}$$

where $k = 1/(4\pi\epsilon_0)$ is the Coulomb constant. The contribution to the stabilisation energy of the nth molecule due to in-plane screening from the surrounding molecule then becomes [248]:

$$\Delta E^{(\mathrm{p})}(n) = \frac{k^2 e^2}{2} \sum_i \frac{\alpha_i'}{|\mathbf{R_i}|^4} \qquad \text{(Eq. 3.15)}$$

with:

$$\alpha'_i = (\alpha_{xx}'\hat{\mathbf{i}} + \alpha_{yy}'\hat{\mathbf{j}}) \cdot \hat{\mathbf{R}}_\mathbf{i} \qquad \text{(Eq. 3.16)}$$

where e is the elementary electric charge, $\mathbf{R_i}$ is the vector displacement between the nth and ith molecule. Here, for a given molecule with label M_n, we consider in-plane screening from the six nearest neighbours with labels $M_{j_1} \ldots M_{j_6}$, as indicated in **Figure 3.8**b. The nearest-neighbour metal-molecule distances $d_{j_1} \ldots d_{j_6}$ for molecules $M_{j_1} \ldots M_{j_6}$ depend on indexes $j_1 \ldots j_6$, which, for a given n, are determined by the periodicity of the charging superstructure as follows:

$$\begin{aligned} j_1 &= n + 1 \bmod(39) \\ j_2 &= n + 18 \bmod(39) \\ j_3 &= n + 17 \bmod(39) \\ j_4 &= n - 1 \bmod(39) \\ j_5 &= n - 18 \bmod(39) \\ j_6 &= n - 17 \bmod(39) \end{aligned} \qquad \text{(Eqs. 3.17)}$$

Using $d_{\min} \approx 2.8$ Å and $\Delta d \approx 0.1$ Å for the expression of $d(n)$ above, we found that $\Delta E^{(\mathrm{p})}(n)$ provides a further increase of ~15% to the stabilisation energy for M_{20} ($\Delta E^{(\mathrm{p})}(n = 20)/\Delta E(d) \approx 0.15$) which in turn results in a reduction in $V_{\mathrm{LUMO}}^{(0)}$ as seen in **Figure 3.8**a (green curve). Note that the calculated molecular polarizabilities are often overestimated [252], and therefore the actual contribution of in-plane molecule-molecule interactions to the total screening stabilisation energy is likely smaller than our estimated ~15 % (for $n = 20$). Since most of the stabilisation energy is due to screening via molecule-metal interactions, we can safely neglect these in-plane molecule-molecule interactions (increase in stabilisation energy is at most ~15% of ΔE). This provides evidence that the observed spatially dependent variations of $V_{\mathrm{LUMO}}^{(0)}$ can be explained by very subtle differences in molecule-surface distance (metal-molecule screening).

3.7 Dielectric constant for DCA monolayer on Ag(111)

Whilst nc-AFM and STM suggest that the molecule-metal distance d is the smallest for M_0 (**Figure 3.1**), **Figure 3.7**c shows that M_0 exhibits the largest effective DCA-Ag(111) potential barrier width d_{eff}. We explain this discrepancy by noting that d and d_{eff} are related via $d_{\mathrm{eff}} = d/\epsilon_{\mathrm{r}}$, where ϵ_{r} is the out-of-plane relative dielectric constant of the molecule-metal barrier [56, 245]. By considering d_{eff} (1.00 ± 0.02 Å and 0.81 ± 0.05 Å) and d (2.80 Å and 2.85 Å) for M_0 and M_{10}, we find values for ϵ_{r} of 2.80 ± 0.06 and 3.51 ± 0.22, for molecules M_0 and M_{10},

respectively. These values are similar to those reported for NaCl/Au(111) [191] and NaCl/Ag(100) [253], and are consistent with the weak DCA-Ag(111) interaction observed and the fact that DCA behaves effectively on Ag(111) as on a thin insulator. For NaCl/Au(111), ϵ_r increases with increasing film thickness due to size effects in the ultra thin material [254, 255], consistent with DCA/Ag(111) where ϵ_r increases with d. The relative dielectric constant, ϵ_r, is a measure of the local out-of-plane polarizability of DCA/Ag(111). A larger ϵ_r translates into a larger dipole moment induced by the applied field, screening the latter and resulting in a larger absolute value $|F_g|$ of the gating field required to charge the molecule. The smaller value of d for M_0 results, at the same time, in a smaller $V_{LUMO}^{(0)}$ and larger d_{eff} (due to a smaller ϵ_r); whereas an electron injected into the LUMO is easier to screen by the metal for M_0 than for M_{10}, it is not so for an external electric field applied perpendicular to the molecule-surface system. These effects are responsible for the substantial variations in the susceptibility of charging observed for the different molecules.

3.8 Charging Hindrance: Lateral Coulomb Repulsion

In **Figure 3.7**c, we could not measure V^* for molecules M_{11} to M_{24} within the negative bias range ($V_b > -3.2$ V) and tip-sample distances considered. This is because, for this set of molecules M_{11} – M_{24}, molecules in the adjacent row can become negatively charged at lower absolute field strengths, resulting in lateral Coulomb repulsion that increases the energy required for charging molecules M_{11} – M_{24} (i.e., lateral Coulomb repulsion). This is illustrated in **Figure 3.9** for molecules M_{11} and M_{27} (different molecular domain from previous figures; here the domain has a superstructure periodicity of 42 molecules along $\mathbf{a_1}$).

Here, at $V_b \approx -2.1$ V, molecule M_{27} charges while M_{11} remains neutral. At $V_b = -2.4$ V (**Figure 3.9**b), M_{27} can be charged if the lateral position of the STM tip is within the charging zone, defined by the charging ring around the molecule observed in the dI/dV maps (see also inset of **Figure 3.5**b inset). At higher absolute biases $|V_b|$, the charging zone area increases (**Figures 3.9**b-e). Molecule M_{11} charges at $V_b = -2.8$ V while at $V_b = -3.0$ V, it reverts to its neutral state. At $V_b = -3.0$ V, the STM tip located above M_{11} is within the charging zone of M_{27}; the negatively charging of adjacent M_{27} results in lateral Coulomb repulsion that impedes charging of M_{11} at this bias. At $V_b = -3.17$ V, this lateral Coulomb repulsion from charged M_{27} is overcome and molecule M_{11} charges again. **Figure 3.9**f shows a dI/dV spectrum taken at M_{11}. The two dips at $V_b = -2.8$ and -3.17 V are associated with the two aforementioned charging events of M_{11}. The difference between the two dips' biases ($U \approx 0.37$ V) corresponds to the energy needed to overcome the lateral Coulomb field imposed by negatively charged M_{27} and to charge M_{11}. Molecules M_{11} to M_{24} in **Figure 3.7** are well within the charging zone of adjacent charged molecules (considering the range of biases and tip-sample distances used there), at bias

voltages with absolute values smaller than $|V^*|$ required for charging. This means that absolute values of charging bias onsets for molecules M_{11} to M_{24} are increased by the charging energy, U, imposed by the adjacent charged molecules, putting them outside the bias range of our measurements (for all the tip-sample distances considered). Probing these molecules at higher bias absolute values proved difficult given the increased susceptibility of damaging the molecules within the nanofilm. We further note that, using the relative dielectric constant $\epsilon_r = 3.51 \pm 0.22$ for M_{10} in **Figure 3.7**, $U_{Coulomb} = (e^2/4\pi\epsilon_0\epsilon_r) \times (1/r) = 0.41 \pm 0.03$ eV with the distance, $r \approx 1$ nm between M_{11} and M_{27} (see **Figure 3.9**e). This is consistent with our measured $U \approx 0.37$ V, corroborating our deduced ϵ_r in the main text as well as our interpretation of the observed charging hindrance (i.e., lateral Coulomb repulsion).

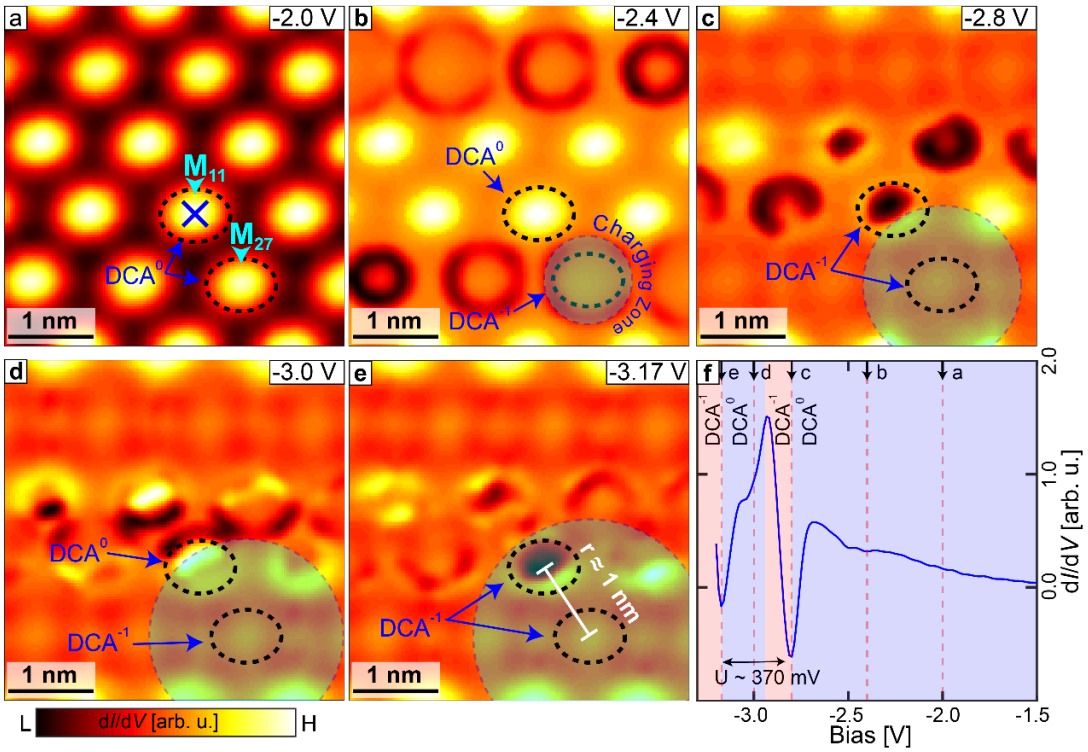

Figure 3.9: Lateral Coulomb repulsion in DCA monolayer on Ag(111). (a) – (e) Constant-height dI/dV maps (set point: $V_b = -0.02$ V, $I_t = 5$ pA measured on M_{11}) of DCA/Ag(111) for different negative bias voltages V_b (shown on maps). For $V_b = -2$ V (a), all DCA molecules are neutral (DCA^0). For $V_b = -2.4$ V (b), M_{27} is negatively charged (DCA^{-1}) and M_{11} remains neutral. Shaded circular area marks the charging zone, defined by the maximum lateral distance between tip and molecule M_{27} at which the latter can be charged, for a given bias voltage; the larger $|V_b|$ is, the larger the lateral tip-DCA distance can be for charging a specific molecule. For $V_b = -2.8$ V (c), both M_{11} and M_{27} are charged. For $V_b = -3$ V (d), the charging zone of M_{27} overlaps with M_{11} where now M_{11}: charging of M_{11} is hindered by lateral Coulomb repulsion from charged M_{27} and M_{11} is neutral again. (e) For $V_b = -3.17$ V, lateral Coulomb repulsion from charged M_{27} is overcome and M_{11} charges once more. (f) dI/dV curve taken on M_{11} (set point: $V_b = -0.02$ V, $I_t = 5$ pA). Dips at $V_b = -2.8$ and -3.17 V are associated with the two charging events. The difference of $U \approx 0.37$ V between these two dips corresponds to the energy required to overcome the lateral Coulomb field from charged M_{27}. Blue (red) transparent background indicates when M_{11} is neutral (charged).

3.9 Formation of DCA Dimers at Low Substrate Temperature

By depositing DCA molecules on Ag(111) held at ~5 K (see subsection 2.1.5 for sample preparation details), we observed the formation of molecular dimers (**Figure 3.10**a). These dimers can be easily moved with the STM tip via lateral manipulation and STM scanning. This indicates weak molecule-surface interactions, consistent with the observed field-induced charging. We performed $\mathrm{d}I/\mathrm{d}V$ STS measurements on a DCA dimer (red and blue crosses in **Figure 3.10**b), showing a prominent dip at bias voltage $V_\mathrm{b} \approx -4.4$ V (**Figure 3.10**c; note the dimers seem to be more stable and less prone to bias-induced damage compared to molecules in the nanofilm) and a peak that we associate with the LUMO of the molecule at $V_\mathrm{b} \approx 470$ mV (see **Figure 3.10**d).

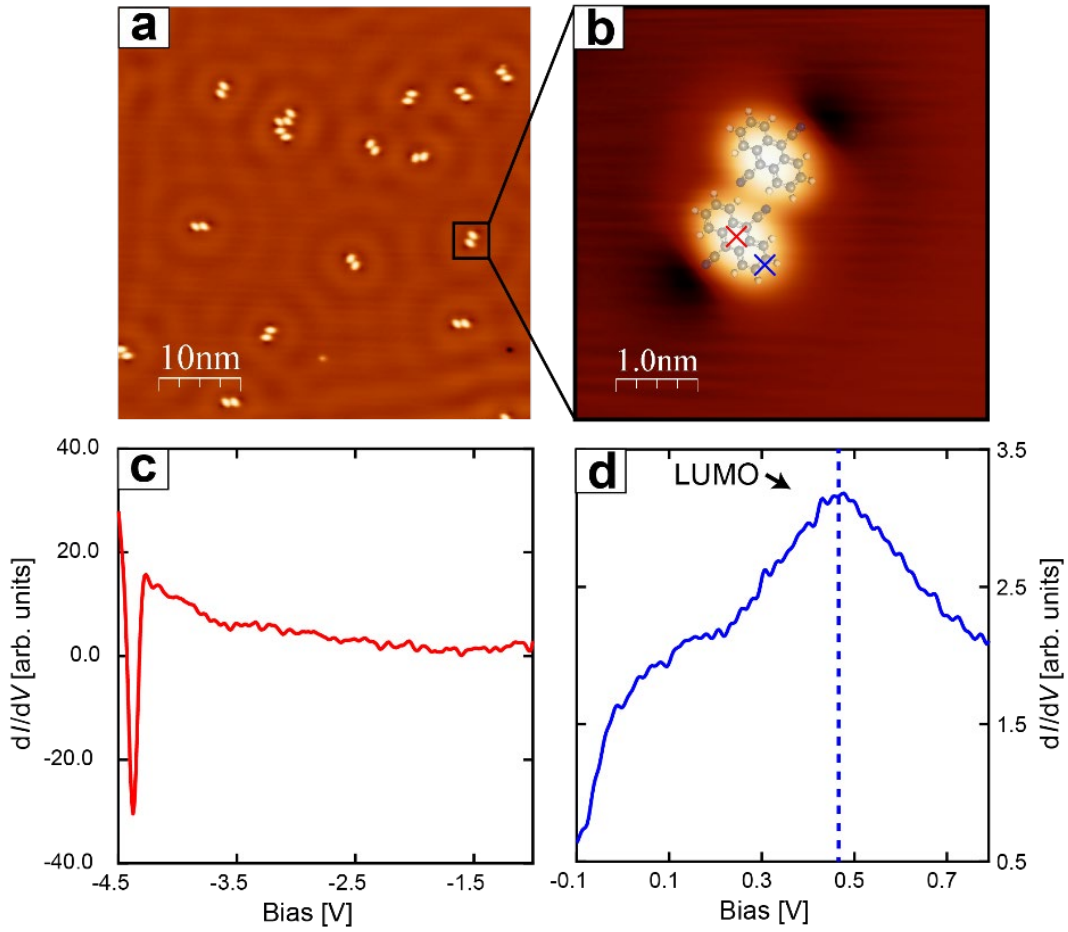

Figure 3.10: STM and STS measurements on DCA dimers. (a) Constant-current STM image after deposition of DCA molecules on Ag(111) at 5 K ($V_\mathrm{b} = -0.02$ V, $I_\mathrm{t} = 200$ pA). (b) Zoomed-in STM image of DCA dimer indicated in (a) (black square; $V_\mathrm{b} = -0.02$ V, $I_\mathrm{t} = 200$ pA). (c) – (d) Point $\mathrm{d}I/\mathrm{d}V$ STS measurements taken on DCA molecule in (b) in the negative bias range at the centre of the molecule (red cross; set point, $V_\mathrm{b} = -1.0$ V, $I_\mathrm{t} = 5$ pA), and in the positive bias range at the anthracene group extremity (blue cross; set point, $V_\mathrm{b} = -0.2$ V, $I_\mathrm{t} = 1$ pA). The charging dip can be observed at ~ –4.4 V and the peak associated with the LUMO (blue dashed line) can be observed at ~0.47 V.

We explain the larger $|V_\mathrm{b}|$ (and hence larger electric field magnitude) required to charge the DCA molecule in this dimer case by two factors: (i) the LUMO energy of the DCA

molecules in the dimer is significantly higher (~470 mV) with respect to the Ag(111) surface Fermi level, compared to the LUMO energy of the DCA molecules in the self-assembled nanofilm (~300 mV); and (ii) greater molecule-surface interaction (resulting in a smaller effective molecule-metal tunnelling barrier). The discrepancy in the LUMO energies can be explained by in-plane screening (or lack thereof in the case of dimers) of surrounding molecules: The LUMO of DCA molecules in the nanofilm is further stabilised (by a larger stabilisation energy ΔE) compared to dimer molecules due to additional screening from surrounding molecules. This leads to a larger electron affinity and lower LUMO energy for molecules in the nanofilm, as seen in other molecular systems [248]. Further, in the dimer case, a greater molecule-surface interaction can be explained by the interaction of the cyano-group lone electron pairs with the underlying surface. In the nanofilm case, this molecule-surface interaction is arguably reduced given the participation of the cyano-group lone electron pairs in in-plane directional hydrogen bonding with adjacent molecules.

3.10 KPFM Measurements on DCA monolayer on Ag(111)

To verify possible local variations of the work functions within a molecular domain, we measured the frequency shift Δf (nc-AFM qPlus sensor with Ag-terminated Pt/Ir tip) as a function of bias voltage V_b, for molecules M_0 and M_{20} (see **Figure 3.11**). The bias voltage for which Δf is maximum corresponds to the local contact potential difference (LCPD; see subsection 2.4.4) The LCPD for both M_0 and M_{20} is ~ –297 mV, whereas the charging onset voltage V^* for M_0 measured by STS is ~ –1.6 V for the same tip-sample distance (M_{20} does not show charging within the bias ranges considered).

This is consistent with the downward kink and deviation of $\Delta f(V_\mathrm{b})$ from a parabolic curve for M_0 at V_b = –1.66 V, indicative of bias-induced charging [205, 213, 256–258] (dashed circle in **Figure 3.11**). That is, although we observe the effect of field-induced charging of DCA on $\Delta f(V_\mathrm{b})$ at $V_\mathrm{b} = -1.66$ V, it is challenging – if not impossible – to reliably derive the LCPD of negatively charged DCA (i.e., via quadratic fitting of $\Delta f(V_\mathrm{b})$ for V_b < = –1.66 V) given the large discrepancy between V^* and the bias voltage required to maximise $\Delta f(V_\mathrm{b})$. Measuring the LCPD accurately for negatively charged DCA (and addressing how this LCPD varies as a function of site in a molecular domain) requires decoupling of the charging voltage (i.e., gating) and the LCPD measurement voltage variable. This is beyond the scope of this work and requires further experiments.

Note that retrieving work function changes due to charging via $\mathrm{d}I/\mathrm{d}z$ STS (at constant bias voltage) is challenging since varying z results in varying the electric field at the junction, and hence potentially varying the charge state of the molecule. That is, the measurement itself would alter the state of the system. It is also worth noting that we attempted resolving the

intramolecular morphology of negatively charged DCA via CO-tip ncAFM imaging. This involves large bias voltage absolute values (required for charging) and small tip-sample distances (required for achieving intramolecular chemical bond resolution and resulting in significant probe-sample interactions). This combination of high tip-sample bias and small tip-sample distance made it impossible to keep the tip functionalised with a CO molecule during the measurement.

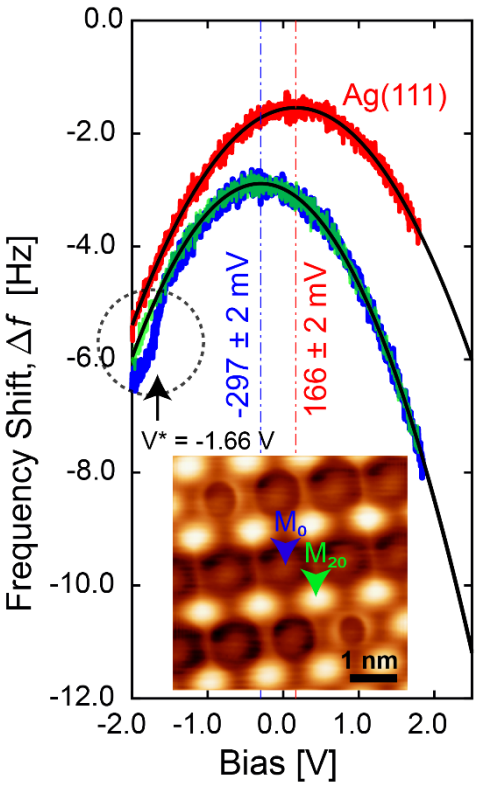

Figure 3.11: KPFM measurements on DCA monolayer on Ag(111). Frequency shift Δf as a function of bias voltage V_b, (set point V_b = –20 mV, I_t = 5 pA on top of M_0) measured on molecule M_0 (blue curve), M_{20} (green), and on bare Ag(111) (red). The bias voltage for which Δf is maximum corresponds to the local contact potential difference (LCPD). Solid black curves are quadratic fits. Inset: constant-current STM image of DCA domain (V_b= –2.4 V, I_t = 50 pA). Obtained LCPD values are –297 ± 2 mV and 166 ± 2 mV for (neutral) DCA and Ag(111), respectively. Kink and downward shift of $\Delta f(V_b)$ (dashed circle) at V_b = –1.66 V (black arrow) for M_0 is due to negative charging of DCA. Measurements were performed using an ncAFM qPlus sensor with an Ag-terminated Pt/Ir tip (oscillation amplitude = 100 pm).

3.11 Summary

In this chapter, we have demonstrated the bottom-up synthesis of a self-assembled 2D nanoarray of organic molecules on a metal surface, whose charge states can be controlled individually by an applied electric field. Field-driven charging is enabled due to weak molecule-metal interactions. The gating field required to alter the molecular charge state depends strongly on the molecules' adsorption site on the surface. This is due to subtle variations of the molecule-surface distance, which result in site-dependent LUMO energies and effective molecule-surface

potential barrier widths. Comparisons with molecular dimers suggests that cyano-participation in the hydrogen-bonding between molecules in the nanoarray mitigates interactions of these cyano-groups with the surface resulting in weak molecule-metal interactions.

The results presented in this chapter is important for the consideration and design of functional 2D molecular devices, particularly for devices where the organic nanostructures are contacted by metal electrodes (e.g., for charge flow/control). By establishing an effective potential barrier at this contact, e.g., like that at the DCA/Ag(111) interface, the intrinsic electronic properties of the 2D organic assembly can still be preserved while still allowing for control of these properties via the metal electrodes.

Chapter 4
Dispersion of DCA/Ag(111) Interface State

4.1 Overview

In the previous chapter, I presented results on a self-assembled 2D DCA monolayer grown on an Ag(111) substrate. $\mathrm{d}I/\mathrm{d}V$ STS measurements performed on the DCA/Ag(111) molecular film revealed features attributed to the LUMO and charging of the DCA molecules. We also identified a step-like feature, in the $\mathrm{d}I/\mathrm{d}V$ STS measurements (see section 3.3). In this chapter, we elucidate the origin and subsequently nature of this step-like feature in the $\mathrm{d}I/\mathrm{d}V$ STS measurements performed on the DCA/Ag(111) system.

By means of STS, I show that this step-like feature is a signature of a 2D electron gas (2DEG) localised at the interface between the DCA molecular film and the underlying Ag(111) metallic substrate. This 2DEG interface state (IS) is derived from the Ag(111) Shockley surface state after a modification of the bare metallic surface potential by the DCA molecular overlayer. Using FT-STS (see subsection 2.3.5), the dispersion relation, $E(\mathbf{k})$, for electrons in the DCA/Ag(111) interface state showed subtle deviations from free electron-like (i.e., parabolic dispersion) behaviour at high energies. These deviations are an indication of the IS electrons' sensitivity to the periodic potential landscape, $U(\mathbf{r})$, imposed by DCA molecular film. From this, we deduced a corrugation in the potential landscape, $\max(U) - \min(U)$, on the order of 1.5 eV.

The study of delocalized states at the organic-metal interfaces is crucial as these states are essential for influencing charge carrier dynamics across the interface [259, 260] and therefore is important for the implementation of functional organic nanostructures on surfaces. Unless otherwise stated, all measurements presented in this chapter were performed at 4.4 K.

4.2 Formation of 2DEG at DCA/Ag(111) Interface

Figure 4.1a shows a constant-current STM image of a closed-packed DCA monolayer on Ag(111) as presented in Chapter 3 (see subsection 2.1.5 for sample preparation details). As reported in section 3.3, $\mathrm{d}I/\mathrm{d}V$ STS measurement performed on the DCA monolayer (see **Figure 4.1**b) show three prominent features: (i) a peak-like feature at positive bias ($V_\mathrm{b} \approx 300$ mV; blue curve in **Figure 4.1**b) measured at the DCA anthracene extremity; (ii) a sharp dip at negative bias ($V_\mathrm{b} \approx -2.2$ V; red curve in **Figure 4.1**b) at the centre of the DCA molecules; and (iii) a step-like feature at both locations with an energy onset of ~120 mV. Features (i) and (ii)

have been attributed to the LUMO and charging of the DCA molecules, respectively (see section 3.3). The step-like feature (iii) is similar to that of a step-like LDOS (as a function of energy) for a 2D electron gas (2DEG) [261] such as that of the bare Ag(111) Shockley surface state (SS; black curve in **Figure 4.1**b; see subsection 2.1.3). Interestingly, we do not observe any step-like signatures, with an energy onset of ~ –66 mV, of the Ag(111) Shockley surface state in our $\mathrm{d}I/\mathrm{d}V$ STS measurement performed on the DCA monolayer on Ag(111). Given this absence and the step-like signature of feature (iii), we speculate that feature (iii) is derived from the Ag(111) Shockley surface state.

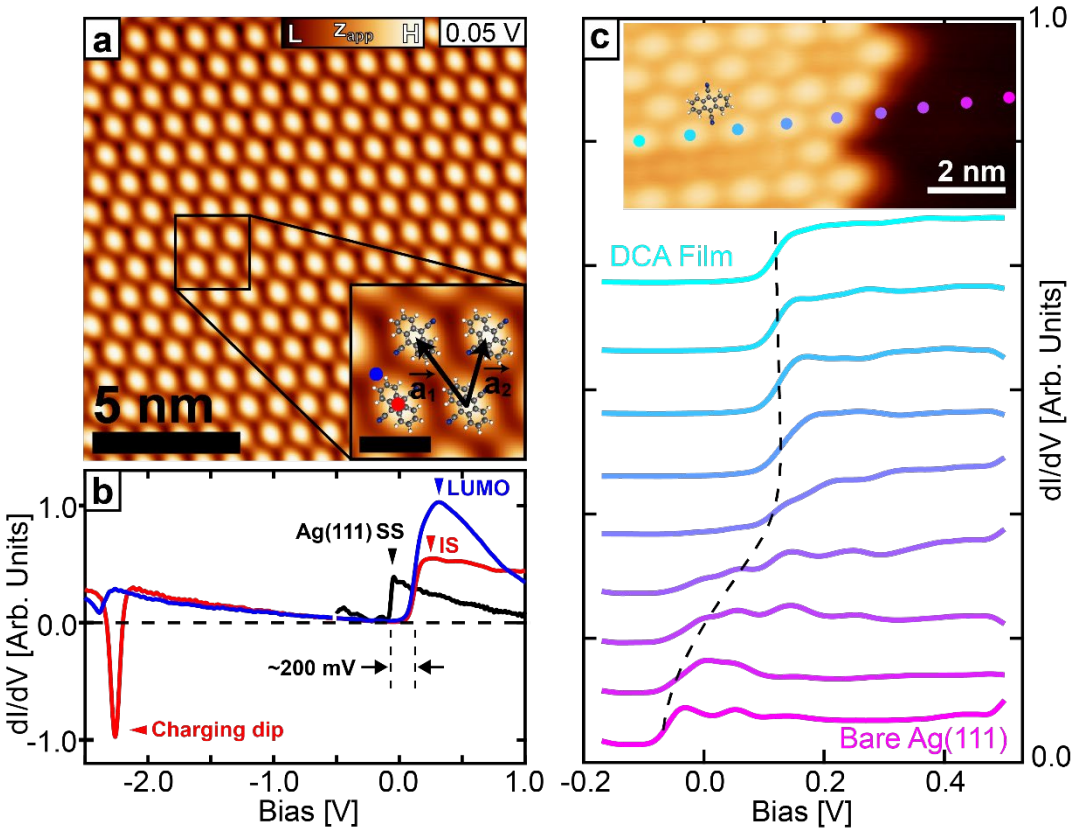

Figure 4.1: Evolution of Ag(111) Shockley surface state across DCA domain boundary and formation of DCA/Ag(111) interface state. (a) Constant-current STM imaging of self-assembled DCA molecular film on Ag(111) at V_b = 50 mV (I_t = 50 pA). The unit cell of the molecular film is defined by the vectors $\mathbf{a_1}$ and $\mathbf{a_2}$. Inset scalebar: 1 nm. (b) $\mathrm{d}I/\mathrm{d}V$ STS spectra taken at locations indicated in inset of (a) (set point V_b = 0.5 V, I_t = 150 pA). Spectra taken at the DCA anthracene extremity (blue) shows a peak-like feature at positive bias which is attributed to the DCA LUMO. Spectra taken at the DCA molecular centre (red) shows a dip at negative bias ($V_b \approx$ –2.2 V) and a step-like feature at positive bias (V_b > 0.12 V). (c) $\mathrm{d}I/\mathrm{d}V$ STS spectra (set point: V_b = –170 mV I_t = 50 pA) taken across DCA domain boundary from the bare Ag(111) surface (magenta curve) to the DCA/Ag(111) domain (cyan curve) as seen in constant-current STM inset (V_b = –2.4 V I_t = 50 pA). We see an evolution of the Ag(111) Shockley surface state as we move from the bare Ag(111) surface to the DCA domain: the onset energy for step-like feature in the $\mathrm{d}I/\mathrm{d}V$ STS spectra gradually shifts from below the Fermi level, $V_b \approx$ –66 mV (on the bare Ag(111) surface) to above the Fermi level, $V_b \approx$ 120 mV (on the DCA molecules). The step-like feature in the $\mathrm{d}I/\mathrm{d}V$ STS spectra at the DCA domain indicates a formation of a 2D electron gas-like interface state (IS). The IS onset is shifted up by ~200 mV relative to the bare Ag(111) Shockley surface (SS) state onset indicated in (b).

To show this, we performed $\mathrm{d}I/\mathrm{d}V$ STS measurements at the boundary of a DCA submonolayer. **Figure 4.1**c shows the $\mathrm{d}I/\mathrm{d}V$ STS measurements performed across the DCA domain boundary from the DCA molecules within the DCA submonolayer to the bare Ag(111) surface (cyan to magenta points). In **Figure 4.1**c, we see the continuous evolution (dashed black curve) of the bare Ag(111) Shockley surface state (with an energy onset of ~ –66 mV; magenta) into the step-like feature at the DCA domain (with an energy onset of ~120 mV; cyan) as we move from the bare Ag(111) surface to the DCA domain (total energy upshift of ~200 mV; see **Figure 4.1**b). Given (i) the evolution of the Ag(111) SS from the bare Ag(111) surface to the DCA domain and (ii) the 2DEG step-like $\mathrm{d}I/\mathrm{d}V$ signature everywhere over the DCA domain, we associate the step-like feature in the $\mathrm{d}I/\mathrm{d}V$ STS measurements on the DCA monolayer with a 2DEG at the molecule-metal [DCA-Ag(111)] interface.

This 2D electronic state that lives at the interface, i.e., interface state (IS), has been observed for variety of molecule-metal systems [56, 242–244, 262], albeit with different energy onsets. It has been shown that the evolution of the noble metal (111) Shockley surface state to the interface states of these molecule-metal systems, characterised by the shifts in the IS energy onsets relative to that of the bare metallic SS, can be modelled using a single parameter: the adsorption height, d_{C}, of the organic overlayer on the metal surface [263]. The model developed in ref. [263] solves the Schrödinger equation for an electron in a semi-periodic 1D potential as shown in **Figure 4.2**a (blue curve). Here, there is break in the translational symmetry of the potential, i.e., the potential is periodic for $z < 0$ Å (here, representing the periodicity of the Ag atoms for $z < 0$ Å perpendicular to the Ag(111) surface) but not for $z > 0$ Å where the Ag(111) surface terminates and where the organic layer sits at $z = d_{\mathrm{C}}$ (here, d_{C} is the adsorption height given by the distance between the carbon plane of the organic layer and the uppermost Ag atomic layer). Here, the model assumes that the organic layer can be modelled by a graphene layer, i.e., the potential of the organic layer is replaced with that of graphene [263]. **Figures 4.2**b-d shows the electron wavefunction solutions (specifically, the probability densities) of the interface state at the graphene/Ag(111) interface for various adsorption heights, d_{C} = 8.00 Å, 4.00 Å and 2.86 Å with an IS energy onset, relative to the Ag(111) Fermi level, E_{IS} = –136 mV, –309 mV, and +331 mV, respectively [263]. The shift in the IS energy onset, relative to the energy onset of the Ag(111) SS (–66 mV), here is due to the modification of the surface potential of the Ag(111) surface termination (e.g., see dashed and continuous black curves in **Figure 4.2**b which refer to the bare Ag(111) and graphene/Ag(111) surface potentials, respectively).

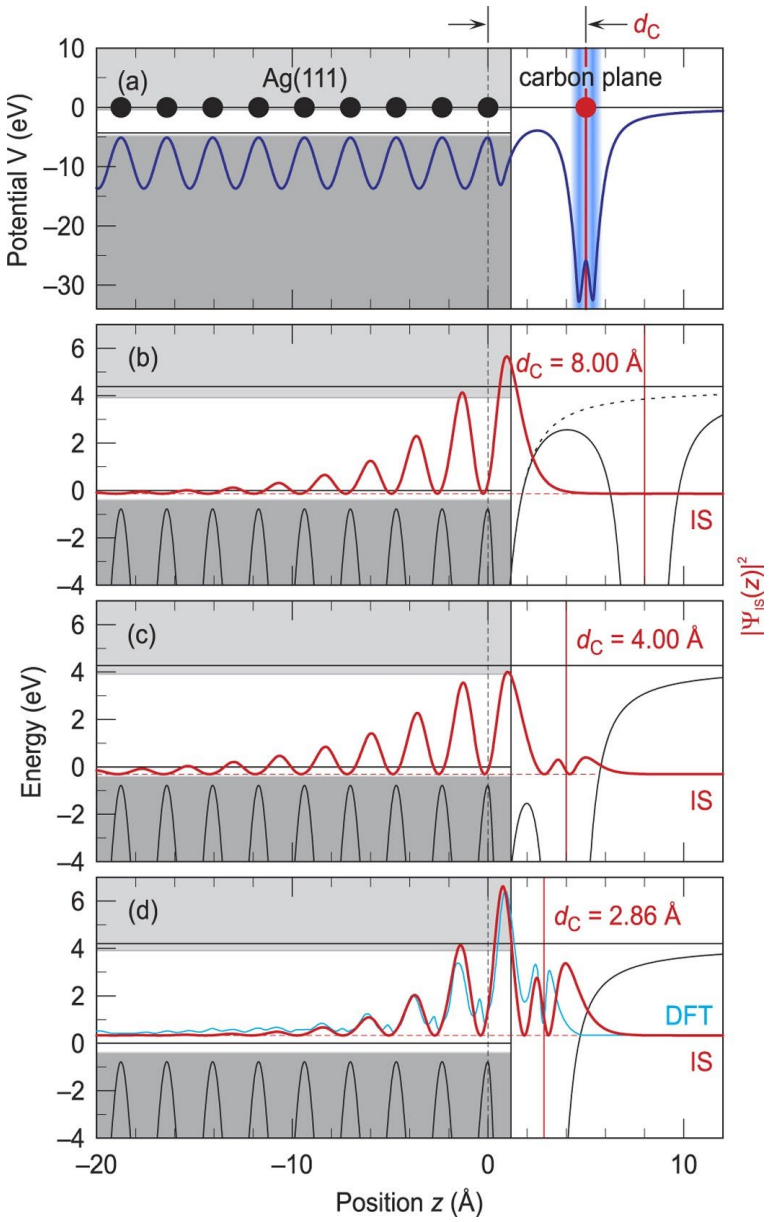

Figure 4.2: One-dimensional potential model for graphene adsorbed on an Ag(111) surface. (a) Semi-periodic 1D potential (blue curve) where the potential for $z < 0$ Å models the periodic potential of the Ag substrate (perpendicular to the Ag(111) surface termination; Ag atoms represented by black circles) and the potential for $z > 0$ Å models the potential of the Ag(111) surface termination and a graphene layer (parallel to the Ag(111) surface; carbon atom represented by red circle) positioned at a distance d_C away from surface. Specifically, d_C is the distance between the carbon plane of the graphene layer and the uppermost Ag atom of the Ag substrate. The grey shaded areas represent the projected bulk band structure. (b)-(d) The probability densities, $|\Psi_{IS}(z)|^2$, of the interface state (IS) at the graphene/Ag(111) interface (red curves) as determined by solving the Schrödinger equation for an electron in a 1D potential schematically shown in (a), however, with different carbon-Ag distances: d_C = 8.00 Å, 4.00 Å, and 2.86 Å for (b), (c), and (d) respectively. The red dashed lines show the IS energy onset (relative to the Fermi level). Here, the IS energy shift is due to the modification of the Ag(111) surface potential by the graphene layer potential. For example, (b) shows the bare Ag(111) 1D potential (dashed black curves) and the resulting 1D potential after graphene adsorption (with d_C = 8 Å). The figure was reprinted from ref. [263] with permission under a Creative Commons Attribution 4.0 International License (CC BY 4.0).

Figure 4.3 shows the predicted IS energy onset shift, ΔE_{IS} (relative to the bare Ag(111) SS energy onset), as a function of the graphene adsorption height, d_C, on Ag(111) (red curve) as predicted by the model developed in ref. [263] and described above (grey regions illustrates ΔE_{IS} as a function of d_C when the work function used for modelling the surface is changed by ±1 eV).

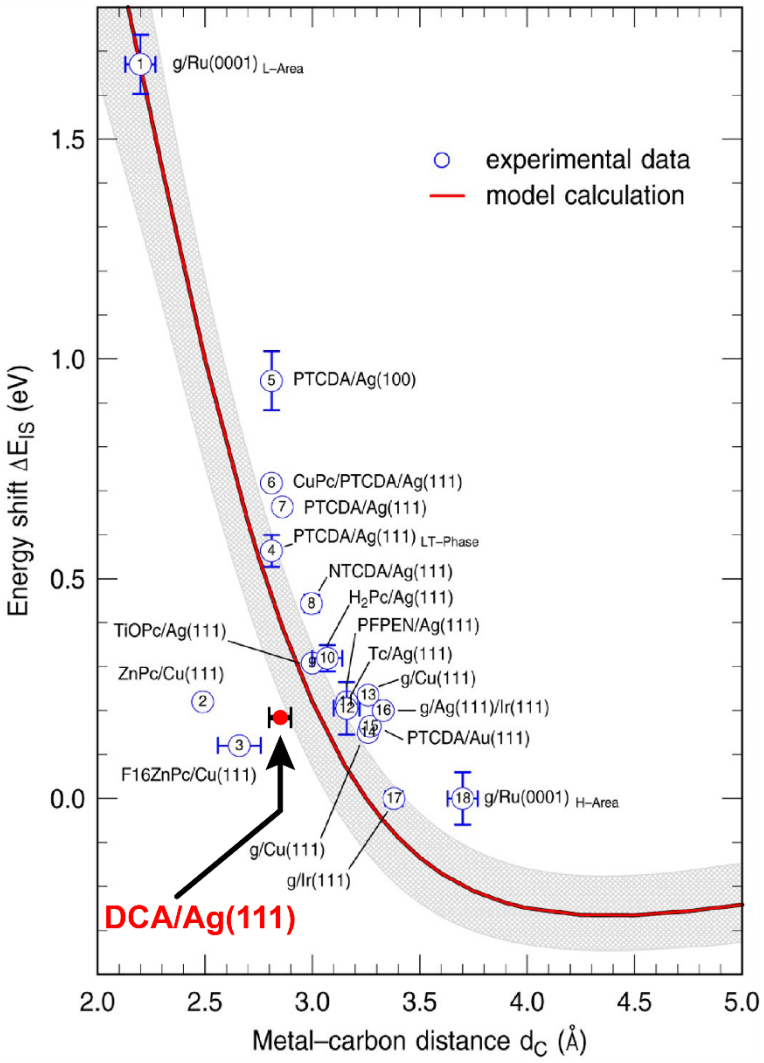

Figure 4.3: Interface state energy shift, ΔE_{IS} as a function of graphene adsorption height, d_C, on a metal. The red curve gives the predicted interface state energy shift, ΔE_{IS}, relative to the energy of the former surface state on the bare metal as a function of graphene adsorption height, d_C, as predicted by the model developed in ref. [263]. The grey region shows the variation of this prediction when the work function of the metal surface is changed by ±1 eV. Superimposed are the experimentally measured ΔE_{IS} and adsorption heights, d_C, for various organic molecular systems on metallic substrates. Here, we include the experimentally measured ΔE_{IS} and d_C for the DCA monolayer grown on Ag(111) (red data point). The error bars give the measured variation in d_C of ±0.05 Å for the DCA/Ag(111) system (see section 3.6 of Chapter 3). Our measurements for the DCA/Ag(111) system show qualitative agreement with the predicted model from ref. [263]. The figure was adapted from ref. [263] with permission under a Creative Commons Attribution 4.0 International License (CC BY 4.0).

Figure 4.3 also shows experimentally measured IS energy onset shifts, ΔE_{IS}, for a multitude of different organic-metal systems. Here, ΔE_{IS} is measured relative to the respective

SS of the underlying metallic substrates. For DCA/Ag(111), where the adsorption height of the DCA molecules were found to be 2.85 ± 0.05 Å (d_{min} = 2.8 Å and Δd = 0.1 Å; see section 3.6), the predicted IS energy shift is qualitatively correct although overestimated compared to the measured IS energy shift of ~186 mV (red data point in **Figure 4.3**).

The model in ref. [263] disregarded chemical interactions between the organic overlayer and the metallic substrate, i.e., the organic layer is physisorbed onto the substrate. Here, we rule out chemical interactions between the DCA monolayer and the underlying Ag(111) substrate as the reason for the discrepancy between our experimentally measured and the predicted IS energy shifts for DCA/Ag(111). This is because of the weak metal-molecule interactions between DCA and Ag(111) established in Chapter 3. We note that of all the organic molecules considered in Figure 4.3, DCA molecules are the smallest in size (by number of carbon rings). We speculate that this might be the source of the discrepancy mentioned above since the model in ref. [263] assumes a molecular potential landscape that is identical with that of graphene. This assumption is reasonable for larger aromatic molecules whose local structure resembles that of π-conjugated graphene, e.g., perylenetetracarboxylic dianhydride (PTCDA) molecules (with 7 carbon rings), but not for smaller aromatic molecules such as DCA molecules (with 3 carbon rings). Nevertheless, the qualitative agreement between the predicted and experimentally DCA/Ag(111) IS energy shifts provides evidence that the DCA molecular film modifies the surface potential of the Ag(111) surface termination, resulting in the upshift of the Ag(111) SS onset energy from below the Fermi level by ~200 mV.

It is important to note that the DCA submonolayers on Cu(111) do not exhibit a formation of a 2DEG at the interface [53]. We attribute this to the fact that Cu(111) is more reactive than Ag(111) [264, 265], resulting in a relatively stronger DCA-Cu(111) than DCA-Ag(111) interaction. In the case of DCA/Cu(111), the strong metal-molecule interaction quenches the formation of a 2D interface state.

4.3 Energy Dispersion of Interface State Measured via FT-STS

The electronic dispersion, $E(\mathbf{k}) = E(k_x, k_y)$, is the key quantitative descriptor of the nature of the interface state between the DCA film and the Ag(111) metallic substrate. Nominally, angle-resolved photoemission spectroscopy (ARPES) is an excellent technique for resolving the band structure or dispersion of electronic surface states [266–269] with energy resolutions as high as a few meV [270, 271]. However, this technique is only useful for investigating states that are occupied. In this case, the DCA/Ag(111) interface state is unoccupied, requiring a different approach. We therefore employ the well-known technique of Fourier-transform scanning tunnelling spectroscopy (FT-STS; see subsection 2.3.5) to investigate the dispersion of the DCA/Ag(111) interface state: acquiring $\mathrm{d}I/\mathrm{d}V(V_{\mathrm{b}}, x, y)$ as a function of tip position (x, y)

within the DCA monolayer, and performing a Fourier transform (FT), allows us to obtain momentum-space information on the local density of states (LDOS) associated with this interface state, i.e., $\mathrm{d}I/\mathrm{d}V(V_\mathrm{b}, q_x, q_y)$, where $\mathbf{q} = (q_x, q_y)$ is the scattering vector [83, 272] (see subsection 2.3.5). These reciprocal space $\mathrm{d}I/\mathrm{d}V(V_\mathrm{b}, q_x, q_y)$ maps contain information on the energy dispersion, $E(\mathbf{k})$, of the DCA/Ag(111) interface state. Generally, FT-STS does not allow for a direct, unequivocal determination of the system's band structure: electron scattering processes, scattering selection rules and matrix elements involved often render interpretation of data acquired via FT-STS challenging [272]. Despite this, FT-STS, unlike ARPES, has the advantage of accessing the information of electronic states that are both occupied and unoccupied. Further, the energy resolution attainable via FT-STS is < 1 meV (at 4.4 K), making FT-STS a viable alternative to studying the IS dispersion.

To this end and analogous to studies of the dispersion on metal (111) surface states via FT-STS [83, 272, 273], we introduced defects to the DCA/Ag(111) molecular film that act as scatterers of interface state electrons. This was done by imaging a large defect-free single DCA/Ag(111) molecular domain (> 130 × 130 nm^2) with scanning parameters V_b = –3 V, I_t = 3.5 nA to induce a significant tip-sample interaction, resulting in some molecules being displaced from their original position within the film (see **Figure 4.4**a). This process is reversible, i.e., the displaced molecules can be pushed back into their original positions within the film via lateral STM manipulation. **Figure 4.4**b shows a subsequent constant-current $\mathrm{d}I/\mathrm{d}V$ STS mapping at V_b = 230 mV of the region in **Figure 4.4**a. Around each defect we observe isotropic modulations of the $\mathrm{d}I/\mathrm{d}V$ signal, given by Friedel oscillations [243, 274, 275] of the LDOS caused by interfering incident and scattered interface state electron wavefunctions. **Figure 4.4**c shows the same $\mathrm{d}I/\mathrm{d}V$ map as in **Figure 4.4**b, but Fourier-filtered (keeping components for 1.4 < $|\mathbf{q}|$ < 2.3 nm^{-1}) to remove the structural periodicity given by the molecular film. Similarly, **Figure 4.4**d displays the Fourier-filtered $\mathrm{d}I/\mathrm{d}V$ map for V_b = 600 mV. We observe that the periodicity of the LDOS modulation (about each defect) decreases with increasing bias voltage (see insets in **Figures 4.4**c,d).

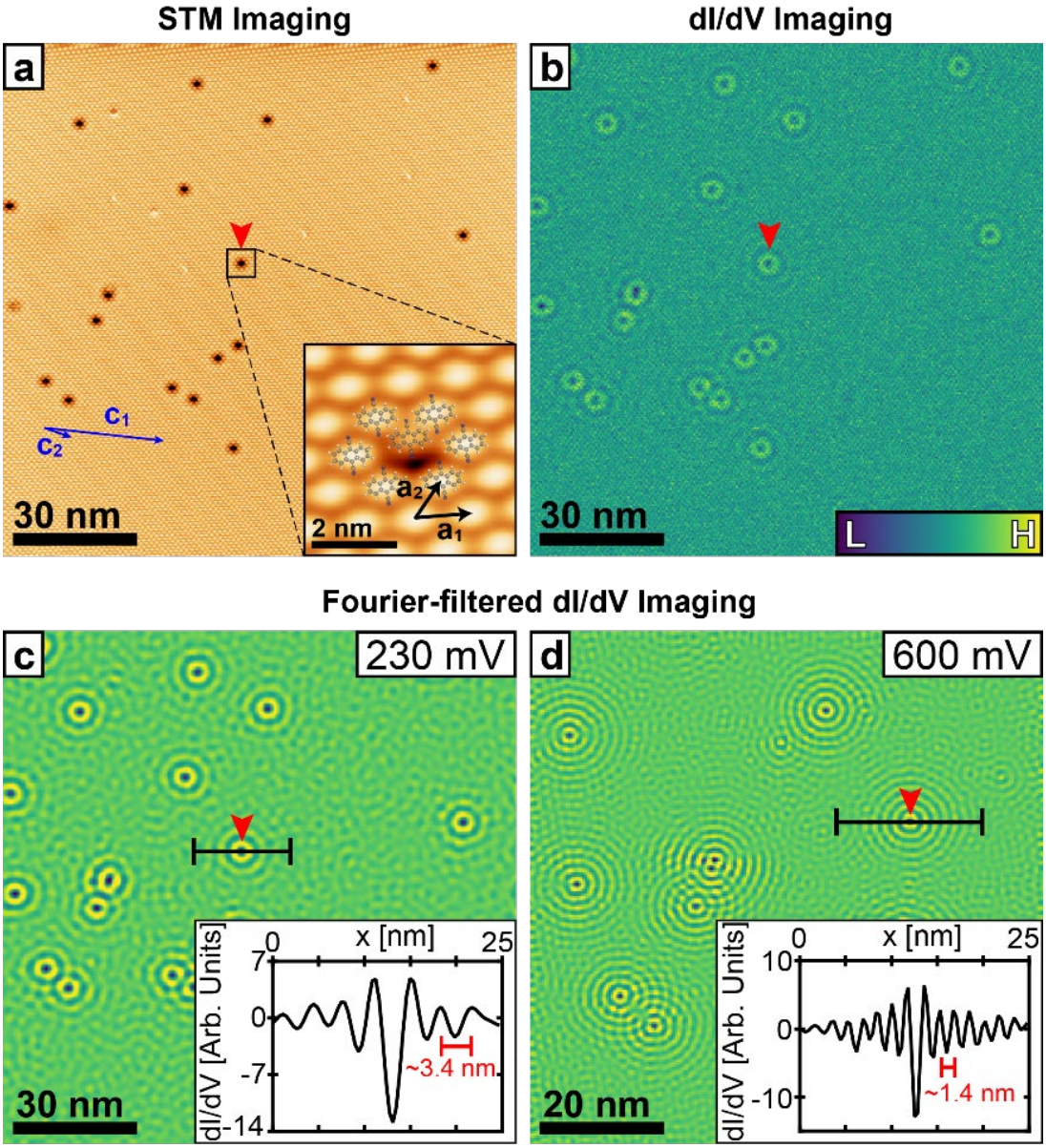

Figure 4.4: d*I*/d*V* STS mapping of a defect-filled DCA/Ag(111) submonolayer. (a) Constant-current STM imaging of a large DCA molecular film (124 × 124 nm^2) with defects (setpoint V_b = 230 mV, I_t = 2 nA). Defects are DCA molecules displaced from their positions within the film as seen in STM image inset. (b) Constant-current d$I/$dV STS mapping of the same region in (a) with V_b = 230 mV. (c)-(d) Fourier-filtered constant-current d$I/$dV STS maps of defect-filled DCA molecular film with V_b = 230 mV and 600 mV, respectively. These maps were obtained by Fourier-filtering, keeping components 1.4 < $|\mathbf{q}|$ < 2.3 nm^{-1} for (c) and 3.1 < $|\mathbf{q}|$ < 4.5 nm^{-1} for (d). In this case, (c) is the result of Fourier filtering the map in (b). (c)-(d) insets: line profiles across a single defect (black line) showing modulation in the d$I/$dV signal, characteristic of Friedel oscillations, with wavelengths of ~3.4 nm and ~1.4 nm, respectively. These bias-dependent differences in the scattering wavelengths are a clear evidence of a dispersive state. The red tick in (a)-(d) marks the same defect within the DCA molecular film. All d$I/$dV STS maps were taken with I_t = 2 nA and with a lock-in frequency, f = 1.13 kHz. A lock-in amplitude, V_{mod} = 1 mV was used for the maps in (b), (c) and V_{mod} = 15 mV for the map in (d).

Since the real-space modulation of the LDOS seen in **Figures 4.4**c,d is the result of interference between incident and scattered electronic waves, Fourier transforms of these

$\mathrm{d}I/\mathrm{d}V$ maps allow us to extract the scattering wavevector, $\mathbf{q}$, of the electronic wavefunctions associated with a specific eigenenergy (i.e. given by the acquisition bias of the $\mathrm{d}I/\mathrm{d}V$ map). For example, **Figure 4.5**a shows the Fourier transform of the $\mathrm{d}I/\mathrm{d}V$ map in **Figure 4.4**b taken at V_b = 230 mV. Here, we observe the FT peaks corresponding to the molecular film periodicity (DCA peaks; cyan dashed circles). Additionally, we observe a prominent ring-like feature about $|\mathbf{q}|$ = 0 nm^{-1} whose radius is related to the real-space periodicity of the LDOS modulation observed about each defect in **Figure 4.4**b (and in the Fourier-filtered map in **Figure 4.4**c). The first Brillouin zone (BZ) superimposed show the high-symmetry points in $\mathbf{q}$-space (blue) and in $\mathbf{k}$-space (green; with $\mathbf{q} = 2\mathbf{k}$) with the vectors $\mathbf{\Gamma X'}$ and $\mathbf{\Gamma Y'}$ being the reciprocal lattice vectors of the DCA molecular film (i.e., corresponding to real-space lattice vectors $\mathbf{a_1}$, $\mathbf{a_2}$ in **Figure 4.1**a inset).

To accurately determine the radius of the ring-like feature in **Figure 4.5**a, we first corrected for any spatial miscalibrations in the acquisition of the $\mathrm{d}I/\mathrm{d}V$ maps necessary for FT-STS. We do this by considering the registration between the DCA molecule film and the underlying Ag(111) substrate (established in subsection 3.2.1 in the previous chapter): $\mathbf{v_1^*} = 3\mathbf{a_1^*}$ and $\mathbf{v_2^*} = 4\mathbf{a_2^*} - \mathbf{c_2^*}$, where $\{\mathbf{v_1^*}, \mathbf{v_2^*}\}$, $\{\mathbf{a_1^*}, \mathbf{a_2^*}\}$, and $\{\mathbf{c_1^*}, \mathbf{c_2^*}\}$ are the reciprocal lattice vectors for the underlying Ag(111) substrate, the DCA molecular film (corresponding to the real-space vectors $\mathbf{a_1}$and $\mathbf{a_2}$ in **Figure 4.1**a inset) and the DCA/Ag(111) charging superstructure (corresponding to the real-space vectors $\mathbf{c_1}$and $\mathbf{c_2}$; see subsection 3.2.1), respectively. Since the length of the vectors $\{\mathbf{v_1^*}, \mathbf{v_2^*}\}$ and their relative angles are known, measurements of $\{\mathbf{a_1^*}, \mathbf{a_2^*}\}$ and $\{\mathbf{c_1^*}, \mathbf{c_2^*}\}$ can help correct for any spatial miscalibrations. Subsequently, we took a line profile of the FT-STS map along the high-symmetry directions e.g., along the direction $\mathbf{X'-\Gamma-Y'}$ as shown in **Figure 4.5**b. Here, the line profile was radially averaged within a ±1° window to increase the signal-to-noise ratio. The two sharp peaks near $|\mathbf{q}| \approx 2$ nm^{-1} in the line profile correspond to the ring-like feature in **Figure 4.5**a. We fit these peaks with a Lorentzian function to determine their location in $\mathbf{q}$-space (red curves in **Figure 4.5**b). The full width at half maximum (FHWM) of these fitted Lorentzian functions was used as the uncertainty in their location in $\mathbf{q}$-space.

We similarly performed Fourier transform of $\mathrm{d}I/\mathrm{d}V$ maps taken at different bias voltages (see **Figure 4.5**c). In addition to the FT-peaks corresponding to the molecular film periodicity, we observe a ring-like feature about $|\mathbf{q}|$ = 0 nm^{-1} in all the FT-STS maps and whose radius grows with increasing bias. Using the procedure described above, we proceeded to extract the radius of these ring-like features in the FT-STS maps as a function of bias, V_b. Specifically, for 0.13 V ≤ V_b ≤ 1.05 V. FT-STS maps with V_b > 1.05 V did not show any peaks that could be reliably fitted (here, the scattering signal is drowned by noise).

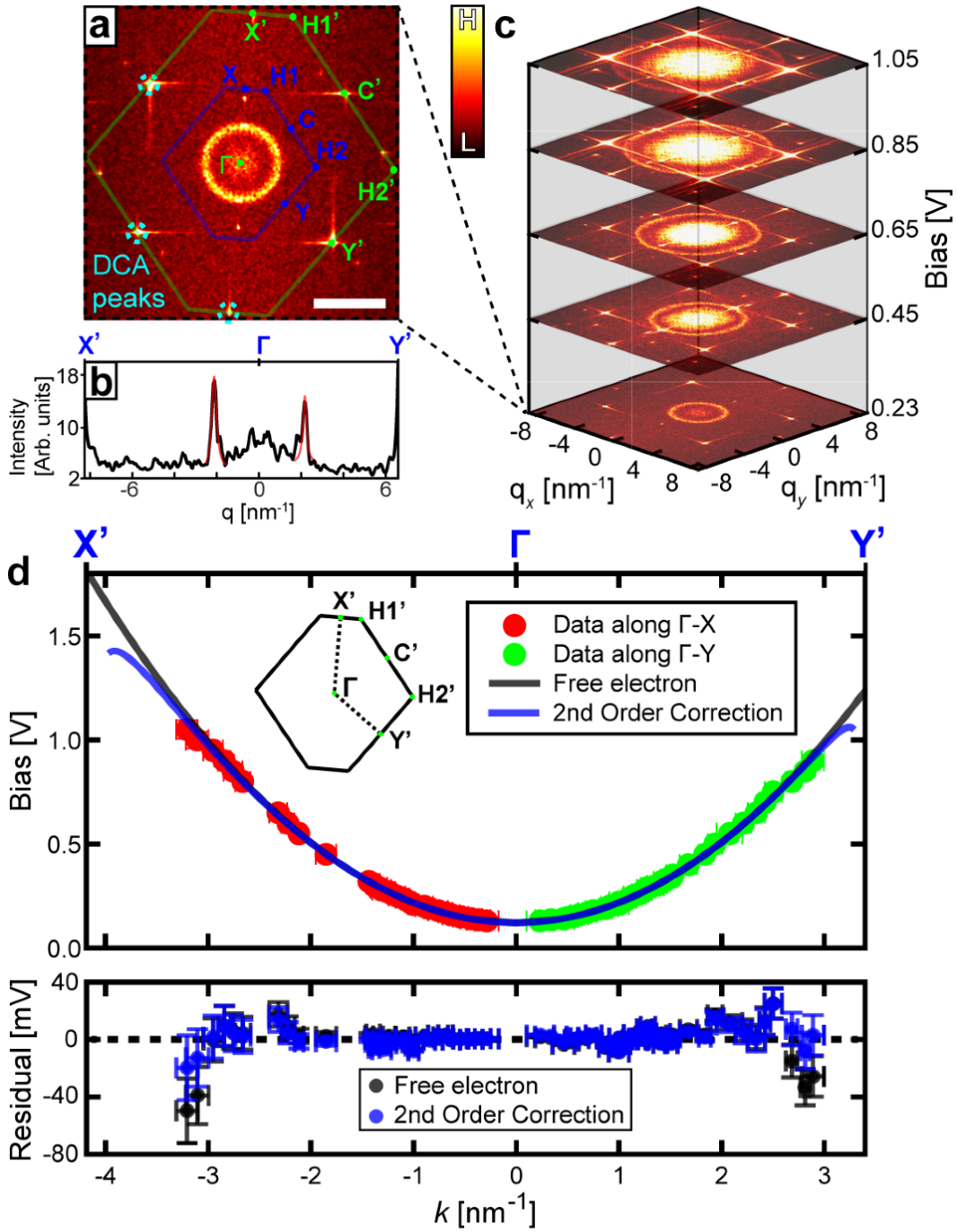

Figure 4.5: FT-STS measurements of defect-filled DCA/Ag(111) submonolayer. Fourier-transform of the d$I/$dV map at V_b = 230 mV in **Figure 4.4**b, showing Fourier peaks attributed to the DCA film periodicity (cyan dashed circles). The radius of the ring-like feature centred at $\mathbf{q} = 0$ gives the real-space LDOS modulation in **Figures 4.4**b,c. Superimposed is the first Brillouin zone (BZ), in **q**-space (blue) and **k**-space (green), for the DCA molecular film with the high-symmetry points indicated ($\mathbf{q} = 2\mathbf{k}$). Scalebar: 4 nm^{-1}. (b) Line profile along $\mathbf{X'-\Gamma-Y'}$ in (a). The positions of the peaks near $|\mathbf{q}|$ = 2 nm^{-1} was extracted from Lorentzian fits (red curves) giving the radius of the ring-like feature in (a). (c) Fourier-transforms of d$I/$dV maps of defect-filled DCA molecular film acquired at different biases. (d) Top plot shows the radius, along the $\mathbf{X'-\Gamma-Y'}$ direction in **k**-space (see BZ inset), of the ring-like features observed in the FT-STS maps of the defect-filled DCA molecular film as a function of bias, i.e., dispersion, $E(\mathbf{k})$, for the IS electrons. The data was fitted assuming a free electron dispersion (black

curve) and with 2nd order corrections to the free electron dispersion (blue curve) giving electron effective masses, m^*/m_e = 0.395 ± 0.005 and 0.385 ± 0.003, respectively. The latter fit shows deviations from parabolic behaviour at energies > 1 V. Bottom plot shows the residuals for the fitted models: free electron dispersion (black) and 2nd order corrections (blue). The latter shows less deviations from the zero-line at larger $|\mathbf{k}|$. All constant-current $\mathrm{d}I/\mathrm{d}V$ maps for FT-STS were acquired via lock-in technique with a lock-in frequency of 1.13 kHz. The lock-in amplitude, V_{mod}, used was increased as the $\mathrm{d}I/\mathrm{d}V$ mapping bias acquisition was increased (e.g., V_{mod} = 1 mV and 15 mV for V_b = 230 mV and 600 mV, respectively). This compensated for the weakening scattering signal at higher biases. $\mathrm{d}I/\mathrm{d}V$ maps with $V_b \leq 350$ mV were obtained over a 124 × 124 nm^2 defect-filled DCA/Ag(111) region with a spatial resolution of ~0.37 nm/pixel (e.g., **Figure 4.4**c). Maps with $V_b > 350$ mV were obtained over an 83 × 83 nm^2 region with a spatial resolution of ~0.35 nm/pixel (e.g., **Figure 4.4**d). This ensured a $\mathbf{q}$-space resolution of $\Delta\mathbf{q} \sim 0.05$ nm^{-1} and $\Delta\mathbf{q} \sim 0.08$ nm^{-1} for $V_b \leq 350$ mV (where scattering is dominant at low $|\mathbf{q}|$) and for $V_b >$ 350 mV (where the scattering is dominant at high $|\mathbf{q}|$), respectively. This further ensured a reliable extraction of scattering wavevectors with $|\mathbf{q}|$ < 8.5 nm^{-1} and $|\mathbf{q}|$ < 9.0 nm^{-1} for maps with $V_b \leq 350$ mV and V_b > 350 mV, respectively (according to the Nyquist-Shannon sampling theorem [276]).

Figure 4.5d shows the radius of the ring-like feature in momentum $\mathbf{k}$-space along the $\mathbf{X'-\Gamma-Y'}$ direction as a function of bias (see Appendix B.1 for data along all high-symmetry directions). Considering that a scattering vector $\mathbf{q}$ sends an electron in a state, $\mathbf{k}_i$, to a final state, $\mathbf{k}_f$, i.e., $\mathbf{q} = \mathbf{k}_f - \mathbf{k}_i$ and that electron scattering are most likely dominated by elastic back-scattering events, we have that $\mathbf{q} = 2\mathbf{k}_f$ (see subsection 2.3.5). Therefore, the momentum $\mathbf{k}$-space and $\mathbf{q}$-space are related by $\mathbf{q} = 2\mathbf{k}$. In addition to the uncertainty in the position of the FT peaks in $\mathbf{k}$-space (estimated from the FHWM of the Lorentzian curve fit above), we further considered the uncertainty in the energy location of these peaks. For a given FT-STS map, the uncertainty in energy is given by the lock-in amplitude that was used to acquire the map: δE = ±(lock-in amplitude).

We fitted the data along all the high-symmetry direction with a free electron dispersion (black curve in **Figure 4.5**d) given by:

$$E(\mathbf{k}) = \hbar^2|\mathbf{k}|^2/2m_{\mathbf{k}}^* + \mu \qquad \text{(Eq. 4.1)}$$

Here $m_{\mathbf{k}}^*$ is the IS electron effective mass along the direction $\mathbf{k}$ and μ is the chemical potential corresponding to the energy onset of the IS state. We find $\mu = 122 \pm 1$mV and that the IS electron effective mass, $m_{\mathbf{k}}^*$, is independent of $\mathbf{k}$ giving m^*/m_e = 0.395 ± 0.005 (here, m_e is the electron mass). The isotropic effective mass (despite the obliqueness of the molecular film structure) and the fact that the extracted effective mass similar to the effective mass of the bare Ag(111) SS (m^*/m_e = 0.41 ± 0.02 [83]) could be an indication that the IS electrons are fairly insensitive to the potential landscape of the DCA overlayer. Furthermore, the similar values for the effective masses, for both the DCA/Ag(111) IS and Ag(111) SS, implies that there is little to no hybridisation between the DCA molecular states and the underlying Ag(111) substrate in the formation of the DCA/Ag(111) interface state. This corroborates the weak DCA-Ag(111) interactions inferred in Chapter 3.

We note the deviations from free electron-like behaviour at higher energies where $\mathbf{k}$ approaches the BZ boundaries (e.g., **X** on the left and **Y** on the right of residual plot, bottom of **Figure 4.5**d; black data points). These deviations are indicative of the case where the corrugation in the molecular potential imposed on the IS electrons is non-negligible. Therefore, we considered a 2nd order correction to the free electron dispersion [84]:

$$E(\mathbf{k}) = E^0(\mathbf{k}) + \sum_{\mathbf{G}} \frac{|U_{\mathbf{G}}|^2}{(E^0(\mathbf{k}) - E^0(\mathbf{k}-\mathbf{G}))} \qquad \text{(Eq. 4.2)}$$

with $E^0(\mathbf{k})$ given by Eq. 4.1. Here, $U_{\mathbf{G}}$ is the Fourier coefficient of the DCA molecular film potential, $U(\mathbf{r})$:

$$U(\mathbf{r}) = \sum_{\mathbf{G}} U_{\mathbf{G}}\, e^{i\mathbf{G}\cdot\mathbf{r}} \qquad \text{(Eq. 4.3)}$$

To a first approximation, we assumed that in Eq. 4.3, the only non-zero Fourier coefficients, $U_{\mathbf{G}}$, are those associated with $\mathbf{G} = \{\pm\mathbf{G_1}, \pm\mathbf{G_2}, \pm(\mathbf{G_1} + \mathbf{G_1})\}$. Here, $\mathbf{G_1}$ and $\mathbf{G_2}$ are the primitive reciprocal lattice vectors for the DCA/Ag(111) lattice structure; they correspond to $\mathbf{a_1^*}$ and $\mathbf{a_2^*}$, respectively. These Fourier coefficients are expected to have the largest contribution to the molecular potential. Further, by symmetry reasons, $U_{\mathbf{G}} = U_{-\mathbf{G}}$, which leaves only three unique Fourier coefficients in Eq. 4.3 to consider. With this, the molecular potential, $U(\mathbf{r})$, can be written as:

$$\begin{aligned} U(\mathbf{r}) = {} & 2U_{\mathbf{G_1}} \cos(\mathbf{G_1}\cdot\mathbf{r}) \\ & + 2U_{\mathbf{G_2}} \cos(\mathbf{G_2}\cdot\mathbf{r}) \\ & + 2U_{\mathbf{G_1}+\mathbf{G_2}} \cos((\mathbf{G_1}+\mathbf{G_2})\cdot\mathbf{r}) \end{aligned} \qquad \text{(Eq. 4.4)}$$

With this simplification, fitting the data for the DCA/Ag(111) dispersion with Eq. 4.2 is made more tenable, with five fitting parameters to consider: $m_{\mathbf{k}}^*$, μ, $U_{\mathbf{G_1}}$, $U_{\mathbf{G_2}}$, and, $U_{\mathbf{G_1}+\mathbf{G_2}}$. For simplicity, $m_{\mathbf{k}}^*$ is assumed to be isotropic, i.e., independent of $\mathbf{k}$. This is reasonable as fitting with Eq. 4.1 yielded an isotropic effective mass. The blue curve in **Figure 4.5**d shows the resulting fit with Eq. 4.2 to our data. We find that the resulting fit shows a slight deviation from parabolic behaviour at higher energies as expected with Eq. 4.2. For low $|\mathbf{k}|$ values, the two models (i.e., free electron model and 2nd order corrections to the free electron model) provide indistinguishable fits, while for high $|\mathbf{k}|$ values, the deviations from the zero-line in our residual plots (blue data; **Figure 4.5**d) are less pronounced when we consider 2nd order corrections to the free electron model, i.e., fitting with Eq. 4.2. The calculated root-mean-square error (RMSE) for the two fits showed a 20% reduction (in the high $|\mathbf{k}|$ regime; see Appendix B.2 for further details) when we considered 2nd order corrections to the free electron model compared to using the unperturbed (free) electron model. From fitting the data with Eq. 4.2, we further find that

the effective mass is m^*/m_e = 0.385 ± 0.003 which is a reduction from the value obtained assuming a free electron dispersion as described by Eq. 4.1. Further, the obtained Fourier coefficients are $U_{\mathbf{G_1}}$ = 0.31 ± 0.03 V, $U_{\mathbf{G_2}}$ = 0.14 ± 0.04 V, and $U_{\mathbf{G_1+G_2}}$ = 0.15 ± 0.04 V. Here, we find that we still maintain a parabolic dispersion for low energies despite being sensitive to the molecular potential as reflected in the reduced effective mass and the non-zero Fourier coefficients.

We note that measurements of $E(\mathbf{k})$ for the DCA/Ag(111) interface state at higher biases (V_b > 1.1 V) was not possible due to the weak $\mathrm{d}I/\mathrm{d}V$ scattering signal in our measurements at these higher energies. As mentioned in subsection 2.3.5, the Ag(111) Shockley surface state lives in the band gap of the Ag(111) projected band structure. At an energy of ~1.5 eV [277], the Ag(111) SS dispersion intersects the Ag(111) bulk dispersion and hence becomes degenerate with bulk state at higher energies, i.e., the Ag(111) surface state ceases to exist for energies > 1.5 eV. For a similar reason, we speculate that the weak $\mathrm{d}I/\mathrm{d}V$ scattering signal for the defect-filled DCA/Ag(111) at high energies is because the DCA/Ag(111) interface state (derived from the Ag(111) SS) dispersion is close to the underlying Ag(111) projected bulk state dispersion at these energies. Nevertheless, the subtle deviations in our measured $E(\mathbf{k})$ data is sufficient for estimating the energy landscape at the DCA/Ag(111) interface as discussed in the following section.

4.4 Molecular Potential Landscape at DCA/Ag(111) Interface

With the obtained Fourier coefficients to the molecular potential, we can reconstruct $U(\mathbf{r})$ according to Eq. 4.4. **Figure 4.6**a shows the reconstructed $U(\mathbf{r})$. Noticeably, the reproduced molecular potential is remarkably similar to the STM imaging of the DCA molecular film (see **Figure 4.4**a inset). This map of $U(\mathbf{r})$ shows fluctuations of the energy landscape ($\Delta U(\mathbf{r}) = \max[U(\mathbf{r})] - \min[U(\mathbf{r})]$) given by the molecular film that could reach $\Delta U(\mathbf{r})$ ~ 1.5 V (see line profile in **Figure 4.6**a inset), despite the dispersion being very close to parabolic near Gamma (see **Figure 4.5**d). With the obtained Fourier coefficients, we can further calculate the full band structure for DCA/Ag(111) interface electrons using the nearly free electron approximation [261]. We solve the following central equation for $E(\mathbf{k})$:

$$\left(\frac{\hbar^2|\mathbf{k}|^2}{2m^*} - E(\mathbf{k})\right) C_{\mathbf{k}} = \sum_{\mathbf{G}} U_{\mathbf{G}}\, C_{\mathbf{k}-\mathbf{G}} \qquad \text{(Eq. 4.5)}$$

with $C_{\mathbf{k}}$ being the Fourier coefficients for the wave function solution for the system. The above expression defines a matrix equation which, through standard methods of inversion, can be solved without explicit knowledge of $C_{\mathbf{k}}$ (see Appendix B.3).

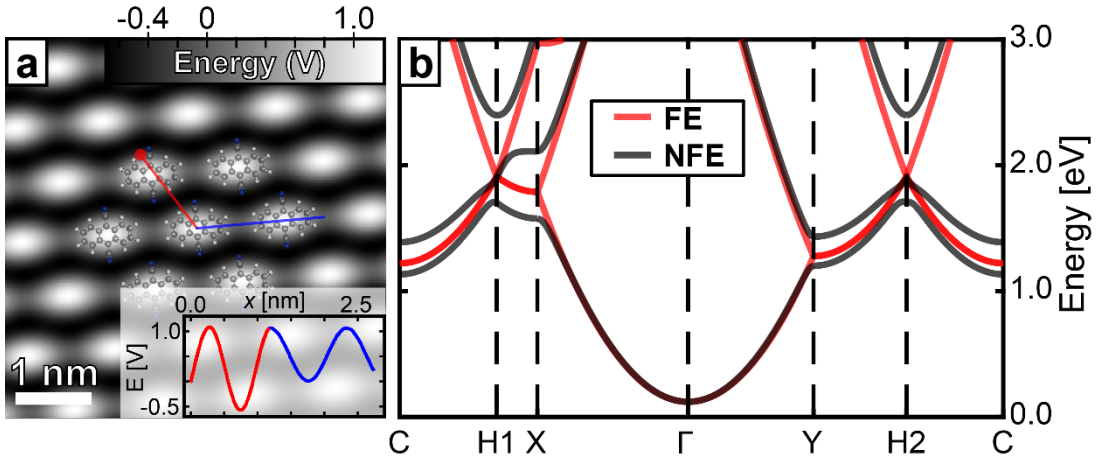

Figure 4.6: DCA/Ag(111) interface potential landscape and band structure calculations. (a) Reconstructed real-space potential, $U(\mathbf{r})$, for the DCA/Ag(111) interface (with $U_{\pm\mathbf{G}_1} = 0.309$ mV, $U_{\pm\mathbf{G}_2} = 0.143$ mV, and $U_{\pm(\mathbf{G}_1+\mathbf{G}_2)} = 0.152$ mV) showing real-space variation in the molecular potential on the order of ~1.5 eV. Inset shows the line profile of $U(\mathbf{r})$ along the red and blue lines in (a). (b) Calculated band structure for the molecular potential in (a) using the nearly-free electron approximation (black) with an electron effective mass, $m^*/m_e = 0.385$. Calculated band structure with free-electron model (red) shown for reference ($m^*/m_e = 0.385$).

Figure 4.6b shows the calculated band structure (black curve). For reference, the calculated band structure with $U(\mathbf{r}) = 0$ everywhere, i.e., free-electron model, is also shown in **Figure 4.6**b (red curve). Here, the shape and strength of $U(\mathbf{r})$ is crucial to the accurate determination of the band structure. Where piecewise constant potentials are a good first approximation to a given system [278], the required $\Delta U(\mathbf{r})$ to reproduce the band structure (for the DCA/Ag(111) interface) may not necessarily reflect the potential landscape encountered by the electrons in the system. A more accurate derivation of $U(\mathbf{r})$ for our system would require using a larger collection of $\{U_{\mathbf{G}}\}$ than the one we have considered. This is possible with more data for the DCA/Ag(111) interface state dispersion at higher energies. However, given that the scattering intensity is severely attenuated at energies far from the IS onset, this is unlikely with the current procedure. Despite this setback, we successfully sampled $E(\mathbf{k})$ with $|\mathbf{k}|$ up to ~80% of the distance from the Γ point to the edge of the BZ (in any direction). This gives us a derived molecular potential, $U(\mathbf{r})$, that is representative of our system.

We note that the authors, Sabitova et al., of ref. [243] developed a method, alternative to the one presented in this chapter, to reconstruct the molecular potential landscape, $U(\mathbf{r})$, at an organic/metal interface with promising success. Their method relied on measuring Bragg scattering of the interface state electrons off a defect-free molecular film. Signatures of Bragg scattering manifest themselves as very subtle peaks in the differential conductance, $\mathrm{d}I/\mathrm{d}V$ data on the molecular film. These subtle peaks are detected using the second derivative in the tunnelling current, $\mathrm{d}^2I/\mathrm{d}V^2$. This method, however, was not feasible in our case, as signatures of Bragg scattering were too weak to be detected. Despite this, our method which does not rely

on measurements of (potentially 'noisy') $\mathrm{d}^2I/\mathrm{d}V^2$, provides a more direct and quantitative deviations of the interface state dispersion from free electron (parabolic) behaviour as **k** approaches the BZ boundary.

4.5 Summary

In this chapter, we looked at a two-dimensional electron gas (2DEG), derived from the bare Ag(111) Shockley surface state, formed at the interface between the DCA molecular film and the underlying Ag(111) substrate. By means of FT-STS, I studied the dispersion of the electrons within this 2DEG interface state. Fitting this dispersion relation with second order corrections to the free electron model revealed slight deviations in the parabolic, i.e., free electron-like, dispersion of these interface state electrons. From the fitting procedure, an effective mass, m^*/m_e = 0.385 ± 0.003, similar to that of the Ag(111) surface state electrons, was determined for these interface state electrons. The slight deviations from the free electron behaviour enabled the reconstruction of the potential landscape, $U(\mathbf{r})$, imposed by the DCA molecular film onto the underlying substrate surface electrons (up to a constant offset). The corrugation of the potential, $\Delta U(\mathbf{r})$, was found to be on the order of 1.5 eV. Here, we see that even if the electrons at hybrid interfaces (e.g., organic/metal interfaces) are free-like, i.e., with an almost perfect quadratic dispersion relation and that molecular-metal interactions are weak (such as between DCA and Ag(111)), the energy landscape that these electrons experience could still show real-space fluctuations greater than 1eV.

The findings of this chapter present an important consideration for the design of 2D functional molecular devices that includes hybrid interfaces e.g., 2D molecular electronics in contact with metal electrodes (for charge control/flow). The real-space potential fluctuations at these hybrid interfaces can lead to a modification of the behaviour of the electrons there. This is particularly true for energies where the interface electron dispersion approaches the BZ boundary of the 2D molecular system. The resulting deviations in the electron dispersion at these energies can have adverse electronic effects that can hinder the electronic properties of the ensemble system (2D molecular system and the hybrid interface). For example, formation of band gaps at BZ boundaries can lead to a decrease in conductivity across the hybrid interface. Tuning of this energy threshold, where the interface electron dispersion deviates from free electron-like behaviour is favourable for 2D molecular electronics. The periodicity of the 2D molecular system offers this capability: with $\Delta U(\mathbf{r})$ being equal, larger 2D molecular periodicities (small BZ) lowers the energy at which the interface electron dispersion meets the BZ boundaries compared to smaller 2D molecular periodicities (large BZ). Therefore, the 2D molecular periodicity essentially sets the energy scale for potential device usage.

Chapter 5
Strongly Correlated Electrons in 2D DCA_3Cu_2 Kagome Metal-Organic Framework on Ag(111)

5.1 Overview

In the previous chapters, I presented results on a 2D organic nanostructure on Ag(111) comprised of only hydrogen-bonded DCA molecules. Extending those results, in this chapter, I present findings on a synthesised 2D metal-organic framework (MOF) on Ag(111) where the metal-ligand coordination within this MOF is facilitated by the coordination between DCA molecules and (co-deposited) Cu adatoms on the surface. It has been predicted that the 2D DCA-Cu MOF hosts non-trivial electronic properties that have relevance for next-generation electronics, e.g., topologically protected edge states [63] and strongly electron-electron interactions [64]. Furthermore, the resulting 2D structure has a local bonding environment that is qualitatively different than those in the preceding chapters. This enables a direct comparison of the impact of different intermolecular interactions on the electronic properties of 2D DCA-based organic nanostructures.

In this chapter, within the 2D MOF, the molecules are shown to self-assemble in a much sought-after kagome arrangement (corner-sharing equilateral triangles) as seen in **Figure 5.1**a. The 2D kagome lattice has three inequivalent lattice sites (red, blue, and green sites in **Figure 5.1**b). Using a tight-binding model with nearest-neighbour electron hopping, one can construct real-space electron eigenfunctions with alternating phases at the neighbouring corners of the kagome hexagon [279–281] (red and blue sites in **Figure 5.1**b). Electron hopping to sites outside the hexagon, i.e., green sites in **Figure 5.1**b, is effectively hindered due to destructive phase interference (hopping from red to green and blue to green sites; see **Figure 5.1**b), resulting in an emergence of a highly localised state within the hexagon. In this non-interacting picture, i.e., without electron-electron interactions, this state appears as a flat band in the electronic band structure for a 2D kagome lattice (see **Figure 5.1**c). In addition to this flat band, the electronic band structure consists of two Dirac bands (the three inequivalent kagome lattice sites in **Figure 5.1**b giving rise to altogether three distinct bands) [279–281]. The flat band, a

direct result of the special geometry of the kagome lattice, when populated can give rise to strong Coulomb electron-electron interactions.

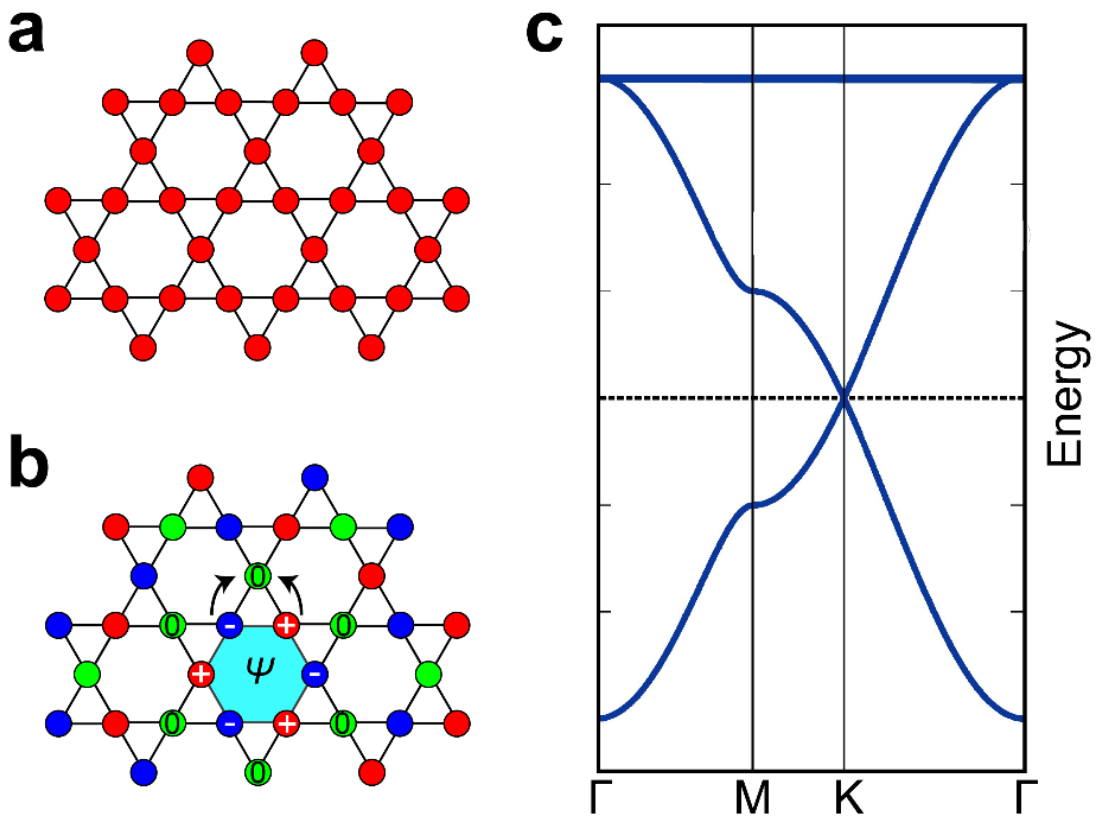

Figure 5.1: Structural and electronic overview for a 2D kagome lattice. (a) 2D kagome lattice structure. (b) The 2D kagome lattice structure have three inequivalent sites indicated by the red, blue, and green sites. Within a given hexagon (cyan), electron eigenfunctions with alternating phases can be constructed at the neighbouring corners of the hexagon (given as '+' and '–' on the red and blue sites, respectively). Destructive quantum phase interference between these eigenfunctions prevents electron hopping to sites outside the hexagon, i.e., the green sites, resulting in a highly localised electronic state within the hexagon. (c) Typical electronic band structure for the 2D kagome lattice. The three inequivalent kagome sites in (b) give rise to three distinct electronic bands: one flat band and two Dirac bands with the Dirac bands meeting at the K-point (i.e., the Dirac point). The flat band here is associated with the highly localised state in (b).

These strong electron-electron interactions can lead to a range of electronic (e.g. Mott transition [282]) and quantum magnetic phases (e.g., ferro-, antiferromagnetic), where transitions can be tuned via control of the valence band (VB) filling. Kagome systems with magnetic order and/or spin-orbit coupling can further exhibit nontrivial Berry phases and topology [283–286]. Recently, correlated electron phenomena and flat bands have been observed experimentally in inorganic kagome lattice single crystals [85, 287, 288]. MOFs and covalent organic frameworks (COFs) with comparably exotic intrinsic electronic structure have been predicted [63, 64, 289], with the additional promise of tuneable electron-electron interactions and topology stemming from bottom-up synthesis approaches to vary coupling parameters [290]. Atomically thin MOFs and COFs with the kagome geometry have been

synthesised; however, flat-bands and correlated phenomena have not yet been observed directly in these systems [52, 69, 291, 292].

Here I show, by means of STM and STS, indications of magnetic moments at both the Cu and DCA sites within the 2D DCA-Cu MOF, which we also refer to as the 2D DCA_3Cu_2 MOF. Density functional theory calculations which include on-site electron-electron interactions (DFT+U) and mean-field Hubbard (MFH) modelling, as performed by collaborator Mr. Bernard Field (co-supervised by Prof. N. Medhekar and Dr. A. Schiffrin), and presented here, rationalises these experimentally observed local magnetic moments as a direct result of strong correlations between the DCA_3Cu_2 kagome MOF electrons. This represents the first demonstration of strongly correlated phenomena in an atomically thin 2D organic nanostructure. Dr. Jack Hellerstedt and Mr. Benjamin Lowe assisted in performing some of the measurements presented in this chapter. Dr. Jack Hellerstedt, Mr. Bernard Field, Mr. Benjamin Lowe, Dr. Yuefeng Yin, Prof. Nikhil Medhekar, and Dr. Agustin Schiffrin all assisted in the interpretation of the findings here. All experimental measurements, presented in this chapter, were performed at 4.4 K unless otherwise stated.

5.2 Structural Characterisation of DCA_3Cu_2 Kagome on Ag(111)

5.2.1 STM and nc-AFM overview of DCA_3Cu_2 kagome on Ag(111)

Figure 5.2a shows a constant-current STM image (V_b = –20 mV) after the co-deposition of DCA molecules and Cu atoms on an atomically clean Ag(111) substrate held at room temperature in UHV (see subsection 2.1.5 for sample preparation details). In contrast with the close-packed crystalline self-assembly of the DCA-only preparation on Ag(111) (see Chapter 3), **Figure 5.2**a shows a porous, less dense and less ordered DCA-Cu arrangement on Ag(111). The Fourier transform (FT) of the STM image in **Figure 5.2**a (see FT inset in **Figure 5.2**a) shows the structural peaks associated with the DCA-Cu structure on Ag(111) (green dashed circles). In the FT image, the anisotropic stretching of these peaks (along cyan arrows) and the diffuse background intensity (centred around $k = 0$) corroborates the observed disorder in DCA-Cu structure in **Figure 5.2**a. Despite the observed partial disorder, the observation of an almost six-fold symmetric FT image implies that the DCA-Cu arrangement, likewise, has a structure that is close to being six-fold symmetric. That is, the DCA-Cu structure on Ag(111) is glassy, i.e., it has short-range order but lacks perfect long-range order.

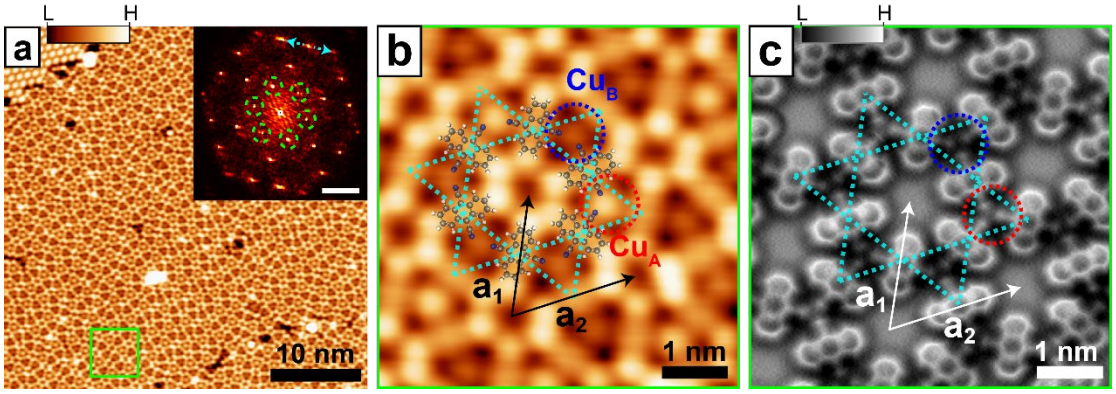

Figure 5.2: STM and nc-AFM overview of DCA_3Cu_2 kagome on Ag(111). (a) Constant-current STM image of the DCA_3Cu_2 kagome structure on Ag(111) performed at 4.4 K (set point: V_b = –20 mV, I_t = 50 pA). Inset: Fourier transform (FT; k = 1/wavelength; scale bar: 1 nm^{-1}) of STM image. Green dashed circles indicate first harmonic peaks corresponding to the hexagonal lattice of the DCA_3Cu_2 kagome crystal. The DCA_3Cu_2 structure is partially disordered and glassy, as shown by anisotropic stretching of peaks (along dashed cyan arrow) and diffuse background (around k = 0) of the Fourier transform. (b) Constant-current STM image of region indicated by green box in (a) (set point: V_b = –20 mV, I_t = 50 pA). Chemical structure of DCA superimposed. Vectors $\mathbf{a_1}$, $\mathbf{a_2}$ define a primitive unit cell, with $\|\mathbf{a_1}\| = \|\mathbf{a_2}\| = 2.045 \pm 0.015$ nm, $\measuredangle(\mathbf{a_1}, \mathbf{a_2}) = 60 \pm 1°$. Dashed cyan lines link centres of DCA molecules, forming the kagome star. (c) CO tip-functionalised nc-AFM image of DCA_3Cu_2 kagome structure in (b). tip retracted 0.3 Å with respect to STM set point V_b = 3 mV, I_t = 150 pA, adjusted on top of DCA molecule centre. Cu atoms follow a honeycomb arrangement and have two different STM and nc-AFM apparent heights ('Cu_A': red dashed circle; 'Cu_B': blue dashed circle).

Figures 5.2b,c shows a constant-current STM image (V_b = –20 mV) and a CO tip-functionalised (see subsection 2.2.7) nc-AFM image of the local DCA-Cu structure observed in **Figure 5.2**a, respectively. In both STM and nc-AFM images, the DCA molecules within the DCA-Cu structure form a kagome-like arrangement (cyan dashed lines in **Figures 5.2**b,c). Here, the kagome arrangement of the DCA molecules are facilitated by the three-fold DCA cyano-Cu coordination (see dashed circles in **Figures 5.2**b,c). The fidelity of the local DCA-Cu, i.e., three-fold, bonding structure means that the resulting 2D DCA_3Cu_2 structure is glassy, i.e., it has short-range order but lacks long-range order. From the FT image in **Figure 5.2**a inset, we estimate that the primitive unit cell of the system (composed of 3 DCA molecules and 2 Cu adatoms) can be defined by the lattice vectors $\mathbf{a_1}$ and $\mathbf{a_2}$ with $\|\mathbf{a_1}\| = \|\mathbf{a_2}\| = 2.045 \pm 0.015$ nm, $\measuredangle(\mathbf{a_1}, \mathbf{a_2}) = 60 \pm 1°$ (see **Figures 5.2**b,c).

Noticeably, within the 2D DCA_3Cu_2 kagome structure, we observe that the Cu atoms, as imaged by STM and nc-AFM imaging, appear with different contrasts (see dashed circles in **Figures 5.2**b,c). In STM imaging, we observe Cu atoms with varying apparent heights. Cu atoms with a larger apparent height (brighter STM contrast) and Cu atoms with a lower apparent height (darker STM contrast) are labelled as Cu_A and Cu_B, respectively (red and blue dashed circles in **Figure 5.2**b, respectively). In nc-AFM imaging, these Cu atoms similarly appear with varying Δf signal. Cu_A atoms appear with a larger Δf signal while Cu_B atoms appear with a

lower Δf signal (red and blue dashed circles in **Figure 5.2**c, respectively). Further, from STM imaging, we find no clear distribution for these different Cu species within the MOF. We discuss both observations, the glassiness of the 2D DCA_3Cu_2 kagome structure on Ag(111) and the appearance of different Cu species (i.e., Cu_A and Cu_B atoms) in the following subsection.

5.2.2 Structural disorder in DCA_3Cu_2/Ag(111)

Here, we address the structural disorder of the DCA_3Cu_2 kagome MOF on Ag(111) in relation to a similarly synthesised DCA_3Cu_2 kagome MOF on Cu(111) [53, 77]. DCA_3Cu_2/Cu(111) was synthesised in UHV by depositing thermally evaporated DCA molecules onto a clean Cu(111) substrate held at room temperature (see subsection 2.1.5 for sample preparation details). **Figure 5.3**e shows a constant-current STM image (V_b = 200 mV) of the resulting DCA_3Cu_2/Cu(111) kagome MOF (**Figure 5.3**a-d. reproduced here from **Figure 5.2** as reference to the 2D DCA_3Cu_2/Ag(111) MOF). Unlike, DCA_3Cu_2/Ag(111), the DCA-Cu kagome structure on Cu(111) appears perfectly ordered. The FT of the STM image in **Figure 5.3**e, likewise, shows sharp structural peaks (green dashed circles) reflecting the crystallinity of the 2D DCA_3Cu_2 kagome structure on Cu(111) (see **Figure 5.3**f). **Figures 5.3**g,h shows a constant-current STM image (V_b = 200 mV) and CO tip-functionalised nc-AFM image of the local DCA_3Cu_2 kagome structure on Cu(111), respectively. In these images, the kagome arrangement for the DCA molecules are indicated by the cyan dashed lines. From the FT image in **Figure 5.3**f, we find that the primitive unit cell for DCA_3Cu_2 on Cu(111) is defined by the lattice vectors $\mathbf{a_1}$ and $\mathbf{a_2}$ such that $\|\mathbf{a_1}\| = \|\mathbf{a_2}\| = 2.045 \pm 0.007$ nm, $\measuredangle(\mathbf{a_1}, \mathbf{a_2}) = 60.0 \pm 0.5°$ (see **Figures 5.3**g,h). Here, we see that the unit cell vectors are similar with those defining the 2D DCA_3Cu_2/Ag(111) kagome structure. Further, like for the MOF on Ag(111), we observe that the Cu atoms within the DCA_3Cu_2/Cu(111) kagome, as imaged by STM and nc-AFM, appear with different contrasts, i.e., different STM apparent heights and different Δf signals, respectively (see dashed circles in **Figures 5.3**g,h). Here, we identify two different Cu species, namely Cu_A (red dashed circles) and Cu_B (blue dashed circles) atoms, with the latter having a larger apparent height and a lower Δf signal in STM and nc-AFM imaging. In contrast with the Cu atoms within the DCA_3Cu_2 MOF on Ag(111), the Cu atoms within the MOF on Cu(111) are positioned with a perfect alternation of Cu_A and Cu_B atoms, i.e., the nearest Cu neighbours for the Cu_A atoms are Cu_B atoms and vice versa.

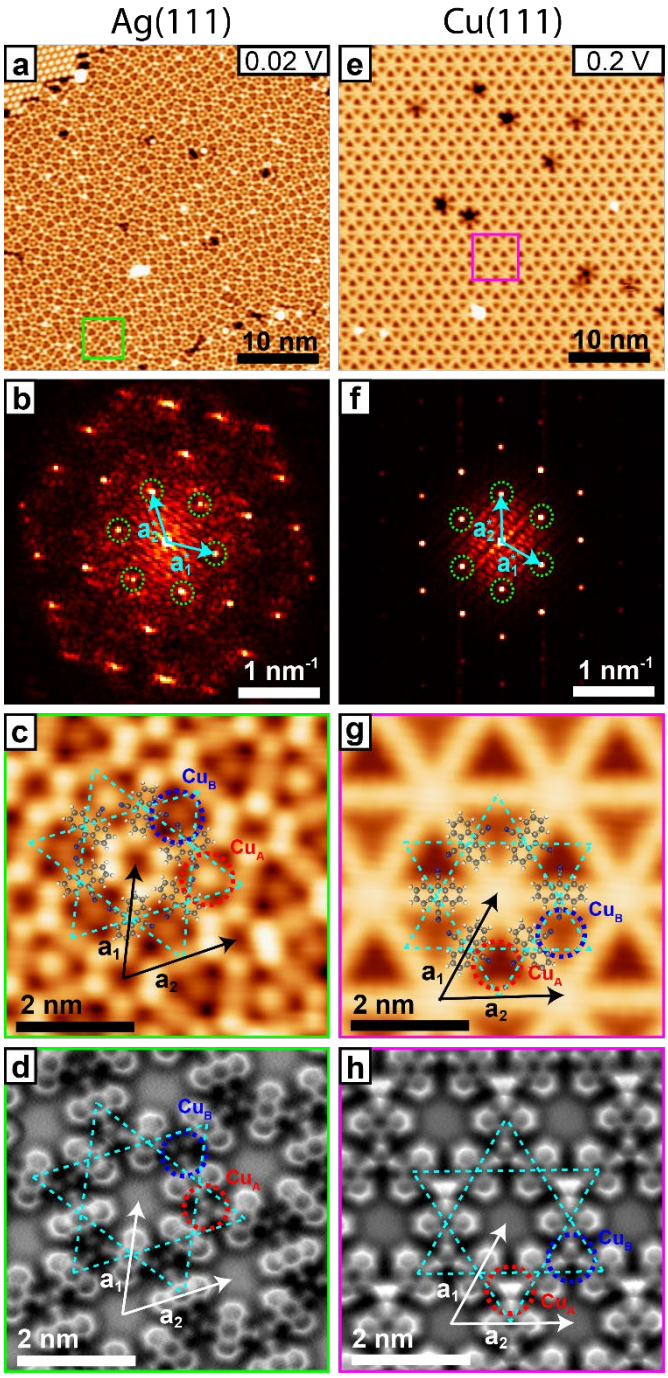

Figure 5.3: STM & nc-AFM imaging of DCA_3Cu_2 kagome structures on Ag(111) and Cu(111). (a)-(d) reproduced here from **Figure 5.2**. (e) Constant-current STM image of the DCA_3Cu_2 kagome structure on Cu(111) performed at 4.4 K (set point: V_b = 200 mV, I_t = 50 pA). (f) Fourier transform (FT; k = 1/wavelength) of STM image. Green dashed circles indicate first harmonic peaks corresponding to the hexagonal lattice of the DCA_3Cu_2 kagome crystal. (g) Constant-current STM image of region indicated by magenta box in (e) (set point: V_b = 200 mV, I_t = 50 pA). Chemical structure of DCA superimposed. Vectors $\mathbf{a_1}$, $\mathbf{a_2}$ define a primitive unit cell, with $\|\mathbf{a_1}\| = \|\mathbf{a_2}\| = 2.045 \pm 0.007$ nm, $\measuredangle(\mathbf{a_1}, \mathbf{a_2}) = 60.0 \pm 0.5°$. Dashed cyan lines link centres of DCA molecules, forming the kagome star. (h) CO tip-functionalised nc-AFM image of DCA_3Cu_2 kagome structure in (g). Tip retracted 0.3 Å with respect to STM set point V_b = 2 mV, I_t = 200 pA, adjusted on top of DCA molecule centre. Unlike DCA_3Cu_2/Ag(111), the MOF system on Cu(111) is perfectly ordered. Here, there is also an alternation in the contrast of the Cu atoms on Cu(111) in both STM and nc-AFM imaging ('Cu_A': red dashed circle; 'Cu_B': blue dashed circle).

To address quantitatively the difference in the level of structural order/disorder between the two systems, we measured the next nearest neighbours' distance, r_{NNN}, for all Cu atom pairs within a large DCA_3Cu_2 MOF domain on both the Ag(111) and Cu(111) substrates (see **Figure 5.4**). Here, we used image processing techniques (via *MATLAB*) to extract the Cu atom positions for both kagome systems on Ag(111) and Cu(111) as seen in **Figures 5.4**a,b (blue and black dots, respectively). These positions were then used to determine r_{NNN}. **Figure 5.4**c shows histograms of the measured r_{NNN} for the DCA_3Cu_2/Ag(111) (blue) and DCA_3Cu_2/Cu(111) (black) MOFs.

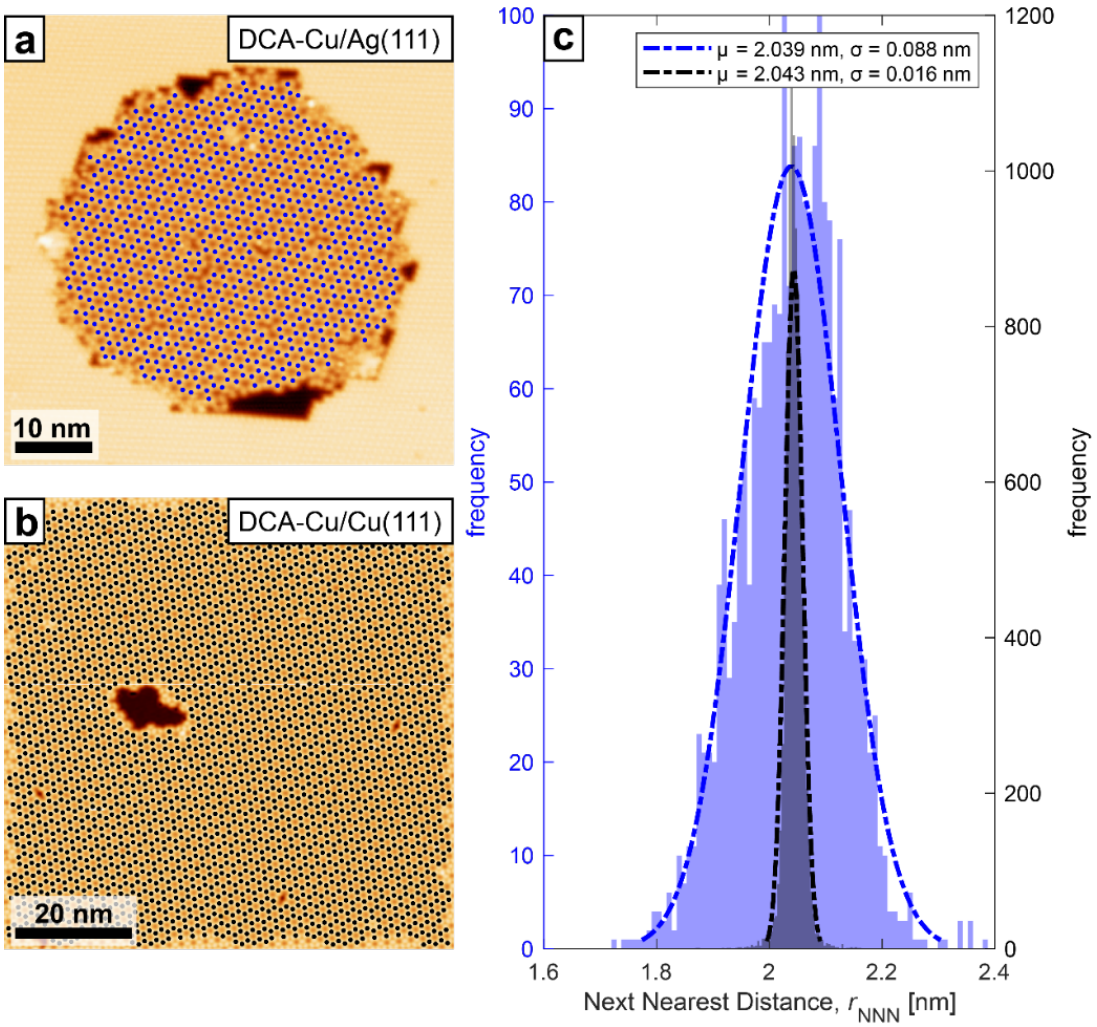

Figure 5.4: Cu atoms next-nearest-neighbour distance in DCA_3Cu_2 MOFs on Ag(111) & Cu(111). (a)-(b) Constant current STM imaging of DCA_3Cu_2 MOF on Ag(111) and Cu(111), respectively (set point: V_b = 1.0 V, I_t = 50 pA). The Cu atoms' positions (blue and black dots) in both systems were extracted using a *MATLAB* image processing algorithm. (c) Histogram of the Cu atoms' next nearest neighbours distance, r_{NNN}, for DCA_3Cu_2 on Ag(111) (blue; left y-axis) and for DCA_3Cu_2 on Cu(111) (black; right y-axis). The calculated average r_{NNN} for both MOFs are similar to one another. However, the distribution width for the Cu atoms' next nearest neighbours distance in the DCA_3Cu_2/Ag(111) system is ~5.5 times broader than that for the DCA_3Cu_2/Cu(111) system.

A normal distribution fit for both histograms shows that the average r_{NNN} for both systems are nearly identical (μ = 2.039 nm and 2.043 nm for DCA_3Cu_2 on Ag(111) and Cu(111), respectively) however the width of the distribution of r_{NNN} differs significantly between the two systems (σ = 0.088 nm and 0.016 nm for DCA_3Cu_2 on Ag(111) and Cu(111), respectively). The larger width of the distribution of r_{NNN} for DCA_3Cu_2/Ag(111) reflects the disordered kagome structure synthesized on Ag(111) compared to Cu(111) which is perfectly crystalline as seen in **Figure 5.3**. We note that this method allowed for a more direct access to the level of structure order/disorder than an analysis of the FT images in **Figures 5.3**b,f. This is particularly so, given the complicated and intricate FT structures seen for the DCA_3Cu_2/Ag(111) kagome structure.

Given the close resemblance between average r_{NNN} for the DCA_3Cu_2 MOFs on Ag(111) and Cu(111) we speculate that the significant difference in the distribution r_{NNN} (i.e., structural disorder/order) is driven by the difference in registry between the MOF and Ag(111) compared to the MOF on Cu(111). To see this, we performed nc-AFM imaging using a CO functionalized tip of the kagome-bare metal surface boundary seen in **Figure 5.5**. The lower halves of the nc-AFM images in **Figure 5.5** show atomically resolved images of the bare Ag(111) (**Figure 5.5**a) and Cu(111) (**Figure 5.5**b) surfaces. Using the surface atom positions for these surfaces, we can infer the positions of the surface atoms (red circles) beneath the DCA_3Cu_2 kagome structure for the top halves of the nc-AFM images in **Figure 5.5**. Here, we see that the there is no clear registry between the DAC_3Cu_2 MOF and the Ag(111) substrate (**Figure 5.5**a), i.e., the MOF is incommensurate with the underlying substrate. This is in contrast with the case on Cu(111) where the DCA_3Cu_2 MOF is perfectly commensurate with the underlying Cu(111) substrate (**Figure 5.5**b) as was previously found [53, 77]. These findings are consistent with the weak DCA-Ag(111) interactions established in Chapter 3 and the nature of reactivities of Ag(111) and Cu(111) substrate (with the Cu(111) substrate being the more reactive of the two) [264, 265]. Therefore, we ascribe the glassiness and partial disorder of the DCA_3Cu_2 kagome structure on Ag(111) to a structural mismatch between the energetically favourable DCA-Cu arrangement within the MOF [which can be achieved commensurately on Cu(111)] and the Ag(111) lattice.

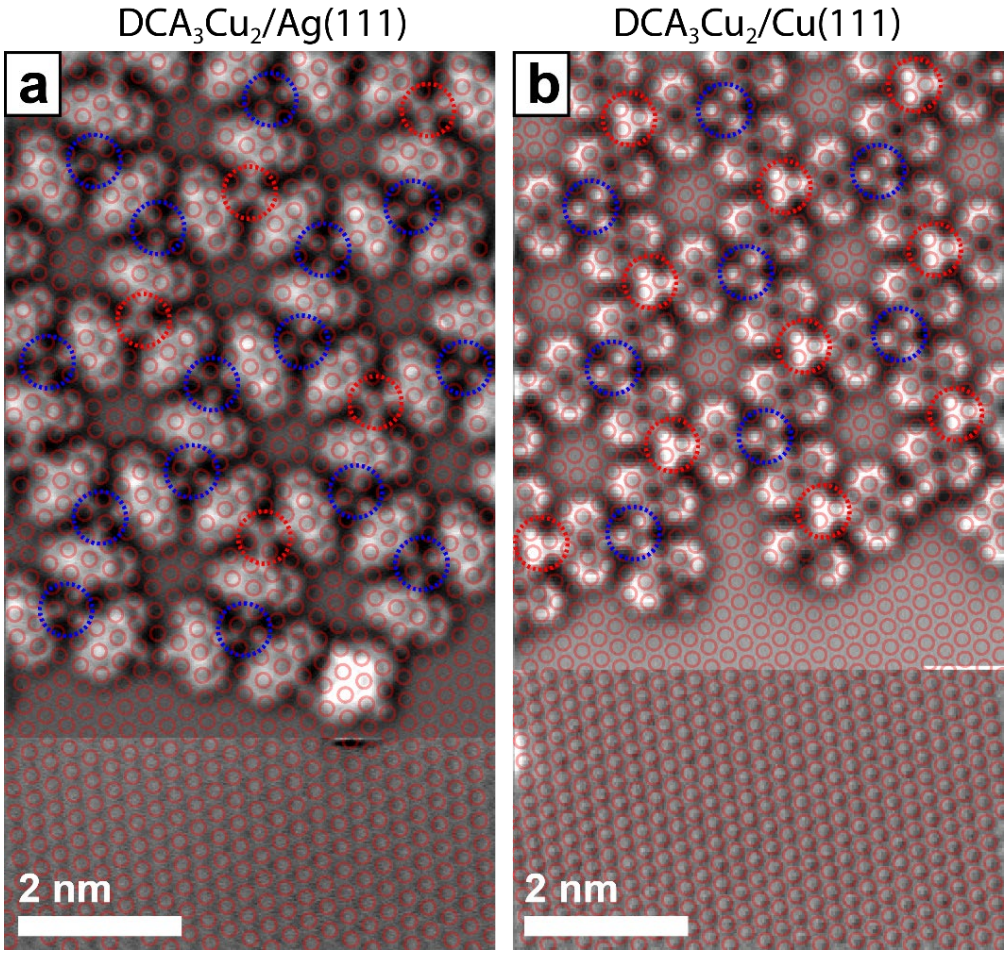

Figure 5.5: Registration of DCA_3Cu_2 on Ag(111) and Cu(111). (a)-(b) Constant-height CO tip-functionalized nc-AFM images for DCA_3Cu_2 on (a) Ag(111) and (b) Cu(111). At the bottom of (a) and (b) are atomically resolved images of the (a) bare Ag(111) and (b) bare Cu(111) surfaces. The positions of these surface atoms are used to determine the registration of the DCA_3Cu_2 kagome systems on both Ag(111) and Cu(111). In this case, the DCA_3Cu_2 is incommensurate with the Ag(111) substrate but commensurate with the Cu(111) substrate. Cu_A and Cu_B sites in both systems are indicated by the red and blue dashed circles, respectively. (Top half of (a), (b) taken with the tip retracted 0.3 Å with respect to STM set point V_b = 3 mV, I_t = 0.2 nA, adjusted on top of DCA molecule centre. Bottom half of (a), (b) taken with STM set point V_b = 3 mV, I_t = 2.5 nA, adjusted on top of DCA molecule centre).

5.2.3 Origin of Cu contrast in STM and nc-AFM imaging of DCA_3Cu_2/Ag(111)

The observed difference in contrast in STM and nc-AFM imaging of the Cu atoms in DCA_3Cu_2 (Cu_A and Cu_B; see section 5.2.1) on Ag(111) can be structural (i.e., difference in real adsorption height) or electronic (i.e., difference in near-Fermi density of electronic states). To determine which, we measured the apparent height difference, Δz_{app}, between Cu_A and Cu_B atoms as a function of tunnelling bias via constant-current STM imaging (see **Figures 5.6**a-c). We find that Δz_{app} shows no strong dependence on STM tunnelling bias indicating that the observed contrast for the Cu atoms in STM and nc-AFM imaging is not due to differences in the near-Fermi density of electronic states. We further performed measurements of the real adsorption height difference, Δz, between the Cu_A and Cu_B atoms via nc-AFM force spectroscopy (see

subsection 2.4.2). This involves measuring the frequency shift, Δf, of the resonating qPlus sensor tip as a function of relative tip-sample distance, z_{rel}, at both Cu atom positions and then determining the relative separation in the minima of the obtained $\Delta f(z)$ curves. With this, we find that Δz to be ~17 pm with Cu_A having the larger adsorption height (see **Figure 5.6**d). We note, however, that this value of Δz varies depending on which Cu_A and Cu_B atoms that are being probed with force spectroscopy. Despite this, we find that Cu_A atoms, which have larger apparent heights as measured by STM, tend to have larger real adsorption heights than Cu_B atoms. Therefore, we conclude that the differing contrast in the appearance of Cu atoms in STM and nc-AFM imaging is due to differing adsorption heights for the Cu atoms: where Cu atoms with a larger adsorption height having a larger apparent height and therefore a brighter contrast in STM and nc-AFM imaging.

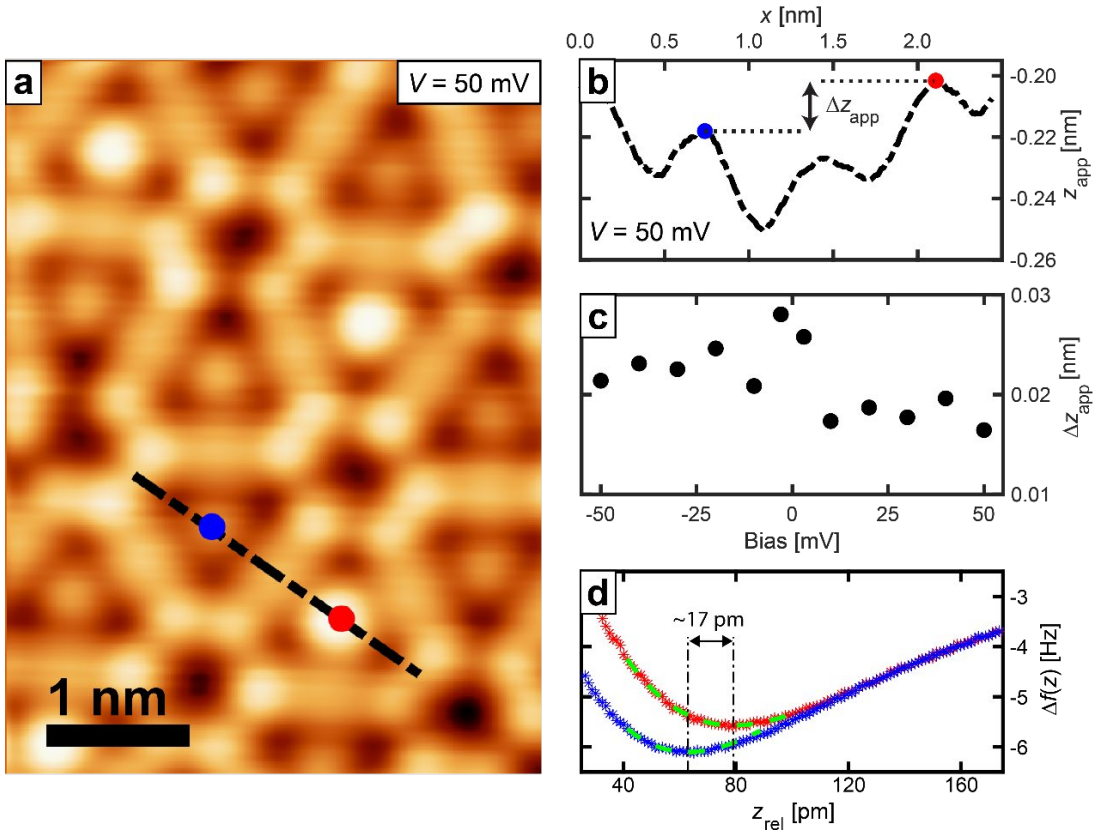

Figure 5.6: Apparent and real adsorption height difference between Cu_A and Cu_B atoms in DCA_3Cu_2/Ag(111). (a) Constant current STM imaging of DCA_3Cu_2/Ag(111) (V_b = 50 mV, I_t = 50 pA). (b) Image line profile along black dashed line in (a). The apparent height difference between the Cu_B (blue dot) and Cu_A (red dot) is indicated by Δz_{app}. (c) Plot of the measured apparent height difference, Δz_{app}, as a function of STM imaging bias. Δz_{app} shows no significant variations as a function of bias suggesting topographic differences between the Cu_A and Cu_B in STM imaging is structural in nature. (d) Frequency shift as a function of relative tip-sample distance, $\Delta f(z)$, for Cu_A (red curve) and Cu_B (blue curve). The minima of the curves were found by fitting a 3rd order polynomial near the vicinity of the minima (green dashed curve). The difference in the minima gives a measure of the difference of adsorption heights between the Cu_A and Cu_B atoms of ~17 pm with Cu_A having the larger adsorption height (nc-AFM oscillations amplitude = 70 pm).

We note that because of the incommensurability of the DCA_3Cu_2 kagome MOF on Ag(111) established in the previous subsection, the Cu atoms necessarily have varying adsorption sites on the underlying Ag(111) substrate (see **Figure 5.5**a). We speculate that different Cu adsorption sites lead to varying Cu adsorption heights such as the case of DCA molecules on Ag(111) (see section 3.2). The resulting distribution of Cu atoms with large (Cu_A atoms) and small (Cu_B atoms) adsorption heights within the 2D DCA_3Cu_2 MOF on Ag(111) could therefore appear quasi-random as seen in **Figure 5.2**.

5.3 STS Characterisation of DCA_3Cu_2 Kagome on Ag(111)

For insights into the electronic properties of the DCA_3Cu_2 MOF on Ag(111), we performed $\mathrm{d}I/\mathrm{d}V$ STS measurements at 4.4 K. **Figure 5.7**a shows the obtained $\mathrm{d}I/\mathrm{d}V$ STS spectra at the high symmetry locations (labelled in STM inset of **Figure 5.7**a) within the MOF. At all locations we observe a broad and prominent resonance between 150 – 500 mV. Near the Fermi level, we identify a rich set of features in the $\mathrm{d}I/\mathrm{d}V$ signal at all the high symmetry locations. To better see these features, **Figure 5.7**b shows the near-Fermi $\mathrm{d}I/\mathrm{d}V$ STS spectra taken at the DCA anthracene extremity (blue curve), the Cu_A atom (black curve) and at the DCA molecular centre (green curve) sites. Spectra taken at the DCA anthracene extremities and the Cu_A atoms (blue and black curves in **Figure 5.7**b, respectively) show zero-bias peaks (ZBPs). We note that the $\mathrm{d}I/\mathrm{d}V$ STS at Cu_B sites are qualitatively identical to those at Cu_A sites but with a reduced ZBP intensity is omitted for clarity. A ZBP with a reduced intensity is also visible at the MOF pore centres (magenta curve in **Figure 5.7**a), which we attribute to a residual signal from the nearby DCA anthracene extremities. At the DCA molecular centre (green curve in **Figure 5.7**b), we observe a prominent energy-symmetric (with respect to the Fermi level) step-like feature. Additionally, we observe energy-symmetric peak features in the $\mathrm{d}I/\mathrm{d}V$ STS at the DCA molecular centre (indicated by grey dashed lines). These peaks are also observed at the DCA anthracene extremity and Cu locations, although subtly (see grey dashed lines). We note that these near-Fermi features were not observed for the DCA-only system on Ag(111) discussed in the Chapter 3.

The zero-bias $\mathrm{d}I/\mathrm{d}V$ STS map in **Figure 5.7**c (acquired using the multi-pass method; see subsection 2.3.4) shows the spatial distribution of the ZBP, with intensity at all Cu atoms and anthracene extremities. The anthracene extremity components closely resemble the spatial extent of the DCA lowest unoccupied molecular orbital (LUMO) that we observed in DCA-only monolayers on Ag(111) in Chapter 3. In contrast, the $\mathrm{d}I/\mathrm{d}V$ STS map taken at a bias below the onset of the step-like $\mathrm{d}I/\mathrm{d}V$ feature in **Figure 5.7**b, i.e., V_b = –100 mV (see **Figure 5.7**d), shows higher intensities at the anthracene centres than at the anthracene extremities and

Cu atom sites (see Appendix C.4 for $\mathrm{d}I/\mathrm{d}V$ STS maps at energies correspond to the satellite peaks in **Figure 5.7**b).

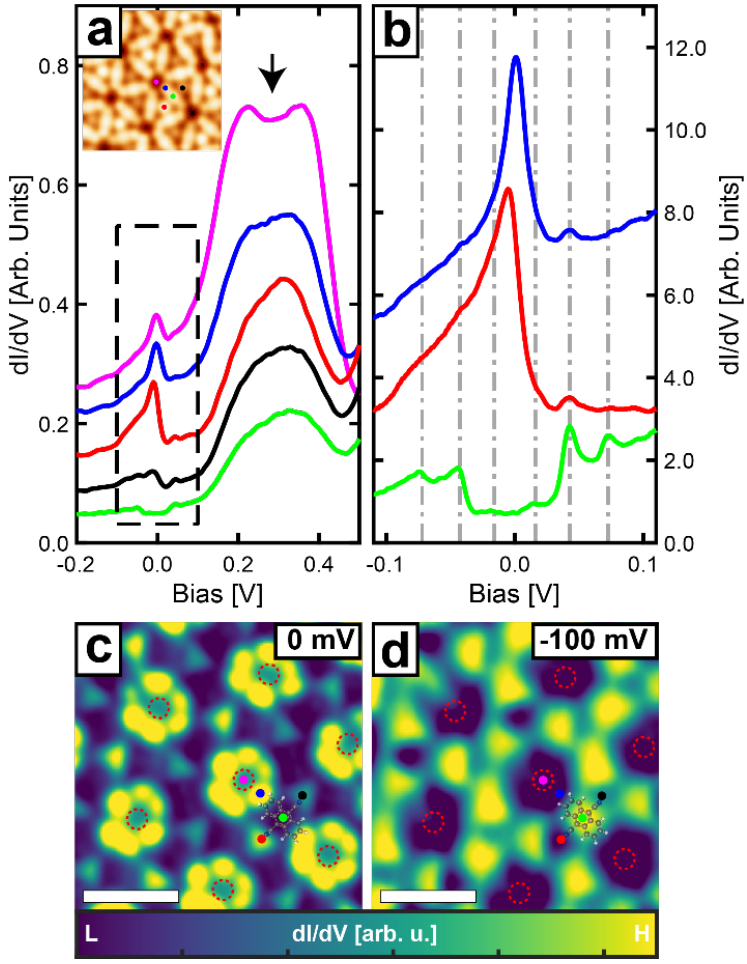

Figure 5.7: STS characterisation of DCA_3Cu_2 kagome MOF on Ag(111). (a) $\mathrm{d}I/\mathrm{d}V$ STS spectra (set point V_b = –250 mV, I_t = 0.5 nA) at high symmetry points of kagome MOF (indicated in inset STM image; V_b = –200 mV, I_t = 500 pA). Spectra vertically offset for clarity. A broad resonance between ~0.15 – 0.5 V (black arrow) is seen at all locations. (b) Near-Fermi $\mathrm{d}I/\mathrm{d}V$ STS spectra (dashed rectangle in (a)) at DCA anthracene extremity (blue) and MOF Cu (Cu_A) atom (red), showing sharp zero-bias resonance. Near-Fermi STS data at DCA centre (green) shows a prominent step-like feature. Energy-symmetric peaks also observed in the STS data are indicated by vertical grey dashed lines. STS data in (a)-(b) were acquired by numerically differentiation of $I(V)$ curves. (c)-(d) $\mathrm{d}I/\mathrm{d}V$ maps at 0 and –100 mV acquired using multi-pass approach (see section 2.3.4). The first pass recorded the STM topographic profile with a constant-current set point: V_b = –200 mV, I_t = 500 pA. The second pass recorded the $\mathrm{d}I/\mathrm{d}V$ signal using the lock-in technique while following the recorded profile in the first pass, with a tip offset of 120 and 30 pm for (c) and (d), respectively. At 0 mV (–100 mV), $\mathrm{d}I/\mathrm{d}V$ intensity is higher at Cu atoms and anthracene extremities (anthracene centres, respectively). Red dashed circles: pores of kagome structure. Scale bars: 1.5 nm.

Previous works [53, 278] have shown that 2D porous metal-organic systems can confine the Shockley surface states of underlying metallic substrates, resulting in resonances in the measured $\mathrm{d}I/\mathrm{d}V$ STS curves. To test whether the features in our experimental $\mathrm{d}I/\mathrm{d}V$ curves in **Figure 5.7** are a result of the confinement of the Ag(111) Shockley surface state by the DCA_3Cu_2 MOF, we simulated the local density of states (LDOS) of 2D free electrons subjected

to a 2D potential following the geometry of the DCA_3Cu_2 MOF. To do this, we utilise the Electron Plane Wave Expansion (EPWE) model as described in ref. [278] (see Appendix C.1.1 for details on model calculations).

Figure 5.8a shows the $\mathrm{d}I/\mathrm{d}V$ STS measurements at the high symmetry points for the DCA_3Cu_2/Ag(111) kagome structure (indicated in **Figure 5.8**c) for biases $V_\mathrm{b} > -0.1$ V. **Figure 5.8**b shows the simulated LDOS at corresponding high-symmetry locations for 2D free electrons confined by a 2D potential kagome geometry as seen in **Figure 5.8**d. Here, we modelled the potential imposed by the DCA_3Cu_2 kagome on the underlying Ag(111) surface state electrons using a piecewise constant periodic function. The red, cyan, green and blue regions in **Figure 5.8**d correspond to regions of constant potential modelling the potential of the Cu atom, DCA anthracene body, DCA anthracene extremity and the bare Ag(111) surface, respectively. We used a potential strength of V_Cu = 1.5 V (red regions; representing Cu atoms), V_mol = 0.15 V (cyan regions; representing DCA anthracene body), V_end = 0.15 V (green regions; representing anthracene extremities), and V_Ag = 0 V (blue regions; representing bare Ag(111) surface). This choice in the potential strengths was made to reproduce the experimental results as close as possible (by means of trial and error).

From **Figures 5.8**a,b, we find the features in our experimental $\mathrm{d}I/\mathrm{d}V$ STS data are reproduced qualitatively in our simulated LDOS for biases $V_\mathrm{b} > 100$ mV. In particular, our model reproduces the broad resonance between V_b = 150 and 500 mV in experimental $\mathrm{d}I/\mathrm{d}V$ STS data our at all kagome geometry high-symmetry points. To corroborate the agreement between the EPWE model results and our experimental $\mathrm{d}I/\mathrm{d}V$ STS data, we further compared experimentally acquired $\mathrm{d}I/\mathrm{d}V$ STS maps for the DCA_3Cu_2/Ag(111) kagome MOF with the corresponding simulated LDOS maps obtained from our EPWE model calculations. **Figures 5.8**e-j show some these experimental $\mathrm{d}I/\mathrm{d}V$ STS maps and simulated LDOS maps for biases $V_\mathrm{b} > -0.1$ V. We find that simulated LDOS maps show similar spatial features with our experimental data. We note that the energy scale of the features seen in both our experimental and simulated data are different. This could be explained by the fact that our simulated geometry assumes a perfect kagome structure whereas experimentally this is not the case, i.e., disorder in the DCA_3Cu_2 kagome structure on Ag(111) is apparent. Furthermore, we assumed a constant piecewise potential landscape whereas a real potential landscape would be smoothly varying. Simulating the latter would be computationally expensive and would affect the energy scale of the system but not the qualitative shape of the simulated LDOS. We also note that there is an increase in the $\mathrm{d}I/\mathrm{d}V$ signal for $V_\mathrm{b} > 1$ V which is not captured by our model. We attribute this increase to an increase in the transmission term in the tunnelling current at larger energies (see subsection 2.2.5) which is not modelled using EPWE.

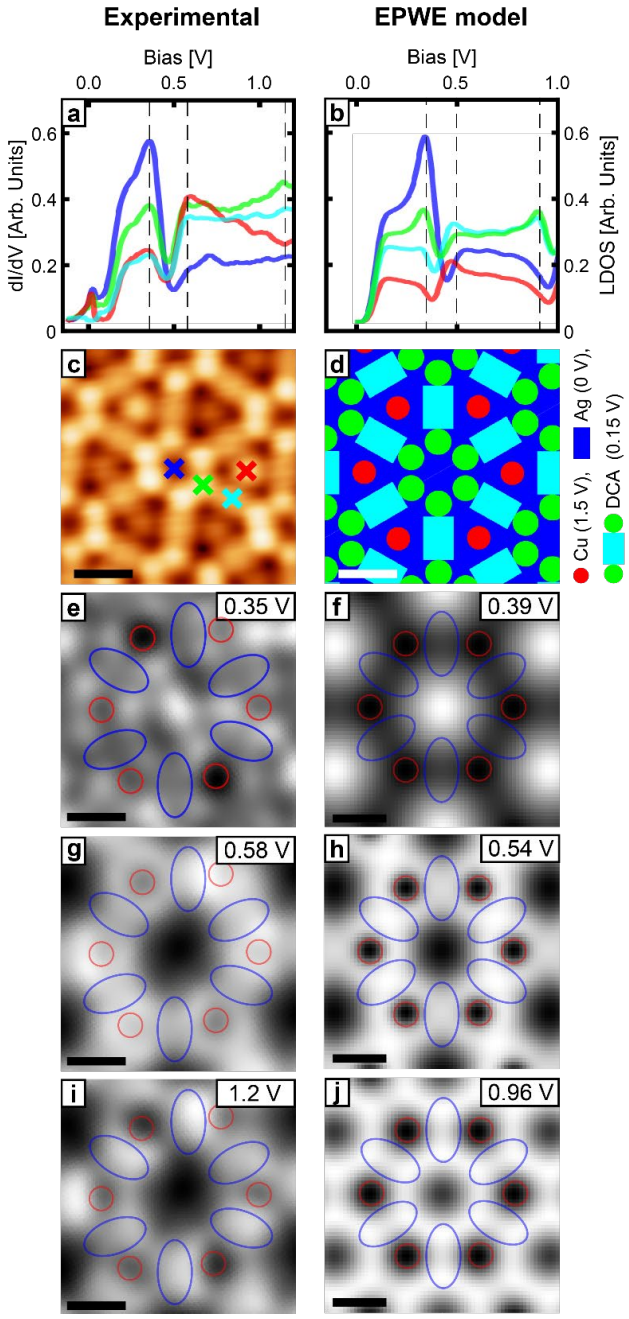

Figure 5.8: LDOS simulation for DCA_3Cu_2/Ag(111) via Electron Plane Wave Expansion (EPWE) modelling. (a) Differential conductance measurements at the high-symmetry points (shown in (c)) for DCA_3Cu_2 kagome on Ag(111) showing intricate features for V_b > –0.1 V (Setpoint: V_b = –0.3 V, I_t = 20 pA). (b) Calculated LDOS at high-symmetry locations (shown in (d)) using the EPWE model for 2D free electrons in a periodic kagome potential. (c) Constant-current STM image of DCA_3Cu_2/Ag(111) kagome MOF (set point: V_b = –20 mV, I_t = 50 pA). (d) The potential geometry and landscape modelled after the DCA_3Cu_2 kagome geometry and used to simulate the LDOS in (b). Here we used V_{Cu} = 1.5 V (red regions; representing Cu atoms), V_{mol} = 0.15 V (cyan regions; representing DCA anthracene body), V_{end} = 0.15 V (green regions; representing anthracene extremities), and V_{Ag} = 0 V (blue regions; representing bare Ag(111) surface). The periodicity of the potential is defined by the lattice vectors $\mathbf{a_1}$ and $\mathbf{a_2}$: $\|\mathbf{a_1}\| = \|\mathbf{a_2}\| = 2.045$ nm with $\measuredangle(\mathbf{a_1}, \mathbf{a_2}) = 60°$. (e), (g), (i) show the bias cuts of a constant-current dI/dV STS grid (V_b = –0.3 V, I_t = 20 pA) at the indicated biases. (f), (h), (j) show the simulated LDOS maps using the EPWE model at the biases indicated. The blue ellipses and red circles in (e)-(j) indicate the DCA molecule and Cu atom positions, respectively. Qualitatively, there is agreement between the bias cuts and the LDOS maps for biases V_b > 0.1 V. Scalebars: 1 nm.

From **Figures 5.8**a,b, we find the features in our experimental $\mathrm{d}I/\mathrm{d}V$ STS data are reproduced qualitatively in our simulated LDOS for biases $V_\mathrm{b} > 100$ mV. In particular, our model reproduces the broad resonance between V_b = 150 and 500 mV in experimental $\mathrm{d}I/\mathrm{d}V$ STS data our at all kagome geometry high-symmetry points. To corroborate the agreement between the EPWE model results and our experimental $\mathrm{d}I/\mathrm{d}V$ STS data, we further compared experimentally acquired $\mathrm{d}I/\mathrm{d}V$ STS maps for the DCA_3Cu_2/Ag(111) kagome MOF with the corresponding simulated LDOS maps obtained from our EPWE model calculations. **Figures 5.8**e-j show some these experimental $\mathrm{d}I/\mathrm{d}V$ STS maps and simulated LDOS maps for biases $V_\mathrm{b} > -0.1$ V. We find that simulated LDOS maps show similar spatial features with our experimental data. We note that the energy scale of the features seen in both our experimental and simulated data are different. This could be explained by the fact that our simulated geometry assumes a perfect kagome structure whereas experimentally this is not the case, i.e., disorder in the DCA_3Cu_2 kagome structure on Ag(111) is apparent. Furthermore, we assumed a constant piecewise potential landscape whereas a real potential landscape would be smoothly varying. Simulating the latter would be computationally expensive and would affect the energy scale of the system but not the qualitative shape of the simulated LDOS. We also note that there is an increase in the $\mathrm{d}I/\mathrm{d}V$ signal for V_b > 1 V which is not captured by our model. We attribute this to an increase in the transmission term in the tunnelling current at larger energies (see subsection 2.2.5) which is not captured using EPWE.

Despite these inconsistencies, the good qualitative agreement between our experimental and simulated data for $V_\mathrm{b} > 100$ mV means that the features (e.g., resonance between V_b = 150 and 500 mV) in our STS data for $V_\mathrm{b} > 100$ mV are a result of the confinement of the underlying Ag(111) Shockley surface state by the DCA_3Cu_2 kagome structure. Notably, the ZBP and the step-like features near the Fermi level is not captured by our model and are not a result of the Ag(111) surface state confinement. The nature of these near-Fermi features will be explored in the following section.

5.4 Nature of ZBP and Near-Fermi Features in d*I*/d*V* STS Data

5.4.1 Temperature-dependent d*I*/d*V* data and fitting overview

As pointed out in subsection 2.3.6, not all features in the $\mathrm{d}I/\mathrm{d}V$ signal necessarily correspond to intrinsic electronic states. To determine if the near-Fermi features, i.e., the ZBP and the off-Fermi, energy symmetric step and peaks observed in our $\mathrm{d}I/\mathrm{d}V$ STS data are intrinsic DCA_3Cu_2 kagome MOF states, we looked at the temperature dependence of these features. **Figure 5.9** shows the acquired $\mathrm{d}I/\mathrm{d}V$ STS spectra at the Cu_A, DCA anthracene extremity, and DCA centre sites, for temperatures between 4.4 and 145 K.

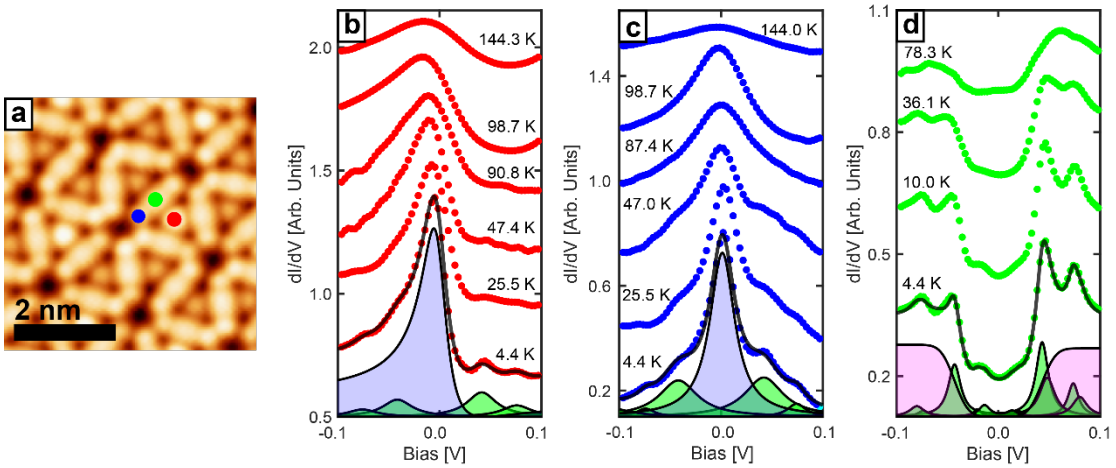

Figure 5.9: Temperature-dependent near-Fermi dI/dV STS data for DCA_3Cu_2/Ag(111) kagome MOF. (a) Constant-current STM image of the DCA_3Cu_2/Ag(111) kagome MOF (set point: V_b = –250 mV, I_t = 1.5 nA). (b)-(d) Background subtracted dI/dV STS spectra at (a) Cu_A, (b) DCA anthracene extremity, and (c) DCA centre, taken at various temperatures. Locations for spectra in (a)-(c) are correspond to red, blue, and green markers in (a), respectively. For temperatures > 4.4 K, the STM was heated to the desired temperature (by applying power to a built-in Zener diode) and was stabilised at that temperature for 1 –1.5 hours to allow for thermal drift to settle prior to performing STS measurements. At higher temperatures, a drift correction software was used to compensate for any residual thermal drift. Black curves: total fits of T = 4.4 K data, consisting of a Fano line shape for the ZBP (blue filled curves), pairs of Lorentzians for the energy-symmetric off-Fermi peaks (green filled) and a pair of error functions for the energy-symmetric step functions (magenta filled). At the Cu sites and the DCA anthracene extremities, the locations of the satellite peaks are at ±43.5 and ±75.6 mV. At the DCA centre, the step-like feature is positioned at ±43.5 mV, while satellite peaks are located at ±17.3, ±43.5, ±56.3, ±75.6, and ±85.8 mV.

We then fitted all the acquired dI/dV spectra, using a non-linear least squares fitting algorithm (via *MATLAB*). To remove contributions of thermal broadening to the acquired dI/dV signal (see Appendix C.6), we considered the following functional form for our fits [293]:

$$(\mathrm{d}I/\mathrm{d}V)_{\mathrm{fit}}(V,T) = \int_{-\infty}^{\infty} \rho_{\mathrm{fit}}(E,T)\frac{\mathrm{d}}{\mathrm{d}V}F(E-eV,T)\,\mathrm{d}E \qquad \text{(Eq. 5.1)}$$

Here T is the temperature of the system, $\rho_{\mathrm{fit}}(E,T)$ is the functional form that we use for fitting the local density of states at a particular site and $F(E,T)$ is the Fermi-Dirac distribution function:

$$F(E,T) = 1/(e^{E/T}+1) \qquad \text{(Eq. 5.2)}$$

For the Cu sites, we consider the following functional form for $\rho_{\mathrm{fit}}(V,T)$:

$$\rho_{\mathrm{fit}}^{\mathrm{Cu}}(V,T) = \mathrm{Fano}(V,E_0,\Gamma,q,A) + \sum_i L(V,E_i,\Gamma_i,A_i) + \mathrm{c}(\mathrm{A},V,E',\sigma) \qquad \text{(Eq. 5.3)}$$

where:

$$\mathrm{Fano}(V, E_0, \Gamma, q, A) = \frac{A}{1+q^2}\frac{(\epsilon+q)^2}{\epsilon^2+1} \qquad \text{(Eq. 5.4)}$$

with $\epsilon = (eV - E_0)/\Gamma$ and where:

$$L(V, E_i, \Gamma_i, A_i) = A_i \frac{\Gamma_i}{(V-E_i)^2 + (\Gamma_i)^2} \qquad \text{(Eq. 5.5)}$$

The first term in the functional form given in Eq. 5.3, $\mathrm{Fano}(V, E_0, \Gamma, q, A)$, is simply a function describing a Fano line shape where the parameters E_0, Γ, q, A are free fitting parameters corresponding to the position of the ZBP, half width at half maximum (HWHM) of the ZBP, line shape parameter, and amplitude of the ZBP, respectively. The second term in Eq. 5.3 is a sum of Lorentzian functions, $L(V, E_i, \Gamma_i, A_i)$, centred at energies E_i, with HWHM and amplitude, Γ_i and A_i, respectively. This term is used to fit the energy-symmetric, off-Fermi satellite peaks observed in the $\mathrm{d}I/\mathrm{d}V$ STS spectra (grey dashed lines in **Figure 5.7**b). In this case, E_i, Γ_i, and A_i are free fitting parameters. The last term, $\mathrm{c}(\mathrm{A}, V, E', \sigma)$, is a bias-dependent background term and is described towards the end of this subsection.

For the DCA anthracene extremities we considered the following functional form for $\rho_{\mathrm{fit}}(V, T)$:

$$\rho_{\mathrm{fit}}^{\mathrm{Lobe}}(V, T) = \sum_i L(V, E_i, \Gamma_i, A_i) + \mathrm{c}(\mathrm{A}, V, E', \sigma) \qquad \text{(Eq. 5.6)}$$

where the functional form is nearly identical to that of Eq. 5.3 for the Cu site except for the omission of the Fano function. In this case, the ZBP at the DCA anthracene extremity site was fitted with a Lorentzian function instead as the peak is sharp and very symmetric. In fact, initial attempts of fitting the ZBP with a Fano function yielded $q > 10^6$. In such a case using simply the Lorentzian function is well justified since the Fano function becomes a Lorentzian function in the limit of $q \to \infty$.

For the $\mathrm{d}I/\mathrm{d}V$ spectra acquired at the DCA molecular centres, we used the following function form for $\rho_{\mathrm{fit}}(V, T)$:

$$\rho_{\mathrm{fit}}^{\mathrm{Centre}}(V, T) = S(V, E_0, \Theta, A_0, A_0') + \sum_i L(V, E_i, \Gamma_i, A_i) + \mathrm{c}(\mathrm{A}, V, E', \sigma) \qquad \text{(Eq. 5.7)}$$

where:

$$S(V, E_0, \Theta, A_0, A_0') = A_0 \,\mathrm{erf}\left(\left(\frac{V-E_0}{\Theta}\right)+1\right) + A'_0 \,\mathrm{erf}\left(1-\left(\frac{V+E_0}{\Theta}\right)\right) \qquad \text{(Eq. 5.8)}$$

The first term in Eq. 5.7, $S(V, E_0, \Theta, A_0, A_0')$, is used to fit the observed symmetric steps about zero bias. Here E_0, Θ, A_0, and A_0' are free fitting parameters corresponding to the steps' location

in energy, a step broadening term, left step amplitude and right step amplitude, respectively (see Eq. 5.8). The second term in Eq. 5.7, the sum of Lorentzian functions, is used again to fit the energy-symmetric, off-Fermi satellite peaks observed in the $\mathrm{d}I/\mathrm{d}V$ STS spectra (grey dashed lines in **Figure 5.7**b).

For all functional forms of $\rho_{\mathrm{fit}}(V,T)$, the following functional form for the background was considered:

$$\mathrm{c}(\mathrm{A},V,E',\sigma) = A\exp\left(\frac{V-E'}{\sigma}\right) + \mathrm{constant} \qquad \text{(Eq. 5.9)}$$

Here, an exponential background, where A, E', and σ are free fitting parameters, was used to model the rise in the $\mathrm{d}I/\mathrm{d}V$ signal for $V_{\mathrm{b}} > 0.1$ V due to the broad feature between 0.15 and 0.5 V in the $\mathrm{d}I/\mathrm{d}V$ STS measurements at all high symmetry locations within the DCA_3Cu_2/Ag(111) kagome MOF (see **Figure 5.7**a). **Figure 5.9**b-d shows the fits for the data obtained at 4.4 K (black curves) as a result from this fitting procedure.

From this fitting procedure, we were able to extract the widths, Γ, of the ZBPs at the Cu sites and the DCA anthracene extremities, as a function of temperature. We discuss their temperature dependence, $\Gamma(T)$, in the next subsection. We further determined that the energy-symmetric, off-Fermi satellite peaks, observed at the Cu and DCA anthracene sites, are located at energies of ±43.5 and ±75.6 mV. At the DCA molecular centre, these peaks are located at ±17.3, ±43.5 and ±75.6 mV. Our fitting procedure also yielded additional subtler energy-symmetric peaks at the DCA molecular centre located at energies of ±56.3 mV and ±85.8 mV. We rule out the possibility that these subtler peaks are tip-related artefacts (see Appendix C.2). Finally, we also determined that the onset of the step-like feature (at the DCA centre) was found to be ±43.5 mV, coinciding with the ±43.5 mV satellite peak in the $\mathrm{d}I/\mathrm{d}V$ STS spectra (at the DCA molecular centre).

5.4.2 Temperature dependence for ZBPs in d*I*/d*V* STS data

Figure 5.10a shows the HWHM, Γ, as a function of temperature for the ZBP observed in the $\mathrm{d}I/\mathrm{d}V$ STS data at the Cu_A and DCA anthracene extremity sites. We find that the ZBP feature diminishes in magnitude and broaden with increasing temperature, beyond trivial thermal broadening (see Appendix C.6). For the Cu_A and anthracene extremity sites, we fit $\Gamma(T)$ with the expression:

$$\Gamma(T) = \sqrt{2(k_B T_K)^2 + (\pi k_B T)^2} \qquad \text{(Eq. 5.10)}$$

where k_B is the Boltzmann constant and T_K is a fitting parameter (see dashed lines in **Figure 5.10**a). From this, we obtained $T_{\mathrm{K}} = 125 \pm 7$ K and 139 ± 6 K for Cu_A and the DCA

anthracene extremity, respectively. Here, Eq. 5.10 describes the temperature dependence of Γ for the Fermi level resonance observed in the density of states (DOS) in the case of the Kondo effect [31, 85, 86], i.e., when a localised magnetic moment is screened by surrounding conduction electrons. T_K, known as the Kondo temperature, reflects coupling strength between the magnetic moment and the conduction electrons (see **Figures 5.10**b-c).

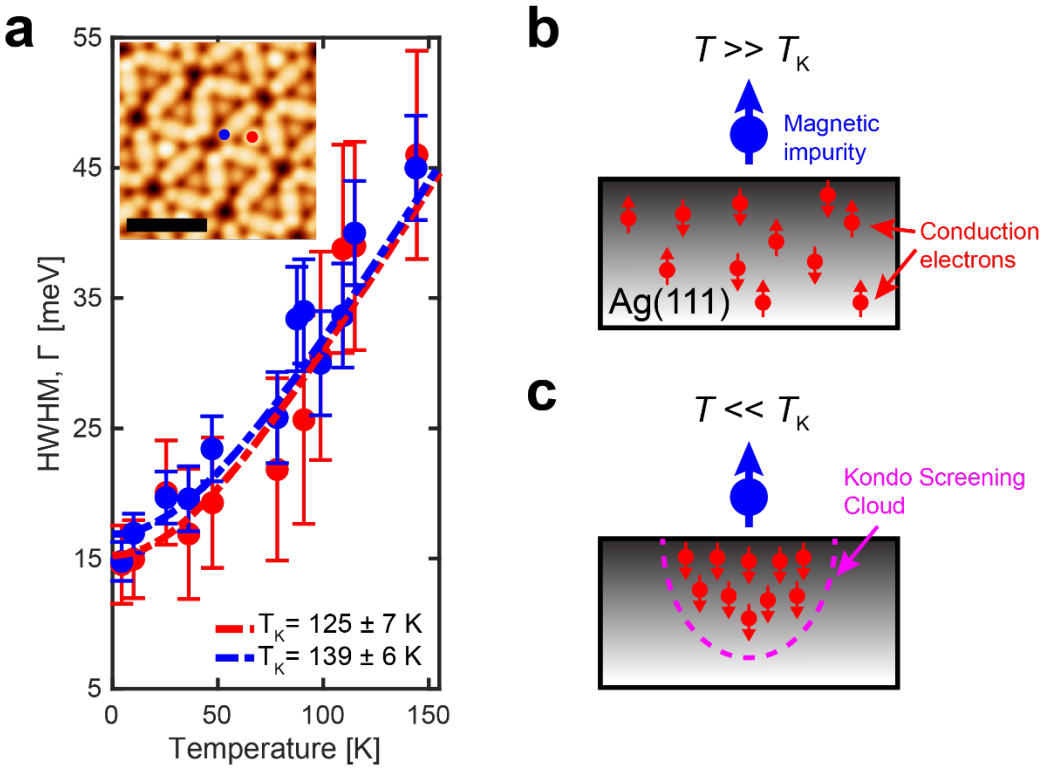

Figure 5.10: Temperature dependence of ZBP width: evidence of the Kondo effect. (a) Half-width at half maximum (HWHM), Γ, of the Cu_A (red) and DCA anthracene extremity (blue) ZBPs, as a function of temperature, T, extracted from fitting of dI/dV STS data in **Figure 5.9**, after removing thermal smearing due to dI/dV acquisition. Dashed curves: fitting of $\Gamma(T)$ with Eq. 5.10, resulting in T_K = 125 ± 7 K and 139 ± 6 K for Cu_A and anthracene extremity, respectively. Inset: Constant-current STM image of DCA_3Cu_2 MOF on Ag(111) (V_b = –250 mV, I_t = 1.5 nA), with locations corresponding to Cu_A (red) and anthracene extremity (blue) sites; scale bar: 2 nm. (b)-(c) Schematic of the Kondo effect on Ag(111). Above a critical temperature, T_K, known as the Kondo temperature, the system behaves nominally in that the spins of the conduction electrons (of the metal) and the spin of magnetic impurity (on the metal) are uncoupled as in (b). Below T_K, the spins of the conduction electrons couple to the spin of the magnetic impurity. In this case, the magnetic moment of the impurity is screened by the spins of the underlying conduction electrons as in (c).

Table 5.1 shows a summary of the obtained values for the fit parameters (at 4.4 K) and the obtained T_K. Here, we include a summary for data obtained at Cu_B site for a comparison. We note that the value for $|q|$ is greater for Cu_A than for Cu_B. $|q|$ represents the ratio of (electron) tunnelling rate from the tip directly into the Kondo impurity (a many-body state comprised of a coupled local magnetic moment and conduction electrons) to the tunnelling rate from the tip directly into the continuum states of the underlying metal substrate. The lower the

value of $|q|$, the greater the coupling between the Kondo impurity and the substrate and vice versa. This means that the Cu_A atoms are less coupled to the substrate than the Cu_B atoms which is consistent with our earlier remarks regarding the adsorption heights of Cu_A vs Cu_B atoms on Ag(111): larger adsorption heights mean less coupling with the substrate. This has been similarly observed in the case of NTCDA molecules on Ag(111) [294].

Location	Line Shape Parameter, q (at 4.4 K)	ZBP Positions (at 4.4 K)	Kondo Temperature, T_K
Cu_A	–3	0.9 meV	125 ± 7 K
Cu_B	–2	2.9 meV	162 ± 16 K
Anthracene extremity	∞	1.2 meV	139 ± 6 K

Table 5.1: ZBP fit results for dI/dV STS data for DCA_3Cu_2/Ag(111) kagome MOF. Obtained values for the fit parameters from the temperature-dependent differential conductance measurements at Cu_A, Cu_B and DCA anthracene extremity sites.

We note that the temperature dependence for the ZBP amplitude can be used to independently corroborate the obtained Kondo temperature (and therefore the Kondo effect) as well as to infer the spin state of the local magnetic moment, e.g., S = ½ vs S = 1 spin state [31]. In our measurements, however, establishing such a trend was not feasible as the ZBP amplitudes were sensitive to the tip location and condition and the tip-sample height. The ZBP widths, however, were insensitive to these conditions (see Appendix C.7). Given the agreement between our temperature-dependent $\mathrm{d}I/\mathrm{d}V$ STS data in **Figure 5.10** and Eq. 5.10, we therefore attribute our observed ZBP to Kondo screening of unpaired magnetic moments in the MOF by the Ag(111) conduction electrons. Our obtained values for T_K > 120 K, are similar to other π-conjugated molecule-on-metal systems [295]. We further rule out that the ZBP is due to an intrinsic electronic state of the system, given that, if that were the case, $\Gamma(T)$ would be constant. Tip-height-dependent $\mathrm{d}I/\mathrm{d}V$ STS measurements also ruled out possible tip-height-dependent effects on the ZBP such as charging effects seen in Chapter 3 (see Appendix C.5).

5.4.3 Temperature dependence for satellite peaks in dI/dV STS data

Our fitting procedure from subsection 5.4.1 allowed for the extraction of the HWHM for the satellite peaks observed near Fermi. At the DCA molecular centre, we could extract a HWHM of ~7 mV at 4.4 K for the satellite peaks at ~±17 mV, ~±43 mV, ~±56 mV, ±73 mV, and ~±86 mV. Extraction of the HWHM of the satellite peaks at ~±17 mV, ~±56 mV, and ~±86 mV was only possible up to ~40 K whereas the extraction of the HWHM of the satellite peaks at ~±43 mV and ±73 mV was possible up to ~80 K. The temperature dependence for the values of the HWHM for these satellite peaks could not be reliably established due to the large uncertainty in HWHM of these peaks, i.e., the value of the HWHM of these depends sensitively on the initial guesses for all the fitting parameters required for our fitting algorithm.

Similarly, we could extract the HWHM for the satellite peaks in the $\mathrm{d}I/\mathrm{d}V$ measurements at the Cu_A and DCA anthracene extremity sites. Unlike the case at the DCA molecular center, we could only reliably extract the HWHM for the satellite peaks at ~±43 mV and ±73 mV at 4.4 K. The HWHM values that we obtained for these peaks ~15 mV which is approximately twice the value we obtained at the DCA molecular center. This could be because our fitting procedure could not distinguish one broad peak (e.g., a peak at 43 mV) and two narrower peaks that are close in energy (e.g., the satellite peaks at 43 mV and 56 mV) leading to an extraction of a HWHM value not representative of the observed satellite peaks at ~±43 mV and ±73 mV in our data. These ambiguities, however, do not affect our extracted HWHM value for the ZBP in $\mathrm{d}I/\mathrm{d}V$ data.

5.4.4 DCA vibrational modes

In the following, I will focus on the energy-symmetric, off-Fermi features observed in the $\mathrm{d}I/\mathrm{d}V$ STS curves in **Figure 5.7** and **Figure 5.9**. DFT calculations were performed by Mr. Bernard Field to determine the vibrational modes for a single Cu_2DCA complex in the gas phase (see Appendix C.1.2 for details on DFT calculations). The DFT calculations yielded many vibrational modes with energies below 100 meV. Of these vibrational modes, only some have the right symmetry to be excited by tunnelling electrons during the tunnelling process. To determine which, the displacement of all the atoms in a negatively charged $[Cu_2DCA]^{-1}$ complex relative to the atoms' positions in a neutral Cu_2DCA complex were calculated (by Mr. Bernard Field): the vibrational modes were calculated as eigenvalues of a Hessian matrix, with the eigenvectors being the displacement vectors times the square root of the atomic masses for each atom. Here, the overlap is defined as being the dot product between these eigenvectors and the displacement vector from charging times the square root of the atomic masses, with a suitable normalization.

Figure 5.11 shows all the vibrational modes (with energies less than 100 meV) that have a non-zero overlap with the charging mode. These four modes, with energies 17.3, 43.1, 58.4 and 83.4 mV in **Figure 5.11**, line up well with the observed satellite peaks at ±17.3 mV, ±43.5 mV, ±56.3 mV, ±85.8 mV. We note, however, that this method does not explain the satellite peak observed at ±75.6 mV. The calculations described above were performed on a molecular complex in the gas-phase whereas the same molecular complex may undergo some conformational changes upon adsorption on Ag(111). This means there may be a non-zero overlap between the atoms' displacement vectors from charging when on Ag(111) and the atoms' displacement vectors from out-of-plane vibrational modes which were necessarily zero when considering the molecular complex in the gas phase. In this case, we note that DFT calculations do reveal an out-of-plane vibrational mode for a single a single Cu_2DCA complex in the gas phase at an energy of 72.4 meV, which is in close agreement with the observed

satellite peak in our dI/dV STS data at ±75.6 mV. We therefore conclude that the energy-symmetric, off-Fermi peaks are due to an inelastic excitation of the DCA (within the DCA_3Cu_2 kagome MOF) molecular vibrational modes.

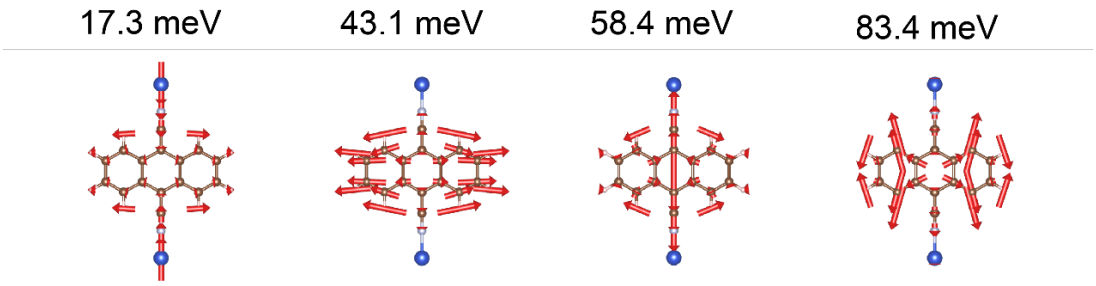

Figure 5.11: DFT-calculated vibrational modes of a single Cu_2DCA molecular complex in the gas phase. The length of the red arrows represents the magnitude and direction of the atoms' displacements. These vibrational modes have the right symmetry to be excited by a tunnelling electron and matches most of the experimentally observed peaks near Fermi in the dI/dV STS data at the DCA molecular center. These results are courtesy of Mr. Bernard Field.

Typically, these inelastically excited vibrational modes appear as symmetric steps near Fermi in the dI/dV STS data. However, coupling between local magnetic moments and molecular vibrations can lead to the appearance of a split Kondo resonance (peaks) precisely at the energies of these vibrational modes. This phenomenon is known as phonon-assisted Kondo tunnelling [31, 175]. The coexistence of peaks and steps located symmetrically about zero bias at ~±43 mV implies that the phonon-assisted Kondo tunnelling rates and inelastic phonon-excitation tunnelling rates for electrons at these energies are comparable.

Interestingly, the observed step at ~±43 mV should be observable in other DCA_3Cu_2 kagome systems such as DCA_3Cu_2 kagome system on Cu(111) [53] and on graphene/Ir(111) [69]. In both these systems, such features in near-Fermi were not observed. In the case of DCA_3Cu_2/Cu(111), we speculate the these steps could not be observed due to strong hybridisation between the kagome system and the Cu(111) substrate. This is, however, unlikely in the case of graphene/Ir(111), where the adsorbate-substrate interaction is arguably weaker than in the case of DCA_3Cu_2 on Ag(111). We speculate that the increased density of states at Fermi (i.e., the Kondo resonance) enhances the features due to inelastic tunnelling (i.e., steps) [296], i.e., there are more electrons available near Fermi that can tunnel inelastically and excite these vibrational modes. No such Kondo resonance was observed for DCA_3Cu_2 on graphene/Ir(111), possibly due to the small density of states near the substrate's Dirac point, in comparison the Ag(111) substrate. The reduced density of states near Fermi, from both the lack of the Kondo resonance and from being near the substrate's Dirac point, can arguably lead to

the suppression of any inelastic tunnelling features (i.e., steps) in the $\mathrm{d}I/\mathrm{d}V$ STS data for DCA_3Cu_2 on graphene/Ir(111) [compared to the case of DCA_3Cu_2/Ag(111)].

5.5 Origin of Local Magnetic Moments within DCA_3Cu_2/Ag(111)

5.5.1 DFT+U calculations for DCA_3Cu_2/Ag(111) kagome MOF

In the previous section, we showed that the ZBPs observed in the $\mathrm{d}I/\mathrm{d}V$ STS data for the DCA_3Cu_2 kagome system on Ag(111) is a manifestation of the Kondo effect. This requires that there be localised magnetic moments within the MOF (precisely where a ZBP is present). To rationalise the Ag(111)-supported MOF electronic structure and possible emergence of localised magnetic moments, I present here spin-polarised DFT calculations, courtesy of Mr. Bernard Field (see Appendix C.1.2 for details on theoretical methods).

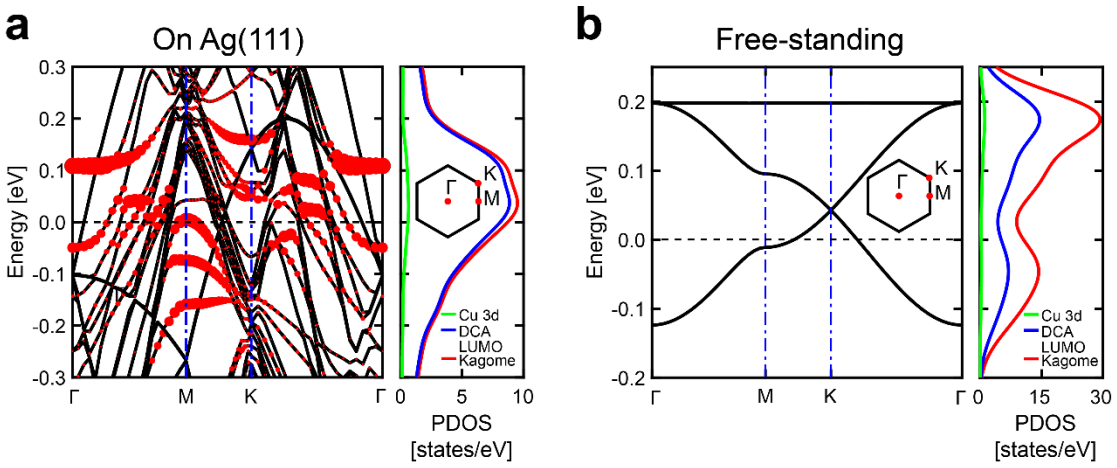

Figure 5.12: DFT-calculated band structures for DCA_3Cu_2 kagome on Ag(111) and free-standing. (a) DFT+U (U = 0 eV) calculated band structure for DCA_3Cu_2/Ag(111) (left) with a calculated charge transfer ~0.3e^- from MOF to Ag(111) and projected density of states (right). Red circles are projection onto the DCA_3Cu_2 orbitals. Partial PDOS curves labelled by inset legend. High-symmetry points (left x-axis) shown on Brillouin zone inset (right). The kagome bands have predominantly molecular (DCA LUMO) character with little Cu 3d contribution consistent with the partial hybridisation between the DCA LUMO and the Cu 3d orbitals (i.e., DCA-Cu metal-ligand coordination). (b) DFT+U (U = 0 eV) calculated band structure for free-standing DCA_3Cu_2 (left) with a charge depletion of 0.25 electrons per UC to match DCA_3Cu_2/Ag(111) charge transfer and projected density of states (right). Here, we see the Dirac and flat bands arising from the geometry of the structure. These calculations are courtesy of Mr. Bernard Field.

Figures 5.12a,b show the DFT-calculated band structure for the DCA_3Cu_2 MOF on Ag(111) and in the gas phase (i.e., free-standing), respectively, with the corrections for the on-site Coulomb interactions for d electrons excluded, i.e., with Hubbard U = 0 eV for Cu atoms within the MOF. For the DCA_3Cu_2 MOF on Ag(111), we find that there is significant distortion of the intrinsic flat and Dirac bands compared to the isolated (free-standing) DCA_3Cu_2 MOF. We further calculated for the DCA_3Cu_2/Ag(111) MOF, a transfer of ~0.33 electrons per primitive unit cell from the MOF to Ag(111) (see Appendix C.1.2 and C.9 for details on MOF-substrate charge transfer calculations), consistent with recent observations of the same MOF on

graphene [69]. Projection of the DCA_3Cu_2/Ag(111) states onto the DCA_3Cu_2 MOF orbitals (red circles; see **Figure 5.12**a) shows their significant contribution to the near-Fermi band structure. This is predominantly from the kagome-arranged DCA LUMOs with a slight contribution from the honeycomb Cu 3*d* character [63] (populated by electron transfer from Cu 4*s* states) as seen in the projected density of states (PDOS) plots in **Figure 5.12**a. The bandwidth of these states is ~300 meV, similar to the freestanding MOF [63] (see also **Figure 5.12**b). These calculations with $U = 0$ eV yield a local magnetic moment per DCA molecule of $\sqrt{\langle m^2 \rangle} \approx 0.027\ \mu_B$, per DCA molecule (see Appendix C.1.2 and C.10.1 for further details). This calculated magnitude for local magnetic moment per DCA molecule is negligible and do not explain the presence of magnetic moments in the DCA_3Cu_2/Ag(111) MOF system as evidenced by manifestation of the Kondo effect for this system.

Recent theoretical work has shown significant electron-electron Coulomb interactions on the order of ~3 eV in the DCA_3Cu_2 system, several times larger than the kagome bandwidth—even at fillings where the Fermi level is far below the flat band [64]. These strong electron-electron interactions are facilitated by description of the DCA_3Cu_2 (low-energy) kagome bands using a basis of highly localised Wannier orbitals (built primarily from the DCA molecule LUMO). Further, typically in 3D solids, the polarizability of surrounding charges helps screen Coulomb interactions between electrons. Here, the reduced dimensionality of the DCA_3Cu_2 system (2D vs 3D) reduces this effect since screening is now confined to the in-plane direction. The reduced screening means an enhanced Coulomb interaction between electrons within the DCA_3Cu_2 kagome MOF [64].

We therefore explored the effect of electron correlations within the DCA_3Cu_2/Ag(111) kagome by including a Hubbard *U* term, within the DFT formalism (courtesy of Mr. Bernard Field), to account for corrections to the electron-electron interactions for electrons in the Cu 3*d* states. Here, we use *U* as a means of introducing electron correlations in our system (see Appendix C.1.2 for further details on DFT+*U*). **Figure 5.13**a shows the calculated average local magnetic moment per DCA molecule as a function of *U* for the DCA_3Cu_2 MOF on Ag(111) (blue curve) and in the free-standing case (with a charge depletion of 0.25 electrons; red curve). The calculated average local magnetic moment per DCA molecule in DCA_3Cu_2/Ag(111) MOF was found to monotonically increase as a function of *U*, reaching $\sqrt{\langle m^2 \rangle} \approx 0.2\ \mu_B$ for $U = 5$ eV (blue curve), in a close agreement with calculations on free-standing DCA_3Cu_2 MOF (red curve). **Figure 5.13**b shows the DFT-calculated ground state spin density of DCA_3Cu_2 MOF on Ag(111) for the case $U = 3$ eV. Here, we see that the spatial distribution of these magnetic moments closely resembles that of the DCA LUMO (see Chapter 3), with some weight on the Cu atoms due to population of the LUMO by the Cu 4*s* electrons and hybridisation between the

respective LUMO and the Cu 3*d* orbitals (i.e., DCA-Cu metal-ligand coordination). We interpret this as interactions between MOF electrons resulting in the emergence of local magnetic moments, with some degree of inter-spin coupling (see opposite nearest neighbour spin in **Figure 5.13**b). **Figures 5.13**c,d show a simulated STM image (courtesy of Mr. Bernard Field; see Appendix C.1.4 for details on STM simulation) based on near-Fermi occupied states given by these DFT+*U* calculations and an experimental STM image of the DCA_3Cu_2/Ag(111) MOF, respectively. The close resemblance between these (simulated and experimental) STM images reinforces that the DFT+*U* (with $U > 0$) calculations capture the fundamental electronic properties of the Ag(111)-supported DCA_3Cu_2 kagome MOF.

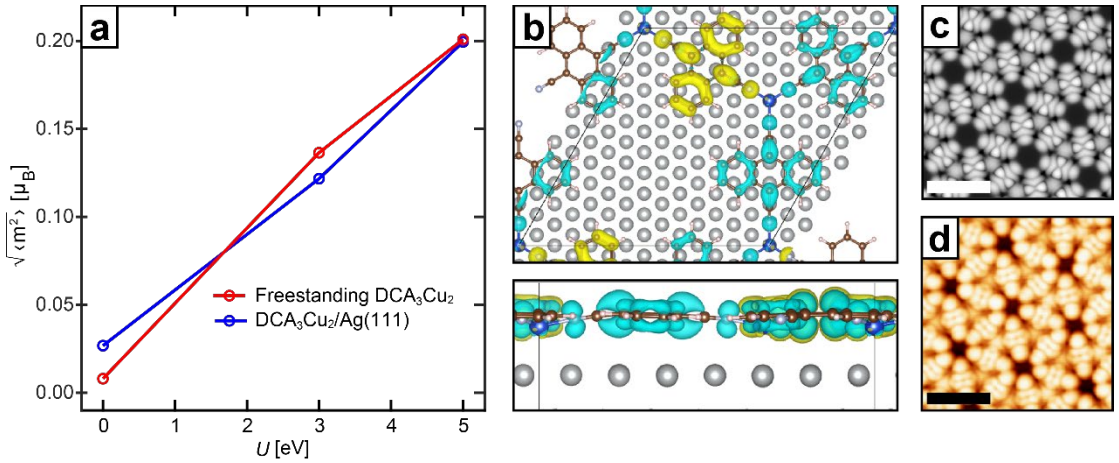

Figure 5.13: DFT+*U* calculated magnetic moment and spin density for DCA_3Cu_2/Ag(111) MOF. (a) Local magnetic moment per DCA molecule calculated via DFT+*U* for different values of *U*, in a single unit cell for the DCA_3Cu_2 kagome MOF on Ag(111) (blue) and free-standing DCA_3Cu_2 kagome MOF (with a charge depletion of 0.25 electrons; red). Here, we see the local magnetic moment per DCA grows monotonically with *U* and is near identical for the on-surface (blue) and free-standing (red) MOF case. (b) Ground state spin density of DCA_3Cu_2 on Ag(111) for the case of $U = 3$ eV. The top and side profile views are shown in the top and bottom panels, respectively (isosurface = 2×10^{-4} $\mu_B/Å^3$). Note magnetic moment orientations (yellow: up; blue: down) indicating frustrated antiferromagnetic coupling. (c) Simulated STM image of DCA_3Cu_2/Ag(111) ($U = 3$ eV; $V_b = -100$ mV; scale bar: 2 nm) near Fermi (see Appendix C.1.4 for details on STM simulation). (d) Experimental STM image of DCA_3Cu_2/Ag(111) taken with CO-functionalised tip ($V_b = -20$ mV, $I_t = 25$ pA; scale bar: 2nm). Theoretical results here are courtesy of Mr. Bernard Field.

Finally, we note that there is no evidence of the Kondo effect for the DCA_3Cu_2 kagome MOF on Cu(111) [53]. DFT+*U* calculations the MOF on Cu(111) (performed by Mr. Bernard Field) show ~0 μ_B per DCA molecule and a higher MOF-to-substrate charge transfer (compared to the MOF on Ag(111) for all $U \leq 5$ eV (see Appendix C.10.1 for DFT+*U* results on DCA_3Cu_2.Cu(111)). This absence of local magnetic moments is consistent with the experimentally non-existent Kondo effect for the MOF on Cu(111). Interestingly, for a similar electron filling as in DCA_3Cu_2/Cu(111) MOF, DFT+*U* calculations for the free-standing MOF show > 0.2 μ_B per DCA molecule. We argue that the strong MOF-substrate interactions such as hybridisation between the DCA_3Cu_2 MOF and the underlying Cu(111) states quenches the

emergence of local magnetic moments. This is consistent with the findings of Chapter 3 where we found weak DCA-Ag(111) interactions and with a general trend that Cu(111) substrate is more reactive than the Ag(111) substrate [264, 265].

5.5.2 Mean-field Hubbard model calculations for the DCA_3Cu_2 kagome MOF

To interpret and extend our DFT+U results, we further modelled the freestanding DCA_3Cu_2 kagome MOF with a mean-field Hubbard (MFH) model (courtesy of Mr. Bernard Field). Within this model, the Hamiltonian of the system consists of a nearest-neighbour tight-binding (TB) term (with a hopping rate, t, between adjacent kagome sites) and a Hubbard interaction term, U_{MFH}, accounting for an on-site Coulomb repulsion (see Appendix C.1.3 for details on MFH modelling). Here, the strength of electron-electron interactions in the 2D kagome model system is directly represented by the magnitude of U_{MFH}. By fitting the kagome band structure given by the non-interacting (U_{MFH} = 0) MFH tight-binding model with that given by DFT calculations (U = 0) for the freestanding DCA_3Cu_2, a hopping rate of $t \approx 53.5$ meV was determined (see Appendix C.10.2 for further details). To be consistent with the DFT+U DCA_3Cu_2 MOF on Ag(111), for the following we considered an electron filling of ~0.29 for the 2D kagome system within the MFH model.

We find that when $U_{\mathrm{MFH}} > \sim 6.5t \approx 350$ meV, MFH modelling shows the emergence of magnetic moments at the kagome sites. In particular, we find that the emerging kagome spin density in a single unit cell with $U_{\mathrm{MFH}} = 6.6t \approx 353$ meV and $U_{\mathrm{MFH}} = 6.9t \approx 370$ meV matches closely with the DFT+U-calculated DCA_3Cu_2/Ag(111) spin density for U = 3 and 5 eV, respectively (see Appendix C.10.2 for further details). Within the MFH model, we further considered a larger supercell for the kagome system. In this case, we find a qualitative agreement between the results of the single unit cell and larger supercell calculations (see Appendix C.10.2). However, with the larger supercell, we find a general enhancement in the local magnetic moment per DCA molecule as a function of U_{MFH}. This enhancement is because a single unit cell for the kagome system is very constrained in terms of what magnetic configuration can arise whereas a larger kagome supercell has a greater degree of freedom to express magnetic order/disorder. **Figure 5.14**a shows the local magnetic moment per DCA molecule as calculated by DFT+U (with U = 0, 3 and 5 eV; blue curve) for the DCA_3Cu_2 MOF on Ag(111) and MFH modelling for a kagome supercell (with $U_{\mathrm{MFH}} = 6.6t$ and $6.9t$; red curve). Here, MFH modelling for $U_{\mathrm{MFH}} = 6.6t$ and $6.9t$ (corresponding to U = 3 and 5 eV within the DFT+U framework) show a larger magnetic moment per DCA molecule compared to that calculated by DFT+U. For reference, the ground state spin density for the DCA_3Cu_2 kagome lattice as calculated by MFH modelling with $U_{\mathrm{MFH}} = 6.6t$ is shown in **Figure 5.14**b. MFH modelling further enabled us to determine the effect of lattice disorder on the magnetic

properties of the 2D kagome system. Our results (courtesy of Mr. Bernard Field) showed that the disorder of the lattice does not significantly affect the spin density within the kagome system (see Appendix C.11).

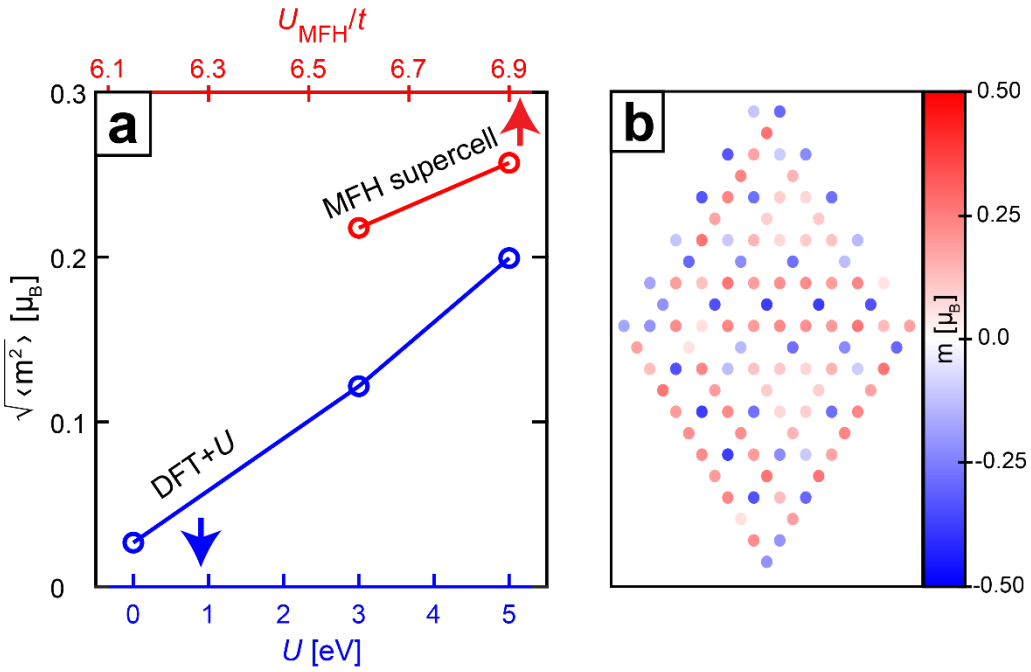

Figure 5.14: Local magnetic moment and spin density for DCA_3Cu_2 calculated via MFH modelling. (a) Local magnetic moment per DCA molecule calculated via DFT+U (blue) for different values of U, in a single unit cell for DCA_3Cu_2 MOF on Ag(111). Local magnetic moment per DCA as calculated by mean-field Hubbard (MFH) modelling (red) for a larger supercell, using values of $U_{MFH} = 6.6t$ and $6.9t$ (and electron filling of ~0.28) that matches closely with DFT+U results for $U = 3$ and 5 eV, respectively (see Appendix C.1 and C.10.2) (b) Ground state spin density for the 2D kagome lattice as calculated by MFH modelling with $U_{MFH} = 6.6t$ (electron filling ~0.28). Here, the calculated spin density closely matches the spin density calculated by DFT+U for DCA_3Cu_2/Ag(111) with $U = 3$ eV (see Appendix C.1 and C.10.2). Each dot corresponds to a single site in the kagome lattice, i.e., a single DCA molecule. Note that the calculated spin density in (b) gives a snapshot of the system at a particular time. These results are courtesy of Mr. Bernard Field.

Our experiments, evidenced by the existence and temperature-dependence of ZBPs in our dI/dV STS measurements (see sections 5.3 and 5.4), unequivocally show the manifestation of the Kondo effect in the DCA_3Cu_2/Ag(111) kagome MOF. The spatial distribution of the ZBP, following the spatial extent of the DCA LUMO (see **Figure 5.7**c), is consistent with the electronic structure of the DCA_3Cu_2 MOF (see **Figure 5.13**b), where the Cu 4*s* electrons populate the DCA LUMO upon coordination [63, 64]. This is a clear signature of the Cu-DCA metal-ligand bonding and that the ZBP spatial distribution is a direct reflection of the spatial distribution of the MOF valence band states. Therefore, the manifestation of the Kondo effect and the ZBP spatial distribution provide compelling evidence for the existence of localised magnetic moments within the DCA_3Cu_2 MOF and associated with the MOF valence band states (i.e., with predominantly DCA LUMO character, but also a small contribution of Cu 3*d* states).

Our DFT+U and MFH model calculations rationalises the emergence of these localised magnetic moments as a direct result of strong electron-electron interactions within the MOF, with energies at least on the order of the bandwidth of the MOF-related valence band ($U_{\mathrm{MFH}} > 6.5t \approx 350$ meV; bandwidth ≈ 300 meV). The enhanced electron-electron interactions even at energies well below the flat kagome band as in free-standing DCA_3Cu_2 where the Fermi level lies below the Dirac point (i.e., with an electron filling of ~0.29, similar to that of DCA_3Cu_2 on Ag(111); see **Figure 5.12**) is facilitated by: (i) the highly localised orbitals, built primarily from the DCA LUMO, describing the low-energy (i.e., near the Dirac point) DCA_3Cu_2 kagome bands; and (ii) the reduced Coulomb screening environment from surrounding electrons within the MOF due to the low-dimensionality of the system (2D vs 3D) [64]. We note that while our DFT+U and MFH model calculations above show local magnetic moments (e.g., ~0.2 μ_{B} per DCA with $U_{\mathrm{MFH}} = 6.6t$; **Figure 5.14**a) that are less than integral values typical for the Kondo effect (e.g., ~1 μ_{B} for a S = ½ system), Kondo screening has been demonstrated for fractional magnetic moments of similar magnitude, experimentally [297] and theoretically [298]. Therefore, we conclude that the strong electron-electron interactions within the DCA_3Cu_2 kagome MOF leads to the emergence of local magnetic moments within the MOF (see **Figures 5.15**a,b). On an Ag(111) substrate, these localised spins within the MOF interact with the conduction electrons of the underlying surface and end up, ultimately, being screened by them (below a critical temperature, T_{K}) as in the Kondo effect (see **Figure 5.15**c). This represents the first time that strong electron-electron interactions in a 2D metal-organic system with a kagome geometry, where these interactions significantly affect the electronic properties of the latter (e.g., the emergence of spin polarization), has been observed experimentally.

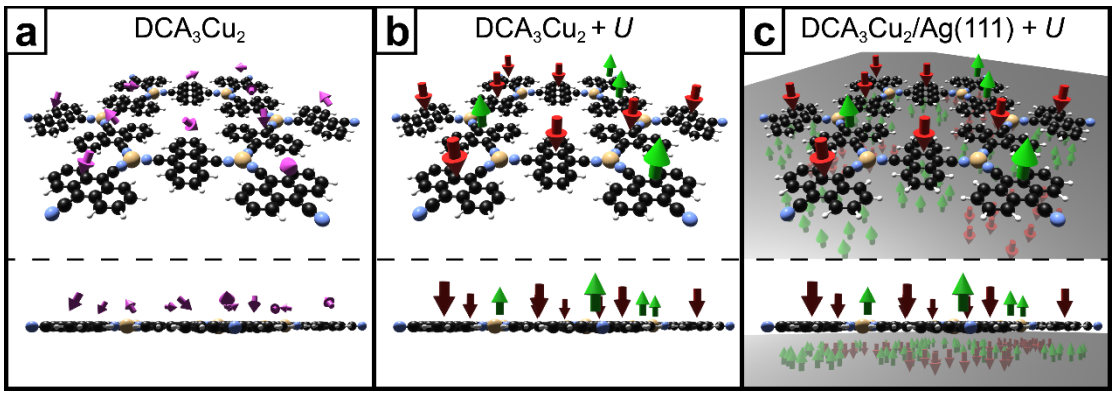

Figure 5.15: Schematic summarising the emergence of local magnetic moments as a result of electron-electron interactions and their subsequent Kondo screening in DCA_3Cu_2/Ag(111). (a) Free-standing DCA_3Cu_2 structure with no (weak) electron-electron interactions showing negligible spin behaviour (magenta arrows) at the kagome sites. (b) free-standing DCA_3Cu_2 structure with strong electron-electron interactions showing presence of ordered magnetic moments (red and green arrows) at the kagome sites. (c) Ag(111)-supported DCA_3Cu_2 kagome structure with the local magnetic moments at the kagome site screened by the Ag(111) conduction electrons, i.e., Kondo screening. The bottom panels in (a)-(c) show the corresponding side views for the DCA_3Cu_2 structure.

5.6 Estimation of Interaction Energies for DCA_3Cu_2/Ag(111) MOF

In this section, we present estimations for relevant interactions energies for DCA_3Cu_2/Ag(111) MOF: (i) the Kondo exchange interaction energy; and (ii) interspin exchange interaction energy.

5.6.1 Kondo exchange interaction energy

From our measurements of the Kondo effect (see subsection 5.4.2), we found T_K ~ 120 K. With this, we can estimate the Kondo exchange interaction energy, J_{K}, that gives a measure of the coupling between the local magnetic moments in our DCA_3Cu_2 kagome structure and the conduction electrons in the underlying Ag(111) substrate. Our DFT+*U* and MFH model results for the DCA_3Cu_2/Ag(111) MOF show a calculated local magnetic moment per DCA molecule (~ 0.25 μ_{B}) and charge per DCA (~0.6e^-) that places the DCA spin state closer to a S = ½ spin state (1 μ_{B}) than to a S =1 spin state (2 μ_{B}). Therefore, assuming a S = ½ spin state for the local magnetic moments within the DCA_3Cu_2/Ag(111) MOF, we can estimate J_{K} from the following relation [299]:

$$k_B T_K = D\sqrt{2\rho J_{\mathrm{K}}}\, e^{-1/\rho J_{\mathrm{K}}} \qquad \text{(Eq. 5.11)}$$

where ρ and D are the Ag(111) density of state and bandwidth, respectively. Taking D ~ 5.5 eV [84] and assuming $\rho = 2/D$ [300, 301], we obtain J_{K} ~ 250 meV. This is comparable to the value reported for a similar type of scanned probe measurement of the Kondo effect on a single atom impurity system [302].

5.6.2 Interspin exchange interaction energy

From the previous subsection, we can assume a S = ½ spin state for the local magnetic moments at the DCA sites within the DCA_3Cu_2/Ag(111) MOF. Naively, it is possible for these local magnetic moments to interact with each other via direct exchange interactions. For simplicity, we consider this interaction between the local magnetic moments at adjacent DCA sites, i.e., we consider the interactions between two S = ½ spins. This interaction leads to a formation of a singlet (S = 0) and a triplet (S = 1) state with an energy splitting between the two that we associate with J_{ex}. Previous works have shown that spin excitations (e.g., triplet-singlet transitions) for two coupled S = ½ states can be induced by tunnelling electrons [31, 176]. Signatures of these spin excitations show up as energy-symmetric and off-Fermi, step-like or peak features in $\mathrm{d}I/\mathrm{d}V$ STS curves (see subsection 2.3.2) at energies corresponding to their excitation energies (e.g., triplet-singlet splitting energy, J_{ex}) [31, 176]. Here, we estimate J_{ex} via our MFH modelling. We considered parameters of our MFH model corresponding to our DFT+*U* results on DCA_3Cu_2/Ag(111) with *U* = 3 and 5 eV (i.e., U_{MFH} = 6.6*t* and 6.9*t*, respectively and with an electron filling of 0.29). We then determined the energy difference

between the ground state configuration (with these parameters) and the next excited paramagnetic/non-magnetic configuration. Normalising this energy difference by the number of DCA molecules provides an estimate for J_{ex} (see Appendix C.12 for details). We find that for $U_{\mathrm{MFH}} = 6.6t$ (corresponding to DFT+U result with U = 3 eV), we obtain $J_{\mathrm{ex}} = -0.00825t$ = –0.44 meV. For $U_{\mathrm{MFH}} = 6.9t$ (corresponding to DFT+U result with U = 5 eV), we get $J_{\mathrm{ex}} = -0.01361t$ = –0.73 meV. Here, because our estimate for J_{ex} do not correspond to the energies of the step-like (at ~±43 mV) or peak features (~±17 mV, ~±43 mV, ~±56 mV, ±73 mV, and ~±86 mV) in our $\mathrm{d}I/\mathrm{d}V$ STS data for the DCA_3Cu_2/Ag(111) MOF (see sections 5.3 and 5.4), we further rule out the possibility that these features are an indication of spin excitations.

It is possible for two S = ½ spins to couple/interact via surrounding conduction electrons. In the case of DCA_3Cu_2/Ag(111), the local magnetic moments at two adjacent DCA sites can couple via the underlying Ag(111) conduction electrons. This substrate-mediated or indirect interspin interaction, known as Ruderman-Kittel-Kasuya-Yosida (RKKY) interaction [303], however, competes with Kondo screening of the local magnetic moments by the (same) underlying conduction electrons. Depending on the sign of the RKKY exchange interaction term, J_{RKKY}, and the distance between the local magnetic moments, RKKY interactions can result in the narrowing or broadening of the measured ZBP widths, Γ, associated with the Kondo effect [304]. RKKY interactions between localised magnetic moments can also lead to a complete quenching of the Kondo effect in the case where $|J_{\mathrm{RKKY}}| \gg \Gamma_{\mathrm{K}}$, with Γ_{K} being the measure of the coupling between the local magnetic moment and the underlying conduction electrons [305, 306]. Here, we make an estimation of the magnitude of RKKY spin-spin interactions within the 2D DCA_3Cu_2 kagome MOF mediated by the underlying Ag(111) substrate electrons. The RKKY exchange term oscillates with interspin distance, R [307]:

$$J_{RKKY}(R) = \frac{16J_{eff}^2 m_e k_F^4}{(2\pi)^3 \hbar^2}\left[\frac{cos(2k_F R)}{(2k_F R)^3} - \frac{sin(2k_F R)}{(2k_F R)^4}\right] \qquad \text{(Eq. 5.12)}$$

where k_F is the Ag Fermi wave vector and J_{eff} is a coefficient as developed from the Anderson impurity model [308]:

$$J_{eff} = -\frac{\Delta}{\pi N(\epsilon_0)}\frac{U}{|\epsilon_0|(U - |\epsilon_0|)} \qquad \text{(Eq. 5.13)}$$

Here, $N(\epsilon)$ is the Ag density of states, U the Hubbard energy, Δ the FWHM of the occupied impurity state, and ϵ_0 its energetic position below the Fermi level. Our STS measurements did not clearly identify a semi-occupied state below Fermi. We, however, took U to be ~1 eV (motivated by our DFT+U calculations as well as by previous studies [64]; a larger value of U yields a lower value of J_{eff}). We assumed ϵ_0 = 70 meV as a conservative estimation in line

with previous similar experimental works [175, 297], and $\Delta = 100$ meV based on measurements of the DCA LUMO on Ag(111) (see Appendix A.5). Here, we considered only the bulk Ag Fermi wavevector [84] and not the Ag(111) surface state Fermi wavevector. This is because our measurements showed that the Ag(111) surface state in our system is completed unpopulated due to confinement by the DCA-Cu kagome structure (see section 5.3). This means that the Ag bulk electrons are the only free conduction electrons that can mediate both the Kondo and RKKY interactions. Under these assumptions, the largest value we found for J_{RKKY}, with an interspin distance $R \sim 0.6$ nm (i.e., separation between DCA anthracene extremity sites), was ~9 meV. This is an order of magnitude smaller than the estimated Kondo exchange interaction energy, J_K (see above), and significantly smaller than the energy positions of the off-Fermi satellite peaks and step features observed in the near-Fermi dI/dV spectra at the DCA molecular centre (that we associate with molecular vibrational modes; see **Figure 5.7**b and see subsection 5.4.4). With this, we therefore conclude that RKKY interactions does not play a significant role in the physics of our system.

5.7 Summary

In this chapter, I demonstrated the on-surface synthesis of a 2D MOF consisting of DCA molecules coordinating with Cu atoms on Ag(111). The DCA molecules within this MOF are arranged according to a kagome structure. We found that the 2D DCA_3Cu_2 kagome MOF on Ag(111) to be partially disordered, i.e., structurally glassy, due to incommensurability with the underlying metallic substrate. This is consistent with the findings presented in previous chapters where the DCA molecule interacts weakly with the underlying Ag(111) surface.

STS measurements revealed a peak positioned at the Fermi level in our $\mathrm{d}I/\mathrm{d}V$ signal when acquired at the Cu and DCA anthracene extremity sites. The spatial distribution of the experimentally observed ZBP were found to follow the kagome-arranged DCA LUMOs and honeycomb Cu atoms, consistent with the partial population of the DCA LUMOs by the Cu 4*s* electrons upon metal-ligand coordination (between the DCA molecules and the Cu atoms), and slight overlap with the Cu 3*d* orbitals. Temperature-dependent STS measurements exclude the possibility that the ZBPs are indications of an intrinsic kagome state. Simultaneously, temperature-dependent STS measurements show conclusively that the ZBPs are a manifestation of the Kondo effect caused by screening of local magnetic moments within the 2D MOF by the underlying conduction electrons.

The observation of the Kondo effect in the DCA_3Cu_2/Ag(111) system provides compelling evidence of magnetic moments localised, therefore, at the kagome sites. Complementary density functional theory and mean-field Hubbard modelling calculations rationalise the emergence of these local magnetic moments as a direct result of enhanced

interactions between the kagome MOF electrons. The findings presented in this chapter represents the first observation of strongly correlated many-electron phenomena in an organic kagome system, an important step towards tuneable electron correlations in self-assembled 2D organic materials. Subsequently this enables the design and synthesis of functional 2D molecular devices with exotic electronic (e.g., Mott insulators [282, 309]) and magnetic (e.g., quantum spin liquids [310, 311]) phases that are driven by these strong electron-electron interactions. Furthermore, here, the intrinsic geometry (2D kagome structure) and material composition (organic molecules) provides a path toward strongly electrons correlations within 2D materials, beyond that of twisted 2D materials (where resulting flat bands and strong electron correlations are extremely sensitive to the twist angle [312]) and beyond that of heavy fermion materials (where strong Coulomb interactions arise because of highly localised f electrons [313]).

Chapter 6
Self-Assembled DCA Monolayers on hBN/Cu(111)

6.1 Overview

In the preceding chapters, we looked at 2D organic nanostructures on a metallic Ag(111) surface. Protocols of on-surface synthesis of organic nanostructures via self-assembly are well-established on metallic substrates. However, metallic substrates as supports for these organic nanostructures can introduce additional effects that must be taken into consideration. These effects can include hybridisation between molecular (adsorbate) and metallic (substrate) states [314, 315], significant charge-transfer between the molecule and the metal [316, 317], screening effects (e.g. metal-molecule screening as in Chapter 3 or Kondo screening in Chapter 5) or the formation of interface states at the molecule-metal interface (such as in Chapter 4). Insulating substrates may prove to be a viable alternative as a support for low-dimensional organic nanostructures. For insulating substrates, the above-mentioned effects can be largely mitigated due to the absence of electronic states within a few eVs of the Fermi level (i.e., a large band gap). Interestingly, the absence of screening by underlying conduction electrons can potentially lead to even stronger electron-electron interactions within the 2D DCA_3Cu_2 kagome MOF presented in Chapter 5. Furthermore, insulating substrates represent an important class of technologically relevant substrates where, for example, insulating substrates can prove to be useful as dielectrics in the implementation of gate-able devices, e.g., organic field-effect transistors [122, 318, 319]. Therefore, translating the synthesis protocols for 2D organic nanostructures onto these substrates represents an important step towards realising these organic nanostructures for next-generation electronics.

Although insulating substrates are useful supports, protocols of self-assembly of organic nanostructures, in particular, of metal-organic frameworks, on these substrates are limited [55, 89–95] and warrants further research. In this chapter, I present results on self-assembled molecular submonolayers comprised of DCA molecules on an ultrathin layer of insulating hBN grown on Cu(111). The ultrathin monolayer of hBN still allows for the conduction of tunnelling electrons between the STM tip and the underlying Cu(111) metallic substrate, thus enabling characterisation of organic nanostructures on hBN/Cu(111) via STM and STS (while retaining near-zero density of states within a few eV of the Fermi level; see

subsection 2.1.3 for further details). The results presented in Chapter 3 allow for a direct comparison between the electronic properties of DCA molecules on a metallic substrate with those on an insulating substrate, as discussed in this chapter. In particular, hBN on Cu(111) is known to have a spatially-modulated surface work function [130]. In this chapter, I look at its effect on the electronic properties of the DCA molecules. All experimental measurements presented in this chapter were performed at 4.4 K unless otherwise stated.

6.2 STM Characterisation of DCA/hBN/Cu(111)

Figure 6.1a shows a constant-current STM image of a hBN/Cu(111) surface after a deposition of DCA molecules, by thermal evaporation, onto the substrate held at room temperature. Here, the surface coverage of DCA molecules is ~50% of the ultrathin hBN layer on Cu(111) [see subsection 2.1.5 for sample preparation details and subsection 2.1.4 for details on hBN growth on Cu(111)]. **Figure 6.1**b shows a constant-current STM image, taken at V_b = 4.0 V, of a bare hBN/Cu(111) surface for this preparation. At this bias, we observe the emergence of the well-known Moiré superstructure (with periodicity characterised by vectors $\mathbf{h_1}$ and $\mathbf{h_2}$ in **Figure 6.1**b) for the hBN/Cu(111) surface [130]. **Figure 6.1**b inset shows an atomically resolved image of the bare hBN/Cu(111) surface. Here, the periodicity of the Moiré superstructure ($\|\mathbf{h_1}\| = \|\mathbf{h_2}\| \approx 9.87$ nm; $\measuredangle(\mathbf{h_1}, \mathbf{h_2}) \approx 60°$) is significantly larger than the periodicity of the hBN 2D lattice structure (hBN lattice constant = 2.488 ± 0.016 Å [124, 125]), with the former resulting from a lattice mismatch between the 2D hBN structure and the underlying Cu(111) substrate [87] (see subsection 2.1.3).

Figure 6.1c shows a constant-current STM image, taken at V_b = 0.7 V, of a DCA-covered hBN/Cu(111) surface (corresponding to black dashed square in **Figure 6.1**a). Here, we find that the DCA molecules form extended self-assembled 2D domains on hBN/Cu(111). We note that the extent of these DCA domains is limited by the amount of DCA molecules deposited on the hBN surface and limited in size by the hBN domain sizes on Cu(111). The size of the features in STM imaging suggests that the DCA molecules, like on Ag(111) (see previous chapters), on other metallic surfaces [53, 73], and on graphene [52], adopt a planar adsorption configuration on hBN/Cu(111) (see **Figure 6.1**c inset). This is corroborated by our measurements that show that these DCA molecules form a 2D monoclinic lattice with unit cell vectors $\mathbf{a_1}$ and $\mathbf{a_2}$ (see inset of **Figure 6.1**c; $\|\mathbf{a_1}\|$ = 1.19 ± 0.03 nm; $\|\mathbf{a_2}\|$ = 0.98 ± 0.02 nm; $\measuredangle(\mathbf{a_1}, \mathbf{a_2})$ = 54 ± 2°). This is very similar to the case of DCA molecules adsorbed on Ag(111) where the DCA interactions with the substrate were found to be weak (see Chapter 3). Furthermore, we note that for some preparations, we can obtain bare patches of the underlying Cu(111) surface (due to an incomplete full monolayer hBN growth). For these preparations, the DCA molecules, when deposited onto the substrate held at room temperature, preferentially

diffuse and adsorb onto these bare patches of the Cu(111) surface. This is consistent with the notion that the DCA molecules is weakly interacting with the hBN surface (compared with Cu(111) surface).

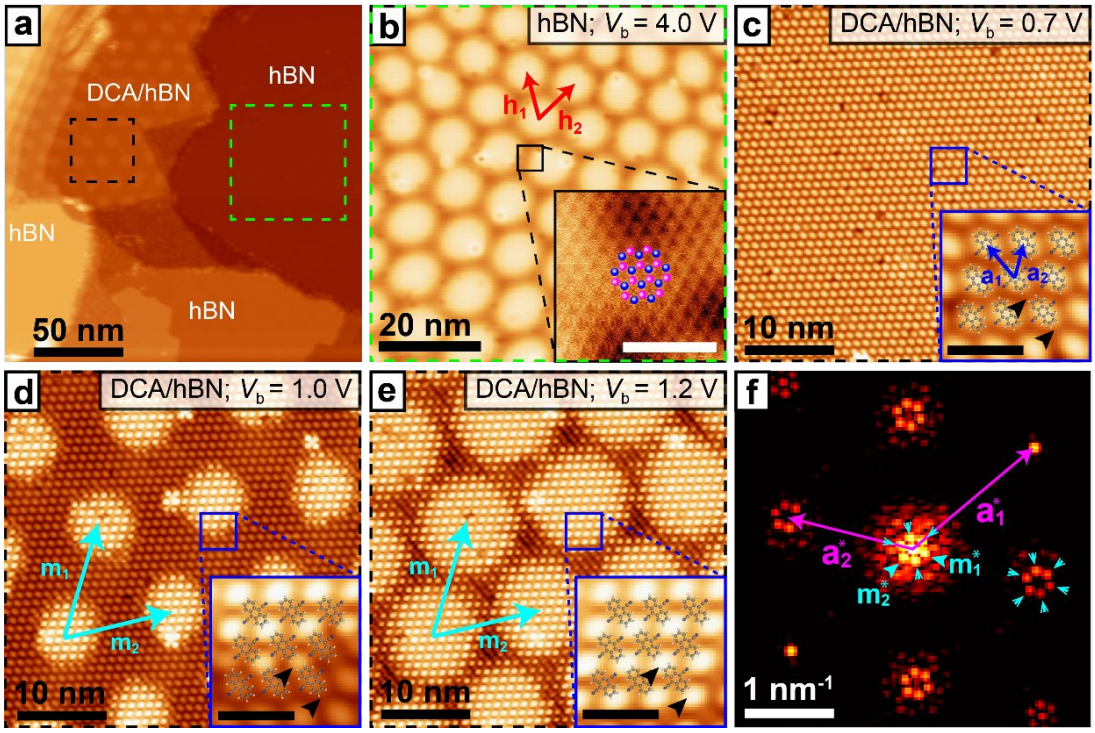

Figure 6.1: STM overview of a self-assembled molecular submonolayer comprised of hydrogen-bonded dicyanoanthracene (DCA) molecules on hBN/Cu(111). (a) Constant-current STM imaging of hBN/Cu(111) surface after a deposition of DCA molecules (V_b = 1.0 V, I_t = 50 pA). Here we find a DCA coverage of ~50% of the hBN/Cu(111) surface. The hBN surface areas that are covered with DCA molecules are annotated as DCA/hBN (b) Constant-current STM image of a bare hBN/Cu(111) surface (green dashed square in (a); V_b = 4.0 V, I_t = 0.1 nA). The Moiré superstructure periodicity for the hBN/Cu(111) domain here is characterised by the vectors $\{\mathbf{h_1}, \mathbf{h_2}\}$with $\|\mathbf{h_1}\| = \|\mathbf{h_2}\| = 9.87 \pm 0.05$ nm; $\measuredangle(\mathbf{h_1}, \mathbf{h_2}) = 60 \pm 2°$. Inset shows an atomically resolved STM image of the bare hBN/Cu(111) surface. Blue and magenta atoms superimposed gives the position of the nitrogen and boron atoms, respectively. Scale bar: 1 nm. (c)–(e) Constant-current STM imaging of a DCA submonolayer on hBN/Cu(111) at V_b = 0.7, 1.0, and 1.2 V (I_t = 50 pA), respectively. These correspond to the area indicated by the black dashed square in (a). The molecular domain forms a periodic structure with vectors $\{\mathbf{a_1}, \mathbf{a_2}\}$ (inset of (c)) with $\|\mathbf{a_1}\| = \|\mathbf{a_2}\| = 1.19 \pm 0.02$ nm; $\measuredangle(\mathbf{a_1}, \mathbf{a_2}) = 54 \pm 2°$. At V_b = 0.7 V, the molecular domain appears homogeneous; each bright ellipse is a DCA molecule (DCA chemical structure in inset). As V_b increases, a bright feature appears at the DCA anthracene extremities (black arrows in (d)-(e) insets) which is associated with the lowest unoccupied molecular orbital (LUMO) of the DCA molecules. Collectively, the appearance of these LUMO features form a Moiré pattern in real space with lattice vectors $\mathbf{m_1}$, $\mathbf{m_2}$ in (d)-(e) with $\|\mathbf{m_1}\| = \|\mathbf{m_2}\| = 13.0 \pm 0.7$ nm; $\measuredangle(\mathbf{m_1}, \mathbf{m_2}) = 62 \pm 2°$. Inset scale bars: 2 nm. (f) Fourier transform (FT) of STM image in (d). Here, the vectors $\{\mathbf{a_1^*}, \mathbf{a_2^*}\}$ correspond to the real-space vectors $\{\mathbf{a_1}, \mathbf{a_2}\}$ in (c). About each FT peak associated with the DCA/hBN molecular periodicity, we observe a set of six symmetrically placed FT peaks (cyan arrows). These peaks, characterised by $\{\mathbf{m_1^*}, \mathbf{m_2^*}\}$, correspond to the real-space vectors $\{\mathbf{m_1}, \mathbf{m_2}\}$ in (d)-(e). The STM image in (b) and corresponding inset were provided courtesy of Mr. Benjamin Lowe.

Figures 6.1d,e show STM images of the same molecular domain in **Figure 6.1**c but at higher biases, i.e., with biases V_b = 1.0 V and V_b = 1.2 V, respectively. With V_b = 0.7 V, the

DCA molecules appear homogenous (see **Figure 6.1**c). At higher biases (e.g., V_b = 1.0 V), STM imaging of the same molecular domain shows a change in the appearances of some of the molecules (see **Figure 6.1**d) with an emergence of a bright feature at the DCA anthracene extremities as seen in the inset of **Figure 6.1**d (black arrows). We associate this feature with the LUMO of the DCA molecules as seen in previous chapters of this dissertation and in other similar systems [52, 320]. At even higher biases, these LUMO features appear for more DCA molecules (see insets of **Figures 6.1**d,e; black arrows). Collectively, these LUMO features emerge as a Moiré superstructure whose periodicity is characterised by lattice vectors $\mathbf{m_1}$, $\mathbf{m_2}$ ($\|\mathbf{m_1}\| = \|\mathbf{m_2}\| = 13.0 \pm 0.7$ nm; $\measuredangle(\mathbf{m_1}, \mathbf{m_2}) = 62 \pm 2°$; see **Figures 6.1**d,e). **Figure 6.1**f shows the Fourier transform (FT) of the STM image in **Figure 6.1**d. Here, the FT peaks associated with the Moiré superstructure (in **Figure 6.1**d) appear as a set of six symmetrically located peaks (cyan arrows) about the FT peaks associated with the DCA structure (i.e., $\{\mathbf{a_1^*}, \mathbf{a_2^*}\}$ in **Figure 6.1**f). That is, the vectors $\{\mathbf{m_1^*}, \mathbf{m_2^*}\}$ in **Figure 6.1**f corresponds to the real-space lattice vectors $\{\mathbf{m_1}, \mathbf{m_2}\}$ in **Figures 6.1**d,e.

The Moiré superstructure (in **Figures 6.1**d,e) observed for the DCA/hBN system is reminiscent of the well-known Moiré pattern of the bare hBN/Cu(111) surface as seen in **Figure 6.1**b. We further note that different DCA/hBN domains show Moiré superstructures with different periodicities (see Appendix D.1). Like DCA/hBN, different Moiré patterns have been observed for hBN/Cu(111). This is due to different hBN domains which have different crystalline axes' orientations with respect to those of the underlying Cu(111) monocrystal (see subsection 2.1.3). These similarities between the Moiré patterns of the hBN/Cu(111) surface and those of the DCA/hBN structure implies a relation between the two.

To test this, we performed STM imaging at the DCA film boundary as seen in **Figure 6.2**. The STM image was taken with a bias of 1.1 V over the DCA film (bottom half of **Figure 6.2**) where the Moiré pattern of the DCA film is visible and with a bias of 4.0 V over the hBN surface (top half of **Figure 6.2**) where the Moiré pattern of the hBN/Cu(111) surface is visible. From the STM image in **Figure 6.2**, we clearly observe that the Moiré pattern of the overlying DCA film layer follows the Moiré pattern of the underlying hBN/Cu(111) substrate (see dashed blue ellipses in **Figure 6.2**), i.e., the DCA Moiré superstructure has a one-to-one correspondence with the underlying hBN/Cu(111) Moiré superstructure. The Moiré pattern of the hBN/Cu(111) surface in STM imaging is a direct result of the modulation in the surface work function of the hBN/Cu(111) substrate (this in return is due to the lattice mismatch between the hBN structure and Cu(111) surface) [130]. It stands to reason that the Moiré superstructure of the DCA film is a direct result of the modulation of the DCA molecules electronic properties by the underlying hBN/Cu(111) surface work function. We explore this hypothesis in the following sections.

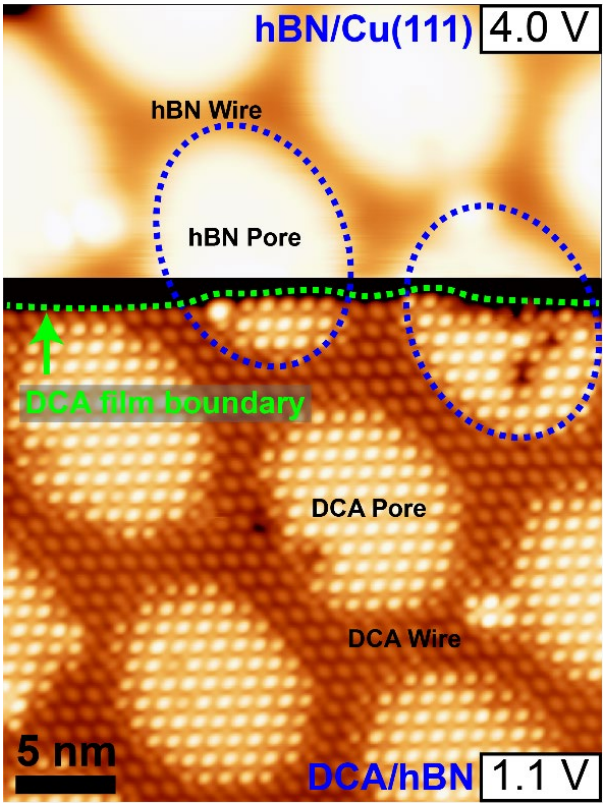

Figure 6.2: STM imaging at DCA/hBN film boundary. Constant-current STM imaging at a DCA film boundary (dashed green curve) with tunnelling set point of V_b = 1.1 V, I_t = 50 pA over the DCA film (bottom half of the image) and with tunnelling set point of V_b = 4.0 V, I_t = 50 pA over the hBN surface (top half of the image). The DCA film Moiré superstructure follows the Moiré superstructure of the underlying hBN/Cu(111) substrate (dashed blue ellipses).

6.3 STS Characterisation of DCA/hBN/Cu(111)

To gain insight into the electronic properties of the system, we performed STS measurements on the DCA molecules within the self-assembled DCA submonolayers on hBN/Cu(111). Here we considered two extreme locations: the DCA pore regions and the regions between the DCA pores, i.e., the DCA wire regions (see **Figure 6.2** for location reference). **Figure 6.3**a shows constant-current $\mathrm{d}I/\mathrm{d}V$ STS measurements (set point: V_b = –0.5 V, I_t = 5 pA) performed on DCA molecules at these two particular locations within the self-assembled DCA monolayer: at the centre of the DCA pore and at the DCA wire region (red and blue crosses, respectively; see STM image in **Figure 6.3**a inset). At the centre of the DCA pore, the STS spectra (red) shows a curve with a prominent peak-like feature at ~0.88 V (magenta tick) with subtle satellite peaks at ~1.05 V (green tick) and ~ 1.23 V (cyan tick). At the DCA wire region, the STS spectra at the DCA molecule (blue) shows a curve that is qualitatively similar in shape to the curve at the DCA pore region but with all peak-like features (magenta, green, and cyan ticks) shifted up in energy by ~0.33 V. Note that the negative differential conductance observed for V_b > 1.5 V is a typical signature in $\mathrm{d}I/\mathrm{d}V$ STS measurements for systems with a localised state weakly coupled to an underlying substrate [89, 321, 322].

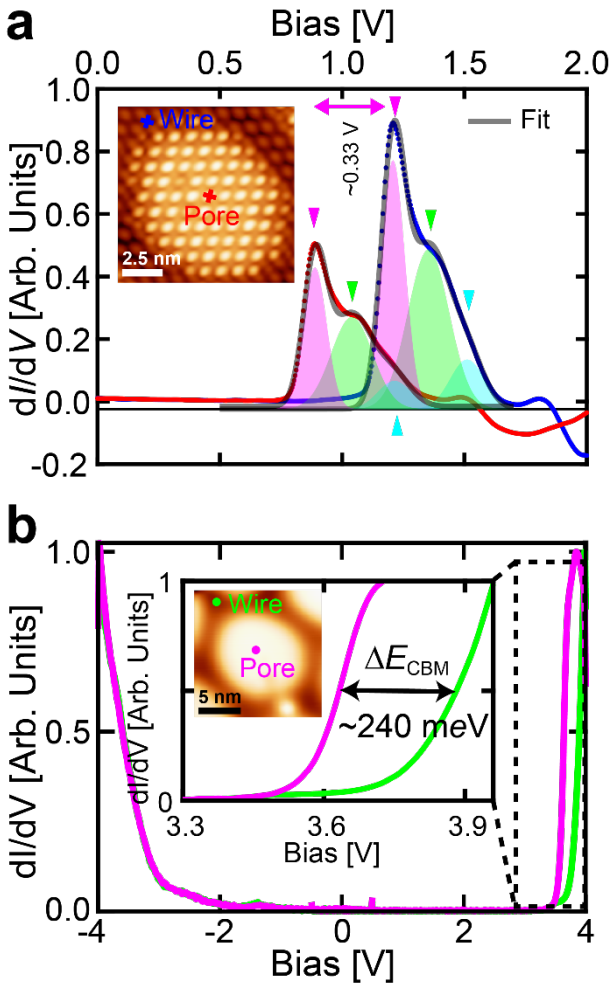

Figure 6.3: dI/dV STS measurements on DCA/hBN/Cu(111) and on hBN/Cu(111). (a) Constant-current dI/dV STS measurements (set point: V_b = –0.5 V, I_t = 5 pA) on a DCA molecule at the centre of the DCA pore region (red curve) and on a DCA molecule at the DCA wire region (blue curve; locations are at red and blue crosses, respectively, in STM inset; STM set point: V_b = 1.1 V, I_t = 50 pA). Both spectra were fitted with a sum of three Lorentzian functions that are spaced apart in energy. The resulting fit (black transparent curves) and the resulting Lorentzian peaks that were used to fit the data (magenta-, green-, and cyan-filled Lorentzian peaks) are shown. The prominent peaks (magenta ticks) correspond to the LUMO peak of the DCA molecules, while the satellite peaks (green and cyan ticks) correspond to DCA vibronic peaks. Qualitatively, both spectra are similar in shape but with the spectra at the DCA wire region upshifted in energy (from Fermi) by ~330 mV compared to the spectra at the DCA pore region. (b) Constant-current dI/dV STS measurements (set point: V_b = 4.0 V, I_t = 200 pA) on the hBN/Cu(111) surface at the pore region (magenta curve) and at the wire region (green curve; locations are indicated in STM inset; STM set point: V_b = 4.0 V, I_t = 50 pA). The conduction band minimum energies, E_{CBM}, at both locations are different with a difference, $\Delta E_{CBM} \approx 240$ mV with the E_{CBM} at the pore region higher up in energy. E_{CBM} was estimated as the energy at which the dI/dV STS signal (performed on the hBN surface) is half of its maximum value, after normalising the dI/dV curves with respect to the dI/dV value at the tunnelling set point.

Fitting each of these STS spectra curves with three Lorentzian functions yields good agreement between the data and the fitted curve (black transparent curve in **Figure 6.3**a). Here, the three Lorentzian peaks that are used to fit each dI/dV STS spectrum are shown in **Figure 6.3**a. For each spectrum, the first Lorentzian peak (magenta-filled Lorentzian curve)

corresponds to the LUMO peak for the DCA molecules. Interestingly, the DCA LUMO energies on hBN/Cu(111), at both the DCA pore (~0.88 V) and wire (~1.2 V) region, is higher than the LUMO energies for DCA molecules on Ag(111) (V_{LUMO} ~ 0.3 V). This is despite the work function of Ag(111) (~4.7 eV) being significantly higher than that of hBN (~4 eV). The discrepancy between these energies highlights the contribution of metal-molecule screening that drives the LUMO energy towards Fermi in the case of DCA on Ag(111) (see Chapter 3), where, classically, i.e., using Eq. 3.10, screening energies > 1 eV are possible. Furthermore, in comparison to DCA/Ag(111), we note the absence of charging for DCA molecules on hBN (for the range of bias voltages considered: $|V_{\mathrm{b}}| < 3$V). Despite the weak DCA-hBN interaction, the absence in charging of the DCA molecules on hBN/Cu(111) is most likely due to the high LUMO energy of the DCA/hBN molecules (compared to that of DCA/Ag(111) molecules). Since the gating field strength is proportional to the LUMO energy [56, 236] (see section 3.5), the gating field strength required to charge the DCA molecules on hBN is 3.5 times(≈ 0.88 mV/0.3 mV, i.e., DCA/hBN LUMO divided by DCA/Ag(111) LUMO) larger than that required to charge the DCA molecules on Ag(111). Counterintuitively, charging of the DCA molecules on a metallic Ag(111) substrate is made easier (compared to on an insulating hBN) because, in addition to the limited DCA-Ag(111) interactions, metal-molecule screening drives the LUMO energy of the DCA molecules closer to the Fermi level.

For the two following Lorentzian peaks in **Figure 6.3**a (green- and cyan-filled Lorentzian curves), we attribute these to vibronic satellite peaks for the DCA molecules. As pointed out in subsection 2.3.2, these vibronic peaks are typical when probing electronic states of molecules on decoupling substrates with STS [89, 323]. On decoupling substrates such as on a hBN, the electron lifetimes in a transient negatively charged molecular state (for molecules on these surfaces) are long enough that they can couple to and excite vibrational modes for these charged molecules. These on-resonant excitations appear as additional peaks next to a peak associated with a molecular state in $\mathrm{d}I/\mathrm{d}V$ STS spectra. Another feature of these vibronic peaks is that they are equally spaced in energy. In **Figure 6.3**a, the peaks are equally spaced by ~0.18 V, for both the DCA molecules at the DCA pore and wire regions, corroborating their association with the vibronic peaks.

The differences in the LUMO energies, V_{LUMO}, for the two DCA molecules in **Figure 6.3**a (~0.33 V) explains the spatial-dependent appearance of the LUMO features for the different DCA molecules. That is, the molecules within the DCA pore regions have a lower V_{LUMO} than the molecules within the DCA wire regions: $V_{\mathrm{LUMO}}^{\mathrm{pore}} < V_{\mathrm{LUMO}}^{\mathrm{wire}}$. Therefore, at a tunnelling bias, V_{b}, such that $V_{\mathrm{LUMO}}^{\mathrm{pore}} < V_{\mathrm{b}} < V_{\mathrm{LUMO}}^{\mathrm{wire}}$, the LUMO features at the anthracene extremities would appear in STM imaging for the DCA molecules within the DCA pore region

but not for the DCA wire region. This results in the observed DCA/hBN Moiré superstructure (characterised by the vectors $\{\mathbf{m_1}, \mathbf{m_2}\}$) in **Figure 6.1**.

Correspondingly, we have performed $\mathrm{d}I/\mathrm{d}V$ STS measurements (set point: V_b = 4.0 V, I_t = 200 pA) on the hBN/Cu(111) surface, just outside the DCA film (i.e., for the same hBN domain for which the DCA molecules in **Figure 6.3**a are adsorbed on). Like for the DCA film, here, we considered measurements on two extreme locations on the hBN/Cu(111) surface: (i) the hBN pore region and (ii) the hBN wire region (see STM image in **Figure 6.3**b inset). **Figure 6.3**b shows the $\mathrm{d}I/\mathrm{d}V$ STS spectra on hBN/Cu(111) surface at these two locations. For both spectra, we see a sharp increase in the $\mathrm{d}I/\mathrm{d}V$ signal in the negative bias regime at ~ –3 V and in the positive bias regime, V_b > 3.5 V. For biases, –3 V < V_b < 3.5 V, the $\mathrm{d}I/\mathrm{d}V$ signal is close to zero, reflecting the insulating nature of the ultrathin hBN layer. The sharp onset in the negative bias regime corresponds to the valence band maximum (VBM) of the hBN layer while the sharp onset in the positive bias regime corresponds to the conduction band minimum (CBM) of the hBN layer. While the $\mathrm{d}I/\mathrm{d}V$ spectra at both locations on the hBN surface are identical for negative biases, V_b < 0 V (VBM is the same for both), they are different in the positive bias regime, V_b > 0 V. That is, at both locations, the CBM energy, E_CBM, is different. Here, the E_CBM at the hBN pore region (magenta curve) is ~3.6 V while at the hBN wire region (green curve), E_CBM ~ 3.9 V (see STS inset of **Figure 6.3**b). Estimating the E_CBM for both curves as the energy at which the $\mathrm{d}I/\mathrm{d}V$ signal is half of its maximum value (after normalising the $\mathrm{d}I/\mathrm{d}V$ curves with respect to the $\mathrm{d}I/\mathrm{d}V$ at the tunnelling setpoint) gives a difference in the E_CBM for both curves, ΔE_CBM ~ 0.24 V. Here, we note that the difference between the CBM energies for the hBN surface in the hBN pore and wire regions (ΔE_CBM ~ 0.24 V) is similar to the difference between the LUMO energies for the DCA molecules in DCA pore and wire regions (ΔE_CBM ~ 0.33 V).

6.4 Modulation of DCA LUMO by hBN/Cu(111) Work Function

In the previous section we saw that the LUMO energies of the DCA molecules are indeed spatially dependent with a lower V_LUMO in the DCA pore region than in the DCA wire region. Similarly, we saw that the E_CBM is smaller in the hBN pore region than in the hBN wire region. The differences in E_CBM for these two regions is similar to the differences in the LUMO energies between the DCA molecules in the DCA pore and wire regions. To see the relationship between E_CBM of the underlying hBN/Cu(111) substrate and the V_LUMO of the DCA molecules within the DCA submonolayer, we performed $\mathrm{d}I/\mathrm{d}V$ STS measurements for the DCA molecules along a DCA pore region and $\mathrm{d}I/\mathrm{d}V$ STS measurements on the hBN/Cu(111) surface (just beyond the DCA film) along a hBN pore region as seen in **Figure 6.4**a. For each $\mathrm{d}I/\mathrm{d}V$ STS spectrum obtained at the DCA molecules along the DCA pore region, we extracted

the LUMO energy, V_{LUMO} by means of curve fitting as in **Figure 6.3**a. The extracted V_{LUMO} as function of distance, x, along the DCA pore region is plotted in **Figure 6.4**a (blue data points). From **Figure 6.4**a, we find that, as we move from the DCA wire region to the DCA pore region, V_{LUMO} decreases gradually from an absolute maximum of ~1.2 V to reaching an absolute minimum of ~0.87 V at the centre of the DCA pore region. This gives a modulation amplitude in V_{LUMO} of the DCA molecules of ~0.33 V across the DCA pore region.

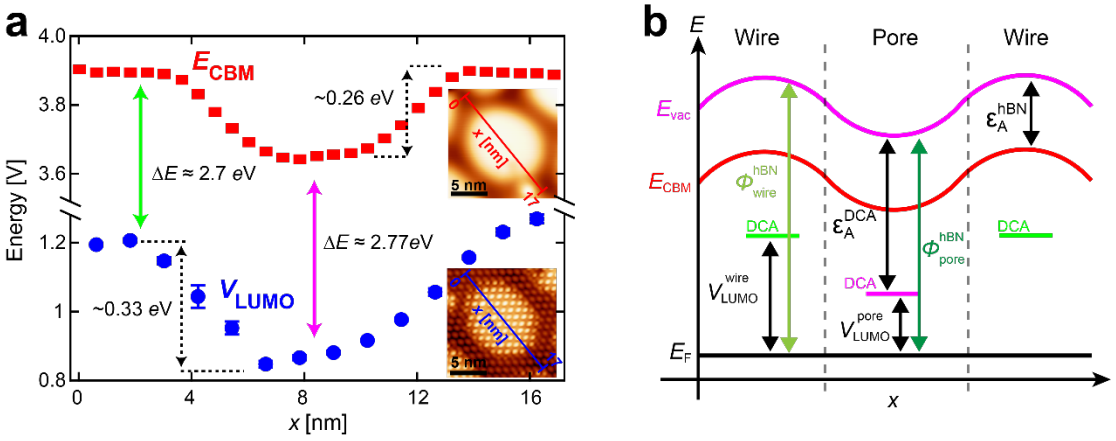

Figure 6.4: Spatial modulation of DCA LUMO and hBN CBM energies. (a) Plot showing the extracted DCA LUMO energies, V_{LUMO}, (blue data points) as a function of distance, x, along a DCA pore (bottom right STM image inset; V_{b} = 1.1 V, I_{t} = 50 pA). Plotted in red are the extracted CBM energies, E_{CBM}, for the hBN/Cu(111) surface, as a function of distance, x, along a hBN pore (top STM image inset; V_{b} = 4.0 V, I_{t} = 50 pA). V_{LUMO} was extracted by fitting the $\mathrm{d}I/\mathrm{d}V$ STS spectra performed on the DCA molecules as in **Figure 6.3**a. E_{CBM} was estimated as the energy at which the $\mathrm{d}I/\mathrm{d}V$ STS signal (performed on the hBN surface) is half of its maximum value, after normalising the $\mathrm{d}I/\mathrm{d}V$ curves with respect to the $\mathrm{d}I/\mathrm{d}V$ value at the tunnelling set point as in **Figure 6.3**b. Both $V_{\mathrm{LUMO}}(x)$ and $E_{\mathrm{CBM}}(x)$ show similar spatial modulation in their energies. (b) Schematic showing the energy level alignment of the DCA molecular states (i.e., LUMO) at the hBN/Cu(111) pore and wire regions. The E_{CBM} is a measure of the work function of the hBN/Cu(111) surface. The modulation in this work function leads to a spatial-modulation vacuum energy level on the hBN/Cu(111) surface. Due to the constant DCA electron affinity, $\varepsilon_{\mathrm{A}}^{\mathrm{DCA}}$, the spatial-modulation of the vacuum energy level causes a spatial-modulation of the DCA LUMO energy, V_{LUMO}.

Similarly, from our $\mathrm{d}I/\mathrm{d}V$ STS measurements on the hBN/Cu(111) surface, we estimated E_{CBM} (according to the procedure outlined in the previous section) along the distance, x, along the hBN pore region as seen in **Figure 6.4**a (red data points). Here, we find a similar trend to $V_{\mathrm{LUMO}}(x)$: as we move from the hBN wire region to the hBN pore region: the E_{CBM} decreases gradually from an absolute maximum of ~3.9 V to an absolute minimum of ~3.6 V at the centre of the hBN pore region. The modulation amplitude in E_{CBM} along x is ~0.26 V across the hBN pore region. From **Figure 6.4**a, we clearly see that the DCA LUMO energies, V_{LUMO} follows the same modulation as the hBN/Cu(111) E_{CBM} with an almost constant energy separation between the two: ~2.7 V at the wire region and ~2.77 V at the pore region. That is, the DCA LUMO energies and the CBM energies have a one-to-one correspondence.

To understand this correspondence, we first note that the work function of the hBN/Cu(111) surface, ϕ_{hBN}, is related to the CBM energy, E_{CBM}, by:

$$\phi_{\mathrm{hBN}} = E_{\mathrm{CBM}} + \varepsilon_{\mathrm{A}}^{\mathrm{hBN}} \qquad \text{(Eq. 6.1)}$$

where $\varepsilon_{\mathrm{A}}^{\mathrm{hBN}}$ is the electron affinity of the hBN/Cu(111) surface, which is constant throughout the surface [128]. This means that E_{CBM} is a measure of the hBN/Cu(111) surface work function up to a constant. The modulation in E_{CBM} reflects the expected modulation in the hBN/Cu(111) surface work function [128, 130] as seen in the schematic in **Figure 6.4**b. The modulation of the work function of the hBN/Cu(111) surface further reflects the modulation of the vacuum energy of the surface, E_{vac} (see **Figure 6.4**b). We note that the observed DCA LUMO is high in energy above the Fermi level and that its spatial extent (based on imaging) is similar to that in the gas phase (see section 3.3). Therefore, it is reasonable to assume that the DCA molecules are electrically neutral on hBN/Cu(111). Additionally, there is little-to-no hybridisation between the DCA molecules and the hBN/Cu(111) surface. Therefore, the energy differences between the vacuum level and the DCA LUMO is relatively unperturbed, i.e., the DCA electron affinity, $\varepsilon_{\mathrm{A}}^{\mathrm{DCA}}$ is constant and independent of the DCA adsorption site. Finally, the combined result of a spatially modulated vacuum level, E_{vac}, and a constant DCA electron affinity, $\varepsilon_{\mathrm{A}}^{\mathrm{DCA}}$, is a spatially modulated DCA LUMO energy, V_{LUMO}, as seen in **Figure 6.4**b. Here, the LUMO energy for a DCA molecule in the pore region, $V_{\mathrm{LUMO}}^{\mathrm{pore}}$, is necessarily lower than the LUMO energy for a DCA molecule in the wire region, $V_{\mathrm{LUMO}}^{\mathrm{wire}}$, since the vacuum energy, E_{vac}, is lower in the pore region than in the wire region.

We note that the above argument does not adequately explain the discrepancy between the DCA LUMO energy modulation (~0.33 V; blue data in **Figure 6.4**a) and the hBN CBM energy modulation (~0.26 V; red data in **Figure 6.4**a) of ~70 mV. We considered additional effects that might, in addition to the hBN/Cu(111) surface work function modulation, lead to the observed spatial modulation in the DCA LUMO energies. We considered the possibility of variations in the screening environments for the DCA molecules on hBN/Cu(111) such as those presented for DCA/Ag(111) in Chapter 3. On Ag(111), screening by neighbouring molecules were found to lead to a negligible spatial modulation of the LUMO energies for the DCA molecules (see section 3.6). Given the similar self-assembled arrangements of the DCA molecules on hBN with those on Ag(111), it is reasonable to assume that screening by neighbouring molecules would be quasi-identical on both surfaces. Therefore, screening by neighbouring molecules on hBN, like on Ag(111), would also be negligible. Additionally, the lack of metal-molecule screening for DCA/hBN means that variations in the DCA/hBN screening environment is insufficient to explain the ~70 mV discrepancy. Further, tip-sample

distance-dependent $\mathrm{d}I/\mathrm{d}V$ STS measurements on the DCA/hBN system showed no obvious shifts in the DCA LUMO energies which rules out any tip-induced field effects. We note that there is an ambiguity in how the CBM energies in **Figure 6.4**a were estimated. We speculate that this ambiguity could explain the ~70 mV discrepancy mentioned above. Future experiments with measurements of the field emission resonances of the hBN/Cu(111) surface can provide for a more accurate and direct measurement of the hBN/Cu(111) surface work function modulation [128] and can help resolve this discrepancy. Nevertheless, our conclusion that the DCA LUMO energies are modulated by the underlying hBN/Cu(111) surface work function remains qualitatively correct.

6.5 Summary

In this chapter, I have presented results of self-assembled 2D DCA submonolayers on an ultrathin insulating hBN layer grown on Cu(111). It was found that the DCA molecules on hBN/Cu(111) assemble themselves in a 2D lattice structure very similar to that of DCA molecules on Ag(111). That is, the bonding geometry and structure in both cases are similar since, in both cases (DCA on hBN/Cu(111) and on Ag(111)), intermolecular interactions are more dominant than molecular-substrate interactions. Further, like on Ag(111), the LUMO energies, V_{LUMO}, of the DCA molecules on hBN/Cu(111) are spatially-modulated according to their adsorption sites. On hBN/Cu(111), the spatial-modulation of V_{LUMO} follows the spatial-modulation of hBN/Cu(111) surface work function. In particular, V_{LUMO} lies further away from Fermi for molecules adsorbed on regions with a higher work function (such as hBN wire regions) compared to molecule adsorbed on regions with a lower work function (such as hBN pore regions).

Unlike the DCA molecules on Ag(111), the DCA molecules on hBN/Cu(111) have their LUMO energies much higher up in energy (relative to the Fermi level), by about ~0.6 – 0.9 V compared to DCA LUMO energies on Ag(111). Despite the differences in the work function for both Ag(111) and hBN/Cu(111) (with Ag(111) work function being larger of the two by ~0.7 eV), the discrepancy was explained by the absence of metal-molecule screening for the DCA molecules on hBN/Cu(111). Here, metal-molecule screening can result in a LUMO stabilization energy on the order ~1 eV, driving the V_{LUMO} closer to the Fermi level as is the case for DCA molecules on Ag(111).

The findings of this chapter represents an important step towards the synthesis of 2D DCA_3Cu_2 MOFs on hBN/Cu(111) where hBN would prove useful as a decoupling layer. The modulation of the electronic properties of the 2D MOF by the underlying hBN/Cu(111) surface work function coupled with an amplified electron-electron interactions between the MOF electrons due to a lack of metal-molecule screening can result in potentially interesting and

exotic quantum phenomena—phenomena that may be useful for the design of functional surface-supported 2D organic nanostructures on hBN/Cu(111).

Chapter 7
Conclusions and Outlook

In this thesis, I have demonstrated the synthesis of self-assembled 2D DCA-based organic nanostructures on different substrates. Subsequent detailed characterisation of these systems, via surface-sensitive techniques such STM, STS and nc-AFM, enabled the study of the electronic properties of these low-dimensional self-assemblies. In particular, the choice of substrates and the versatility of the DCA molecules to facilitate different in-plane interactions enabled the study of the impact of different intermolecular and substrate-mediated interactions on the electronic properties of these 2D organic nanostructures. This offers further perspectives for the precise understanding of the physics and chemistry at the nanoscale and therefore the design and synthesis of functional 2D organic nanostructures for real-world applications.

In Chapter 3, I presented results on a self-assembled 2D nanoarray of DCA molecules on a noble metal Ag(111) surface. We observed spatially periodic negative charging of individual DCA molecules, within the nanoarray, induced by an externally applied electric field (from the STM tip). The charging of these DCA molecules on a metal is facilitated by two key factors: (i) an effective potential barrier between the molecules and the underlying metallic substrate; and (ii) proximity of the DCA molecular states, in energy, to the Ag(111) Fermi level. Here, a potential barrier between DCA and Ag(111) is established due to the limited interactions between the molecule and the underlying metal. This in turn is enabled by the full participation of the DCA cyano-functional groups in the lateral hydrogen-bonding with adjacent molecules within the 2D self-assembled nanoarray on Ag(111). These findings are pertinent for engineering metal-molecule contacts in the design and synthesis of functional 2D molecular devices. Contact with metal electrodes is necessary for charge control or charge flow (i.e., current flow) within these low-dimensional molecular devices, e.g., in the implementation of organic quantum dots (charge control) [6, 57, 222, 223] or molecular transistors (charge flow) [24, 122]. However, these organic/inorganic contacts can inadvertently result in the pinning of molecular states to the metal Fermi level or quenching of intrinsic and important electronic properties of the molecular system e.g., through hybridisation between metal and molecular states. Establishing a potential barrier at these interfaces, like that at the DCA/Ag(111) interface, through manipulation of intermolecular bonding between molecular units (e.g., DCA-DCA hydrogen bonding) can mitigate these untoward effects and still allow for charge flow/control. Furthermore, engineering such organic/inorganic interfaces can simplify synthesis protocols for functional 2D molecular devices where the effective potential barriers

between molecular systems and metal electrodes are made inherent to the ensemble system rather than introduced via growth of insulating materials at the organic/inorganic interfaces.

The findings on the self-assembly of the DCA molecules on Ag(111) are in stark contrast with that on a thin insulating hBN monolayer grown on a Cu(111) substrate (Chapter 6). On hBN/Cu(111), the DCA molecules self-arrange to form a structure very much like that on Ag(111). We observed a significant spatial modulation of the DCA LUMO energies that, by means of vacuum alignment, follows the known spatial modulation of the hBN/Cu(111) surface work function. Here, although, thin insulating layers are efficient for electronic decoupling between adsorbates and underlying metal electrode, subtle spatial variations in adsorption site can still severely affect the molecular energy level alignment (like here, due to spatial variations of the hBN/Cu(111) surface work function), having important implications in the electronic functionality.

Furthermore, despite the weak DCA-hBN interactions and unlike on Ag(111), DCA molecules on hBN/Cu(111) do not exhibit charging as induced by an externally applied electric field. The higher LUMO energy for the DCA molecules on hBN/Cu(111) compared to those on Ag(111) meant a required gating field strength of ~3.5 times larger to charge the molecules on hBN/Cu(111) than on Ag(111). The higher DCA LUMO energy on hBN/Cu(111) is attributed to the absence of metal screening [which is present for DCA/Ag(111)], which can stabilise and drive the LUMO energy closer to the Fermi level. In the case of Ag(111), this metal-molecule screening results in a stabilisation energy for the DCA LUMO that is on the order of ~1 eV. We further found that the strength of this screening is intimately dependent on the DCA adsorption height, i.e., metal-molecule distance. These findings introduce further considerations for the engineering of metal-molecule contacts in the case of functional low-dimensional molecular electronics. That is, metal-molecule screening has a considerable impact on the electronic properties of the organic self-assemblies and can result in shifts of molecular states on the order eVs, even in the limit of weak metal-molecule interactions, i.e., with no significant hybridisation between metal and molecular states. However, by tuning the metal-molecule distance, through tailoring the morphology and chemical reactivity of the molecular units, one can tune the metal-molecule screening strength and therefore appropriately shift the molecular energy levels in a desired way. This implies another level of control in the design and synthesis of functional low-dimensional self-assembled organic nanostructure for molecular electronics.

Further study of the interface between the 2D self-assembled DCA monolayers and the underlying Ag(111) substrate (Chapter 4) revealed the existence of a 2D electron gas (2DEG) localised at the interface. This 2DEG interface state was found to be an upshift in energy of the

bare Ag(111) Shockley surface state, a direct consequence of the modification of the Ag(111) surface potential by the DCA monolayer. We found that the dispersion of this interface state showed slight deviations from a parabolic dispersion (i.e., free electron-like behaviour) for electron wavevectors close to the 2D DCA monolayer Brillouin zone (BZ) boundary. These slight deviations in the interface state dispersion reflected corrugations on the order of ~1.5 eV in the potential energy landscape experienced by the electrons at the DCA/Ag(111) interface. This highlights a further important issue in the context of functional low-dimensional organic nanostructures contacting metallic electrodes. Particularly so for metal-molecule contacts which hosts a delocalised interface state (e.g., the DCA/Ag(111) 2DEG interface state). Real-space potential fluctuations at these hybrid interfaces (due to the molecular system) can modify the behaviour of electrons within the interface state, particularly at energies where the electron wavevectors approach the BZ boundary of the molecular system. Modifications of this electron behaviour can hinder the electronic properties of the metal-molecule contact and subsequently affect the functionality of the low-dimensional organic nanostructure. These modifications can include, for example, band gap formations at the BZ boundary (where the Bragg condition [84] is fulfilled), resulting in a decrease in electron conductivity across the hybrid interface at energies where the dispersion approaches the BZ boundary. Depending on the corrugation in the real-space potential, deviations of the interface state dispersion from free electron-like behaviour sets an energy scale for device usage. Beyond which, the electronic properties of the ensemble system (2D organic nanostructure and metal-molecule contacts) are altered. Here, changing the molecular periodicity results in a different BZ size and ultimately different energies at which the interface state dispersion cuts the BZ boundary. Furthermore, adjusting the metal-molecule distance can alter the corrugation in the real-space potential at the interface. Therefore, by tailoring the morphology of the molecules to form 2D systems with different molecular periodicities or even different metal-molecule distance one can tune the energy scale for functional device usage.

In Chapter 5, I extended the results on the self-assembled 2D DCA monolayer on Ag(111) by introducing Cu atoms in the self-assembly process. This resulted in a, structurally and electronically, distinct 2D DCA_3Cu_2 kagome metal-organic framework (MOF) structure on Ag(111). Facilitated by weak MOF-Ag(111) interactions, observation of the Kondo effect evinces the presence of local magnetic moments associated with the MOF valence band states. We rationalised the emergence of these local magnetic moments as a direct result of strong electron-electron interactions between the 2D DCA_3Cu_2 kagome MOF electrons. This is in agreement with a previous prediction on the same system [64]. The enhancement in electron interactions is given by the localised nature of the DCA LUMO—which the MOF valence band states are primarily built from—and the reduced Coloumb screening given by the reduced

dimensionality (2D vs 3D) of the DCA-Cu kagome structure. This, therefore, represents the first observation of a strongly correlated many-electron phenomenon in a 2D organic kagome system. These findings on the 2D DCA_3Cu_2 kagome MOF on Ag(111) presents self-assembled 2D organic materials as viable platform for tuneable electron correlations. This opens new avenues for the research and subsequent development of 2D organic materials with exotic quantum phases (e.g, Mott insulating phase [282, 309], quantum spin liquids [310, 311], topologically non-trivial phases [283–285]) driven by these strong electron-electron interactions. This enables the incorporation of these materials with non-trivial phases in next-generation electronics (e.g., Mott-metal phase transitions for field-effect transistors [324, 325]; and topologically non-trivial phases for energy-efficient spintronic devices [285]). Popular classes of materials that exhibit strong electron-electron interactions include twisted 2D materials and heavy fermion materials. In twisted 2D materials, strong electron-electron interactions manifest because of interactions between two monolayers (one situated on top the other) oriented at a specific angle, i.e., twist angle, with respect to each other [326]. However, this effect is extremely sensitive to the twist angle [312]. In heavy fermion materials, strong electron-electron interactions are introduced, for example, via costly rare-earth atoms with highly localised *f*-orbitals [313]. Strong electron-electrons arising from the intrinsic kagome geometry and (inexpensive) organic material composition (e.g., in 2D DCA_3Cu_2 kagome MOF), therefore, paves the way for 2D strongly correlated materials beyond that of twisted 2D materials and heavy fermion materials.

The findings of this thesis have led to the formulation of new and interesting questions that would make for excellent follow-up experiments and research: the likelihood of charging for the DCA molecules on Ag(111) was found to depend sensitively on the DCA adsorption height on Ag(111) (Chapter 3). The DCA adsorption height, in turn, depended subtly on the DCA adsorption site on Ag(111). Here, it would be interesting to investigate the exact configuration of these molecules with respect to the underlying Ag(111) surface atoms and how these result in varying adsorption heights. The outcome of these questions can help direct the tailoring of molecular morphology (e.g., molecular size) to achieve a desired molecular adsorption height, i.e., to tune the metal-molecule distance. As highlighted previously, tuning the metal-molecule distance means tuning the screening strength by the underlying metal and tuning the strength of interactions (i.e., potential barrier) between the metal and molecule.

Furthermore, throughout this thesis we considered substrates with a hexagonal symmetry (Ag(111) and hBN). It would be interesting to investigate the impact of substrate symmetry on the structural and electronic properties of the self-assembled 2D organic nanostructures. Here, a first proposal would be to study the DCA molecules on Ag(100). This substrate is a promising candidate, as Ag(100), like Ag(111), is a noble metal surface with a

low chemical reactivity [327]. However, unlike Ag(111), Ag(100) has a square lattice structure and does not exhibit a Shockley surface state near the Fermi level [86]. The different surface packing densities for the different Ag surfaces can lead to a difference in how the DCA molecules are arranged on Ag(100) compared to Ag(111). This may further lead to a difference in the average DCA adsorption height on Ag(100) compared to Ag(111). Understanding these differences, if any, can help inform the choice of metal electrodes for metal-molecule contacts in 2D molecular-based devices.

In Chapter 5, we explored 2D MOFs where the metal-ligand bonding is facilitated by the coordination of DCA molecules with Cu adatoms. Here, this system necessitates the exploration of using different transition metal adatoms as part of the MOF coordination structure. A prime candidate would be to use Au atoms instead of Cu atoms. Both atoms have similar valence orbital characters (single electron in the 4*s* and 6*s* orbitals for Cu and Au, respectively). Theoretical predictions have been made that the free-standing DCA_3Au_2 kagome structure is topologically non-trivial [63]. Experimental progress, on the other hand, include only limited success at synthesising the structure on Au(111) [73]. Here, synthesising the 2D DCA_3Au_2 kagome structure on Ag(111) would prove useful for a comparative study with the 2D DCA_3Cu_2 kagome structure on Ag(111). In particular, the predicted unit cell lattice constant for the 2D DCA_3Au_2 kagome structure is bigger than that for the 2D DCA_3Cu_2 kagome structure [63]. Naively, the larger unit cell could translate to a decrease in the electron-electron interaction strength (i.e., due to a lower electron density) in the DCA-Au kagome structure compared to the DCA-Cu kagome structure. The results of these follow-up experiments can highlight ways to enhance or to diminish electron-electron interactions within self-assembled 2D organic materials.

Lastly, a natural extension to the results presented in Chapter 5 and Chapter 6, is to translate the synthesis protocol for 2D DCA_3Cu kagome MOF on Ag(111) onto a more technologically relevant substrate such as hBN/Cu(111). Growing the MOF structure on this decoupling layer would better preserve the MOF states and would make it tenable for gate-able devices [122] e.g., organic field effect transistors where the hBN layer acts as a gate dielectric layer [318, 319]. Furthermore, the study of the 2D DCA_3Cu_2 kagome MOF on hBN/Cu(111) would be promising for two reasons: (i) enhanced electron-electron interactions between the MOF electrons; and (ii) unscreened magnetic moments. The absence of a metallic substrate for the DCA-Cu kagome MOF structure grown on hBN/Cu(111) implies the absence of screening of charges within the MOF by underlying free conduction electrons. This lack of screening, should in principle, enhance the Coulomb repulsion between the MOF electrons [compared to the DCA_3Cu_2 kagome MOF on Ag(111)]. The absence of these free conduction electrons also implies the absence of screening of any local magnetic moments within the MOF, i.e., Kondo

screening is highly unlikely on hBN/Cu(111). These local magnetic moments, therefore, would be detectable by spin-sensitive probing techniques such as spin-polarised STM [328, 329] (unlike on Ag(111) where the spins are screened). These factors make the resulting MOF on hBN/Cu(111) an exciting playground to study strong electron-electron interactions and their resulting electronic (e.g., via STM and STS) and magnetic (e.g., via spin-polarised STM) quantum phases.

Overall, this thesis expounds the impact of different intermolecular (e.g., hydrogen bonding, metal-ligand bonding, Coulomb repulsion) and substrate-mediated (e.g., metal screening, metal-molecule potential barrier, 2DEG interface state, surface work function modulation) interactions on the structural and electronic properties of on-surface organic self-assemblies. Combined with (i) the tunability and self-assembly capability of organic molecules and (ii) the emergence of novel quantum effects in low-dimensional materials (e.g., strong electron correlations), this thesis paves the way for atomically engineered 2D organic nanostructures with tailored electronic and structural properties for the implementation in next-generation electronics.

Bibliography

[1] Brattain, W. H. Genesis of the Transistor. *Phys. Teach.* **1968**, *6* (3), 109–114.

[2] Koomey, J. G.; Berard, S.; Sanchez, M.; Wong, H. Web Extra Appendix: Implications of Historical Trends in the Electrical Efficiency of Computing. *IEEE Ann. Hist. Comput.* **2011**, *33* (3), S1–S30.

[3] Thompson, S. MOS Scaling: Transistor Challenges for the 21st Century. In *Intel Technology Journal*; Citeseer, 1998.

[4] Packan, P. A. Pushing the Limits. *Science* **1999**, *285* (5436), 2079–2081.

[5] Pop, E. Energy Dissipation and Transport in Nanoscale Devices. *Nano Res.* **2010**, *3* (3), 147–169.

[6] Khademhosseini, V.; Dideban, D.; Ahmadi, M.; Ismail, R.; Heidari, H. Single Electron Transistor Scheme Based on Multiple Quantum Dot Islands: Carbon Nanotube and Fullerene. *ECS J. Solid State Sci. Technol.* **2018**, *7* (10), M145.

[7] Hasan, M. Z.; Kane, C. L. Colloquium: Topological Insulators. *Rev. Mod. Phys.* **2010**, *82* (4), 3045–3067.

[8] Scheiderer, P.; Schmitt, M.; Gabel, J.; Zapf, M.; Stübinger, M.; Schütz, P.; Dudy, L.; Schlueter, C.; Lee, T.; Sing, M. Tailoring Materials for Mottronics: Excess Oxygen Doping of a Prototypical Mott Insulator. *Adv. Mater.* **2018**, *30* (25), 1706708.

[9] Grigorescu, A. E.; Hagen, C. W. Resists for Sub-20-Nm Electron Beam Lithography with a Focus on HSQ: State of the Art. *Nanotechnology* **2009**, *20* (29), 292001.

[10] Ito, T.; Okazaki, S. Pushing the Limits of Lithography. *Nature* **2000**, *406* (6799), 1027–1031.

[11] Vieu, C.; Carcenac, F.; Pepin, A.; Chen, Y.; Mejias, M.; Lebib, A.; Manin-Ferlazzo, L.; Couraud, L.; Launois, H. Electron Beam Lithography: Resolution Limits and Applications. *Appl. Surf. Sci.* **2000**, *164* (1–4), 111–117.

[12] Mack, C. A. Line-Edge Roughness and the Ultimate Limits of Lithography. In *Advances in Resist Materials and Processing Technology XXVII*; International Society for Optics and Photonics, 2010; Vol. 7639, p 763931.

[13] Biswas, A.; Bayer, I. S.; Biris, A. S.; Wang, T.; Dervishi, E.; Faupel, F. Advances in Top–down and Bottom–up Surface Nanofabrication: Techniques, Applications & Future Prospects. *Adv. Colloid Interface Sci.* **2012**, *170* (1–2), 2–27.

[14] Sharma, A.; Das, J. Small Molecules Derived Carbon Dots: Synthesis and Applications in Sensing, Catalysis, Imaging, and Biomedicine. *J. Nanobiotechnology* **2019**, *17* (1), 92.

[15] Lehn, J.-M. Supramolecular Chemistry: From Molecular Information towards Self-Organization and Complex Matter. *Reports Prog. Phys.* **2004**, *67* (3), 249.

[16] Kippelen, B.; Brédas, J.-L. Organic Photovoltaics. *Energy Environ. Sci.* **2009**, *2* (3), 251–261.

[17] Chung, I.-J.; Kang, I. Flexible Display Technology–Opportunity and Challenges to New Business Application. *Mol. Cryst. Liq. Cryst.* **2009**, *507* (1), 1–17.

[18] Mattia, E.; Otto, S. Supramolecular Systems Chemistry. *Nat. Nanotechnol.* **2015**, *10* (2), 111–119.

[19] Press Release Page. www.nobelprize.org/prizes/chemistry/1987/press-release (accessed Jan 12, 2021).

[20] Abdulrazzaq, O. A.; Saini, V.; Bourdo, S.; Dervishi, E.; Biris, A. S. Organic Solar Cells: A Review of Materials, Limitations, and Possibilities for Improvement. *Part. Sci. Technol.* **2013**, *31* (5), 427–442.

[21] Tsai, Y.-T.; Raffy, G.; Liu, H.-F.; Peng, B.-J.; Tseng, K.-P.; Hirsch, L.; Del Guerzo, A.; Bassani, D. M.; Wong, K.-T. Incorporation of Narcissistic Self-Sorting Supramolecular Interactions for the Spontaneous Fabrication of Multiple-Color Solid-State Materials for OLED Applications. *Mater. Chem. Front.* **2020**, *4* (3), 845–850.

[22] Liu, J.; Lewis, L. N.; Duggal, A. R. Photoactivated and Patternable Charge Transport

Materials and Their Use in Organic Light-Emitting Devices. *Appl. Phys. Lett.* **2007**, *90* (23), 233503.

[23] Torsi, L.; Dodabalapur, A.; Sabbatini, L.; Zambonin, P. G. Multi-Parameter Gas Sensors Based on Organic Thin-Film-Transistors. *Sensors Actuators B Chem.* **2000**, *67* (3), 312–316.

[24] Zhang, W.; Yu, G. Organic Semiconductors for Field-Effect Transistors. In *Organic Optoelectronic Materials*; Springer, 2015; pp 51–164.

[25] Barth, J. V; Costantini, G.; Kern, K. Engineering Atomic and Molecular Nanostructures at Surfaces. *Nature* **2005**, *437* (7059), 671–679.

[26] Barth, J. V. Molecular Architectonic on Metal Surfaces. *Annu. Rev. Phys. Chem.* **2007**, *58*, 375–407.

[27] Barth, J. V; Weckesser, J.; Lin, N.; Dmitriev, A.; Kern, K. Supramolecular Architectures and Nanostructures at Metal Surfaces. *Appl. Phys. A* **2003**, *76* (5), 645–652.

[28] Wang, J.; Li, S.; Zhu, G.; Zhao, W.; Chen, R.; Pan, M. Novel Non-Noble Metal Electrocatalysts Synthesized by Heat-Treatment of Iron Terpyridine Complexes for the Oxygen Reduction Reaction. *J. Power Sources* **2013**, *240*, 381–389.

[29] Jiang, Y.; Li, F.; Zhang, B.; Li, X.; Wang, X.; Huang, F.; Sun, L. Promoting the Activity of Catalysts for the Oxidation of Water with Bridged Dinuclear Ruthenium Complexes. *Angew. Chemie* **2013**, *125* (12), 3482–3485.

[30] Wang, J.-L.; Wang, C.; Lin, W. Metal–Organic Frameworks for Light Harvesting and Photocatalysis. *Acs Catal.* **2012**, *2* (12), 2630–2640.

[31] Mugarza, A.; Krull, C.; Robles, R.; Stepanow, S.; Ceballos, G.; Gambardella, P. Spin Coupling and Relaxation inside Molecule–Metal Contacts. *Nat. Commun.* **2011**, *2* (1), 490.

[32] Komeda, T.; Isshiki, H.; Liu, J.; Zhang, Y. F.; Lorente, N.; Katoh, K.; Breedlove, B. K.; Yamashita, M. Observation and Electric Current Control of a Local Spin in a Single-Molecule Magnet. *Nat. Commun.* **2011**, *2* (1).

[33] Krull, C.; Robles, R.; Mugarza, A.; Gambardella, P. Site-and Orbital-Dependent Charge Donation and Spin Manipulation in Electron-Doped Metal Phthalocyanines. *Nat. Mater.* **2013**, *12* (4), 337–343.

[34] Novoselov, K. S.; Geim, A. K.; Morozov, S. V.; Jiang, D.; Katsnelson, M. I.; Grigorieva, Iv.; Dubonos, Sv.; Firsov, and A. A. Two-Dimensional Gas of Massless Dirac Fermions in Graphene. *Nature* **2005**, *438* (7065), 197–200.

[35] Morozov, S. V; Novoselov, K. S.; Katsnelson, M. I.; Schedin, F.; Elias, D. C.; Jaszczak, J. A.; Geim, A. K. Giant Intrinsic Carrier Mobilities in Graphene and Its Bilayer. *Phys. Rev. Lett.* **2008**, *100* (1), 16602.

[36] Otero, R.; Gallego, J. M.; de Parga, A. L. V.; Martín, N.; Miranda, R. Molecular Self-Assembly at Solid Surfaces. *Adv. Mater.* **2011**, *23* (44), 5148–5176.

[37] Krull, C.; Castelli, M.; Hapala, P.; Kumar, D.; Tadich, A.; Capsoni, M.; Edmonds, M. T.; Hellerstedt, J.; Burke, S. A.; Jelinek, P. Iron-Based Trinuclear Metal-Organic Nanostructures on a Surface with Local Charge Accumulation. *Nat. Commun.* **2018**, *9* (1), 1–7.

[38] Hao, D.; Song, C.; Ning, Y.; Wang, Y.; Wang, L.; Ma, X.-C.; Chen, X.; Xue, Q.-K. Self-Assembly of Manganese Phthalocyanine on Pb (111) Surface: A Scanning Tunneling Microscopy Study. *J. Chem. Phys.* **2011**, *134* (15), 154703.

[39] Järvinen, P.; Hämäläinen, S. K.; Banerjee, K.; Häkkinen, P.; Ijäs, M.; Harju, A.; Liljeroth, P. Molecular Self-Assembly on Graphene on SiO2 and h-BN Substrates. *Nano Lett.* **2013**, *13* (7), 3199–3204.

[40] Chen, Z.; Lin, T.; Li, H.; Cheng, F.; Su, C.; Loh, K. P. Hydrogen Bond Guided Synthesis of Close-Packed One-Dimensional Graphdiyne on the Ag (111) Surface. *Chem. Sci.* **2019**, *10* (47), 10849–10852.

[41] Pham, T. A.; Song, F.; Nguyen, M.-T.; Stöhr, M. Self-Assembly of Pyrene Derivatives on Au (111): Substituent Effects on Intermolecular Interactions. *Chem. Commun.* **2014**, *50* (91), 14089–14092.

[42] Klappenberger, F.; Kühne, D.; Krenner, W.; Silanes, I.; Arnau, A.; García De Abajo, F.

J.; Klyatskaya, S.; Ruben, M.; Barth, J. V. Tunable Quantum Dot Arrays Formed from Self-Assembled Metal-Organic Networks. *Phys. Rev. Lett.* **2011**, *106* (2), 1–4.

[43] Teyssandier, J.; De Feyter, S.; Mali, K. S. Host–Guest Chemistry in Two-Dimensional Supramolecular Networks. *Chem. Commun.* **2016**, *52* (77), 11465–11487.

[44] Mao, J.; Zhang, H.; Jiang, Y.; Pan, Y.; Gao, M.; Xiao, W.; Gao, H.-J. Tunability of Supramolecular Kagome Lattices of Magnetic Phthalocyanines Using Graphene-Based Moiré Patterns as Templates. *J. Am. Chem. Soc.* **2009**, *131* (40), 14136–14137.

[45] Piquero-Zulaica, I.; Lobo-Checa, J.; Sadeghi, A.; El-Fattah, Z. M. A.; Mitsui, C.; Okamoto, T.; Pawlak, R.; Meier, T.; Arnau, A.; Ortega, J. E.; Takeya, J.; Goedecker, S.; Meyer, E.; Kawai, S. Precise Engineering of Quantum Dot Array Coupling through Their Barrier Widths. *Nat. Commun.* **2017**, *8* (1).

[46] Stöhr, M.; Boz, S.; Schär, M.; Nguyen, M.; Pignedoli, C. A.; Passerone, D.; Schweizer, W. B.; Thilgen, C.; Jung, T. A.; Diederich, F. Self-assembly and Two-dimensional Spontaneous Resolution of Cyano-functionalized [7] Helicenes on Cu (111). *Angew. Chemie Int. Ed.* **2011**, *50* (42), 9982–9986.

[47] Sk, R.; Arra, S.; Dhara, B.; Miller, J. S.; Kabir, M.; Deshpande, A. Enhancing Intermolecular Interaction by Cyano Substitution in Copper Phthalocyanine. *J. Phys. Chem. C* **2018**, *122* (1), 429–437.

[48] Miao, K.; Hu, Y.; Zha, B.; Xu, L.; Miao, X.; Deng, W. Hydroxyl versus Carboxyl Substituent: Effects of Competitive and Cooperative Multiple Hydrogen Bonds on Concentration-Controlled Self-Assembly. *J. Phys. Chem. C* **2016**, *120* (26), 14187–14197.

[49] Janica, I.; Patroniak, V.; Samorì, P.; Ciesielski, A. Imine-Based Architectures at Surfaces and Interfaces: From Self-Assembly to Dynamic Covalent Chemistry in 2D. *Chem. Asian J.* **2018**, *13* (5), 465–481.

[50] Shi, Z.; Liu, J.; Lin, T.; Xia, F.; Liu, P. N.; Lin, N. Thermodynamics and Selectivity of Two-Dimensional Metallo-Supramolecular Self-Assembly Resolved at Molecular Scale. *J. Am. Chem. Soc.* **2011**, *133* (16), 6150–6153.

[51] Adisoejoso, J.; Li, Y.; Liu, J.; Liu, P. N.; Lin, N. Two-Dimensional Metallo-Supramolecular Polymerization: Toward Size-Controlled Multi-Strand Polymers. *J. Am. Chem. Soc.* **2012**, *134* (45), 18526–18529.

[52] Kumar, A.; Banerjee, K.; Foster, A. S.; Liljeroth, P. Two-Dimensional Band Structure in Honeycomb Metal–Organic Frameworks. *Nano Lett.* **2018**, *18* (9), 5596–5602.

[53] Zhang, J.; Shchyrba, A.; Nowakowska, S.; Meyer, E.; Jung, T. a; Muntwiler, M. Probing the Spatial and Momentum Distribution of Confined Surface States in a Metal Coordination Network. *Chem. Commun.* **2014**, *50* (82), 12289–12292.

[54] Urgel, J. I.; Ecija, D.; Lyu, G.; Zhang, R.; Palma, C.-A.; Auwaerter, W.; Lin, N.; Barth, J. V. Quasicrystallinity Expressed in Two-Dimensional Coordination Networks. *Nat. Chem.* **2016**, *8* (7), 657–662.

[55] Urgel, J. I.; Schwarz, M.; Garnica, M.; Stassen, D.; Bonifazi, D.; Ecija, D.; Barth, J. V; Auwärter, W. Controlling Coordination Reactions and Assembly on a Cu (111) Supported Boron Nitride Monolayer. *J. Am. Chem. Soc.* **2015**, *137* (7), 2420–2423.

[56] Fernández-Torrente, I.; Kreikemeyer-Lorenzo, D.; Stróżecka, A.; Franke, K. J.; Pascual, J. I. Gating the Charge State of Single Molecules by Local Electric Fields. *Phys. Rev. Lett.* **2012**, *108* (3), 36801.

[57] Rasmussen, T. E. Single Molecule Applications of Quantum Dots. *J. Mod. Phys.* **2013**, *4* (11), 27.

[58] Kloeffel, C.; Loss, D. Prospects for Spin-Based Quantum Computing in Quantum Dots. *Annu. Rev. Condens. Matter Phys.* **2013**, *4* (1), 51–81.

[59] Choi, M. K.; Yang, J.; Hyeon, T.; Kim, D.-H. Flexible Quantum Dot Light-Emitting Diodes for next-Generation Displays. *npj Flex. Electron.* **2018**, *2* (1), 1–14.

[60] Sanvito, S. Molecular Spintronics. *Chem. Soc. Rev.* **2011**, *40* (6), 3336–3355.

[61] Zhang, J.; Zhao, B.; Ma, C.; Yang, Z. Prediction of Intrinsic Two-Dimensional Non-Dirac Topological Insulators in Triangular Metal-Organic Frameworks. *Appl. Phys. Lett.* **2019**, *114* (4).

[62] Hsu, C. H.; Huang, Z. Q.; Macam, G. M.; Chuang, F. C.; Huang, L. Prediction of Two-Dimensional Organic Topological Insulator in Metal-DCB Lattices. *Appl. Phys. Lett.* **2018**, *113* (23), 4–9.

[63] Zhang, L. Z.; Wang, Z. F.; Huang, B.; Cui, B.; Wang, Z.; Du, S. X.; Gao, H.-J.; Liu, F. Intrinsic Two-Dimensional Organic Topological Insulators in Metal–Dicyanoanthracene Lattices. *Nano Lett.* **2016**, *16* (3), 2072–2075.

[64] Fuchs, M.; Liu, P.; Schwemmer, T.; Sangiovanni, G.; Thomale, R.; Franchini, C.; Di Sante, D. Kagome Metal-Organic Frameworks as a Platform for Strongly Correlated Electrons. *J. Phys. Mater.* **2020**, *3* (2), 025001.

[65] Su, N.; Jiang, W.; Wang, Z.; Liu, F. Prediction of Large Gap Flat Chern Band in a Two-Dimensional Metal-Organic Framework. *Appl. Phys. Lett.* **2018**, *112* (3), 33301.

[66] Zhang, X.; Zhou, Y.; Cui, B.; Zhao, M.; Liu, F. Theoretical Discovery of a Superconducting Two-Dimensional Metal–Organic Framework. *Nano Lett.* **2017**, *17* (10), 6166–6170.

[67] Barth, J. V. Fresh Perspectives for Surface Coordination Chemistry. *Surf. Sci.* **2009**, *603* (10–12), 1533–1541.

[68] Gottardi, S.; Müller, K.; Moreno-López, J. C.; Yildirim, H.; Meinhardt, U.; Kivala, M.; Kara, A.; Stöhr, M. Cyano-Functionalized Triarylamines on Au (111): Competing Intermolecular versus Molecule/Substrate Interactions. *Adv. Mater. Interfaces* **2014**, *1* (1), 1300025.

[69] Yan, L.; Silveira, O. J.; Alldritt, B.; Krejčí, O.; Foster, A. S.; Liljeroth, P. Synthesis and Local Probe Gating of a Monolayer Metal-organic Framework. *Adv. Funct. Mater.* **2021**, 2100519.

[70] Rodriguez-Fernandez, J.; Wang, Y.; Alcami, M.; Martin, F.; Otero, R.; Gallego, J. M.; Miranda, R. Thermal Transition from a Disordered, 2D Network to a Regular, 1D, Fe (II)–DCNQI Coordination Network. *J. Phys. Chem. C* **2016**, *120* (30), 16712–16721.

[71] Henningsen, N.; Rurali, R.; Limbach, C.; Drost, R.; Pascual, J. I.; Franke, K. J. Site-Dependent Coordination Bonding in Self-Assembled Metal-Organic Networks. *J. Phys. Chem. Lett.* **2011**, *2* (2), 55–61.

[72] Stepanow, S.; Lin, N.; Payer, D.; Schlickum, U.; Klappenberger, F.; Zoppellaro, G.; Ruben, M.; Brune, H.; Barth, J. V.; Kern, K. Surface-Assisted Assembly of 2D Metal-Organic Networks That Exhibit Unusual Threefold Coordination Symmetry. *Angew. Chemie - Int. Ed.* **2007**, *46* (5), 710–713.

[73] Yan, L.; Pohjavirta, I.; Alldritt, B.; Liljeroth, P. On-Surface Assembly of Au-Dicyanoanthracene Coordination Structures on Au(111). *ChemPhysChem* **2019**, *20* (18), 2297–2300.

[74] Ceccatto dos Santos, A.; de Campos Ferreira, R. C.; Moreno-Lopez, J. C.; Barreto, L.; Lepper, M.; Landers, R.; Steinrück, H.-P.; Marbach, H.; de Siervo, A. Cyano-Functionalized Porphyrins on Cu (111) from One-Dimensional Wires to Two-Dimensional Molecular Frameworks: On the Role of Co-Deposited Metal Atoms. *Chem. Mater.* **2020**, *32* (5), 2114–2122.

[75] Adhikari, R.; Siglreithmaier, G.; Gurrath, M.; Meusel, M.; Kuliga, J.; Lepper, M.; Hölzel, H.; Jux, N.; Meyer, B.; Steinrück, H.-P. Formation of Highly Ordered Molecular Porous 2D Networks from Cyano-Functionalized Porphyrins on Cu (111). *Chemistry* **2020**, *26* (59), 13408–13418.

[76] Baker Cortés, B. D.; Schmidt, N.; Enache, M.; Stöhr, M. Coverage-Dependent Structural Transformation of Cyano-Functionalized Porphyrin Networks on Au (111) via Addition of Cobalt Atoms. *J. Phys. Chem. C* **2019**, *123* (32), 19681–19687.

[77] Pawin, G.; Wong, K. L.; Kim, D.; Sun, D.; Bartels, L.; Hong, S.; Rahman, T. S.; Carp, R.; Marsella, M. A Surface Coordination Network Based on Substrate-Derived Metal Adatoms with Local Charge Excess. *Angew. Chemie - Int. Ed.* **2008**, *47* (44), 8442–8445.

[78] Swart, I.; Gross, L.; Liljeroth, P. Single-Molecule Chemistry and Physics Explored by Low-Temperature Scanning Probe Microscopy. *Chem. Commun. (Camb).* **2011**, *47* (32), 9011–9023.

[79] Zhang, Y.; Wei, Z.; Zhang, M.; Gu, X.; Huang, L. Giant Magnetic Anisotropy of a Two-Dimensional Metal–Dicyanoanthracene Framework. *Nanoscale* **2018**, *10* (36), 17335–17340.
[80] Wang, Y.; Ji, W.; Zhang, C.; Li, P.; Wang, P.; Kong, B.; Li, S.; Yan, S.; Liang, K. Discovery of Intrinsic Quantum Anomalous Hall Effect in Organic Mn-DCA Lattice. *Appl. Phys. Lett.* **2017**, *110* (23), 233107.
[81] Kumar, D.; Krull, C.; Yin, Y.; Medhekar, N. V.; Schiffrin, A. Electric Field Control of Molecular Charge State in a Single-Component 2D Organic Nanoarray. *ACS Nano* **2019**, *13* (10), 11882–11890.
[82] Shockley, W. On the Surface States Associated with a Periodic Potential. *Phys. Rev.* **1939**, *56* (4), 317.
[83] Grothe, S.; Johnston, S.; Chi, S.; Dosanjh, P.; Burke, S. A.; Pennec, Y. Quantifying Many-Body Effects by High-Resolution Fourier Transform Scanning Tunneling Spectroscopy. *Phys. Rev. Lett.* **2013**, *111* (24), 246804.
[84] Ashcroft, N. W.; Mermin, N. D. *Solid State Physics*; Holt, Rinehart and Winston, New York, 1976.
[85] Zhang, S. S.; Yin, J.-X.; Ikhlas, M.; Tien, H.-J.; Wang, R.; Shumiya, N.; Chang, G.; Tsirkin, S. S.; Shi, Y.; Yi, C. Many-Body Resonance in a Correlated Topological Kagome Antiferromagnet. *Phys. Rev. Lett.* **2020**, *125* (4), 46401.
[86] Ternes, M.; Heinrich, A. J.; Schneider, W. D. Spectroscopic Manifestations of the Kondo Effect on Single Adatoms. *J. Phys. Condens. Matter* **2009**, *21* (5), 053001.
[87] Auwärter, W. Hexagonal Boron Nitride Monolayers on Metal Supports: Versatile Templates for Atoms, Molecules and Nanostructures. *Surf. Sci. Rep.* **2019**, *74* (1), 1–95.
[88] Repp, J.; Meyer, G.; Stojković, S. M.; Gourdon, A.; Joachim, C. Molecules on Insulating Films: Scanning-Tunneling Microscopy Imaging of Individual Molecular Orbitals. *Phys. Rev. Lett.* **2005**, *94* (2), 26803.
[89] Joshi, S.; Bischoff, F.; Koitz, R.; Ecija, D.; Seufert, K.; Seitsonen, A. P.; Hutter, J.; Diller, K.; Urgel, J. I.; Sachdev, H. Control of Molecular Organization and Energy Level Alignment by an Electronically Nanopatterned Boron Nitride Template. *ACS Nano* **2014**, *8* (1), 430–442.
[90] Ducke, J.; Riss, A.; Perez Paz, A.; Seufert, K.; Schwarz, M.; Garnica, M.; Rubio, A.; Auwärter, W. Layered Insulator/Molecule/Metal Heterostructures with Molecular Functionality through Porphyrin Intercalation. *ACS Nano* **2018**, *12* (3), 2677–2684.
[91] Brülke, C.; Heepenstrick, T.; Krieger, I.; Wolff, B.; Yang, X.; Shamsaddinlou, A.; Weiß, S.; Bocquet, F. C.; Tautz, F. S.; Soubatch, S. Quantitative Analysis of the Electronic Decoupling of an Organic Semiconductor Molecule at a Metal Interface by a Monolayer of Hexagonal Boron Nitride. *Phys. Rev. B* **2019**, *99* (12), 121404.
[92] Tan, A.; Zhang, P. P. Interfacial Charge Transfer Enhancement via Formation of Binary Molecular Assemblies on Electronically Corrugated Boron Nitride. *Phys. Chem. Chem. Phys.* **2019**, *21* (47), 26146–26153.
[93] Palma, C.-A.; Joshi, S.; Hoh, T.; Ecija, D.; Barth, J. V; Auwärter, W. Two-Level Spatial Modulation of Vibronic Conductance in Conjugated Oligophenylenes on Boron Nitride. *Nano Lett.* **2015**, *15* (4), 2242–2248.
[94] Pörtner, M.; Wei, Y.; Riss, A.; Seufert, K.; Garnica, M.; Barth, J. V; Seitsonen, A. P.; Diekhöner, L.; Auwärter, W. Charge State Control of F16CoPc on H-BN/Cu (111). *Adv. Mater. Interfaces* **2020**, *7* (15), 2000080.
[95] Zimmermann, D. M.; Seufert, K.; Đorđević, L.; Hoh, T.; Joshi, S.; Marangoni, T.; Bonifazi, D.; Auwärter, W. Self-Assembly and Spectroscopic Fingerprints of Photoactive Pyrenyl Tectons on HBN/Cu (111). *Beilstein J. Nanotechnol.* **2020**, *11* (1), 1470–1483.
[96] Steed, J. W.; Atwood, J. L. *Supramolecular Chemistry*; John Wiley & Sons, 2013.
[97] Kolesnichenko, I. V; Anslyn, E. V. Practical Applications of Supramolecular Chemistry. *Chem. Soc. Rev.* **2017**, *46* (9), 2385–2390.
[98] Zhang, D.; Martinez, A.; Dutasta, J.-P. Emergence of Hemicryptophanes: From

Synthesis to Applications for Recognition, Molecular Machines, and Supramolecular Catalysis. *Chem. Rev.* **2017**, *117* (6), 4900–4942.
[99] Leclercq, L.; Douyère, G.; Nardello-Rataj, V. Supramolecular Chemistry and Self-Organization: A Veritable Playground for Catalysis. *Catalysts* **2019**, *9* (2), 163.
[100] Keijer, T.; Bouwens, T.; Hessels, J.; Reek, J. N. H. Supramolecular Strategies in Artificial Photosynthesis. *Chem. Sci.* **2021**, *12* (1), 50–70.
[101] Ghosh, T.; Panicker, J. S.; Nair, V. C. Self-Assembled Organic Materials for Photovoltaic Application. *Polymers (Basel).* **2017**, *9* (3), 112.
[102] Caballo, C.; Sicilia, M. D.; Rubio, S. Supramolecular Solvents for Green Chemistry. In *The application of green solvents in separation processes*; Elsevier, 2017; pp 111–137.
[103] Ishiwari, F.; Shoji, Y.; Fukushima, T. Supramolecular Scaffolds Enabling the Controlled Assembly of Functional Molecular Units. *Chem. Sci.* **2018**, *9* (8), 2028–2041.
[104] Scriven, L. E. Physics and Applications of Dip Coating and Spin Coating. *MRS Online Proc. Libr.* **1988**, *121*.
[105] Roberts, G. *Langmuir-Blodgett Films*; Springer Science & Business Media, 2013.
[106] Ariga, K. Don't Forget Langmuir–Blodgett Films 2020: Interfacial Nanoarchitectonics with Molecules, Materials, and Living Objects. *Langmuir* **2020**, *36* (26), 7158–7180.
[107] Tanigaki, K.; Kuroshima, S.; Ebbesen, T. W.; Ichihashi, T. Growth of Thin Film Crystals of Monochloro (Meso-Tetraphenylporphyrinato) Gallium by Organic MBE. *J. Cryst. Growth* **1991**, *114* (1–2), 3–6.
[108] Toolan, D. T. W.; Fujii, S.; Ebbens, S. J.; Nakamura, Y.; Howse, J. R. On the Mechanisms of Colloidal Self-Assembly during Spin-Coating. *Soft Matter* **2014**, *10* (44), 8804–8812.
[109] Komikado, T.; Inoue, A.; Masuda, K.; Ando, T.; Umegaki, S. Multi-Layered Mirrors Fabricated by Spin-Coating Organic Polymers. *Thin Solid Films* **2007**, *515* (7–8), 3887–3892.
[110] Dong, R.; Pfeffermann, M.; Liang, H.; Zheng, Z.; Zhu, X.; Zhang, J.; Feng, X. Large-Area, Free-Standing, Two-Dimensional Supramolecular Polymer Single-Layer Sheets for Highly Efficient Electrocatalytic Hydrogen Evolution. *Angew. Chemie - Int. Ed.* **2015**, *54* (41), 12058–12063.
[111] Jenkins, S. J. Aromatic Adsorption on Metals via First-Principles Density Functional Theory. *Proc. R. Soc. A Math. Phys. Eng. Sci.* **2009**, *465* (2110), 2949–2976.
[112] Xia, M.; Jiang, J.; Ye, Z. R.; Wang, Y. H.; Zhang, Y.; Chen, S. D.; Niu, X. H.; Xu, D. F.; Chen, F.; Chen, X. H.; Xie, B. P.; Zhang, T.; Feng, D. L. Angle-Resolved Photoemission Spectroscopy Study on the Surface States of the Correlated Topological Insulator YbB6. *Sci. Rep.* **2014**, *4*, 5999.
[113] Lepper, M.; Schmitt, T.; Gurrath, M.; Raschmann, M.; Zhang, L.; Stark, M.; Hölzel, H.; Jux, N.; Meyer, B.; Schneider, M. A. Adsorption Behavior of a Cyano-Functionalized Porphyrin on Cu (111) and Ag (111): From Molecular Wires to Ordered Supramolecular Two-Dimensional Aggregates. *J. Phys. Chem. C* **2017**, *121* (47), 26361–26371.
[114] Ekin, J. *Experimental Techniques for Low-Temperature Measurements: Cryostat Design, Material Properties and Superconductor Critical-Current Testing*; Oxford university press, 2006.
[115] Hinaut, A.; Meier, T.; Pawlak, R.; Feund, S.; Jöhr, R.; Kawai, S.; Glatzel, T.; Decurtins, S.; Müllen, K.; Narita, A. Electrospray Deposition of Structurally Complex Molecules Revealed by Atomic Force Microscopy. *Nanoscale* **2018**, *10* (3), 1337–1344.
[116] Satterley, C. J.; Perdigão, L. M. A.; Saywell, A.; Magnano, G.; Rienzo, A.; Mayor, L. C.; Dhanak, V. R.; Beton, P. H.; O'Shea, J. N. Electrospray Deposition of Fullerenes in Ultra-High Vacuum: In Situ Scanning Tunneling Microscopy and Photoemission Spectroscopy. *Nanotechnology* **2007**, *18* (45), 455304.
[117] Tait, S. L.; Langner, A.; Lin, N.; Chandrasekar, R.; Fuhr, O.; Ruben, M.; Kern, K. Assembling Isostructural Metal-Organic Coordination Architectures on Cu(100), Ag(100) and Ag(111) Substrates. *ChemPhysChem* **2008**, *9* (17), 2495–2499.
[118] Zhang, X.; Li, N.; Wang, H.; Yuan, C.; Gu, G.; Zhang, Y.; Nieckarz, D.; Szabelski, P.;

Hou, S.; Teo, B. K.; Wang, Y. Influence of Relativistic Effects on Assembled Structures of V-Shaped Bispyridine Molecules on M(111) Surfaces Where M = Cu, Ag, Au. *ACS Nano* **2017**, *11* (8), 8511–8518.

[119] Lischka, M.; Dong, R.; Wang, M.; Martsinovich, N.; Fritton, M.; Grossmann, L.; Heckl, W. M.; Feng, X.; Lackinger, M. Competitive Metal Coordination of Hexaaminotriphenylene on Cu(111) by Intrinsic Copper Versus Extrinsic Nickel Adatoms. *Chem. - A Eur. J.* **2019**, *25* (8), 1975–1983.

[120] John, R. R. *CRC Handbook of Chemistry and Physics*; CRC Press, Boca Raton, 2019.

[121] Jung, M.; Sohn, S.-D.; Park, J.; Lee, K.-U.; Shin, H.-J. Fingerprints of Multiple Electron Scatterings in Single-Layer Graphene. *Sci. Rep.* **2016**, *6* (1), 1–6.

[122] DiBenedetto, S. A.; Facchetti, A.; Ratner, M. A.; Marks, T. J. Molecular Self-assembled Monolayers and Multilayers for Organic and Unconventional Inorganic Thin-film Transistor Applications. *Adv. Mater.* **2009**, *21* (14-15), 1407–1433.

[123] Orofeo, C. M.; Suzuki, S.; Kageshima, H.; Hibino, H. Growth and Low-Energy Electron Microscopy Characterization of Monolayer Hexagonal Boron Nitride on Epitaxial Cobalt. *Nano Res.* **2013**, *6* (5), 335–347.

[124] Khan, A. I.; Navid, I. A.; Noshin, M.; Subrina, S. Thermal Transport Characterization of Hexagonal Boron Nitride Nanoribbons Using Molecular Dynamics Simulation. *Aip Adv.* **2017**, *7* (10), 105110.

[125] Li, X.-D.; Cheng, X.-L. Predicting the Structural and Electronic Properties of Two-Dimensional Single Layer Boron Nitride Sheets. *Chem. Phys. Lett.* **2018**, *694*, 102–106.

[126] Schwarz, M.; Riss, A.; Garnica, M.; Ducke, J.; Deimel, P. S.; Duncan, D. A.; Thakur, P. K.; Lee, T.-L.; Seitsonen, A. P.; Barth, J. V. Corrugation in the Weakly Interacting Hexagonal-BN/Cu (111) System: Structure Determination by Combining Noncontact Atomic Force Microscopy and X-Ray Standing Waves. *ACS Nano* **2017**, *11* (9), 9151–9161.

[127] Wang, L.; Zihlmann, S.; Liu, M.-H.; Makk, P.; Watanabe, K.; Taniguchi, T.; Baumgartner, A.; Schönenberger, C. New Generation of Moiré Superlattices in Doubly Aligned HBN/Graphene/HBN Heterostructures. *Nano Lett.* **2019**, *19* (4), 2371–2376.

[128] Zhang, Q.; Yu, J.; Ebert, P.; Zhang, C.; Pan, C. R.; Chou, M. Y.; Shih, C. K.; Zeng, C.; Yuan, S. Tuning Band Gap and Work Function Modulations in Monolayer HBN/Cu(111) Heterostructures with Moiré Patterns. *ACS Nano* **2018**, *12* (9), 9355–9362.

[129] Rizzo, D. J.; Dai, Q.; Bronner, C.; Veber, G.; Smith, B. J.; Matsumoto, M.; Thomas, S.; Nguyen, G. D.; Forrester, P. R.; Zhao, W.; Jørgensen, J. H.; Dichtel, W. R.; Fischer, F. R.; Li, H.; Bredas, J. L.; Crommie, M. F. Revealing the Local Electronic Structure of a Single-Layer Covalent Organic Framework through Electronic Decoupling. *Nano Lett.* **2020**, *20* (2), 963–970.

[130] Joshi, S.; Ecija, D.; Koitz, R.; Iannuzzi, M.; Seitsonen, A. P.; Hutter, J.; Sachdev, H.; Vijayaraghavan, S.; Bischoff, F.; Seufert, K. Boron Nitride on Cu (111): An Electronically Corrugated Monolayer. *Nano Lett.* **2012**, *12* (11), 5821–5828.

[131] Chen, C. J. *Introduction to Scanning Tunneling Microscopy*; Oxford University Press on Demand, 1993; Vol. 4.

[132] Press Release Page. https://www.nobelprize.org/prizes/physics/1986/press-release/ (accessed Jan 21, 2021).

[133] Schmid, M.; Pietrzak, G. Schematic Diagram of a Scanning Tunneling Microscope https://commons.wikimedia.org/wiki/File:Rastertunnelmikroskop-schema.svg (accessed Jan 14, 2021).

[134] Shankar, R. *Principles of Quantum Mechanics*; Springer Science & Business Media, 2012.

[135] Bardeen, J. Tunnelling from a Many-Particle Point of View. *Phys. Rev. Lett.* **1961**, *6* (2), 57.

[136] Tersoff, J.; Hamann, D. R. Theory and Application for the Scanning Tunneling Microscope. *Phys. Rev. Lett.* **1983**, *50* (25), 1998.

[137] Tersoff, J.; Hamann, D. R. Theory of the Scanning Tunneling Microscope. *Phys. Rev.*

B **1985**, *31* (2), 805.
[138] Selloni, A.; Carnevali, P.; Tosatti, E.; Chen, C. D. Voltage-Dependent Scanning-Tunneling Microscopy of a Crystal Surface: Graphite. In *Scanning Tunneling Microscopy*; Springer, 1985; pp 168–171.
[139] Binnig, G.; Rohrer, H.; Gerber, C.; Weibel, E. 7× 7 Reconstruction on Si (111) Resolved in Real Space. *Phys. Rev. Lett.* **1983**, *50* (2), 120.
[140] Becker, R. S.; Golovchenko, J. A.; McRae, E. G.; Swartzentruber, B. S. Tunneling Images of Atomic Steps on the Si (111) 7× 7 Surface. *Phys. Rev. Lett.* **1985**, *55* (19), 2028.
[141] Jelic, V.; Iwaszczuk, K.; Nguyen, P. H.; Rathje, C.; Hornig, G. J.; Sharum, H. M.; Hoffman, J. R.; Freeman, M. R.; Hegmann, F. A. Ultrafast Terahertz Control of Extreme Tunnel Currents through Single Atoms on a Silicon Surface. *Nat. Phys.* **2017**, *13* (6), 591–598.
[142] Li, Q. L.; Zheng, C.; Wang, R.; Miao, B. F.; Cao, R. X.; Sun, L.; Wu, D.; Wu, Y. Z.; Li, S. C.; Wang, B. G. Role of the Surface State in the Kondo Resonance Width of a Co Single Adatom on Ag (111). *Phys. Rev. B* **2018**, *97* (3), 35417.
[143] Meierott, S.; Néel, N.; Kröger, J. Kondo Effect of Single Co Atoms on Au (110). *Phys. Rev. B* **2015**, *91* (20), 201111.
[144] Simic-Milosevic, V.; Heyde, M.; Nilius, N.; Nowicki, M.; Rust, H.-P.; Freund, H.-J. Substrate-Mediated Interaction and Electron-Induced Diffusion of Single Lithium Atoms on Ag (001). *Phys. Rev. B* **2007**, *75* (19), 195416.
[145] Schiffrin, A.; Capsoni, M.; Farahi, G.; Wang, C.-G.; Krull, C.; Castelli, M.; Roussy, T.; Cochrane, K. A.; Yin, Y.; Medhekar, N. V. Designing Optoelectronic Properties by On-Surface Synthesis: Formation and Electronic Structure of an Iron–Terpyridine Macromolecular Complex. *ACS Nano* **2018**, *12* (7), 6545–6553.
[146] Civita, D.; Kolmer, M.; Simpson, G. J.; Li, A.-P.; Hecht, S.; Grill, L. Control of Long-Distance Motion of Single Molecules on a Surface. *Science* **2020**, *370* (6519), 957–960.
[147] Garlant, A.; Maughan, B.; Zahl, P.; Monti, O. L. A. H2Pc and Pentacene on Cu (110)-(2× 1) O: A Combined STM and Nc-AFM Study. *Surf. Sci.* **2020**, *696*, 121590.
[148] Blowey, P. J.; Rochford, L. A.; Duncan, D. A.; Ryan, P. T. P.; Warr, D. A.; Lee, T.-L.; Costantini, G.; Woodruff, D. P. The Structure of 2D Charge Transfer Salts Formed by TCNQ/Alkali Metal Coadsorption on Ag (111). *Surf. Sci.* **2020**, *701*, 121687.
[149] Gao, Z.; Gao, Y.; Hua, M.; Liu, J.; Huang, L.; Lin, N. Design and Synthesis of a Single-Layer Ferromagnetic Metal–Organic Framework with Topological Nontrivial Gaps. *J. Phys. Chem. C* **2020**, *124* (49), 27017–27023.
[150] Zhang, R.; Liu, J.; Gao, Y.; Hua, M.; Xia, B.; Knecht, P.; Papageorgiou, A. C.; Reichert, J.; Barth, J. V; Xu, H. On-surface Synthesis of a Semiconducting 2D Metal–Organic Framework Cu3 (C6O6) Exhibiting Dispersive Electronic Bands. *Angew. Chemie* **2020**, *132* (7), 2691–2695.
[151] Xue, Q.; Xue, N.; Li, J.; Li, Y.; Li, R.; Zhang, Y.; Li, N.; Shen, Z.; Hou, S.; Wang, Y. Self-Assembly of a Metal–Organic Framework by Stepwise Coordination of Carboxyl and Pyrrolyl Groups. *J. Phys. Chem. C* **2020**, *124* (14), 7790–7796.
[152] Seifert, T. S.; Kovarik, S.; Nistor, C.; Persichetti, L.; Stepanow, S.; Gambardella, P. Single-Atom Electron Paramagnetic Resonance in a Scanning Tunneling Microscope Driven by a Radio-Frequency Antenna at 4 K. *Phys. Rev. Res.* **2020**, *2* (1), 13032.
[153] Willke, P.; Yang, K.; Bae, Y.; Heinrich, A. J.; Lutz, C. P. Magnetic Resonance Imaging of Single Atoms on a Surface. *Nat. Phys.* **2019**, *15* (10), 1005–1010.
[154] Fernandes, E.; Donati, F.; Patthey, F.; Stavrić, S.; Šljivančanin, Ž.; Brune, H. Adsorption Sites of Individual Metal Atoms on Ultrathin MgO (100) Films. *Phys. Rev. B* **2017**, *96* (4), 45419.
[155] Peng, Z.; Di, B.; Li, W.; Liu, D.; Wen, X.; Zhu, H.; Song, H.; Zhang, Y.; Yin, C.; Zhou, X. Reversibly Switching the Charge State and Adsorption Location of Single Potassium Atom on Ultrathin CuO Film. *Angew. Chemie Int. Ed.* **2020**, *59* (34), 14321–14325.
[156] Zhou, X.; Yang, W.; Chen, Q.; Geng, Z.; Shao, X.; Li, J.; Wang, Y.; Dai, D.; Chen, W.;

Xu, G. Stable Pt Single Atoms and Nanoclusters on Ultrathin CuO Film and Their Performances in CO Oxidation. *J. Phys. Chem. C* **2016**, *120* (3), 1709–1715.
[157] Repp, J.; Meyer, G.; Olsson, F. E.; Persson, M. Controlling the Charge State of Individual Gold Adatoms. *Science* **2004**, *305* (5683), 493–495.
[158] Miwa, K.; Imada, H.; Kawahara, S.; Kim, Y. Effects of Molecule-Insulator Interaction on Geometric Property of a Single Phthalocyanine Molecule Adsorbed on an Ultrathin NaCl Film. *Phys. Rev. B* **2016**, *93* (16), 165419.
[159] Ardhuin, T.; Guillermet, O.; Gourdon, A.; Gauthier, S. Molecular Resonance Imaging and Manipulation of Hexabenzocoronene on NaCl (001) and KBr (001) on Ag (111). *J. Phys. Chem. C* **2018**, *122* (22), 11905–11910.
[160] Khajetoorians, A. A.; Valentyuk, M.; Steinbrecher, M.; Schlenk, T.; Shick, A.; Kolorenc, J.; Lichtenstein, A. I.; Wehling, T. O.; Wiesendanger, R.; Wiebe, J. Tuning Emergent Magnetism in a Hund's Impurity. *Nat. Nanotechnol.* **2015**, *10* (11), 958–964.
[161] Yan, L.; Kuang, G.; Zhang, Q.; Shang, X.; Liu, P. N.; Lin, N. Self-Assembly of a Binodal Metal–Organic Framework Exhibiting a Demi-Regular Lattice. *Faraday Discuss.* **2017**, *204*, 111–121.
[162] Crommie, M. F.; Lutz, C. P.; Eigler, D. M. Confinement of Electrons to Quantum Corrals on a Metal Surface. *Science* **1993**, *262* (5131), 218–220.
[163] Gomes, K. K.; Mar, W.; Ko, W.; Guinea, F.; Manoharan, H. C. Designer Dirac Fermions and Topological Phases in Molecular Graphene. *Nature* **2012**, *483* (7389), 306–310.
[164] IBM Research. A Boy And His Atom: The World's Smallest Movie https://www.research.ibm.com/articles/madewithatoms.shtml (accessed Jan 15, 2021).
[165] Chiang, C.; Xu, C.; Han, Z.; Ho, W. Real-Space Imaging of Molecular Structure and Chemical Bonding by Single-Molecule Inelastic Tunneling Probe. *Science* **2014**, *344* (6186), 885–888.
[166] Gross, L.; Moll, N.; Mohn, F.; Curioni, A.; Meyer, G.; Hanke, F.; Persson, M. High-Resolution Molecular Orbital Imaging Using a p-Wave STM Tip. *Phys. Rev. Lett.* **2011**, *107* (8), 86101.
[167] Gross, L.; Mohn, F.; Moll, N.; Liljeroth, P.; Meyer, G. The Chemical Structure of a Molecule Resolved by Atomic Force Microscopy. *Science* **2009**, *325* (5944), 1110–1114.
[168] Krejčí, O.; Hapala, P.; Ondráček, M.; Jelínek, P. Principles and Simulations of High-Resolution STM Imaging with a Flexible Tip Apex. *Phys. Rev. B* **2017**, *95* (4), 45407.
[169] Chutora, T.; de la Torre, B.; Mutombo, P.; Hellerstedt, J.; Kopeček, J.; Jelínek, P.; Švec, M. Nitrous Oxide as an Effective AFM Tip Functionalization: A Comparative Study. *Beilstein J. Nanotechnol.* **2019**, *10* (1), 315–321.
[170] Mönig, H.; Amirjalayer, S.; Timmer, A.; Hu, Z.; Liu, L.; Arado, O. D.; Cnudde, M.; Strassert, C. A.; Ji, W.; Rohlfing, M. Quantitative Assessment of Intermolecular Interactions by Atomic Force Microscopy Imaging Using Copper Oxide Tips. *Nat. Nanotechnol.* **2018**, *13* (5), 371–375.
[171] Bartels, L.; Meyer, G.; Rieder, K.-H. Controlled Vertical Manipulation of Single CO Molecules with the Scanning Tunneling Microscope: A Route to Chemical Contrast. *Appl. Phys. Lett.* **1997**, *71* (2), 213–215.
[172] Zandvliet, H.; van Houselt, A. Scanning Tunneling Spectroscopy. *Annu. Rev. Anal. Chem.* **2009**, *2* (1), 37–55.
[173] Ho, W. Single-Molecule Chemistry. *J. Chem. Phys.* **2002**, *117* (24), 11033–11061.
[174] Franke, K. J.; Pascual, J. I. Effects of Electron-Vibration Coupling in Transport through Single Molecules. *J. Phys. Condens. Matter* **2012**, *24* (39), 394002.
[175] Fernández-Torrente, I.; Franke, K. J.; Pascual, J. I. Vibrational Kondo Effect in Pure Organic Charge-Transfer Assemblies. *Phys. Rev. Lett.* **2008**, *101* (21), 217203.
[176] Heinrich, A. J.; Gupta, J. A.; Lutz, C. P.; Eigler, D. M. Single-Atom Spin-Flip Spectroscopy. *Science* **2004**, *306* (5695), 466–469.
[177] Ünal, A. A.; Tusche, C.; Ouazi, S.; Wedekind, S.; Chiang, C.-T.; Winkelmann, A.; Sander, D.; Henk, J.; Kirschner, J. Hybridization between the Unoccupied Shockley Surface State and Bulk Electronic States on Cu (111). *Phys. Rev. B* **2011**, *84* (7), 73107.

[178] Schouteden, K.; Lievens, P.; Van Haesendonck, C. Fourier-Transform Scanning Tunneling Microscopy Investigation of the Energy versus Wave Vector Dispersion of Electrons at the Au (111) Surface. *Phys. Rev. B* **2009**, *79* (19), 195409.
[179] Rutter, G. M.; Crain, J. N.; Guisinger, N. P.; Li, T.; First, P. N.; Stroscio, J. A. Scattering and Interference in Epitaxial Graphene. *Science* **2007**, *317* (5835), 219–222.
[180] Leicht, P.; Tesch, J.; Bouvron, S.; Blumenschein, F.; Erler, P.; Gragnaniello, L.; Fonin, M. Rashba Splitting of Graphene-Covered Au (111) Revealed by Quasiparticle Interference Mapping. *Phys. Rev. B* **2014**, *90* (24), 241406.
[181] Hoffman, J. E.; McElroy, K.; Lee, D.-H.; Lang, K. M.; Eisaki, H.; Uchida, S.; Davis, J. C. Imaging Quasiparticle Interference in Bi2Sr2CaCu2O8+ δ. *Science* **2002**, *297* (5584), 1148–1151.
[182] Kreisel, A.; Choubey, P.; Berlijn, T.; Ku, W.; Andersen, B. M.; Hirschfeld, P. J. Interpretation of Scanning Tunneling Quasiparticle Interference and Impurity States in Cuprates. *Phys. Rev. Lett.* **2015**, *114* (21), 217002.
[183] Hao, Z.; Zou, C.; Luo, X.; Ji, Y.; Xu, M.; Ye, S.; Zhou, X.; Lin, C.; Wang, Y. Anomalous Doping Evolution of Superconductivity and Quasiparticle Interference in Bi 2 Sr 2 Ca 2 Cu 3 O 10+ δ Trilayer Cuprates. *Phys. Rev. Lett.* **2020**, *125* (23), 237005.
[184] Gyenis, A.; Drozdov, I. K.; Nadj-Perge, S.; Jeong, O. B.; Seo, J.; Pletikosić, I.; Valla, T.; Gu, G. D.; Yazdani, A. Quasiparticle Interference on the Surface of the Topological Crystalline Insulator Pb 1− x Sn x Se. *Phys. Rev. B* **2013**, *88* (12), 125414.
[185] Lee, W.-C.; Wu, C.; Arovas, D. P.; Zhang, S.-C. Quasiparticle Interference on the Surface of the Topological Insulator Bi 2 Te 3. *Phys. Rev. B* **2009**, *80* (24), 245439.
[186] Lin, C.-L.; Arafune, R.; Liu, R.-Y.; Yoshimura, M.; Feng, B.; Kawahara, K.; Ni, Z.; Minamitani, E.; Watanabe, S.; Shi, Y. Visualizing Type-II Weyl Points in Tungsten Ditelluride by Quasiparticle Interference. *ACS Nano* **2017**, *11* (11), 11459–11465.
[187] Inoue, H.; Gyenis, A.; Wang, Z.; Li, J.; Oh, S. W.; Jiang, S.; Ni, N.; Bernevig, B. A.; Yazdani, A. Quasiparticle Interference of the Fermi Arcs and Surface-Bulk Connectivity of a Weyl Semimetal. *Science* **2016**, *351* (6278), 1184–1187.
[188] Pham, V. D.; Repain, V.; Chacon, C.; Bellec, A.; Girard, Y.; Rousset, S.; Smogunov, A.; Dappe, Y. J.; Lagoute, J. Control of Molecule–Metal Interaction by Hydrogen Manipulation in an Organic Molecule. *J. Phys. Chem. Lett.* **2016**, *7* (8), 1416–1421.
[189] Tu, X. W.; Mikaelian, G.; Ho, W. Controlling Single-Molecule Negative Differential Resistance in a Double-Barrier Tunnel Hunction. *Phys. Rev. Lett.* **2008**, *100* (12), 2–5.
[190] Ménard, G. C.; Mesaros, A.; Brun, C.; Debontridder, F.; Roditchev, D.; Simon, P.; Cren, T. Isolated Pairs of Majorana Zero Modes in a Disordered Superconducting Lead Monolayer. *Nat. Commun.* **2019**, *10* (1), 1–7.
[191] Imai-Imada, M.; Imada, H.; Miwa, K.; Jung, J.; Shimizu, T. K.; Kawai, M.; Kim, Y. Energy-Level Alignment of a Single Molecule on Ultrathin Insulating Film. *Phys. Rev. B* **2018**, *98* (20), 201403.
[192] Binnig, G.; Quate, C. F.; Gerber, C. Atomic Force Microscope. *Phys. Rev. Lett.* **1986**, *56* (9), 930.
[193] Giessibl, F. J. Atomic Resolution of the Silicon (111)-(7x7) Surface by Atomic Force Microscopy. *Science* **1995**, *267* (5194), 68–71.
[194] Lennard-Jones, J. E.; Devonshire, A. F. Critical Phenomena in Gases-I. *Proc. R. Soc. London. Ser. A-Mathematical Phys. Sci.* **1937**, *163* (912), 53–70.
[195] Dürig, U.; Gimzewski, J. K.; Pohl, D. W. Experimental Observation of Forces Acting during Scanning Tunneling Microscopy. *Phys. Rev. Lett.* **1986**, *57* (19), 2403.
[196] Albrecht, T. R.; Grütter, P.; Horne, D.; Rugar, D. Frequency Modulation Detection Using High-Q Cantilevers for Enhanced Force Microscope Sensitivity. *J. Appl. Phys.* **1991**, *69* (2), 668–673.
[197] Giessibl, F. J. Advances in Atomic Force Microscopy. *Rev. Mod. Phys.* **2003**, *75* (3), 949.
[198] Peng, J.; Guo, J.; Hapala, P.; Cao, D.; Ma, R.; Cheng, B.; Xu, L.; Ondráček, M.; Jelínek, P.; Wang, E. Weakly Perturbative Imaging of Interfacial Water with Submolecular Resolution by Atomic Force Microscopy. *Nat. Commun.* **2018**, *9* (1), 1–7.

[199] Sader, J. E.; Jarvis, S. P. Accurate Formulas for Interaction Force and Energy in Frequency Modulation Force Spectroscopy. *Appl. Phys. Lett.* **2004**, *84* (10), 1801.
[200] Labidi, H.; Koleini, M.; Huff, T.; Salomons, M.; Cloutier, M.; Pitters, J.; Wolkow, R. A. Indications of Chemical Bond Contrast in AFM Images of a Hydrogen-Terminated Silicon Surface. *Nat. Commun.* **2017**, *8* (1), 1–7.
[201] Schuler, B.; Liu, W.; Tkatchenko, A.; Moll, N.; Meyer, G.; Mistry, A.; Fox, D.; Gross, L. Adsorption Geometry Determination of Single Molecules by Atomic Force Microscopy. *Phys. Rev. Lett.* **2013**, *111* (10), 106103.
[202] Lee, A. J.; Sakai, Y.; Kim, M.; Chelikowsky, J. R. Repulsive Tip Tilting as the Dominant Mechanism for Hydrogen Bond-like Features in Atomic Force Microscopy Imaging. *Appl. Phys. Lett.* **2016**, *108* (19), 193102.
[203] Hapala, P.; Kichin, G.; Wagner, C.; Tautz, F. S.; Temirov, R.; Jelínek, P. Mechanism of High-Resolution STM/AFM Imaging with Functionalized Tips. *Phys. Rev. B* **2014**, *90* (8), 85421.
[204] Mönig, H. Copper-Oxide Tip Functionalization for Submolecular Atomic Force Microscopy. *Chem. Commun.* **2018**, *54* (71), 9874–9888.
[205] Gross, L.; Mohn, F.; Liljeroth, P.; Repp, J.; Giessibl, F. J.; Meyer, G. Measuring the Charge State of an Adatom with Noncontact Atomic Force Microscopy. *Science* **2009**, *324* (5933), 1428–1431.
[206] Gross, L.; Mohn, F.; Moll, N.; Meyer, G.; Ebel, R.; Abdel-Mageed, W. M.; Jaspars, M. Organic Structure Determination Using Atomic-Resolution Scanning Probe Microscopy. *Nat. Chem.* **2010**, *2* (10), 821–825.
[207] Lämmle, K.; Trevethan, T.; Schwarz, A.; Watkins, M.; Shluger, A.; Wiesendanger, R. Unambiguous Determination of the Adsorption Geometry of a Metal− Organic Complex on a Bulk Insulator. *Nano Lett.* **2010**, *10* (8), 2965–2971.
[208] Wickenburg, S.; Lu, J.; Lischner, J.; Tsai, H.-Z.; Omrani, A. A.; Riss, A.; Karrasch, C.; Bradley, A.; Jung, H. S.; Khajeh, R. Tuning Charge and Correlation Effects for a Single Molecule on a Graphene Device. *Nat. Commun.* **2016**, *7* (1), 1–7.
[209] Gross, L.; Mohn, F.; Moll, N.; Schuler, B.; Criado, A.; Guitián, E.; Peña, D.; Gourdon, A.; Meyer, G. Bond-Order Discrimination by Atomic Force Microscopy. *Science* **2012**, *337* (6100), 1326–1329.
[210] Riss, A.; Wickenburg, S.; Gorman, P.; Tan, L. Z.; Tsai, H.-Z.; de Oteyza, D. G.; Chen, Y.-C.; Bradley, A. J.; Ugeda, M. M.; Etkin, G. Local Electronic and Chemical Structure of Oligo-Acetylene Derivatives Formed through Radical Cyclizations at a Surface. *Nano Lett.* **2014**, *14* (5), 2251–2255.
[211] Pavliček, N.; Schuler, B.; Collazos, S.; Moll, N.; Pérez, D.; Guitián, E.; Meyer, G.; Peña, D.; Gross, L. On-Surface Generation and Imaging of Arynes by Atomic Force Microscopy. *Nat. Chem.* **2015**, *7* (8), 623–628.
[212] Leoni, T.; Guillermet, O.; Walch, H.; Langlais, V.; Scheuermann, A.; Bonvoisin, J.; Gauthier, S. Controlling the Charge State of a Single Redox Molecular Switch. *Phys. Rev. Lett.* **2011**, *106* (21), 216103.
[213] Steurer, W.; Fatayer, S.; Gross, L.; Meyer, G. Probe-Based Measurement of Lateral Single-Electron Transfer between Individual Molecules. *Nat. Commun.* **2015**, *6* (1), 1–5.
[214] Mohn, F.; Gross, L.; Moll, N.; Meyer, G. Imaging the Charge Distribution within a Single Molecule. *Nat. Nanotechnol.* **2012**, *7* (4), 227–231.
[215] Albrecht, F.; Repp, J.; Fleischmann, M.; Scheer, M.; Ondráček, M.; Jelínek, P. Probing Charges on the Atomic Scale by Means of Atomic Force Microscopy. *Phys. Rev. Lett.* **2015**, *115* (7), 76101.
[216] Schuler, B.; Zhang, Y.; Collazos, S.; Fatayer, S.; Meyer, G.; Pérez, D.; Guitián, E.; Harper, M. R.; Kushnerick, J. D.; Pena, D. Characterizing Aliphatic Moieties in Hydrocarbons with Atomic Force Microscopy. *Chem. Sci.* **2017**, *8* (3), 2315–2320.
[217] Schuler, B.; Fatayer, S.; Mohn, F.; Moll, N.; Pavliček, N.; Meyer, G.; Peña, D.; Gross, L. Reversible Bergman Cyclization by Atomic Manipulation. *Nat. Chem.* **2016**, *8* (3), 220–224.

[218] Pan, S. H.; Hudson, E. W.; Davis, J. C. 3 He Refrigerator Based Very Low Temperature Scanning Tunneling Microscope. *Rev. Sci. Instrum.* **1999**, *70* (2), 1459–1463.
[219] Schwarz, U. D.; Haefke, H.; Reimann, P.; Güntherodt, H. Tip Artefacts in Scanning Force Microscopy. *J. Microsc.* **1994**, *173* (3), 183–197.
[220] Hanke, F.; Björk, J. Structure and Local Reactivity of the Au (111) Surface Reconstruction. *Phys. Rev. B* **2013**, *87* (23), 235422.
[221] Walen, H.; Liu, D.-J.; Oh, J.; Lim, H.; Evans, J. W.; Kim, Y.; Thiel, P. A. Self-Organization of S Adatoms on Au (111):√ 3R30 Rows at Low Coverage. *J. Chem. Phys.* **2015**, *143* (1), 14704.
[222] Roch, N.; Florens, S.; Bouchiat, V.; Wernsdorfer, W.; Balestro, F. Quantum Phase Transition in a Single-Molecule Quantum Dot. *Nature* **2008**, *453* (7195), 633–637.
[223] Martínez-Blanco, J.; Nacci, C.; Erwin, S. C.; Kanisawa, K.; Locane, E.; Thomas, M.; Von Oppen, F.; Brouwer, P. W.; Fölsch, S. Gating a Single-Molecule Transistor with Individual Atoms. *Nat. Phys.* **2015**, *11* (8), 640–644.
[224] Roth, K. M.; Dontha, N.; Dabke, R. B.; Gryko, D. T.; Clausen, C.; Lindsey, J. S.; Bocian, D. F.; Kuhr, W. G. Molecular Approach toward Information Storage Based on the Redox Properties of Porphyrins in Self-Assembled Monolayers. *J. Vac. Sci. Technol. B Microelectron. Nanom. Struct. Process. Meas. Phenom.* **2000**, *18* (5), 2359–2364.
[225] Loss, D.; DiVincenzo, D. P. Quantum Computation with Quantum Dots. *Phys. Rev. A* **1998**, *57* (1), 120.
[226] McCreery, R. L. Molecular Electronic Junctions. *Chem. Mater.* **2004**, *16* (23), 4477–4496.
[227] Frank, K. H.; Yannoulis, P.; Dudde, R.; Koch, E. E. Unoccupied Molecular Orbitals of Aromatic Hydrocarbons Adsorbed on Ag(111). *J. Chem. Phys.* **1988**, *89* (12), 7569–7576.
[228] Duhm, S.; Bürker, C.; Niederhausen, J.; Salzmann, I.; Hosokai, T.; Duvernay, J.; Kera, S.; Schreiber, F.; Koch, N.; Ueno, N.; Gerlach, A. Pentacene on Ag(111): Correlation of Bonding Distance with Intermolecular Interaction and Order. *ACS Appl. Mater. Interfaces* **2013**, *5* (19), 9377–9381.
[229] Eremtchenko, M.; Temirov, R.; Bauer, D.; Schaefer, J. A.; Tautz, F. S. Formation of Molecular Order on a Disordered Interface Layer: Pentacene/Ag (111). *Phys. Rev. B* **2005**, *72* (11), 115430.
[230] Lu, M. C.; Wang, R. Bin; Yang, A.; Duhm, S. Pentacene on Au(1 1 1), Ag(1 1 1) and Cu(1 1 1): From Physisorption to Chemisorption. *J. Phys. Condens. Matter* **2016**, *28* (9).
[231] Li, H. I.; Franke, K. J.; Pascual, J. I.; Bruch, L. W.; Diehl, R. D. Origin of Moiré Structures in c 60 on Pb (111) and Their Effect on Molecular Energy Levels. *Phys. Rev. B* **2009**, *80* (8), 85415.
[232] Parkinson, B. A.; Ohuchi, F. S.; Ueno, K.; Koma, A. Periodic Lattice Distortions as a Result of Lattice Mismatch in Epitaxial Films of Two-dimensional Materials. *Appl. Phys. Lett.* **1991**, *58* (5), 472–474.
[233] Hermann, K. Periodic Overlayers and Moiré Patterns: Theoretical Studies of Geometric Properties. *J. Phys. Condens. Matter* **2012**, *24* (31), 314210.
[234] Likharev, K. K. Single-Electron Devices and Their Applications. **1999**, *87* (4), 606–632.
[235] Kubatkin, S.; Danilov, A.; Hjort, M.; Cornil, J.; Bredas, J.-L.; Stuhr-Hansen, N.; Hedegård, P.; Bjørnholm, T. Single-Electron Transistor of a Single Organic Molecule with Access to Several Redox States. *Nature* **2003**, *425* (6959), 698–701.
[236] Kocić, N.; Decurtins, S.; Liu, S. X.; Repp, J. Forces from Periodic Charging of Adsorbed Molecules. *J. Chem. Phys.* **2017**, *146* (9).
[237] Sessi, P.; Bathon, T.; Kokh, K. A.; Tereshchenko, O. E.; Bode, M. Single Electron Gating of Topological Insulators. *Adv. Mater.* **2016**, *28* (45), 10073–10078.
[238] Brar, V. W.; Decker, R.; Solowan, H. M.; Wang, Y.; Maserati, L.; Chan, K. T.; Lee, H.; Girit, Ç. O.; Zettl, A.; Louie, S. G.; Cohen, M. L.; Crommie, M. F. Gate-Controlled Ionization and Screening of Cobalt Adatoms on a Graphene Surface. *Nat. Phys.* **2011**,

7 (1), 43–47.
[239] Nazin, G. V.; Qiu, X. H.; Ho, W. Charging and Interaction of Individual Impurities in a Monolayer Organic Crystal. *Phys. Rev. Lett.* **2005**, *95* (16), 1–4.
[240] Pradhan, N. A.; Liu, N.; Silien, C.; Ho, W. Atomic Scale Conductance Induced by Single Impurity Charging. *Phys. Rev. Lett.* **2005**, *94* (7), 1–4.
[241] Teichmann, K.; Wenderoth, M.; Loth, S.; Ulbrich, R. G.; Garleff, J. K.; Wijnheijmer, A. P.; Koenraad, P. M. Controlled Charge Switching on a Single Donor with a Scanning Tunneling Microscope. *Phys. Rev. Lett.* **2008**, *101* (7), 76103.
[242] Temirov, R.; Soubatch, S.; Luican, A.; Tautz, F. S. Free-Electron-like Dispersion in an Organic Monolayer Film on a Metal Substrate. *Nature* **2006**, *444* (7117), 350–353.
[243] Sabitova, A.; Temirov, R.; Tautz, F. S. Lateral Scattering Potential of the PTCDA/Ag(111) Interface State. *Phys. Rev. B* **2018**, *98* (20), 205429.
[244] Heinrich, B. W.; Limot, L.; Rastei, M. V; Iacovita, C.; Bucher, J. P.; Djimbi, D. M.; Massobrio, C.; Boero, M. Dispersion and Localization of Electronic States at a Ferrocene/Cu (111) Interface. *Phys. Rev. Lett.* **2011**, *107* (21), 216801.
[245] Wu, S. W.; Nazin, G. V.; Chen, X.; Qiu, X. H.; Ho, W. Control of Relative Tunneling Rates in Single Molecule Bipolar Electron Transport. *Phys. Rev. Lett.* **2004**, *93* (23), 1–4.
[246] Nazin, G. V; Wu, S. W.; Ho, W. Molecular Electronics Special Feature: Tunneling Rates in Electron Transport through Double-Barrier Molecular Junctions in a Scanning Tunneling Microscope. *Pnas* **2005**, *102* (25), 8832–8837.
[247] Liu, L.; Dienel, T.; Widmer, R.; Gröning, O. Interplay between Energy-Level Position and Charging Effect of Manganese Phthalocyanines on an Atomically Thin Insulator. *ACS Nano* **2015**, *9* (10), 10125–10132.
[248] Fernández Torrente, I.; Franke, K. J.; Ignacio Pascual, J. Spectroscopy of C60 Single Molecules: The Role of Screening on Energy Level Alignment. *J. Phys. Condens. Matter* **2008**, *20* (18).
[249] Hesper, R.; Tjeng, L. H.; Sawatzky, G. A. Strongly Reduced Band Gap in a Correlated Insulator in Close Proximity to a Metal. *Europhys. Lett.* **1997**, *40* (2), 177–182.
[250] Frisch, M. J.; Trucks, G. W.; Schlegel, H. B.; Scuseria, G. E.; Robb, M. A.; Cheeseman, J. R.; Scalmani, G.; Barone, V.; Petersson, G. A.; Nakatsuji, H. Gaussian 16. Gaussian, Inc. Wallingford, CT 2016.
[251] Teodorescu, C. M. Image Molecular Dipoles in Surface Enhanced Raman Scattering. *Phys. Chem. Chem. Phys.* **2015**, *17* (33), 21302–21314.
[252] Sekino, H.; Maeda, Y.; Kamiya, M.; Hirao, K. Polarizability and Second Hyperpolarizability Evaluation of Long Molecules by the Density Functional Theory with Long-Range Correction. *J. Chem. Phys.* **2007**, *126* (1), 14107.
[253] Ploigt, H. C.; Brun, C.; Pivetta, M.; Patthey, F.; Schneider, W. D. Local Work Function Changes Determined by Field Emission Resonances: NaCl/Ag (100). *Phys. Rev. B - Condens. Matter Mater. Phys.* **2007**, *76* (19), 1–5.
[254] Natori, K.; Otani, D.; Sano, N. Thickness Dependence of the Effective Dielectric Constant in a Thin Film Capacitor. *Appl. Phys. Lett.* **1998**, *73* (5), 632–634.
[255] Sacha, G. M.; Verdaguer, A.; Salmeron, M. A Model for the Characterization of the Polarizability of Thin Films Independently of the Thickness of the Film. *J. Phys. Chem. B* **2018**, *122* (2), 904–909.
[256] Scheuerer, P.; Patera, L. L.; Simbürger, F.; Queck, F.; Swart, I.; Schuler, B.; Gross, L.; Moll, N.; Repp, J. Charge-Induced Structural Changes in a Single Molecule Investigated by Atomic Force Microscopy. *Phys. Rev. Lett.* **2019**, *123* (6), 066001.
[257] Fatayer, S.; Albrecht, F.; Zhang, Y.; Urbonas, D.; Peña, D.; Moll, N.; Gross, L. Molecular Structure Elucidation with Charge-State Control. *Science* **2019**, *365* (6449), 142–145.
[258] Fatayer, S.; Schuler, B.; Steurer, W.; Scivetti, I.; Repp, J.; Gross, L.; Persson, M.; Meyer, G. Reorganization Energy upon Charging a Single Molecule on an Insulator Measured by Atomic Force Microscopy. *Nat. Nanotechnol.* **2018**, *13* (5), 376–380.
[259] Scott, J. C. Metal–Organic Interface and Charge Injection in Organic Electronic

Devices. *J. Vac. Sci. Technol. A* **2003**, *21* (3), 521–531.
[260] Zhu, X.-Y. Electronic Structure and Electron Dynamics at Molecule–Metal Interfaces: Implications for Molecule-Based Electronics. *Surf. Sci. Rep.* **2004**, *56* (1), 1–83.
[261] Marder, M. P. *Condensed Matter Physics*; John Wiley & Sons, 2010.
[262] Eschmann, L.; Sabitova, A.; Temirov, R.; Tautz, F. S.; Krüger, P.; Rohlfing, M. Coverage-Dependent Anisotropy of the NTCDA/Ag(111) Interface State Dispersion. *Phys. Rev. B* **2019**, *100* (12), 1–16.
[263] Armbrust, N.; Schiller, F.; Güdde, J.; Höfer, U. Model Potential for the Description of Metal/Organic Interface States. *Sci. Rep.* **2017**, *7* (1), 1–8.
[264] Tautz, F. S. Structure and Bonding of Large Aromatic Molecules on Noble Metal Surfaces: The Example of PTCDA. *Prog. Surf. Sci.* **2007**, *82* (9–12), 479–520.
[265] Stadtmüller, B.; Kröger, I.; Reinert, F.; Kumpf, C. Submonolayer Growth of CuPc on Noble Metal Surfaces. *Phys. Rev. B* **2011**, *83* (8), 85416.
[266] Malterre, D.; Kierren, B.; Fagot-Revurat, Y.; Pons, S.; Tejeda, A.; Didiot, C.; Cercellier, H.; Bendounan, A. ARPES and STS Investigation of Shockley States in Thin Metallic Films and Periodic Nanostructures. *New J. Phys.* **2007**, *9* (10), 391.
[267] Tamai, A.; Meevasana, W.; King, P. D. C.; Nicholson, C. W.; De La Torre, A.; Rozbicki, E.; Baumberger, F. Spin-Orbit Splitting of the Shockley Surface State on Cu (111). *Phys. Rev. B* **2013**, *87* (7), 75113.
[268] Yaji, K.; Harasawa, A.; Kuroda, K.; Li, R.; Yan, B.; Komori, F.; Shin, S. Rashba Spin Splitting of L-Gap Surface States on Ag (111) and Cu (111). *Phys. Rev. B* **2018**, *98* (4), 41404.
[269] Analytis, J. G.; Chu, J.-H.; Chen, Y.; Corredor, F.; McDonald, R. D.; Shen, Z. X.; Fisher, I. R. Bulk Fermi Surface Coexistence with Dirac Surface State in Bi 2 Se 3: A Comparison of Photoemission and Shubnikov–de Haas Measurements. *Phys. Rev. B* **2010**, *81* (20), 205407.
[270] Liu, D.; Li, C.; Huang, J.; Lei, B.; Wang, L.; Wu, X.; Shen, B.; Gao, Q.; Zhang, Y.; Liu, X. Orbital Origin of Extremely Anisotropic Superconducting Gap in Nematic Phase of FeSe Superconductor. *Phys. Rev. X* **2018**, *8* (3), 31033.
[271] Rhodes, L. C.; Watson, M. D.; Haghighirad, A. A.; Evtushinsky, D. V; Eschrig, M.; Kim, T. K. Scaling of the Superconducting Gap with Orbital Character in FeSe. *Phys. Rev. B* **2018**, *98* (18), 180503.
[272] Simon, L.; Bena, C.; Vonau, F.; Cranney, M.; Aubel, D. Fourier-Transform Scanning Tunnelling Spectroscopy: The Possibility to Obtain Constant-Energy Maps and Band Dispersion Using a Local Measurement. *J. Phys. D. Appl. Phys.* **2011**, *44* (46), 464010.
[273] Petersen, L.; Laitenberger, P.; Lægsgaard, E.; Besenbacher, F. Screening Waves from Steps and Defects on Cu (111) and Au (111) Imaged with STM: Contribution from Bulk Electrons. *Phys. Rev. B* **1998**, *58* (11), 7361.
[274] Bena, C. Friedel Oscillations: Decoding the Hidden Physics. *Comptes Rendus Phys.* **2016**, *17* (3), 302–321.
[275] Chen, L.; Cheng, P.; Wu, K. Quasiparticle Interference in Unconventional 2D Systems. *J. Phys. Condens. Matter* **2017**, *29* (10), 103001.
[276] Jerri, A. J. The Shannon Sampling Theorem—Its Various Extensions and Applications: A Tutorial Review. *Proc. IEEE* **1977**, *65* (11), 1565–1596.
[277] Becker, M.; Crampin, S.; Berndt, R. Lifetimes of Electrons in the Shockley Surface State Band of Ag (111). *Appl. Phys. A* **2007**, *88* (3), 555–557.
[278] Piquero-Zulaica, I.; Abd El-Fattah, Z. M.; Popova, O.; Kawai, S.; Nowakowska, S.; Matena, M.; Enache, M.; Stöhr, M.; Tejeda, A.; Taleb, A. Effective Determination of Surface Potential Landscapes from Metal-Organic Nanoporous Network Overlayers. *New J. Phys.* **2019**, *21* (5), 53004.
[279] Sachdev, S. Kagomé-and Triangular-Lattice Heisenberg Antiferromagnets: Ordering from Quantum Fluctuations and Quantum-Disordered Ground States with Unconfined Bosonic Spinons. *Phys. Rev. B* **1992**, *45* (21), 12377.
[280] Zheng, L.; Feng, L.; Yong-Shi, W. Exotic Electronic States in the World of Flat Bands: From Theory to Material. *Chinese Phys. B* **2014**, *23* (7), 77308.

[281] Alexandradinata, A.; Armitage, N. P.; Baydin, A.; Bi, W.; Cao, Y.; Changlani, H. J.; Chertkov, E.; Neto, E. H.; Delacretaz, L.; Baggari, I. El. The Future of the Correlated Electron Problem. *arXiv Prepr. arXiv2010.00584* **2020**.

[282] Ohashi, T.; Kawakami, N.; Tsunetsugu, H. Mott Transition in Kagomé Lattice Hubbard Model. *Phys. Rev. Lett.* **2006**, *97* (6), 66401.

[283] Tang, E.; Mei, J.-W.; Wen, X.-G. High-Temperature Fractional Quantum Hall States. *Phys. Rev. Lett.* **2011**, *106* (23), 236802.

[284] Guo, H.-M.; Franz, M. Topological Insulator on the Kagome Lattice. *Phys. Rev. B* **2009**, *80* (11), 113102.

[285] Guterding, D.; Jeschke, H. O.; Valentí, R. Prospect of Quantum Anomalous Hall and Quantum Spin Hall Effect in Doped Kagome Lattice Mott Insulators. *Sci. Rep.* **2016**, *6* (1), 1–8.

[286] Kim, H. S.; Mishra, A.; Lee, S. Emergent Chiral Spin Ordering and Anomalous Hall Effect in a Kagome Lattice at a 1/3 Filling. *Phys. Rev. B* **2020**, *102* (15), 155113.

[287] Ye, L.; Kang, M.; Liu, J.; Von Cube, F.; Wicker, C. R.; Suzuki, T.; Jozwiak, C.; Bostwick, A.; Rotenberg, E.; Bell, D. C. Massive Dirac Fermions in a Ferromagnetic Kagome Metal. *Nature* **2018**, *555* (7698), 638–642.

[288] Yin, J.-X.; Ma, W.; Cochran, T. A.; Xu, X.; Zhang, S. S.; Tien, H.-J.; Shumiya, N.; Cheng, G.; Jiang, K.; Lian, B. Quantum-Limit Chern Topological Magnetism in $TbMn_6Sn_6$. *Nature* **2020**, *583* (7817), 533–536.

[289] Cui, B.; Zheng, X.; Wang, J.; Liu, D.; Xie, S.; Huang, B. Realization of Lieb Lattice in Covalent-Organic Frameworks with Tunable Topology and Magnetism. *Nat. Commun.* **2020**, *11* (1), 1–8.

[290] Dong, L.; Gao, Z. A.; Lin, N. Self-Assembly of Metal–Organic Coordination Structures on Surfaces. *Prog. Surf. Sci.* **2016**, *91* (3), 101–135.

[291] Galeotti, G.; De Marchi, F.; Hamzehpoor, E.; MacLean, O.; Rajeswara Rao, M.; Chen, Y.; Besteiro, L. V.; Dettmann, D.; Ferrari, L.; Frezza, F.; Sheverdyaeva, P. M.; Liu, R.; Kundu, A. K.; Moras, P.; Ebrahimi, M.; Gallagher, M. C.; Rosei, F.; Perepichka, D. F.; Contini, G. Synthesis of Mesoscale Ordered Two-Dimensional π-Conjugated Polymers with Semiconducting Properties. *Nat. Mater.* **2020**, *19* (8), 874–880.

[292] Hsu, C.-H.; Liu, J.; Chuang, F.-C.; Zhang, R.; Xia, B.; Xu, H.; Huang, L.; Jin, Q.; Liu, P. N.; Lin, N. Synthesis and Characterization of a Single-Layer Conjugated Metal–Organic Structure Featuring a Non-Trivial Topological Gap. *Nanoscale* **2019**, *11* (3), 878–881.

[293] Nagaoka, K.; Jamneala, T.; Grobis, M.; Crommie, M. F. Temperature Dependence of a Single Kondo Impurity. *Phys. Rev. Lett.* **2002**, *88* (7), 077205.

[294] Eickhoff, F.; Kolodzeiski, E.; Esat, T.; Fournier, N.; Wagner, C.; Deilmann, T.; Temirov, R.; Rohlfing, M.; Tautz, F. S.; Anders, F. B. Inelastic Electron Tunneling Spectroscopy for Probing Strongly Correlated Many-Body Systems by Scanning Tunneling Microscopy. *Phys. Rev. B* **2020**, *101* (12), 125405.

[295] Zhao, A.; Li, Q.; Chen, L.; Xiang, H.; Wang, W.; Pan, S.; Wang, B.; Xiao, X.; Yang, J.; Hou, J. G.; Zhu, Q. Physics: Controlling the Kondo Effect of an Adsorbed Magnetic Ion through Its Chemical Bonding. *Science* **2005**, *309* (5740), 1542–1544.

[296] Lorente, N.; Persson, M.; Lauhon, L. J.; Ho, W. Symmetry Selection Rules for Vibrationally Inelastic Tunneling. *Phys. Rev. Lett.* **2001**, *86* (12), 2593–2596.

[297] Garnica, M.; Stradi, D.; Barja, S.; Calleja, F.; Díaz, C.; Alcamí, M.; Martín, N.; Vázquez de Parga, A. L.; Martín, F.; Miranda, R. Long-Range Magnetic Order in a Purely Organic 2D Layer Adsorbed on Epitaxial Graphene. *Nat. Phys.* **2013**, *9* (6), 368–374.

[298] Agarwala, A.; Shenoy, V. B. Quantum Impurities Develop Fractional Local Moments in Spin-Orbit Coupled Systems. *Phys. Rev. B* **2016**, *93* (24), 241111.

[299] Kuramoto, Y.; Kitaoka, Y. *Dynamics of Heavy Electrons*; Clarendon Press Oxford, 2000.

[300] Bulla, R.; Costi, T. A.; Pruschke, T. Numerical Renormalization Group Method for Quantum Impurity Systems. *Rev. Mod. Phys.* **2008**, *80* (2), 395.

[301] Perera, U. G. E.; Kulik, H. J.; Iancu, V.; Dias Da Silva, L. G. G. V; Ulloa, S. E.; Marzari,

N.; Hla, S. W. Spatially Extended Kondo State in Magnetic Molecules Induced by Interfacial Charge Transfer. *Phys. Rev. Lett.* **2010**, *105* (10), 106601.
[302] Choi, D.-J.; Guissart, S.; Ormaza, M.; Bachellier, N.; Bengone, O.; Simon, P.; Limot, L. Kondo Resonance of a Co Atom Exchange Coupled to a Ferromagnetic Tip. *Nano Lett.* **2016**, *16* (10), 6298–6302.
[303] Prüser, H.; Dargel, P. E.; Bouhassoune, M.; Ulbrich, R. G.; Pruschke, T.; Lounis, S.; Wenderoth, M. Interplay between the Kondo Effect and the Ruderman–Kittel–Kasuya–Yosida Interaction. *Nat. Commun.* **2014**, *5* (1), 1–8.
[304] Tsukahara, N.; Shiraki, S.; Itou, S.; Ohta, N.; Takagi, N.; Kawai, M. Evolution of Kondo Resonance from a Single Impurity Molecule to the Two-Dimensional Lattice. *Phys. Rev. Lett.* **2011**, *106* (18), 1–4.
[305] Spinelli, A.; Gerrits, M.; Toskovic, R.; Bryant, B.; Ternes, M.; Otte, A. F. Exploring the Phase Diagram of the Two-Impurity Kondo Problem. *Nat. Commun.* **2015**, *6* (1), 1–6.
[306] Prüser, H. Two-Impurity Kondo Physics. In *Scanning Tunneling Spectroscopy of Magnetic Bulk Impurities*; Springer, 2015; pp 75–95.
[307] Stöhr, J.; Siegmann, H. C. *Magnetism: From Fundamentals to Nanoscale Dynamics*; Springer-Verlag, Berlin, Heidelberg, 2006.
[308] Phillips, P. *Advanced Solid State Physics*; Cambridge University Press, Cambridge, 2012.
[309] Mott, N. F. Metal-Insulator Transition. *Rev. Mod. Phys.* **1968**, *40* (4), 677.
[310] Misumi, Y.; Yamaguchi, A.; Zhang, Z.; Matsushita, T.; Wada, N.; Tsuchiizu, M.; Awaga, K. Quantum Spin Liquid State in a Two-Dimensional Semiconductive Metal–Organic Framework. *J. Am. Chem. Soc.* **2020**, *142* (39), 16513–16517.
[311] Balents, L. Spin Liquids in Frustrated Magnets. *Nature* **2010**, *464* (7286), 199–208.
[312] Goodwin, Z. A. H.; Corsetti, F.; Mostofi, A. A.; Lischner, J. Twist-Angle Sensitivity of Electron Correlations in Moiré Graphene Bilayers. *Phys. Rev. B* **2019**, *100* (12), 121106.
[313] Coleman, P. Heavy Fermions: Electrons at the Edge of Magnetism. *Handb. Magn. Adv. Magn. Mater.* **2007**.
[314] Harutyunyan, H.; Callsen, M.; Allmers, T.; Caciuc, V.; Blügel, S.; Atodiresei, N.; Wegner, D. Hybridisation at the Organic–Metal Interface: A Surface-Scientific Analogue of Hückel's Rule? *Chem. Commun.* **2013**, *49* (53), 5993–5995.
[315] Hori, M.; Katano, S.; Kim, Y.; Kawai, M. Effect of the Substituent on Metal–Molecule Hybridization. *Surf. Sci.* **2008**, *602* (20), 3140–3143.
[316] Hollerer, M.; Lüftner, D.; Hurdax, P.; Ules, T.; Soubatch, S.; Tautz, F. S.; Koller, G.; Puschnig, P.; Sterrer, M.; Ramsey, M. G. Charge Transfer and Orbital Level Alignment at Inorganic/Organic Interfaces: The Role of Dielectric Interlayers. *ACS Nano* **2017**, *11* (6), 6252–6260.
[317] Lu, X.; Grobis, M.; Khoo, K. H.; Louie, S. G.; Crommie, M. F. Charge Transfer and Screening in Individual C 60 Molecules on Metal Substrates: A Scanning Tunneling Spectroscopy and Theoretical Study. *Phys. Rev. B* **2004**, *70* (11), 115418.
[318] Lee, T. H.; Kim, K.; Kim, G.; Park, H. J.; Scullion, D.; Shaw, L.; Kim, M.-G.; Gu, X.; Bae, W.-G.; Santos, E. J. G. Chemical Vapor-Deposited Hexagonal Boron Nitride as a Scalable Template for High-Performance Organic Field-Effect Transistors. *Chem. Mater.* **2017**, *29* (5), 2341–2347.
[319] Kang, S. J.; Lee, G.; Yu, Y.; Zhao, Y.; Kim, B.; Watanabe, K.; Taniguchi, T.; Hone, J.; Kim, P.; Nuckolls, C. Organic Field Effect Transistors Based on Graphene and Hexagonal Boron Nitride Heterostructures. *Adv. Funct. Mater.* **2014**, *24* (32), 5157–5163.
[320] Liljeroth, P.; Swart, I.; Paavilainen, S.; Repp, J.; Meyer, G. Single-Molecule Synthesis and Characterization of Metal− Ligand Complexes by Low-Temperature STM. *Nano Lett.* **2010**, *10* (7), 2475–2479.
[321] Grobis, M.; Wachowiak, A.; Yamachika, R.; Crommie, M. F. Tuning Negative Differential Resistance in a Molecular Film. *Appl. Phys. Lett.* **2005**, *86* (20), 1–3.
[322] Franke, K. J.; Schulze, G.; Henningsen, N.; Fernández-Torrente, I.; Pascual, J. I.; Zarwell, S.; Rück-Braun, K.; Cobian, M.; Lorente, N. Reducing the Molecule-Substrate

Coupling in C 60-Based Nanostructures by Molecular Interactions. *Phys. Rev. Lett.* **2008**, *100* (3), 36807.
[323] Qiu, X. H.; Nazin, G. V.; Ho, W. Vibronic States in Single Molecule Electron Transport. *Phys. Rev. Lett.* **2004**, *92* (20), 1–4.
[324] Newns, D. M.; Misewich, J. A.; Tsuei, C. C.; Gupta, A.; Scott, B. A.; Schrott, A. Mott Transition Field Effect Transistor. *Appl. Phys. Lett.* **1998**, *73* (6), 780–782.
[325] Zhou, C.; Newns, D. M.; Misewich, J. A.; Pattnaik, P. C. A Field Effect Transistor Based on the Mott Transition in a Molecular Layer. *Appl. Phys. Lett.* **1997**, *70* (5), 598–600.
[326] Kerelsky, A.; McGilly, L. J.; Kennes, D. M.; Xian, L.; Yankowitz, M.; Chen, S.; Watanabe, K.; Taniguchi, T.; Hone, J.; Dean, C. Maximized Electron Interactions at the Magic Angle in Twisted Bilayer Graphene. *Nature* **2019**, *572* (7767), 95–100.
[327] Clair, S.; de Oteyza, D. G. Controlling a Chemical Coupling Reaction on a Surface: Tools and Strategies for on-Surface Synthesis. *Chem. Rev.* **2019**, *119* (7), 4717–4776.
[328] Ara, F.; Oka, H.; Sainoo, Y.; Katoh, K.; Yamashita, M.; Komeda, T. Spin Properties of Single-Molecule Magnet of Double-Decker Tb (III)-Phthalocyanine (TbPc2) on Ferromagnetic Co Film Characterized by Spin Polarized STM (SP-STM). *J. Appl. Phys.* **2019**, *125* (18), 183901.
[329] Wiesendanger, R. Spin Mapping at the Nanoscale and Atomic Scale. *Rev. Mod. Phys.* **2009**, *81* (4), 1495.
[330] Kresse, G.; Furthmüller, J. Efficiency of Ab-Initio Total Energy Calculations for Metals and Semiconductors Using a Plane-Wave Basis Set. *Comput. Mater. Sci.* **1996**, *6* (1), 15–50.
[331] Perdew, J. P.; Burke, K.; Ernzerhof, M. Generalized Gradient Approximation Made Simple. *Phys. Rev. Lett.* **1996**, *77* (18), 3865–3868.
[332] Grimme, S. Semiempirical GGA-type Density Functional Constructed with a Long-range Dispersion Correction. *J. Comput. Chem.* **2006**, *27* (15), 1787–1799.
[333] Kalambet, Y.; Kozmin, Y.; Mikhailova, K.; Nagaev, I.; Tikhonov, P. Reconstruction of Chromatographic Peaks Using the Exponentially Modified Gaussian Function. *J. Chemom.* **2011**, *25* (7), 352–356.
[334] Blöchl, P. E. Projector Augmented-Wave Method. *Phys. Rev. B* **1994**, *50* (24), 17953–17979.
[335] Joubert, D. From Ultrasoft Pseudopotentials to the Projector Augmented-Wave Method. *Phys. Rev. B* **1999**, *59* (3), 1758–1775.
[336] Grimme, S.; Antony, J.; Ehrlich, S.; Krieg, H. A Consistent and Accurate Ab Initio Parametrization of Density Functional Dispersion Correction (DFT-D) for the 94 Elements H-Pu. *J. Chem. Phys.* **2010**, *132* (15), 154104.
[337] Dudarev, S.; Botton, G. Electron-Energy-Loss Spectra and the Structural Stability of Nickel Oxide: An LSDA+U Study. *Phys. Rev. B* **1998**, *57* (3), 1505–1509.
[338] Tolba, S. A.; Gameel, K. M.; Ali, B. A.; Almossalami, H. A.; Allam, N. K. *Density Functional Calculations: Recent Progresses of Theory and Application Ch. 1*; IntechOpen, London: London, 2018.
[339] Manz, T. A.; Sholl, D. S. Methods for Computing Accurate Atomic Spin Moments for Collinear and Noncollinear Magnetism in Periodic and Nonperiodic Materials. *J. Chem. Theory Comput.* **2011**, *7* (12), 4146–4164.
[340] Manz, T. A.; Limas, N. G. Introducing DDEC6 Atomic Population Analysis: Part 1. Charge Partitioning Theory and Methodology. *RSC Adv.* **2016**, *6* (53), 47771–47801.
[341] Limas, N. G.; Manz, T. A. Introducing DDEC6 Atomic Population Analysis: Part 2. Computed Results for a Wide Range of Periodic and Nonperiodic Materials. *RSC Adv.* **2016**, *6* (51), 45727–45747.
[342] Manz, T. A.; Limas, N. G. Program Computing DDEC Atomic Charges ddec.sourceforge.net.
[343] Tang, W.; Sanville, E.; Henkelman, G. A Grid-Based Bader Analysis Algorithm without Lattice Bias. *J. Phys. Condens. Matter* **2009**, *21* (8), 084204.
[344] Momma, K.; Izumi, F. VESTA 3 for Three-Dimensional Visualization of Crystal, Volumetric and Morphology Data. *J. Appl. Crystallogr.* **2011**, *44* (6), 1272–1276.

[345] Pulay, P. Convergence Acceleration of Iterative Sequences. the Case of Scf Iteration. *Chem. Phys. Lett.* **1980**, *73* (2), 393–398.
[346] Rohwedder, T.; Schneider, R. An Analysis for the DIIS Acceleration Method Used in Quantum Chemistry Calculations. *J. Math. Chem.* **2011**, *49* (9), 1889–1914.
[347] Vanpoucke, D. E. P.; Brocks, G. Formation of Pt-Induced Ge Atomic Nanowires on Pt/Ge (001): A Density Functional Theory Study. *Phys. Rev. B* **2008**, *77* (24), 241308.
[348] Hiraoka, R.; Minamitani, E.; Arafune, R.; Tsukahara, N.; Watanabe, S.; Kawai, M.; Takagi, N. Single-Molecule Quantum Dot as a Kondo Simulator. *Nat. Commun.* **2017**, *8* (1), 16012.
[349] Anderson, P. W. Absence of Diffusion in Certain Random Lattices. *Phys. Rev.* **1958**, *109* (5), 1492–1505.

Appendix A
DCA Monolayers on Ag(111)

Here, I present further details supporting the results presented on self-assembled DCA monolayers grown on Ag(111) such as in Chapter 3.

A.1 Theoretical Methods

The following details all the calculations, as performed by Dr. Yuefeng Yin, that were used to complement the experimental findings in Chapter 3.

The electronic structures of isolated DCA (**Figure 3.5**f) and DCA adsorbed on Ag(111) (**Figure 3.4**) were calculated by Density Functional Theory (DFT) as implemented in the Vienna *ab initio* simulation package (VASP) [330]. The Perdew-Burke-Ernzerhof (PBE) form of the generalised gradient approximation (GGA) was used to describe electron exchange and correlation [331] while a semi-empirical functional (DFT-D2) was used to describe dispersion forces [332]. In all relevant calculations, the plane-wave kinetic energy cut-off was set to 600 eV and all structures were relaxed until the ionic forces were smaller than 0.01 eV/Å. The Brillouin zone was sampled in a 9 × 9 × 1 Γ-centred cell for accurate calculations of the electronic structures.

A.2 DCA/Ag(111) Domains and Superstructure Periodicity

Given the three equivalent crystallographic axes <1,1,0> of Ag(111), and the relationship between these crystallographic axes and vectors $\{\mathbf{a_1}, \mathbf{a_2}\}$ defining a primitive unit of the molecular self-assembly (see section 3.2), there are six equivalent molecular domains. That is, two mirror-symmetric domains associated with each crystallographic axis <1,1,0>; see **Figure A.1**. It is important to note that the periodicity of the superstructure defined by the field-induced charging of DCA (unit cell vectors $\{\mathbf{c_1}, \mathbf{c_2}\}$; see section 3.2) can change slightly throughout the extent of the molecular film. That is, the relationship between vectors $\{\mathbf{c_1}, \mathbf{c_2}\}$ and $\{\mathbf{a_1}, \mathbf{a_2}\}$ [and hence $\{\mathbf{v_1}, \mathbf{v_2}\}$ defining a unit cell of Ag(111)] can vary slightly from one molecular domain to another, but remains commensurate. In **Figure 3.5** and **Figure 3.7** of Chapter 3 (where the periodicity of the superstructure along $\mathbf{a_1}$ is of 39 molecules), the relationship between $\{\mathbf{c_1}, \mathbf{c_2}\}$, $\{\mathbf{a_1}, \mathbf{a_2}\}$ is as follows:

$$\begin{pmatrix} \mathbf{c_1} \\ \mathbf{c_2} \end{pmatrix} = \begin{bmatrix} 33/2 & -1 \\ 6 & 2 \end{bmatrix} \begin{pmatrix} \mathbf{a_1} \\ \mathbf{a_2} \end{pmatrix} \qquad \text{(Eq. A.1)}$$

That is, $\mathbf{a_1}$ = 155/39$\mathbf{v_1}$ (≈ 3.97$\mathbf{v_1}$), $\mathbf{a_2}$ = 45/78$\mathbf{v_1}$ + 3$\mathbf{v_2}$ (≈ 0.577$\mathbf{v_1}$ + 3$\mathbf{v_2}$) and $\angle(\mathbf{a_1}, \mathbf{a_2}) = 50 \pm 2°$. This is very similar to the unit cell of the molecular domain in Figure 1 of the main text, where $\mathbf{a_1}$ = 199/50$\mathbf{v_1}$ (= 3.98$\mathbf{v_1}$), $\mathbf{a_2}$ = 14/25$\mathbf{v_1}$ + 3$\mathbf{v_2}$ (= 0.56$\mathbf{v_1}$ + 3$\mathbf{v_2}$) and $\angle(\mathbf{a_1}, \mathbf{a_2}) = 53 \pm 1°$. We can also observe this in **Figure A.1**, where the vectors $\mathbf{c_2}$ for each of the six equivalent molecular domains are different relative to $\{\mathbf{a_1}, \mathbf{a_2}\}$. We attribute these slight variations to: (i) the long range of the superstructure periodicity with respect to the molecular arrangement (i.e., the large number of molecular domain unit cells comprised in a superstructure unit cell can vary, with the relationship between vectors $\{\mathbf{a_1}, \mathbf{a_2}\}$ and $\{\mathbf{v_1}, \mathbf{v_2}\}$ remaining quasi-identical); and (ii) boundary effects, e.g., confinement of molecular domains to Ag(111) terraces of finite size, and morphology of boundaries between different molecular domains. Even if the unit cell of the 2D charging lattice may vary slightly due to the long-range periodicity of the superstructure, these variations remain small, with the superstructure unit cell area of 42 ± 5 nm^2.

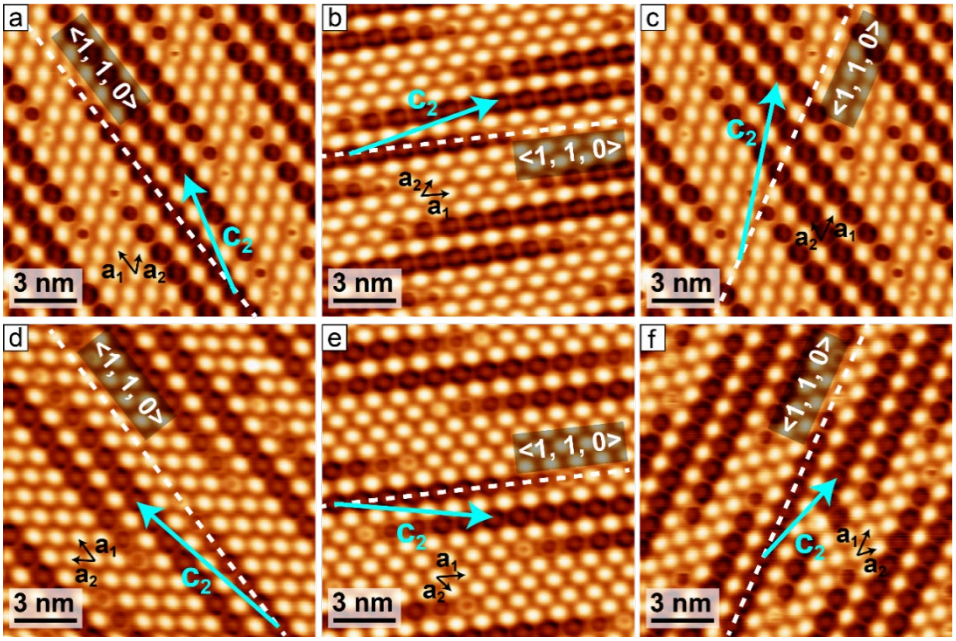

Figure A.1: Different DCA monolayer domains on Ag(111). (a)-(f) Constant-current STM images (V_b = –2.4 V, I_t = 50 pA) showing the six equivalent molecular domains of DCA on Ag(111). White dashed lines: <1,1,0> crystallographic axis of Ag(111). Molecular arrangement in (a) [(b), (c)] is mirror-symmetric to that of (d) [(e), (f), respectively]. The molecular self-assembly unit cell vectors, $\{\mathbf{a_1}, \mathbf{a_2}\}$ (black arrows), and superstructure lattice vector, $\mathbf{c_2}$ (cyan arrows), for each domain are superimposed. Note that the superstructure for each of these six molecular domains differs relative to $\{\mathbf{a_1}, \mathbf{a_2}\}$ with (a) $\mathbf{c_2} = 4\mathbf{a_1} + 2\mathbf{a_2}$, (b) $\mathbf{c_2} = 5\mathbf{a_1} + 2\mathbf{a_2}$, (c) $\mathbf{c_2} = 6\mathbf{a_1} + 2\mathbf{a_2}$, (d) $\mathbf{c_2} = 6\mathbf{a_1} + 2\mathbf{a_2}$, (e) $\mathbf{c_2} = 5\mathbf{a_1} + 2\mathbf{a_2}$, and (f) $\mathbf{c_2} = 3\mathbf{a_1} + 2\mathbf{a_2}$.

A.3 dI/dV STS measurements for molecules M_0 to M_{39} (negative bias range)

Figures A.2b,c show point dI/dV spectra for DCA molecules M_0 to M_{39} along $\mathbf{a_1}$ (see **Figure A.2**a) for $-2.7\ \text{V} < V_b < -1.0\ \text{V}$. Note that, due to the periodicity of this molecular domain, M_0 is equivalent to M_{39}. We observe that the absolute value $|V^*|$ of the charging bias onset (i.e.,

bias voltage corresponding to the negative differential conductance dip) increases the further a molecule is from M_0 along $\mathbf{a_1}$ (M_0 to M_{10}). For molecules M_{29} to M_{39} (i.e., as the distance to M_0 diminishes, given that M_{39} is equivalent to M_0), $|V^*|$ decreases. Note that these measurements were performed for the same molecules as in **Figure 3.7** of Chapter 3.

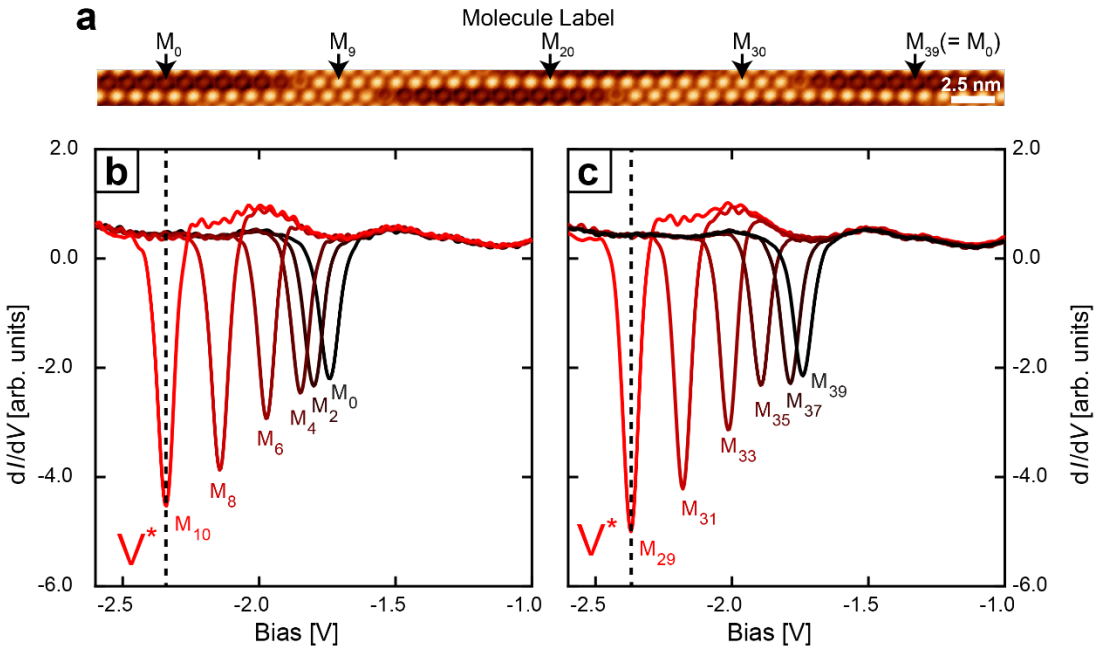

Figure A.2: V^* measurements for different molecules along $\mathbf{a_1}$ in a DCA monolayer. (a) Constant-current STM image (V_b = –2.4 V, I_t = 50 pA) of the same molecular domain as in **Figure 3.7** of Chapter 3. Here, the bias-dependent charging behaviour of DCA along $\mathbf{a_1}$ repeats after 39 molecules. (b)-(c) dI/dV STS measurements (set point V_b = –20 mV, I_t = 5 pA on top of M_0) in the negative bias regime for molecules M_0 to M_{39} as indicated in (a). The charging bias onsets, V^*, correspond to the voltage positions of the negative differential conductance dips in the spectra.

A.4 Topography Contribution to Constant Height dI/dV maps

Figures A.3a,b show the constant-height (dI/dV) (x, y) maps of **Figures 3.5**c,d of Chapter 3, at V_b = 0.15 and 0.30 V, after normalising [i.e., such that $0 \leq (dI/dV)_{norm}(x, y) \leq 1$] and dividing by the normalised tunnelling current map $I_{norm}(x, y)$ ($0 \leq I_{norm}(x, y) \leq 1$). The increased dI/dV intensity observed at the anthracene extremities when V_b = 0.30 V (black arrows in **Figure A.3**b and in the corresponding intensity line profile in **Figure A.3**f) is a signature of the LUMO. This LUMO signature at the anthracene extremities is corroborated in **Figures A.3**c,d, showing the normalised dI/dV maps subtracted by the normalised tunnelling current map $I_{norm}(x, y)$ (at V_b = 0.15 and 0.30 V), and in **Figure A.3**e, showing the difference $\Delta(dI/dV)_{norm}(x,y) = (dI/dV)_{norm}(x,y)|_{V_b=300\ mV} - (dI/dV)_{norm}(x,y)|_{V_b=150\ mV}$.

The lack of intensity at the molecule centre (red arrows) for $(dI/dV)_{norm}/I_{norm}$ (**Figures A.3**a,b), $(dI/dV)_{norm} - I_{norm}$ (**Figures A.3**c,d) and $\Delta(dI/dV)_{norm}$ (**Figure A.3**e) indicates

that the features seen at the centre of the molecules in **Figures 3.5**c,d of Chapter 3 are mainly an effect of topography.

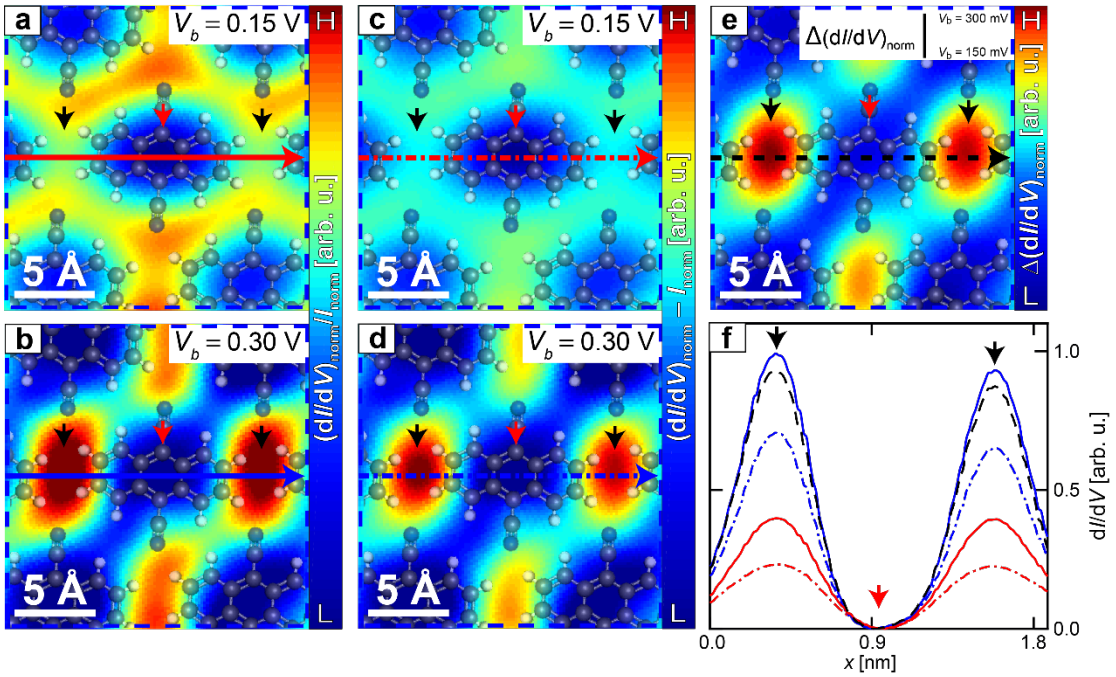

Figure A.3: Topography contribution to constant height d*I*/d*V* maps. (a)-(b) Constant-height $(dI/dV)_{\mathrm{norm}}/I_{\mathrm{norm}}$ and (c)-(d) $(dI/dV)_{\mathrm{norm}}-I_{\mathrm{norm}}$ maps (for bias voltages V_{b} displayed). (e) $\Delta(dI/dV)_{\mathrm{norm}} = (dI/dV)_{\mathrm{norm}}|_{V_{\mathrm{b}}=300\,\mathrm{mV}} - (dI/dV)_{\mathrm{norm}}|_{V_{\mathrm{b}}=150\,\mathrm{mV}}$ where $(dI/dV)_{\mathrm{norm}}(x,y) = (dI/dV)(x,y)/(dI/dV)_{\mathrm{max}}$ and $I_{\mathrm{norm}}(x,y) = I(x,y)/I_{\mathrm{max}}$, calculated using data in **Figures 3.5**c,d of Chapter 3. (f) Intensity line profiles along lines in (a) – (e). Increased intensity at black colored arrow locations when V_{b} = 300 mV are due to the LUMO which has strong contributions from the anthracene extremities (data taken with tip retracted 50 pm from STM set point V_{b} = –20 mV, I_{t} = 5 pA measured on top of central molecule; red arrow).

A.5 Determination of V_{LUMO} and tip-sample distance

We determined V_{LUMO} (as seen in **Figure 3.7**c) by fitting our $\mathrm{d}I/\mathrm{d}V$ spectra at positive biases (**Figure 3.5**b of Chapter 3) with a sum of a Fermi-Dirac distribution-like function an exponentially modified Gaussian function [333]:

$$(\mathrm{d}I/\mathrm{d}V)_{\mathrm{fit}}(E) = \frac{a}{\exp(-(E-E_{\mathrm{IS}})/b)+1} + \frac{c\exp\left(-\frac{1}{2}\left(\frac{E-g}{k}\right)^2\right)}{1+\frac{(E-g)e}{k^2}} \qquad \text{(Eq. A.2)}$$

where *a*, *b*, *c*, *g*, *e*, *k*, are free fitting parameters. E_{IS} is the interface state onset which was experimentally measured to be ~ 117 mV. We performed a constant background subtraction such that $\mathrm{d}I/\mathrm{d}V$ = 0 for $V_{\mathrm{b}} < 0$ before the fitting procedure. We associate V_{LUMO} with the position (in energy) of the apex of the exponentially modified gaussian which is given by the following formula:

$$V_{\mathrm{LUMO}} = g - \mathrm{sgn}(e)\sqrt{2}k\ \mathrm{erfcxinv}\left(\frac{|e|}{k}\sqrt{\frac{2}{\pi}}\right) + \frac{k^2}{e} \qquad \text{(Eq. A.3)}$$

where erfcxinv(…) is the inverse of the scaled complementary error function. **Figure A.4**a shows an example of a fitted $\mathrm{d}I/\mathrm{d}V$ curve taken on M_{20} (black circles: experimental data; solid red curve: fit) with V_{LUMO} = 355 ± 10 mV. The uncertainty in V_{LUMO} is determined through the propagation of the uncertainties (standard deviation) in the fitting parameters.

The tip-molecule distance in section 3.5 corresponding to the set point of V_b = –0.02 V, I_t = 5 pA at the location M_0, z_{setpoint}, was estimated by using Eq. 3.8. **Figure A.4**b shows the value obtained for each molecule (excluding M_{11} to M_{24}) referred to in **Figure 3.7** of Chapter 3. The dashed blue line indicates the weighted mean value for all data shown, resulting in $\langle z_{\mathrm{setpoint}} \rangle$ = 5.8 ± 0.3 Å (uncertainty in weighted mean).

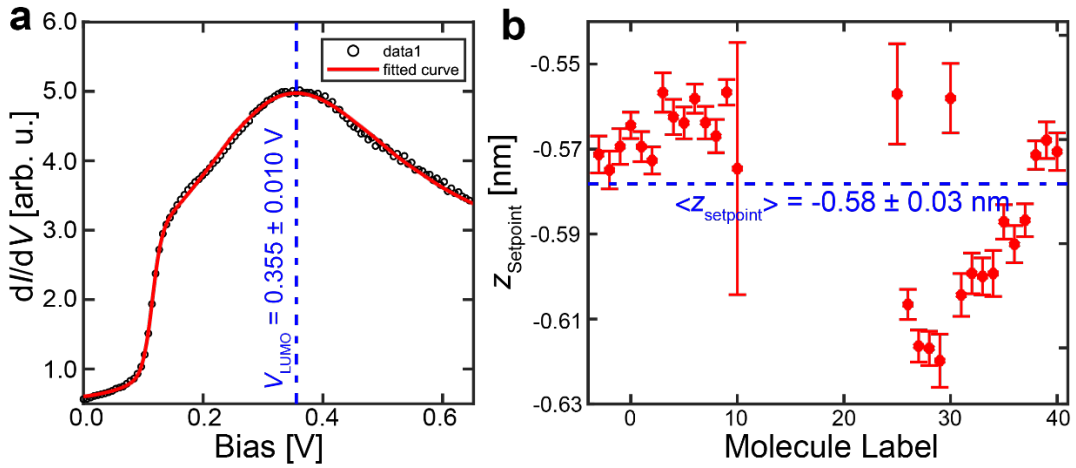

Figure A.4: Determination of V_{LUMO} and tip-sample distance in Chapter 3. (a) Experimental $\mathrm{d}I/\mathrm{d}V$ curve (black circles) and fit (solid red curve) taken above molecule M_{20}. V_{LUMO} corresponds to the energy position of the exponentially modified Gaussian peak. (b) Estimated tip-molecule distance z_{setpoint} as a function of molecule label (corresponding to molecules in **Figure 3.7** of Chapter 3). This results in $\langle z_{\mathrm{setpoint}} \rangle$ = –5.8 ± 0.3 Å which was used to fix z = 0 in **Figure 3.7** of Chapter 3.

Appendix B

DCA/Ag(111) Interface State Dispersion

In Chapter 4, I presented results on the dispersion of a 2D free-electron-like state at the interface between DCA submonolayers and an underlying Ag(111) substrate. Here I provide further pertinent details.

B.1 Interface State Dispersion Along High-Symmetry Directions

In section 4.3, I showed, via FT-STS measurements, the extracted dispersion relation, $E(\mathbf{k})$, for electrons in the DCA/Ag(111) interface state along $\mathbf{X'-\Gamma-Y'}$ direction indicated here in **Figure B.1**a. For completeness, here I show the dispersion relation, $E(\mathbf{k})$, along all the high-symmetry directions: $\mathbf{X'-\Gamma-X'}$, $\mathbf{H1'-\Gamma-H1'}$, $\mathbf{C'-\Gamma-C'}$, $\mathbf{H2'-\Gamma-H2'}$, $\mathbf{Y'-\Gamma-Y'}$, and $\mathbf{H3'-\Gamma-H3'}$ as seen in **Figures B.1**b-g below.

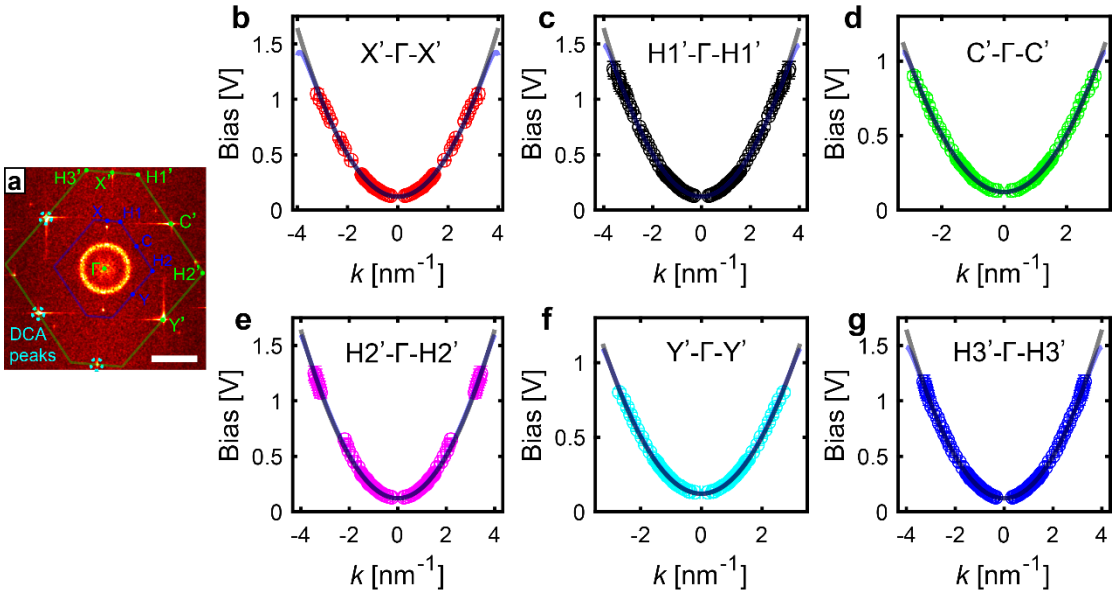

Figure B.1: Dispersion, $E(\mathbf{k})$, plots along DCA/Ag(111) high-symmetry directions. (a) Fourier-transformed STS (FT-STS) map reproduced here from **Figure 4.5**a of Chapter 4. Scalebar: 4 nm^{-1}. (b)-(g) $E(\mathbf{k})$ dispersion for the DCA/Ag(111) interface state along the indicated high-symmetry directions indicated in the FT-STS in (a). The data in (b)-(g) were fitted assuming a free-electron model (black fit curves) using Eq. 4.1. Additionally, the data were fitted with second order correctios to the free-electron dispersion relation (blue fit curves) using Eq. 4.2.

B.2 RMSE Calculations for Evaluating Dispersion Fits

In section 4.3, we presented fits to the extracted dispersion data, $E(\mathbf{k})$, for the DCA/Ag(111) interface state using the unperturbed (free) electron model and 2nd order corrections to the free electron model given by Eq. 4.1 and Eq. 4.2, respectively (e.g., see **Figure 4.5**d). How well

these models capture the trend in our data was evaluated by calculating the fit residuals (difference between the fit and the data; see residual plot in **Figure 4.5**d) and the subsequent root-mean-square errors (RMSE) for the resulting fits. The RMSE can be calculated using a weighted or an unweighted scheme. The unweighted RMSE calculated using:

$$\mathrm{RMSE} = \sqrt{\frac{\sum_i [E(\mathbf{k}_i) - E^{\mathrm{fit}}(\mathbf{k}_i)]^2}{N}} \qquad \text{(Eq. B.1)}$$

where $E(\mathbf{k}_i)$ and $E^{\mathrm{fit}}(\mathbf{k}_i)$ are the data and fitted value to the data at $\mathbf{k}_i$ and N is the number of data points. The weighted RMSE, on the other hand is calculated using:

$$\mathrm{RMSE}_w = \sqrt{\frac{\sum_i w_i \cdot [E(\mathbf{k}_i) - E^{\mathrm{fit}}(\mathbf{k}_i)]^2}{\sum_i w_i}} \qquad \text{(Eq. B.2)}$$

where w_i are the weights associated with the i^{th} $[E(\mathbf{k}_i) - E^{\mathrm{fit}}(\mathbf{k}_i)]^2$ term. Here, the weights are related to the uncertainties in the data at $\mathbf{k}_i$, $\delta E(\mathbf{k}_i)$:

$$w_i = \left(\frac{1}{\delta E(\mathbf{k}_i)}\right)^2 \qquad \text{(Eq. B.3)}$$

The calculated weighted and unweighted RMSE for the different fits to our entire experimental $E(\mathbf{k})$ dataset is summarised in **Table B.1**. The resulting fits were indistinguishable for most of the experimental dataset except for high $|\mathbf{k}|$ values. To evaluate the resulting fits at this high $|\mathbf{k}|$ regime, we further calculated the RMSE for the fits to our experimental data, $E(\mathbf{k})$, where $|\mathbf{k}| > 1.9\ \mathrm{nm}^{-1}$. We find that in all cases, the fit using 2nd order corrections to the free electron expression, i.e., using Eq. 4.2, yielded a better agreement with our experimental data.

	Full Experimental Range		**High $\lvert\mathbf{k}\rvert$ regime**	
	RMSE (mV)	**RMSE_w (mV)**	**RMSE (mV)**	**RMSE_w (mV)**
Free Electron	14.11	2.79	23.42	19.90
2nd Order Correction	11.33	2.70	18.86	15.42
Difference	2.81 (–19.7 %)	0.09 (–3.3 %)	4.56 (–19.5 %)	4.48 (–22.5 %)

Table B.1: RMSE for fits to experimentally measured DCA/Ag(111) interface state dispersion. The table shows the calculated unweighted and weighted root-mean-square errors (RMSE and RMSE_w, respectively) for the fits to the experimentally measured DCA/Ag(111) interface state dispersion, $E(\mathbf{k})$ discussed in section 4.3. Here, we also calculated the relevant RMSE and RMSE_w values for the fits to $E(\mathbf{k})$ with $|\mathbf{k}|$ restricted to values greater than 1.9 nm^{-1}, i.e., high $|\mathbf{k}|$ regime. In this regime, we note deviations of $E(\mathbf{k})$ from a parabolic/free electron behaviour (see **Figure 4.5**d). In all cases the RMSE value is lower for the fit to $E(\mathbf{k})$ using 2nd order corrections to the free electron model.

B.3 Band Structure Calculation

In section 4.4, we calculated the band structure for the interface state electrons by solving the central equation given by Eq. 4.5. Here, I outline how this was done. For simplicity, we will solve Eq. 4.5 for an electron in a 1D periodic potential, $U(\mathrm{r})$. We will further assume that the only non-zero Fourier coefficients, U_G, to the periodic potential are those associated with $\pm G$. Since the real-space potential, $U(\mathrm{r})$, must be a real function, we have that $U_G = U_{-G}$ [84]. Recasting Eq. 4.5 as a matrix equation, we obtain:

$$\begin{pmatrix} \dots & \dots & \dots & \dots & \dots & \dots & \dots \\ \dots & \lambda_{k+2G}-\epsilon & -U_G & 0 & 0 & 0 & \dots \\ \dots & -U_G & \lambda_{k+G}-\epsilon & -U_G & 0 & 0 & \dots \\ \dots & 0 & -U_G & \lambda_k-\epsilon & -U_G & 0 & \dots \\ \dots & 0 & 0 & -U_G & \lambda_{k-G}-\epsilon & -U_G & \dots \\ \dots & 0 & 0 & 0 & -U_G & \lambda_{k-2G}-\epsilon & \dots \\ \dots & \dots & \dots & \dots & \dots & \dots & \dots \end{pmatrix} \begin{pmatrix} \dots \\ C_{k+2G} \\ C_{k+G} \\ C_k \\ C_{k-G} \\ C_{k-2G} \\ \dots \end{pmatrix} = 0 \quad \text{(Eq. B.4)}$$

where $\lambda_k = \hbar^2 k^2/2m^*$, $\epsilon = E(k)$, and C_k's are Fourier coefficients for the electron wavefunction. For practical calculations, we truncate the matrix in Eq. B.4 by constraining $|G| < G_{\max}$. For example, if we let $G_{\max} = 2G$, we obtain:

$$\begin{pmatrix} \lambda_{k+2G}-\epsilon & -U_G & 0 & 0 & 0 \\ -U_G & \lambda_{k+G}-\epsilon & -U_G & 0 & 0 \\ 0 & -U_G & \lambda_k-\epsilon & -U_G & 0 \\ 0 & 0 & -U_G & \lambda_{k-G}-\epsilon & -U_G \\ 0 & 0 & 0 & -U_G & \lambda_{k-2G}-\epsilon \end{pmatrix} \begin{pmatrix} C_{k+2G} \\ C_{k+G} \\ C_k \\ C_{k-G} \\ C_{k-2G} \end{pmatrix} = 0 \quad \text{(Eq. B.5)}$$

which can be solved for the eigenenergies, ϵ, by taking the determinant of the matrix:

$$\begin{vmatrix} \lambda_{k+2G}-\epsilon & -U_G & 0 & 0 & 0 \\ -U_G & \lambda_{k+G}-\epsilon & -U_G & 0 & 0 \\ 0 & -U_G & \lambda_k-\epsilon & -U_G & 0 \\ 0 & 0 & -U_G & \lambda_{k-G}-\epsilon & -U_G \\ 0 & 0 & 0 & -U_G & \lambda_{k-2G}-\epsilon \end{vmatrix} = 0 \quad \text{(Eq. B.6)}$$

Solving Eq. B.6 for k's all over the Brillouin zone allows, then, for the construction of the band structure $E(k)$. However, here we are limited to the first five energy bands of the band structure. This is a result of truncating the matrix in Eq. B.4. By considering a larger $G_{\max}$, we can solve for higher energy bands. This procedure can be generalised to our case (see section 4.4) where the electron is in a 2D periodic potential that is more intricate (i.e., more non-zero Fourier coefficients to real-space potential than the one considered above).

Appendix C

DCA_3Cu_2 Kagome MOF on Ag(111)

Here, I present further details supporting the results presented in Chapter 5 on the self-assembled DCA_3Cu_2 kagome MOFs grown on Ag(111).

C.1 Theoretical Methods

The following details all the theoretical calculations that were used to complement the experimental findings in Chapter 5. All these calculations, except for those involving the electron plane wave expansion (EPWE) model, were performed by a collaborator, Mr. Bernard Field (co-supervised by Prof. N. Medhekar and Dr. Agustin Schiffrin).

C.1.1 Electron plane wave expansion (EPWE) model

In section 5.3, we presented simulated local density of states (LDOS) for free electrons in a 2D potential, $U(\mathbf{r})$, following a kagome geometry (as shown in **Figure 5.8**d). This was done using the EPWE model as described in ref. [278]. This model aims to solve the central equation for $E(\mathbf{k})$ and the coefficients $C_{\mathbf{k}}$ [84]:

$$H\left(\frac{\hbar^2|\mathbf{k}|^2}{2m^*} - E(\mathbf{k})\right) C_{\mathbf{k}} = \sum_{\mathbf{G}} U_{\mathbf{G}}\, C_{\mathbf{k}-\mathbf{G}} \qquad \text{(Eq. C.1)}$$

Here, the sum is performed over the reciprocal lattice vectors, $\mathbf{G}$, for the 2D kagome geometry in **Figure 5.8**d. $U_{\mathbf{G}}$ and $C_{\mathbf{k}}$, respectively, are the coefficients in the Fourier expansions for the 2D potential, $U(\mathbf{r})$, and for the wavefunction solution, $\psi_{\mathbf{k}}(\mathbf{r})$, for the system:

$$\psi_{\mathbf{k}}(\mathbf{r}) = \sum_{\mathbf{G}} C_{\mathbf{k}-\mathbf{G}}\, e^{i(\mathbf{k}-\mathbf{G})\cdot\mathbf{r}} \qquad \text{(Eq. C.2)}$$

and

$$U(\mathbf{r}) = \sum_{\mathbf{G}} U_{\mathbf{G}}\, e^{i\mathbf{G}\cdot\mathbf{r}} \qquad \text{(Eq. C.3)}$$

Within this model, Eq. C.1 is solved numerically (using matrix inversion) by terminating the expansions in Eq. C.2 and Eq. C.3 at some finite reciprocal lattice vector such that $|\mathbf{G}| \leq G_{\max}$ (similar to the procedure described in Appendix B.3). Having found $E(\mathbf{k})$ and $C_{\mathbf{k}}$, the LDOS, at a location $\mathbf{r}$ and as a function of energy, E_0, for the system is computed via:

$$\mathrm{LDOS}(E_0, \mathbf{r}) = \sum_{\mathbf{k}} |\psi_{\mathbf{k}}(\mathbf{r})|^2\, \delta(E_0 - E(\mathbf{k})) \qquad \text{(Eq. C.4)}$$

To ensure a reasonable LDOS output, the summation above was carried out with an energy binning of 30 mV rather than a strict delta function. Finally, the simulated LDOS data is shifted appropriately in energy to line up as best as possible with the experimental data. This is justified because there is a freedom of choice in the energy offset afforded by this model.

C.1.2 Density functional theory (DFT) calculations

Spin-polarised density functional theory (DFT) calculations were performed (by Mr. Bernard Field) as implemented in the Vienna Ab-initio Simulation Package (VASP) [330]. The Perdew-Burke-Ernzerhof (PBE) functional under the generalised gradient approximation (GGA) was used to describe exchange-correlation effects [331]. Projector augmented wave (PAW) pseudopotentials were also used [334, 335]. A 400 eV cut-off was used for the plane wave basis set. A semi-empirical potential developed by Grimme (DFT-D3) was used to describe van der Waals forces [336]. For an enhanced description of electron correlations for *d* electrons, Dudarev's implementation of DFT+*U* [337] was used. Within this computational framework we considered a systematic variation of *U* (e.g., see **Figure 5.13**a) which represents a correction term to the interactions between electrons occupying the Cu 3*d* states ($U = 0$ for substrate). Values of large U (i.e., $U > 3$ eV) is not inconsistent with other values in the literature [338].

Structural relaxations were performed with a 3×3×1 Monkhorst-Pack Gamma-centred k-points grid, with ionic positions relaxed until Hellman-Feynman force on each atom was less than 0.01 eV/Å. Relaxation was performed without DFT+*U*. Relaxation of free-standing DCA_3Cu_2 kagome structure used Gaussian smearing with a width of 0.05 eV, while relaxation of DCA_3Cu_2 on a metal substrate used first order Methfessel Paxton smearing with a width of 0.2 eV.

For calculations on a metal substrate, we used a three-atom thick metal slab, with hydrogen atoms on the bottom surface as a passivation layer. The bottom layer of metal atoms was frozen in place at their bulk coordinates during structural relaxation. 15 Å of vacuum spacing above the slabs was included to minimise interactions between their periodic images.

For DCA_3Cu_2 kagome on Ag(111), a 7×7 silver supercell was used, with the bulk lattice constant of the primitive unit cell the same as the experimental value of 2.889 Å [120]. Further, we used a unit cell that was commensurate with the underlying substrate due to boundary condition and computational constraints, despite the evidence of disorder (see section 5.2a). For DCA_3Cu_2 kagome on Cu(111), an 8×8 Cu supercell was used, with the experimental bulk lattice constant of 2.554 Å [120], and an adsorption geometry chosen to match our nc-AFM measurements, namely the Cu atoms of the MOF in hollow sites of Cu(111) (see **Figure 5.5**b).

For accurate calculation of the electronic structure of DCA_3Cu_2/Ag(111) system without considering spin, we used a 7×7×1 k-points grid and considered the self-consistency cycle to be converged when the energy changed by less than 10^{-4} eV between steps. Tetrahedral interpolation with Blöchl corrections was used for Brillouin zone integration. These parameters were adequate to converge the charge density for further calculations of the band structure and density of states (DOS) with finer k-point sampling. For calculations with spin polarisation, a dense 11×11×1 k-points grid and an energy convergence criterion of 1×10^{-6} eV was used due to small energy scales involved for different spin configurations. DOS calculations used a 15×15×1 k-points grid and Gaussian smearing with a width of 0.05 eV while keeping the charge density constant.

For spin configurations, we tested initial conditions where all the carbon atoms in a DCA molecule were either spin up, spin down or without spin. We tested each unique combination of DCA spins up to symmetry (which gives six distinct permutations for three-fold rotational symmetry and time-reversal symmetry). We then presented the data for the lowest energy spin configuration. We note that, for our calculations of DCA_3Cu_2 kagome on a metal, where a low spin configuration was energetically favoured, no high spin configurations remained after self-consistency was achieved.

Charge and spin densities were partitioned using DDEC6 in order to assign spin and charge to the components of the DCA_3Cu_2 kagome MOF and the metal substrate [339–342]. We also performed partitioning with Bader charge analysis for comparison purposes [343]. We found that the predictions by DDEC of the charge transfer between the MOF and metal substrate were far more robust than those made by Bader analysis. DDEC calculations show a transfer of ~0.3 electrons per primitive unit cell from MOF to Ag(111) (see Appendix C.9). The spin analysis was found to be reasonably consistent between Bader and DDEC.

For isolated molecules, such as DCA and Cu_2DCA, calculations were performed with the Gamma point only, with a Gaussian smearing width of 0.05 eV and no van der Waals corrections. Vibrational mode calculations (see subsection 5.4.4) were performed by calculating the Hessian matrix by central differences with a step size of 0.015 Å, as implemented in VASP.

Finally, all structure visualization were performed with the VESTA software package [344].

C.1.3 Mean-field Hubbard (MFH) model

To gain insight into how variables such as electron-electron interactions, supercell size, electron filling and disorder affect the kagome lattice, we investigated (courtesy of Mr. Bernard Field) the Hubbard model, which we solved using the Hartree-Fock mean-field approximation

assuming collinear spins (making it equivalent to Hartree theory). This approximation treats the problem as a single-particle problem with a potential which depends on the electron density, which needs to be solved self-consistently from the single electron eigenstates. In this regard, the mean-field Hubbard model treats many-body effects in a similar manner to DFT, albeit with a simpler potential. The mean-field Hubbard Hamiltonian is:

$$H = -t \sum_{\langle i,j\rangle,\sigma} \left(c_{i,\sigma}^{\dagger} c_{j,\sigma}\right) + U_{\mathrm{MFH}} \sum_{i} \left(n_{i,\uparrow}\langle n_{i,\downarrow}\rangle + n_{i,\downarrow}\langle n_{i,\uparrow}\rangle - \langle n_{i,\uparrow}\rangle\langle n_{i,\downarrow}\rangle\right) \qquad \text{(Eq. C.5)}$$

where $c_{i,\sigma}^{\dagger}$ creates a spin σ at lattice site i, $n_{i,\sigma}$ is the number operator for spin σ electrons at site i, and $\langle n_{i,\sigma}\rangle$ is the average or 'mean-field' spin σ electron density at site i (and may take a value between 0 and 1). The parameter t is the nearest-neighbour hopping parameter, and its corresponding sum is taken over nearest-neighbour pairs. U_{MFH} is the Hubbard on-site interaction parameter, which has a related but distinct definition compared to U used in DFT+U calculations. Here U_{MFH} represents all electron-electron interactions, in the basis of the kagome lattice, while the U in DFT+U accounts for some of the interactions not captured by the Hartree and approximate exchange-correlation functionals, and only in the Cu *d* orbitals.

We wrote a Python script to solve the mean-field Hubbard Hamiltonian. We briefly summarise the algorithm here. For the initial ansatz for the electron density $\langle n_{i,\sigma}\rangle$, we typically use a random electron density produced by a symmetric Dirichlet distribution with a high concentration parameter for the spin up and down electron densities separately. Keeping the mean-field electron density constant, the Hubbard Hamiltonian is divided into spin up and down sectors and solved for its single particle eigenvalues $\epsilon_{j,\sigma}$ and eigenvectors $v_{i,j,\sigma}$ (with i indexing site, j indexing eigenstate and σ indexing spin). We determine the new electron density by filling eigenstates according to the Fermi Dirac distribution:

$$F(E,T) = 1/(e^{E/T} + 1) \qquad \text{(Eq. C.6)}$$

using a small 'temperature' T (we use $T = 0.1t$). The chemical potential μ is found by solving for the total electron number N_e:

$$N_e = \sum_{j,\sigma} F\left(\epsilon_{j,\sigma} - \mu, T\right) \qquad \text{(Eq. C.7)}$$

The output electron density is obtained from the elements of the eigenvectors by:

$$\langle n_{i,\sigma}^{\mathrm{out}}\rangle = \sum_{j} F\left(\epsilon_{j,\sigma} - \mu, T\right) \left|v_{i,j,\sigma}\right|^2 \qquad \text{(Eq. C.8)}$$

and the energy by:

$$E = \sum_{j,\sigma} F\left(\epsilon_{j,\sigma}, T, \mu\right)\epsilon_{j,\sigma} - U_{\mathrm{MFH}} \sum_{i} \langle n_{i,\uparrow}\rangle\langle n_{i,\downarrow}\rangle \qquad \text{(Eq. C.9)}$$

The difference between the input and output electron densities are quantified by the residual:

$$\text{Residual} = \sqrt{\sum_{i} \left(\langle n_{i,\sigma}^{\mathrm{out}}\rangle - \langle n_{i,\sigma}^{\mathrm{in}}\rangle\right)^2} \qquad \text{(Eq. C.10)}$$

If the residual is sufficiently small, then the calculation has reached self-consistency. Otherwise, we construct a new ansatz for the electron density by mixing the new and old electron densities. For mixing, we use simple mixing followed by direct inversion of the iterative subspace (DIIS) (also known as Pulay mixing) [345]. This process is repeated until self-consistency is achieved. Simple mixing sets the new density to be a linear combination of the input and output densities:

$$\langle n_{i,\sigma}\rangle = \alpha\langle n_{i,\sigma}^{\mathrm{out}}\rangle + (1-\alpha)\langle n_{i,\sigma}^{\mathrm{in}}\rangle \qquad \text{(Eq. C.11)}$$

where α is an empirically chosen parameter between 0 and 1. We typically use a value of 0.5, although smaller values are useful for systems where convergence is difficult.

Once simple mixing has reduced the residual to below a threshold, which we chose to be 0.01, we changed to using DIIS [345]. We used the algorithm of ref. [346], which allows for expansion of the subspace using only DIIS, with checking for linear dependencies done by inspection of the condition number. DIIS provided a two-fold increase in convergence speed compared to simple mixing, consistent with ref. [346]. On the rare occasion that DIIS became badly behaved, we found that a few steps of simple mixing corrected the procedure. We used DIIS until the residual was less than 10^{-4}.

For the calculations of the magnetic moment of the mean-field Hubbard model in the kagome lattice, we used a 6×6 supercell with periodic boundary conditions and a 4×4 Monkhorst-Pack k-point grid. We took t = 1 for simplicity. To search for the ground state, we sampled different initial electron densities, stepping through ratios of spin up to spin down electrons and trialling several different random initial configurations for each initial magnetization. Among these trials, the one with the lowest energy was kept and its data reported.

For a direct comparison with the DFT results, we also did calculations with a single unit cell while sampling the Brillouin zone with a 25×25 Monkhorst-Pack k-point grid. We fit the DFT spin configuration on the DCA molecules to the Hubbard model to find the Hubbard U_{MFH} which minimised the difference between the DFT and Hubbard model spin densities (as measured by the 2-norm). The DFT spin density and a uniform charge density was used as the

initial configuration for the Hubbard model in this fitting calculation. The parameters of interest were the net magnetization:

$$\langle m \rangle = \sum_i \left(\langle n_{i,\uparrow} \rangle - \langle n_{i,\downarrow} \rangle \right) / N_{\text{sites}} \qquad \text{(Eq. C.12)}$$

where N_{sites} is the number of sites in the lattice, and the local magnetic moment:

$$\sqrt{\langle m^2 \rangle} = \sqrt{\left(\sum_i \left(\langle n_{i,\uparrow} \rangle - \langle n_{i,\downarrow} \rangle \right)^2 \right) / N_{\text{sites}}} \qquad \text{(Eq. C.13)}$$

which is a measure of the magnitude of the magnetic moment on each lattice site.

C.1.4 STM simulations

Simulated STM images (such as in **Figure 5.13**c) were calculated under the Tersoff-Hamann approximation, as implemented in HIVE-STSM [347], integrating over states from –100 meV to the Fermi level.

C.2 Subtle Satellite Peaks in d*I*/d*V* STS Data

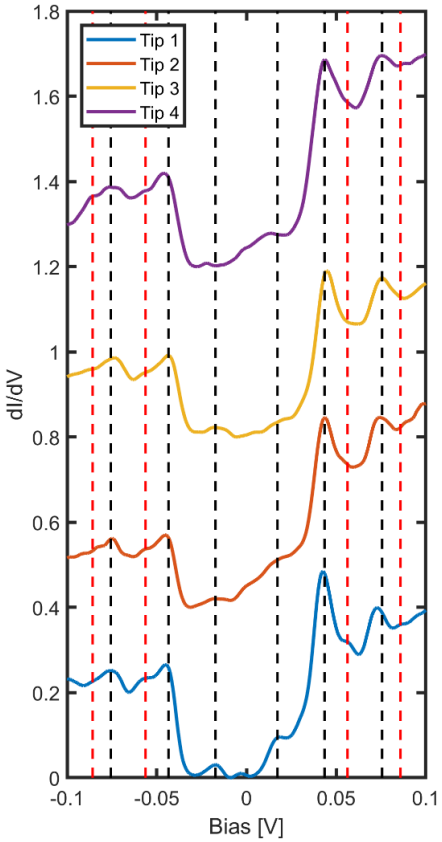

Figure C.1: Differential conductance measurements at the DCA molecular centre with various tips. In addition to the peaks observed at ±17.3 mV, ±43.5 mV, and ±75.6 mV (black dashed lines), we observe subtler peaks at energies of ±56.3 mV, ±85.8 mV (red dashed lines). Different tips seem to accentuate some of these side peaks more than others. dI/dV STS set point: V_b = –250 mV, I_t = 0.5 nA adjusted at the DCA molecular centre.

We acquired $\mathrm{d}I/\mathrm{d}V$ STS data at the DCA molecule centre using different tips to ensure that any features in the $\mathrm{d}I/\mathrm{d}V$ signal that we observe are intrinsic to the sample and are not related to the tip (see **Figure C.1**). In addition to the satellite peaks observed at ~±17mV, ~±43 mV, and at ~±72 mV (black dashed lines; these peaks were observed at other high-symmetry locations within the DCA_3Cu_2 MOF locations but with much lower intensities), we note that we can identify additional features near the Fermi level at ~±56 mV, and ~±85 mV (red dashed lines). Therefore, we rule out that these features are tip-related artefacts.

C.3 d*I*/d*V* STS Measurements along High-symmetry Lines

We acquired $\mathrm{d}I/\mathrm{d}V$ STS data along two high symmetry lines in the DCA_3Cu_2 kagome system (see **Figure C.2**): (i) along the DCA long molecular axis (**Figure C.2**b); and (ii) along a Cu_A-Cu_B axis (**Figure C.2**c). In this case, we can note that at biases $|V_b| > 40$ mV, there is greater intensity in the $\mathrm{d}I/\mathrm{d}V$ signal on the DCA molecular centre compared to the DCA anthracene extremities and the Cu atoms. For biases $|V_b| < 40$ mV, the opposite is true, i.e., there is greater intensity in the $\mathrm{d}I/\mathrm{d}V$ signal on the DCA anthracene extremity sites and the Cu atoms compared to the DCA molecular centre.

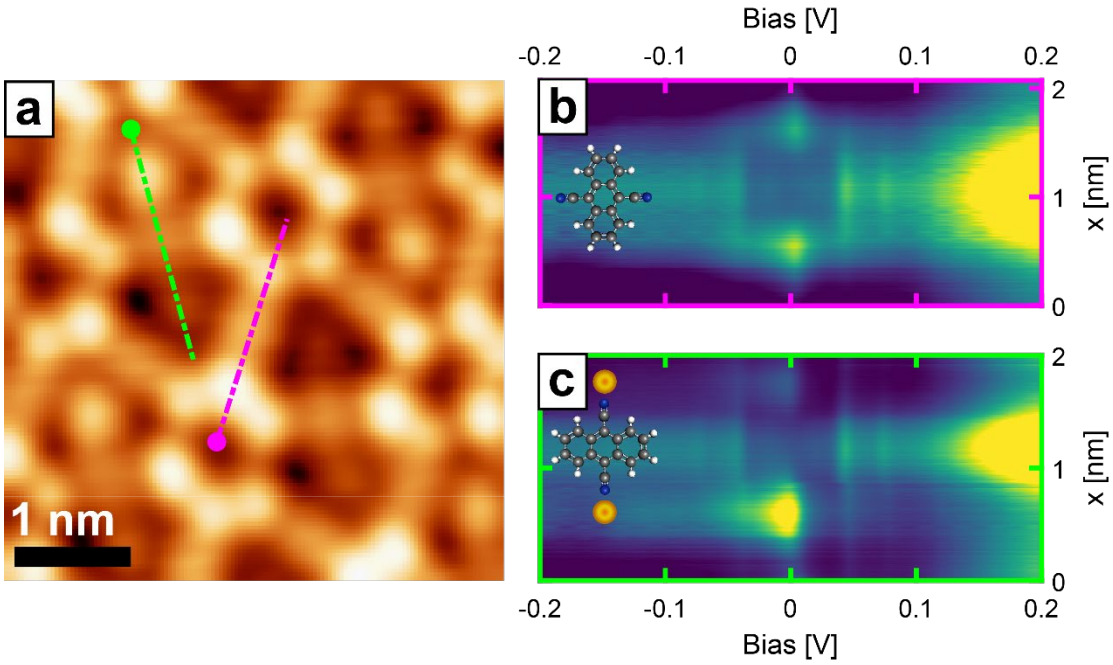

Figure C.2: Differential conductance measurements along high-symmetry lines for the DCA_3Cu_2 kagome structure. (a) Constant-current STM image of DCA_3Cu_2 kagome structure on Ag(111) (set point: V_b = 20 mV, I_t = 50 pA). (b) Differential conductance, $\mathrm{d}I/\mathrm{d}V$ STS data along a DCA long molecular axis [magenta dashed line in (a); set point: V_b = –200 mV, I_t = 0.4 nA] where the disk marker in (a) indicates x = 0 nm position. (c) Differential conductance, $\mathrm{d}I/\mathrm{d}V$ STS data along Cu_A-Cu_B axis [green dashed line in (a); set point: V_b = –200 mV, I_t = 0.4 nA] where the disk marker in (a) indicates x = 0 nm position. At $|V_b| > 43$ mV, there is a greater intensity in the $\mathrm{d}I/\mathrm{d}V$ signal on the DCA molecular centre than on the Cu atoms or the DCA anthracene extremities. Conversely, for $|V_b| < 43$ mV there is greater intensities, in the $\mathrm{d}I/\mathrm{d}V$ signal, at the Cu atoms positions and the DCA anthracene extremities than on the DCA molecular centre.

C.4 Near-Fermi dI/dV Maps

Here, I show dI/dV STS maps performed on the DCA_3Cu_2/Ag(111) kagome MOF (see **Figure C.3**). The maps here were performed at energies corresponding to the energies where the satellite/side peaks were observed in the dI/dV STS data at the high-symmetry locations within the 2D MOF.

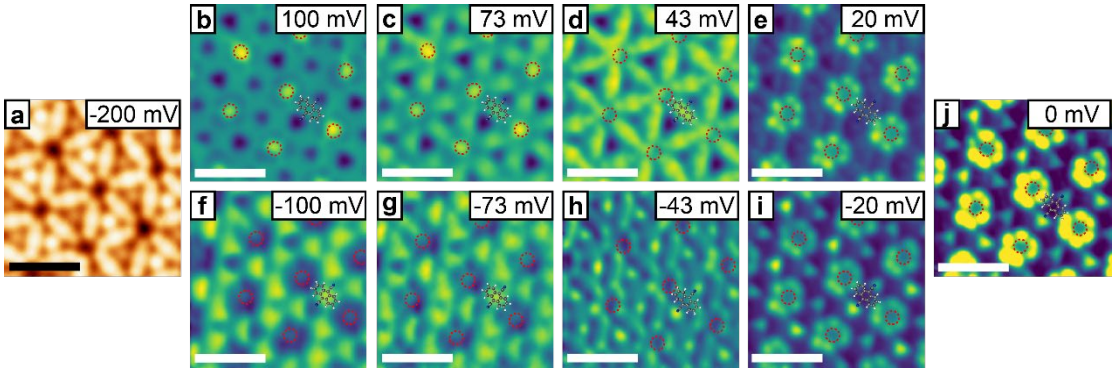

Figure C.3: dI/dV STS maps obtained at energies corresponding to side peaks observed in dI/dV data at high symmetry locations in DCA_3Cu_2/Ag(111). (a) Constant-current STM image of DCA_3Cu_2 kagome structure on Ag(111) (set point: V_b = –200 mV, I_t = 500 pA). (b)-(j), Differential conductance, dI/dV STS maps of the DCA_3Cu_2 kagome structure on Ag(111) taken at biases indicated in each panel and following the topography of the corresponding STM images in panel (a). The maps here were acquired using a multi-pass (MP) approach (see subsection 2.3.4). The first pass recorded the STM topographic profile with a scanning speed of 1.6 nm s^{-1} and with a constant-current set point: V_b = –200 mV, I_t = 500 pA. The second pass recorded the dI/dV signal using the lock-in technique while following the recorded profile in the first pass. The second pass was scanned with a scanning speed of 0.8 nm s^{-1}. In all cases, a lock-in amplifier frequency of 1.13 kHz and a lock-in modulation amplitude of 10 mV and was used. Scale bars: 2 nm. DCA structure imposed as a guide. Red dashed circles in (b)-(j) indicate the extent of the kagome pores.

C.5 Tip-sample Distance-dependent dI/dV STS Measurements

It has been reported in literature that the tip can influence the electronic properties of the system: strong tip-sample interactions can lead to conformational changes in the molecular system being probed and consequently alter the electronic features observed in the dI/dV signal [348]. Alternatively, for systems where the adsorbates are weakly interacting with the substrate, the tip can have a gating effect and result in the shifting of electronic features in the dI/dV signal which has a known dependence on the tip-sample distance (as seen in Chapter 3).

To rule out any tip-induced changes in the electronic structure of our system, we performed tip-sample distance-dependent dI/dV STS measurements. We looked for any changes in the ZBP features in our system. **Figures C.4**a-c show dI/dV STS measurements acquired on a (a) Cu_A, (b) Cu_B, and (c) DCA anthracene extremity sites at representative tip heights of 0 pm, 50 pm and 100 pm relative to a fixed set point (V_b = –300 mV, I_t = 1.5 nA). Unsurprisingly, the signal intensity decreases monotonically with increasing tip-sample distance. Qualitatively, however, the shape of the dI/dV signals remain unperturbed. **Figure**

C.4d shows the ZBP peak intensity (normalized by dI/dV signal at V_b = –300 mV) for each of the three sites as a function of tip-sample distance. We note that there is a very slight decrease in the peak intensity as the tip-sample distance is increased. We rationalize this trend with the fact that as the tip-sample distance is increased, the background dI/dV signal, to which the peak height is measured relative to, becomes saturated at the noise level. Therefore, we can interpret that the peak intensity remains essentially constant with tip-sample distance. From this we conclude that there is no strong tip-induced changes on the electronic properties of the DCA_3Cu_2/Ag(111) kagome system.

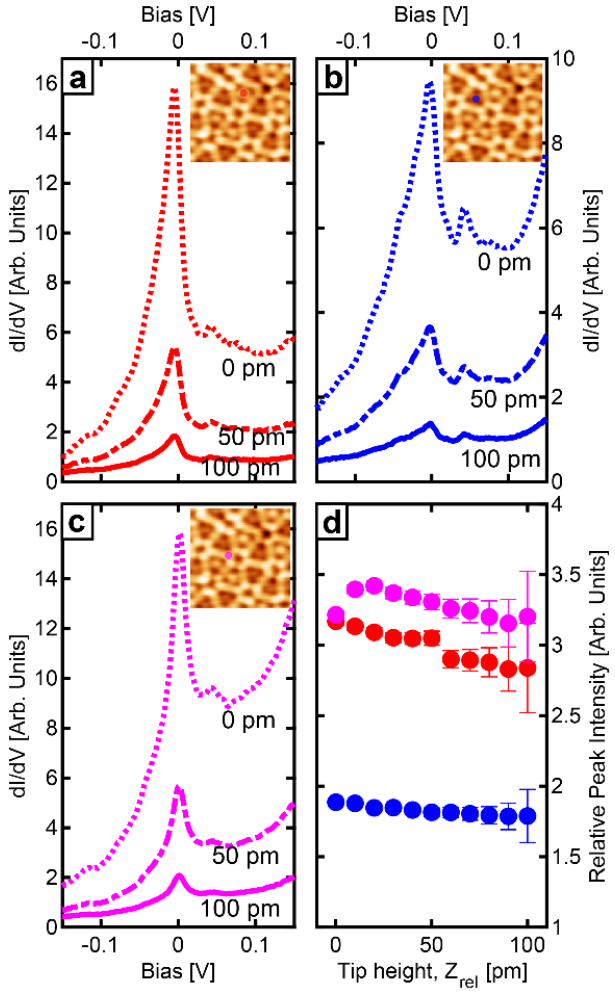

Figure C.4: Tip-sample distance-dependent dI/dV STS data at the high symmetry locations within the DCA_3Cu_2/Ag(111) MOF. (a)-(c) Differential conductance data taken at a (a) Cu_A, (b) Cu_B, and (c) DCA anthracene extremity sites at various tip-sample distances. A set point of V_b = –300 mV, I_t = 1.5 nA was used for all measurements. Subsequently, the tip was retracted from the sample by an amount ranging from 0 pm to 100 pm (as indicated). Qualitatively, the shape of the data looks similar with increasing tip-sample distance despite the decrease in the ZBP intensity. (d) The ZBP peak intensity, normalized by the dI/dV intensity at –300 mV, as function of tip-sample distance showing only minor changes with tip-sample distance. This excludes any strong tip-induced field-effect on the ZBP features.

C.6 Thermal Smearing in Temperature-dependent dI/dV STS Data

For reference, we have plotted the result of the fitting procedure in described in subsection 5.4.1 without considering thermal broadening in the $\mathrm{d}I/\mathrm{d}V$ acquisition of the ZBPs, i.e., Eq. 5.1. **Figure C.5**a shows the half width at half maximum (HWHM), γ, as a function of temperature where γ is the HWHM of the ZBPs in our $\mathrm{d}I/\mathrm{d}V$ data without thermal smearing considered. We find that while there is agreement between $\gamma(T)$ and Eq. 5.10 of the Chapter 5 at lower temperatures (where thermal smearing is negligible), there is a greater deviation between them at higher temperatures (where thermal smearing is more dominant). The only free parameter in Eq. 5.10 is the Kondo temperature, T_K, which is constrained by low-temperature measurements since $\Gamma(T \to 0) = \sqrt{2}k_B T_K$. The slope of Eq. 5.10 for $T \gg T_K$, is $d\Gamma/dT \to \pi k_B$, i.e., it is fixed regardless of T_K. **Figure C.5**b (reproduced here from **Figure 5.10**a) shows $\Gamma(T)$ where Γ is the HWHM of the ZBPs with thermal smearing considered.

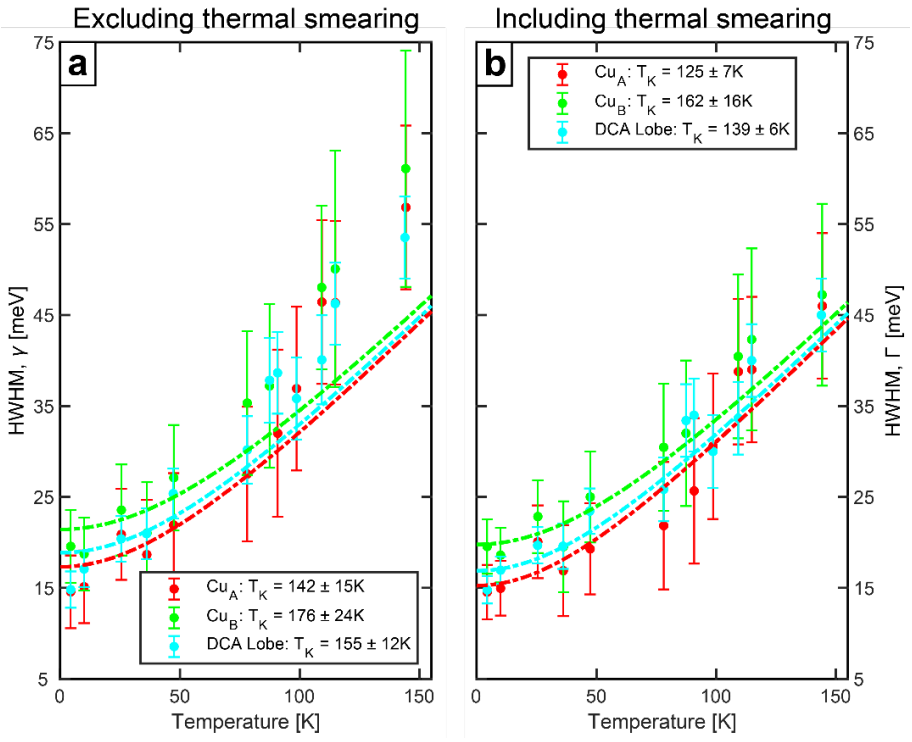

Figure C.5: Extracted HWHM of ZBP in dI/dV data without and with thermal smearing considered. (a) Extracted HWHM, γ, for the ZBPs in the dI/dV STS curves acquired over Cu_A (red), Cu_B (green) and DCA anthracene extremity (cyan) sites at different temperature without accounting for thermal broadening (see subsection 5.4.1). Dashed lines are fits to the Kondo trend described by Eq. 5.1 of Chapter 5 showing disagreement at higher temperatures where thermal broadening is increasingly dominant. (b) Extracted HWHM, Γ, for dI/dV STS curves acquired over CuA (red), CuB (green) and DCA anthracene extremity (cyan) sites at different temperatures. The data for Cu_A and DCA anthracene extremity sites have been reproduced here from Figure 5.10a of Chapter 5 (dashed lines; fits using Eq. 5.1 of Chapter 5). Here we see good agreement between the Kondo trend and the data at all temperatures.

C.7 Spatial-dependent dI/dV STS Data

It has been reported widely in literature that the temperature dependence for the ZBP amplitude can be used to independently corroborate the obtained Kondo temperature as well as to infer the spin state of the system (e.g., whether the system is in a S = 1/2 or S = 1 spin state) [31]. In our measurements however, establishing such a trend was not possible. In **Figure C.6** we show the dI/dV STS measurements performed on five different DCA anthracene extremity sites (**Figure C.6**a) and five different Cu_A sites (**Figure C.6**b) with the same tip and same STM set point. **Figure C.6**c shows the measured peak intensity (extracted by fitting a Fano function for the Cu_A ZBP and a Lorentzian function for the DCA anthracene extremity ZBP; see subsection 5.4.1 for fitting details) for the each of the different sites (red). Our measurements show that the ZBP heights vary considerably from one site to another. In principle, ZBP heights extracted from dI/dV STS measurements at the same location at different temperatures can yield a reliable trend. However, it was not feasible to perform temperature-dependent dI/dV STS measurements on the same location with the exact same tip due to experimental difficulties (e.g., thermal drift).

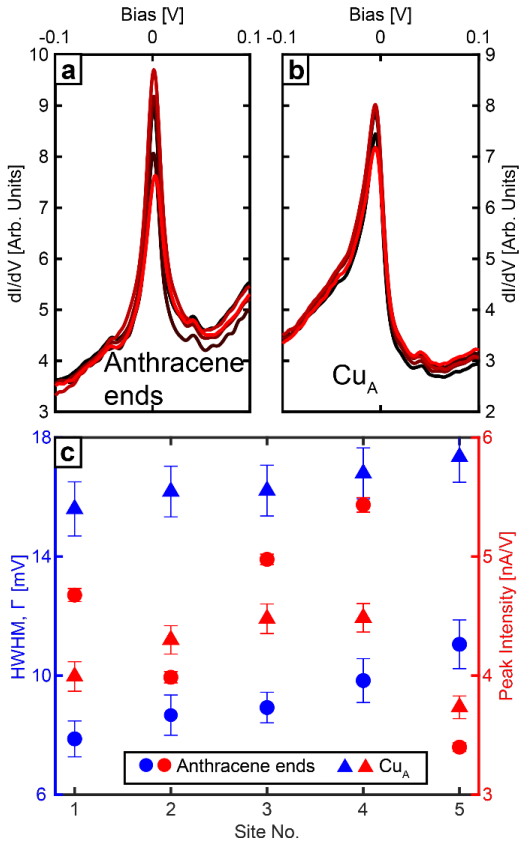

Figure C.6: ZBP spatial dependence measurements. (a)-(b) Differential conductance, dI/dV STS data taken at (a) different DCA anthracene extremity sites and at (b) different Cu_A sites within the DCA_3Cu_2 kagome MOF on Ag(111) (set point: V_b = –250 mV, I_t = 1 nA). (c) Extracted HWHM (blue) and the extracted peak intensity (red) from the curves in (a) and (b) via fitting procedure as outlined in subsection 5.4.1. The HWHM does not show huge variations between the different sites while the peak intensity depends strongly on the site at which the dI/dV data curve was acquired.

Despite this, the extracted HWHM for the curves in **Figures C.6**a,b is fairly constant as seen in **Figure C.6**c (blue) for the different Cu_A and the DCA anthracene extremity sites. This is unsurprising, as the HWHM is intrinsic to the system and should be somewhat insensitive to the exact probe location, set point, and the kind of tip used. This justifies our trend of the HWHM as a function of temperature obtained in **Figure 5.10**a of Chapter 5 which were extracted from different DCA anthracene extremity and Cu_A sites.

C.8 Band Structure Calculations

The calculations presented here, in this section, were all performed by Mr. Bernard Field. **Figure C.7**a shows the DFT+U calculated band structure for the freestanding DCA_3Cu_2 kagome structure with U = 0 eV and a charge depletion of 0.25 electrons per UC [to match calculated charge for DCA_3Cu_2 kagome structure on Ag(111)]. As noted in the Chapter 5, the kagome structure hosts Dirac bands and a flat band (at ~0.2 eV). The projected density of states onto the DCA LUMO (blue) and Cu 3d (green) states show that the kagome bands have a largely molecular character with little contribution from the Cu 3d states. **Figure C.7**b shows the DFT+U calculated spin-polarized band structure for the freestanding DCA_3Cu_2 kagome structure with U = 3eV (and a charge depletion of 0.25 electrons per UC). The spin-polarized bands resemble that of the case with U = 0 eV (**Figure C.7**a) with some splitting between the spin-up (magenta) and spin-down (green) bands. We note that with the inclusion of U > 0 eV, there is a break in symmetry in the electronic band structure, i.e., the K and M points in the Brillouin zones (BZ) (insets of **Figures C.7**a,b) are no longer equivalent. However, the band structure along other high symmetry directions e.g., $\Gamma - M_1 - K_1 - \Gamma$, is qualitatively similar with that shown in **Figure C.7**b.

Figure C.7c shows the DFT+U calculated band structure for the DCA_3Cu_2 kagome structure on Ag(111) with U = 0 eV (reproduced here from the **Figure 5.12**a of Chapter 5). **Figure C.7**d shows the DFT+U calculated spin-polarized band structure for the DCA_3Cu_2 kagome structure on Ag(111) with U = 3 eV with the spin-up and spin-down bands shown by the magenta and green curves, respectively. The red and blue circles are projections onto the MOF spin-up and spin-down orbitals, respectively. Their relative sizes to one another represent the weight of the orbital projections.

For reference, we plotted the DFT+U calculated band structure for the DCA_3Cu_2 kagome structures on Ag(111) and Cu(111) (with U = 0 eV) in **Figure C.8**a and **Figure C.8**b, respectively.

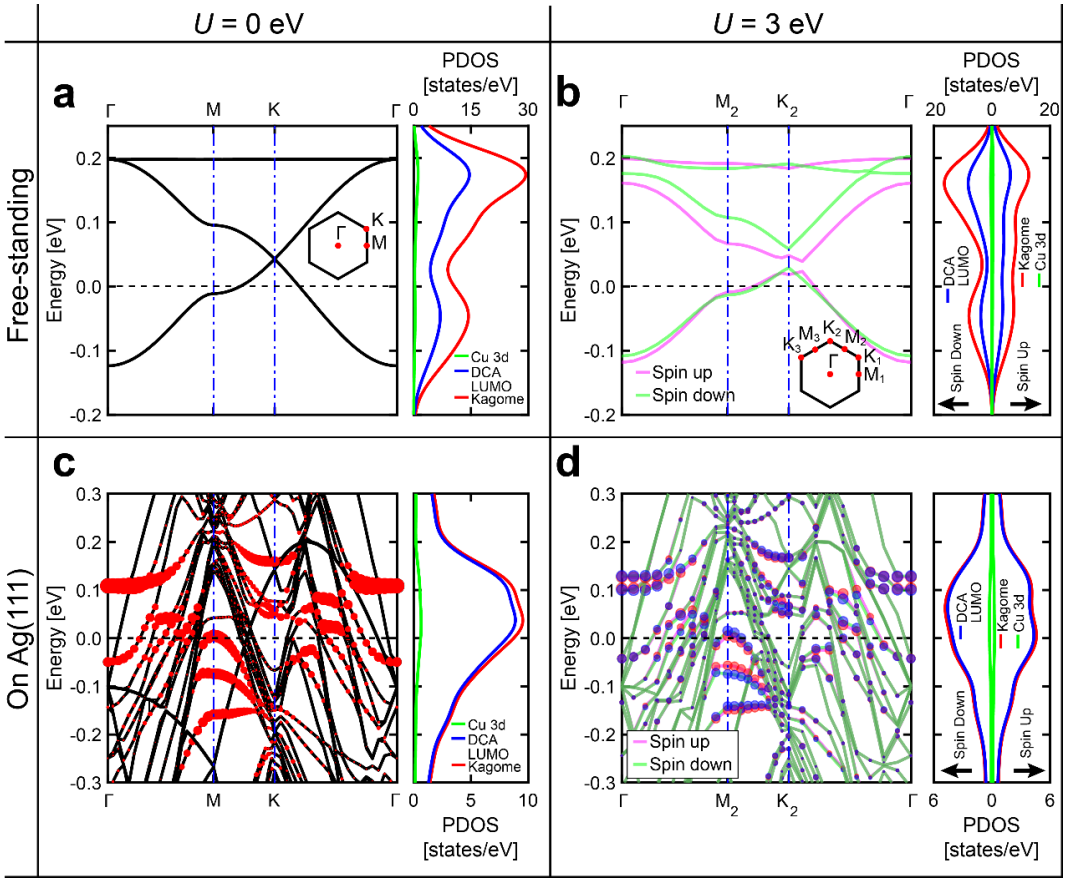

Figure C.7: DFT calculated band structure for freestanding DCA_3Cu_2 and DCA_3Cu_2/Ag(111) kagome structure with and without *U*. (a)-(b) DFT+*U* calculated band structure for freestanding DCA_3Cu_2 with a charge depletion of 0.25 electrons per UC with $U = 0$ eV and 3 eV used in (a) and (b), respectively. The projected density of states (PDOS) plots are shown to the right. The Brillouin zone with the corresponding high symmetry points are shown inset with the Brillouin zone in (b) showing a break in symmetry due to the increased electron-electron interaction. In (b) the displayed band structure and PDOS are spin-polarized. (c)-(d) DFT+*U* calculated band structure for the DCA_3Cu_2 kagome structure on Ag(111) with $U = 0$ eV and 3 eV used in (c) and (d), respectively. The PDOS plots are shown to the right. In (c), the red circles are projection onto the DCA_3Cu_2 orbitals. In (d) the band structure and PDOS are spin-polarized. The red (blue) circles are projection onto the DCA_3Cu_2 spin-up (spin-down) orbitals. The results here are courtesy of Mr. Bernard Field.

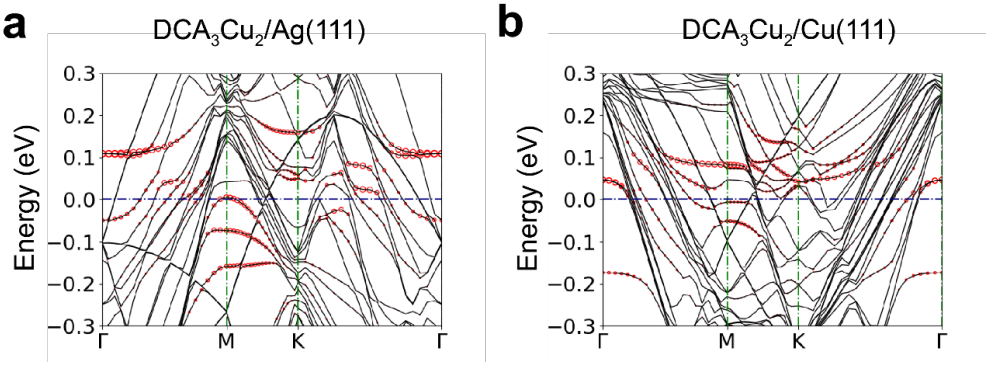

Figure C.8: DFT calculated band structure for DCA_3Cu_2/Ag(111) and DCA_3Cu_2/Cu(111) kagome. (a) DFT+*U* calculated band structure for the DCA_3Cu_2 kagome structure on Ag(111) with $U = 0$ eV. (b) DFT+*U* calculated band structure for the DCA_3Cu_2 kagome structure on Cu(111) with $U = 0$ eV. The red circles in (a) and (b) are projection onto the DCA_3Cu_2 orbitals. The results here are courtesy of Mr. Bernard Field.

C.9 MOF-substrate Charge Transfer

To find the charge transfer between the DCA_3Cu_2 kagome structure and the metal substrate, we considered how the charge transfer changed with increasing DCA_3Cu_2-substrate separation. At the equilibrium position there is substantial overlap between the DCA_3Cu_2 and substrate charge densities, which makes partioning the charge density ambiguous. However, increasing the separation removes the overlap and makes determining the charge transfer simple. The following calculations, here in this section, were all performed by Mr. Bernard Field.

We took the relaxed on-substrate geometry, vertically translated the DCA_3Cu_2 kagome structure atoms, then performed a single point electronic calculation to acquire the charge density, without spin or DFT+*U* for simplicity. The calculated charge transfer in **Figure C.9** shows that the DCA_3Cu_2 kagome structure tends to lose electrons to the substrate, with a greater charge transfer on Cu(111) than on Ag(111). At large distances, Bader and DDEC analysis (see Appendix C.1.2 for details on calculations) agree in their calculations of the charge transfer. However, they disagree at short distance where there is a strong overlap of the DCA_3Cu_2 and substrate orbitals.

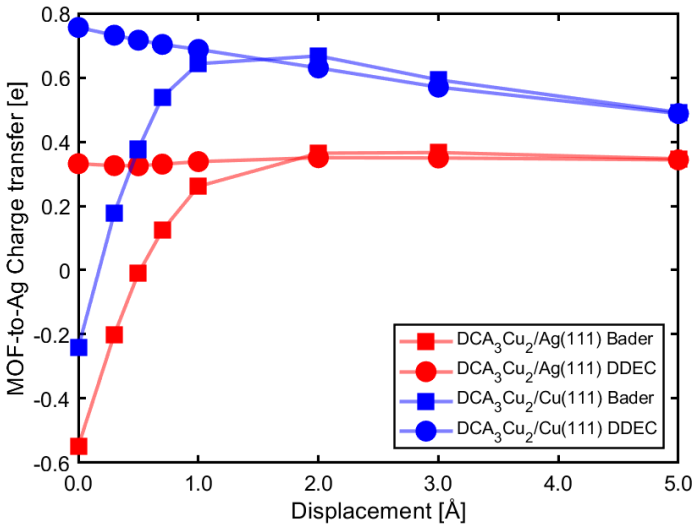

Figure C.9: MOF-substrate calculated charge transfer as function of MOF-substrate separation. Calculated charge transfer between DCA_3Cu_2 kagome structure and Ag(111) substrate (red curves) and Cu(111) substrate (blue curves) as a function of vertical displacement of the kagome structure from the respective substrates. At large separations, Bader (square markers) and DDEC (disk markers) analysis provide consistent results. At small separations, the two methods disagree, with DDEC analysis providing a more accurate estimate measure of the charge transfer. The results here are courtesy of Mr. Bernard Field.

We found in **Figure C.9** that the charge transfer calculated by DDEC varies monotonically and slowly with distance, while the charge density calculated by Bader varies non-monotonically and rapidly. At zero displacement, the charge density overlap between

DCA3Cu2 MOF and the substrate is high enough that grid-based ambiguities in determining the Bader partitions could lead to errors of approximately one electron. DDEC does not depend on the grid, instead fitting the charge to spherical functions and therefore does not share the same ambiguity as Bader. As such, for this system, we conclude that DDEC provides an accurate measure of the charge transfer while Bader does not.

DCA_3Cu_2/Ag(111) has a charge transfer of 0.33 electrons (to the substrate) while DCA_3Cu_2/Cu(111) has a charge transfer of 0.76 electrons (to the substrate). This electron transfer is consistent with the work functions of the materials. We calculated the work function of DCA_3Cu_2 to be 3.95 eV, by subtracting the Fermi energy from the electrostatic potential in vacuum. This is approximately 1 eV less than the work functions of Cu(111) and Ag(111), which are 4.94 eV and 4.74 eV, respectively [120]. The lower work function of DCA_3Cu_2 compared to the metals implies that there will be charge transfer from the DCA_3Cu_2 kagome structure to the Cu(111) and Ag(111) substrate. The lower Ag(111) work function between the two substrates mean that there will be a lower charge transfer from the DCA_3Cu_2 kagome structure to Ag(111) compared to Cu(111). This agrees with the calculations in **Figure C.9**.

The band structures for the DCA_3Cu_2 kagome structures vertically translated from the Ag(111) and Cu(111) substrates by different amounts is shown in **Figure C.10**. The plots show the charge transfer (see the Fermi level at 0 eV) as well as the distortions of the DCA_3Cu_2 kagome bands with the substrates as a function of vertical translation from the respective substrates. For vertical translations greater than 2 Å, distortions of the bands are negligible. The Fermi level, in this case, is below the Dirac point, indicating p-doping of the kagome structures. This is consistent with the DDEC charge analysis.

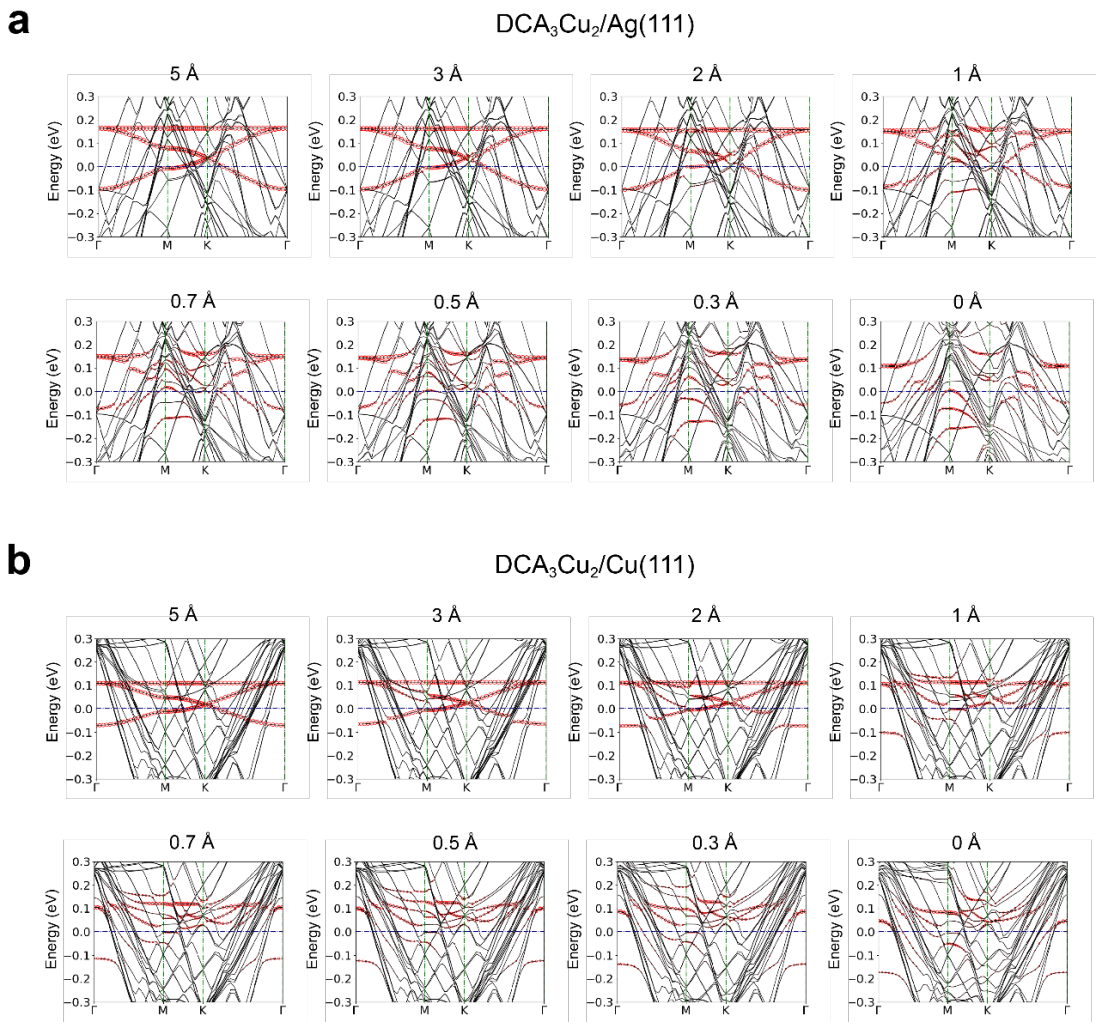

Figure C.10: Band structures for DCA_3Cu_2 on Ag(111) and Cu(111) as a function of vertical displacement from the respective substrates. DFT-calculated band structures for (a) DCA_3Cu_2/Ag(111) and (b) DCA_3Cu_2/Cu(111) where the relaxed on-surface structure was vertically translated away from the surface by the distance indicated at the top of the plots. The red-marked parts of the band structures correspond to the MOF orbitals. The results here are courtesy of Mr. Bernard Field.

C.10 Magnetic Moment and Spin Density Calculations

All the calculations presented in this section were performed by Mr. Bernard Field and serves to rationalise the experimental findings presented in Chapter 5.

C.10.1 DFT+*U* local magnetic moment calculation

In addition to DFT+*U* calculations performed on DCA_3Cu_2 kagome structure on Ag(111), we performed similar calculations on Cu(111) (see Appendix C.1.2 for calculation details). **Figure C.11**a shows the DFT+*U* calculations for both DCA_3Cu_2 kagome structures on Ag(111) and Cu(111) (solid and dashed curves, respectively) ranging from $U = 0$ to 5 eV. We find that there are negligible differences in the calculated charge transfer between the MOF and the substrates as a function of U (red curves) with a calculated charge transfer of ~0.3e^- and ~0.7e^- from the MOF to the Ag(111) and Cu(111), respectively (consistent with the results in Appendix C.9).

The calculated average local magnetic moment per DCA in the MOF on Cu(111) shows ~0 μ_B for values up to U = 5 eV (blue dashed curve) in stark contrast to the case on Ag(111) (blue solid curve). This is consistent with experimental $\mathrm{d}I/\mathrm{d}V$ STS measurements on Cu(111) where the Kondo effect was not observed [53] since there are no local magnetic moments to be screened by the underlying Cu(111) conduction electrons.

We further explored the role of electron-electron interaction in the substrate atoms on the calculated magnetic moments per DCA for DCA_3Cu_2/Ag(111) as seen in **Figure C.11**b. We performed DFT+U calculations on DCA_3Cu_2/Ag(111) for U between 0 and 5 eV and for U_{sub} = 0, 3 and 5 eV, where U_{sub} refers to the correction term for electron-electron interaction on the Ag 3*d* orbital in the Ag substrate. We find that the MOF-to-substrate charge transfer decreases with increasing U_{sub} (red curves) and that the average magnetic moment per DCA molecule increases with greater U_{sub} for a fixed U for DCA_3Cu_2/Ag(111). Despite this, with U = 0 eV, the average magnetic moment per DCA molecule remains small for values U_{sub} < 5 eV ($\sqrt{\langle m^2 \rangle} < 0.07\ \mu_B$). This implies the greatest contribution to the increase in the average magnetic moment per DCA is electron-electron interaction term in the MOF rather than in the substrate, i.e., $\sqrt{\langle m^2 \rangle}$ per DCA is greater with U = 3 eV and U_{sub} = 0 eV than with U = 0 eV and U_{sub} = 5 eV (see **Figure C.11**b). With this, the presentation of theoretical results in Chapter 5 with U_{sub} = 0 eV is justified.

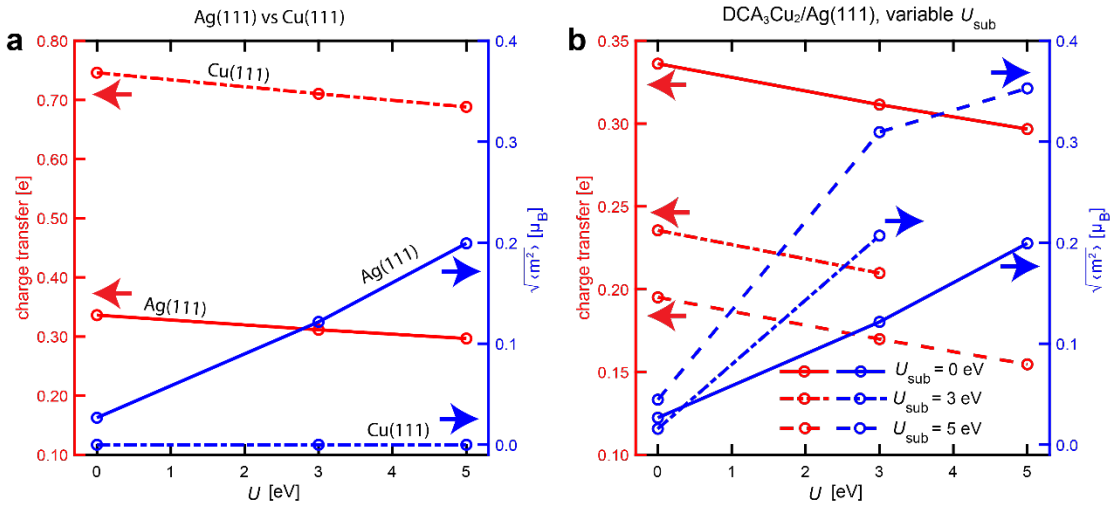

Figure C.11: DFT+U local magnetic moment calculation for DCA_3Cu_2 kagome structure in gas phase, on Ag(111) and on Cu(111). (a) Local magnetic moment per DCA molecule (blue, right) and DDEC charge transfer (MOF-to-substrate, red, left) calculated for different values of U (within DFT+U framework) for the DCA_3Cu_2 kagome structure on Ag(111) (solid lines) and on Cu(111) (dashed lines). (b) Local magnetic moment per DCA molecule (blue, right) and DDEC charge transfer (MOF-to-substrate, red, left) calculated for different values of U for DCA_3Cu_2/Ag(111) with different values of U_{sub} representing correction to the electron-electron interaction strength in the substrate Ag atoms. The results here are courtesy of Mr. Bernard Field.

C.10.2 DFT and MFH model-calculated magnetic phase diagrams

Via DFT+U, we calculated the average magnetic moment per DCA, $\sqrt{\langle m^2 \rangle}$, as a function of both electron filling and U for the freestanding DCA_3Cu_2 structure. The resulting magnetic phase diagram is shown in **Figure C.12**a. To determine the magnetic configuration of the system, we considered the normalized standard deviation of the magnetic moment, $\sigma_m = \sqrt{\langle m^2 \rangle - \langle m \rangle^2}/\sqrt{\langle m^2 \rangle}$. We classify our system according to the following: For $\sigma_m < 0.02$, the system is paramagnetic (PM). For $0.02 < \sigma_m < 0.1$, the system is ferromagnetic (FM). For $\sigma_m > 0.9$, the system is said to host a spin density wave (SDW). Finally, for $0.1 < \sigma_m < 0.9$, we have a pinned phase (PIN), where localised spin down electrons are pinned in a sea of spin-up electrons. From **Figure C.12**a, we find that for low electron filling (~1/6), the system remains in a paramagnetic phase for $U < 6$ eV. With increasing electron filling and moderate U values (e.g., $U = 3$ eV), the system hosts non-zero magnetic moments. In particular, with an electron filling of 7/24 which is close to the electron filling of DCA_3Cu_2 on Ag(111), as determined from our DFT calculations, we find that the system is paramagnetic for $U < 1$eV and is said to be in a SDW phase for $U > 1$ eV, consistent with DFT+U results for DCA_3Cu_2 on Ag(111).

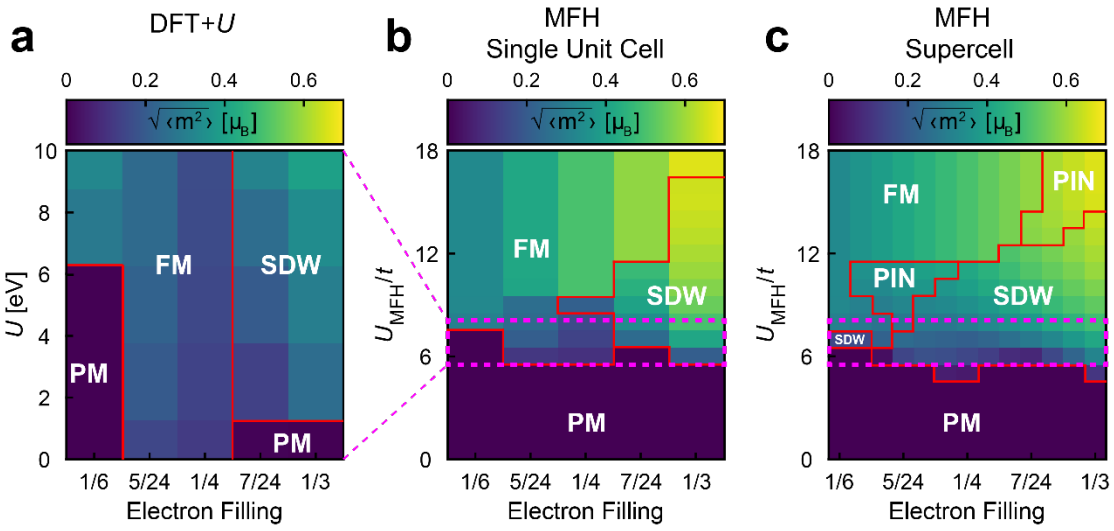

Figure C.12: Magnetic phase diagram calculated via DFT+U and MFH modelling for the DCA_3Cu_2 kagome structure. (a) Local magnetic moment with respect to electron filling and U for freestanding DCA_3Cu_2 calculated by DFT+U. (b) Local magnetic moment with respect to electron filling and U_{MFH} calculated via MFH modelling for a single kagome unit cell. (c) Local magnetic moment with respect to electron filling and U_{MFH} calculated via MFH modelling for a 6×6 kagome supercell. In all, cases, the red lines delineate the boundaries for the different phases for the kagome structure with PM, FM, SDW, and PIN referring to paramagnetic, ferromagnetic, spin density wave, and pinned metallic phases, respectively. The region enclosed in dashed rectangles (magenta) in (b) and (c) approximately correspond to the phase diagram in (a). These calculations were courtesy of Mr. Bernard Field.

The mean-field Hubbard model (see Appendix C.1.3) was used to explore the effect of electron filling and electron-electron interactions on the magnetic properties of the 2D kagome lattice. Electron filling is given as $N_e/2N_{\text{sites}}$ (see Appendix C.1.3) such that an electron filling

of 1/2 has an average of one electron per lattice site. Neutral free DCA_3Cu_2 has an electron filling of 1/3, while DCA_3Cu_2/Ag(111) has a filling close to 7/24 and DCA_3Cu_2/Cu(111) has a filling close to 5/24. We tested electron fillings between $1/6$ and 1/3 and on-site interaction, U_{MFH}, between 0 and $18t$. The resulting magnetic phase diagram for a single unit cell is shown in **Figure C.12**b.

We found that, for a single unit cell, the local magnetic moment generally increases with increasing U_{MFH} and electron filling, as shown in **Figure C.12**b. The increasing magnetic moment with U_{MFH} is due to the energetic penalty of having spin up and down electrons occupy the same lattice site. The increasing magnetic moment with electron filling is due to having more electrons to interact with each other, enhancing electron-electron interactions, and by having more electrons to form magnetic moments. For intermediate U_{MFH}, a SDW phase is preferred, where the net magnetization, $\langle m \rangle$, is near zero while the local magnetic moment, $\sqrt{\langle m^2 \rangle}$, is nonzero. Ferromagnetism occurs at higher U_{MFH}, where putting all electrons in a single spin channel is energetically favourable to having electrons of opposite spin which can interact. For sufficiently high U_{MFH}, the spin saturates. The onset of ferromagnetism occurs at a lower U_{MFH} for lower electron fillings, likely due to a smaller change in band energy needed to separate the spin channels at lower fillings and the greater frustration at higher fillings. Between the FM and SDW phases is a pinned phase, where localised spin down electrons are pinned in a sea of spin up electrons, with both a net magnetization and standard deviation greater than zero. A thorough investigation of the spin order in this system is beyond the scope of this work, although the spin order at 2/3 filling has already been investigated [286].

We further considered a 6×6 supercell kagome structure (see Appendix C.1.3). The resulting magnetic phase diagram (**Figure C.12**c) is in qualitative agreement with the results of the single unit cell calculation (**Figure C.12**b). The most notable difference between the two is that the local magnetic moment per kagome site, $\sqrt{\langle m^2 \rangle}$, is higher in the supercell case than in the single unit cell case (for the same electron filling and U_{MFH} values). This is not too surprising since the single cell is very constrained in terms of what magnetic configurations can arise while the supercell has much more freedom to express magnetic order/disorder.

To determine the parameters for the Hubbard model which reproduce the DFT results, we fit the spin density of the Hubbard model to the spin moments of the three DCA molecules obtained from our DFT results. It is a standard result that a non-interacting tight binding model of a kagome lattice has a bandwidth of six times the nearest-neighbour hopping constant. The freestanding DCA_3Cu_2 structure has a band structure which closely approximates an ideal kagome band structure. We calculated DCA_3Cu_2 to have a bandwidth of 321 meV. Therefore,

we can fix the hopping constant t (within the MFH model) to be 53.5 meV. From fitting the DFT-calculated spin density of DCA_3Cu_2/Ag(111) with the MFH model spin density for a single unit cell, we found that our DFT+U results (i.e., spin density) with U = 3 and 5 eV matches closely with that of the MFH model with $U_{\mathrm{MFH}} = 6.63t = 0.355$ eV and $U_{\mathrm{MFH}} = 6.90t = 0.369$ eV, respectively. The U = 0 eV case, with its small magnetization, could not be fit confidently, although we estimate it has $U_{\mathrm{MFH}} < 6.5t$.

Similar results were obtained for free-standing DCA_3Cu_2 with a charge depletion of 0.25 per UC (i.e., electron filling of 7/24). The U = 3 eV case matches closely with $U_{\mathrm{MFH}} = 6.49t = 0.347$ eV, while the U = 5 eV case matches closely with $U_{\mathrm{MFH}} = 6.72t = 0.360$ eV. Inspecting electron fillings between 1/6 and 1/3 per UC and values of U up to 10 eV in **Figure C.12**a, our fitting procedure, for where the magnetization was non-zero and not saturated, gave values of U_{MFH} between $5.5t$ (0.29 eV) and $8.5t$ (0.45 eV). Comparing the magnetic phase diagrams for DFT+U in **Figure C.12**a with that for a single unit cell of the MFH model in **Figure C.12**b, we find that they are indeed similar for $5.5t < U_{\mathrm{MFH}} < 8.5t$ (dashed magenta lines). This corroborates the fitting procedure. Furthermore, we note that the band structures calculated by MFH compare favourably with DFT-calculated band structures, albeit with a few minor differences, confirming the ability of our Hubbard model to reproduce the DFT results.

Finally, **Figure C.13** shows spin densities for the kagome supercell as considered by our MFH modelling for select U_{MFH} and electron filling values. In particular, the spin densities in **Figures C.13**a,b correspond to the DFT+U spin density results for DCA_3Cu_2/Ag(111) for U = 3 eV and U = 5 eV, respectively.

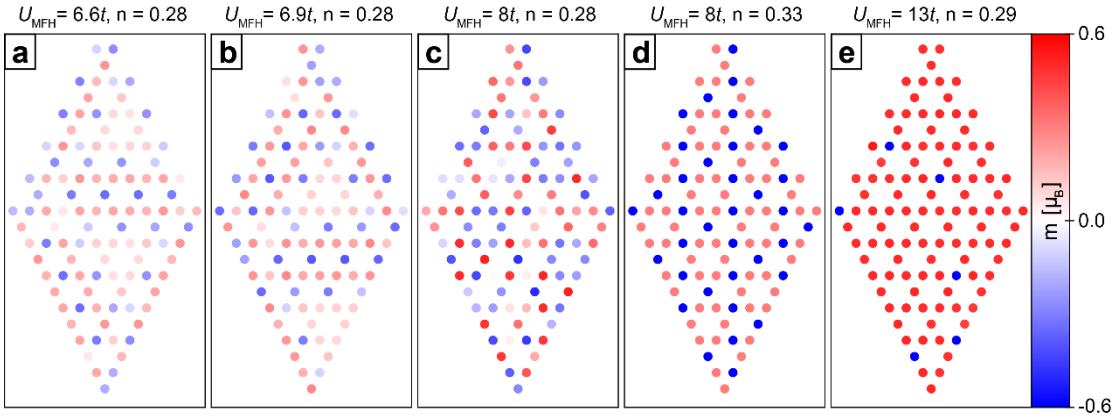

Figure C.13: Spin densities as calculated by the MFH model for selected values of U_{MFH} and electron filling, n. (a) Spin density most closely matches DFT+U calculations of DCA_3Cu_2/Ag(111) with U = 3 eV. (b) Spin density most closely matches corresponding calculation with U = 5 eV. (c)-(e) Selected other points in the SDW phase. Note that, due to the stochastic methods used, there may exist additional spin densities of similar or slightly lower energy, although the qualitative features should be consistent. These results were courtesy of Mr. Bernard Field.

C.11 Effect of Structural Disorder in DCA_3Cu_2/Ag(111)

The results presented in this section are courtesy of Mr. Bernard Field. Using our MFH model (see Appendix C.1.3), we also explored the effect of disorder on the magnetic properties of our system. Disorder was modelled by applying random variations to the hopping parameters and on-site energy within the supercell. Specifically, the Hamiltonian we consider is given by:

$$H = -\sum_{\langle i,j\rangle,\sigma}\left(t_{ij}c_{i,\sigma}^{\dagger}c_{j,\sigma}\right) + \sum_{i,\sigma}\varepsilon_i n_{i,\sigma} + U_{MFH}\sum_{i}\left(n_{i,\uparrow}\langle n_{i,\downarrow}\rangle + n_{i,\downarrow}\langle n_{i,\uparrow}\rangle - \langle n_{i,\uparrow}\rangle\langle n_{i,\downarrow}\rangle\right) \quad \text{(Eq. C.14)}$$

where t_{ij} is randomly uniformly distributed on the interval [t–Δt/2, t+Δt/2] and ε_i is randomly uniformly distributed on the interval [–$\Delta\varepsilon$/2, +$\Delta\varepsilon$/2]. From this Hubbard model, we find that disorder has a relatively small effect on the magnetic configuration. Very severe disorder has an effect similar to only a modest change in U_{MFH} or electron filling. We considered U_{MFH} = 6.6t and an electron filling of ~0.28, which closely fits our DFT+U results for DCA_3Cu_2/Ag(111) with U = 3 eV. Without disorder, $\sqrt{\langle m^2\rangle}$ is 0.22 μ_B, while for extreme disorder on the order of the hopping constant we get a local magnetic moment of no more than 0.34 μ_B, as shown in **Figures C.14**c,d. For comparison, increasing U_{MFH} to 8t increases the local magnetic moment to 0.37 μ_B. It is possible that disorder may play some role not captured by our mean-field Hubbard model. It may be that Anderson localisation [349], a dynamical effect, enhances localisation of spins and thus enhances the Kondo effect in DCA-Cu/Ag(111) but not the ordered DCA-Cu/Cu(111). However, this is beyond the capabilities of our model.

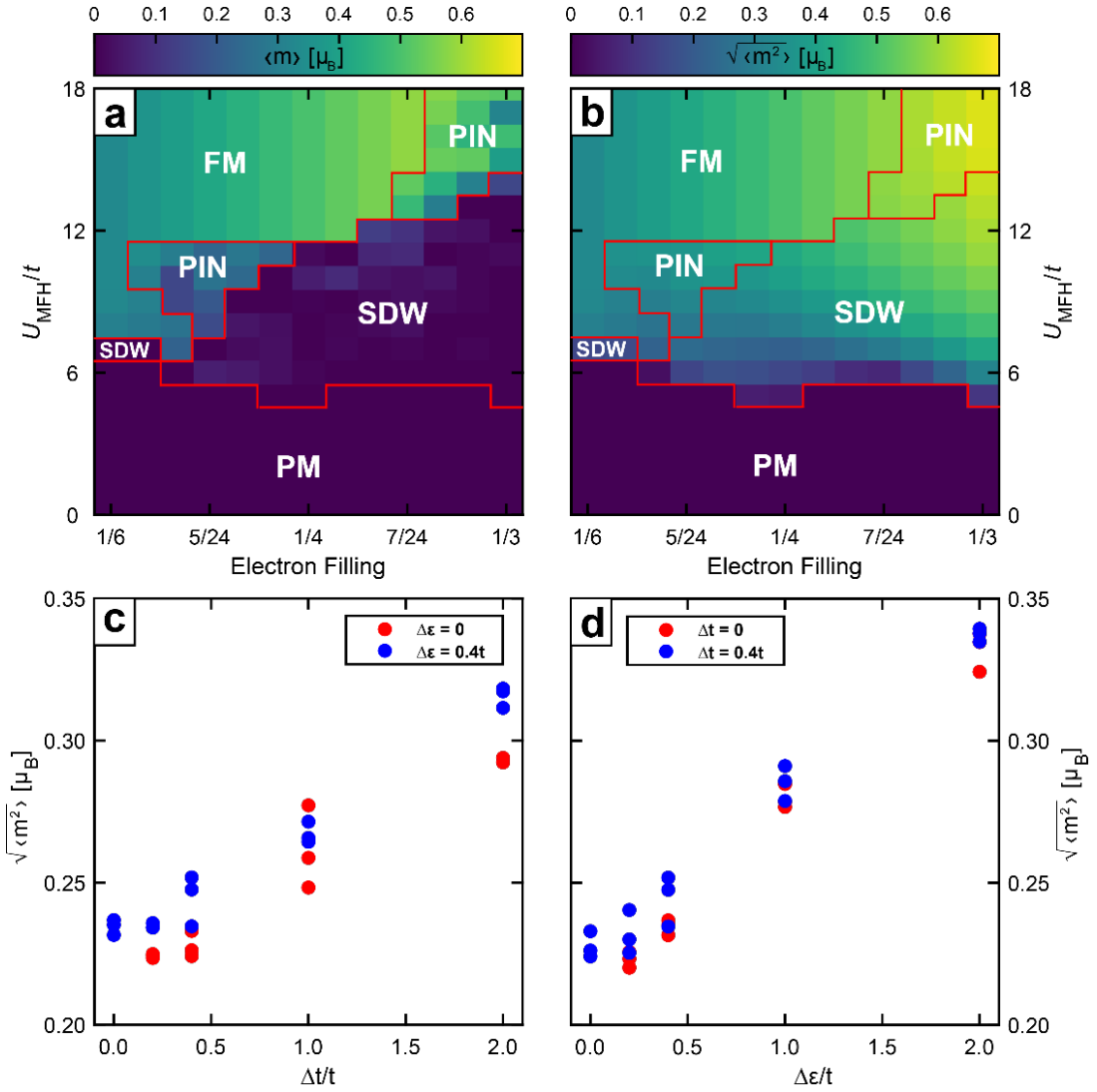

Figure C.14: Effect of disorder on the magnetic properties of DCA_3Cu_2 via MFH modelling. (a)-(b) Magnetic phase diagrams showing the (a) net magnetization and (b) local magnetic moment of the kagome supercell structure with respect to the electron filling and the Hubbard U_{MFH} parameter. (c)-(d) Dependence of local magnetic moment on the disorder parameters $\Delta\varepsilon$ and Δt, respectively, for U_{MFH} = $6.6t$ and an electron filling of ~0.28. The results here are courtesy of Mr. Bernard Field.

C.12 Estimation of Exchange Interaction Energy, J_{ex}

In subsection 5.6.2, the exchange interaction energy, J_{ex}, was estimated, within the formalism of the mean-field Hubbard model (MFH; see Appendix C.1.3), using the equation below:

$$J_{\mathrm{ex}} = \frac{1}{N_{\mathrm{DCA}}} \left(E_{\mathrm{ES}} - E_{\mathrm{GS}}\right) \qquad \text{(Eq. C.15)}$$

where N_{DCA} is the number of DCA molecules (i.e., kagome sites) within the unit cell and where E_{GS} and E_{ES} are the energies for the ground state and the excited paramagnetic state (as calculated by MFH), respectively. The ground state energy, E_{GS}, was calculated using Eq. C.9 as described in Appendix C.1.3. However, to calculate E_{ES}, a uniform electron density and zero spin density (corresponding to a paramagnetic/non-magnetic state) were used in Eq. C.9.

Appendix D

DCA Monolayers on hBN/Cu(111)

Here, I present further details supporting the results presented in Chapter 6 on the self-assembled DCA monolayers on hBN/Cu(111).

D.1 Different Moiré Superstructures for DCA/hBN/Cu(111)

We observe different Moiré patterns for different DCA molecular domains on hBN/Cu(111) as seen in the STM images in **Figures D.1**a,b (V_b = 1.0 V, I_t = 50 pA).

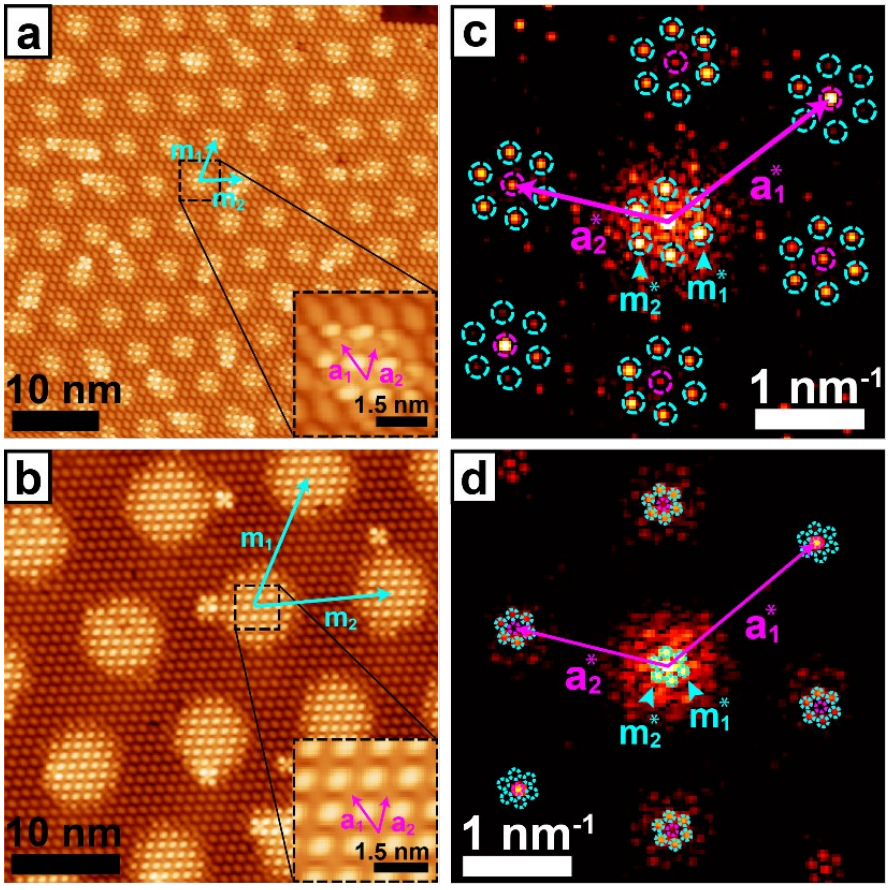

Figure D.1: STM imaging of different self-assembled DCA domains on hBN/Cu(111). (a)-(b) Constant-current STM images of different DCA submonolayer domains on hBN/Cu(111) (V_b = 1.0 V, I_t = 50 pA). The different DCA domains exhibit different Moiré superstructure periodicities with $\|\mathbf{m_1}\| = \|\mathbf{m_2}\|$ = 5.1 ± 0.5 nm; $\measuredangle(\mathbf{m_1}, \mathbf{m_2})$ = 67 ± 1° in (a) and $\|\mathbf{m_1}\| = \|\mathbf{m_2}\|$ = 12.6 ± 1.0 nm; $\measuredangle(\mathbf{m_1}, \mathbf{m_2})$ = 62 ± 1° in (b). (c)-(d) Fourier transform of the STM images in (a), (b). The molecular peaks in the FT images ($\mathbf{a_1^*}$, $\mathbf{a_2^*}$; dashed magenta circles) correspond to the real-space lattice vectors, $\mathbf{a_1}$, $\mathbf{a_2}$ in (a), (b), respectively. About each molecular peak are six symmetrically located peaks ($\mathbf{m_1^*}$, $\mathbf{m_2^*}$; dashed cyan circles) corresponding to the real-space Moiré superstructures ($\mathbf{m_1}, \mathbf{m_2}$) in (a), (b), respectively.

Both the molecular domains in **Figures D.1**a,b are oriented the same and have similar unit cell vectors $\{\mathbf{a_1}, \mathbf{a_2}\}$ (see inset for **Figures D.1**a,b) but they show different Moiré superstructure periodicities characterised by the vectors $\{\mathbf{m_1}, \mathbf{m_2}\}$. For the DCA molecular domain in **Figure D.1**a, we have $\|\mathbf{m_1}\| = \|\mathbf{m_2}\| = 5.1 \pm 0.5$ nm; $\measuredangle(\mathbf{m_1}, \mathbf{m_2}) = 67 \pm 1°$. Whereas for the DCA molecular domain in **Figure D.1**b, we have $\|\mathbf{m_1}\| = \|\mathbf{m_2}\| = 12.6 \pm 1.0$ nm; $\measuredangle(\mathbf{m_1}, \mathbf{m_2}) = 62 \pm 1°$. This is reflected in the Fourier transform (FT) of the respective STM images in **Figures D.1**a,b (see **Figures D.1**c,d). About each molecular peak in the FT images (dashed magenta circles; $\{\mathbf{a_1^*}, \mathbf{a_2^*}\}$) we see a set of six symmetrically located peaks (dashed cyan circles; $\{\mathbf{m_1^*}, \mathbf{m_2^*}\}$) which is associated with the Moiré superstructure in real-space i.e., the vectors $\{\mathbf{m_1^*}, \mathbf{m_2^*}\}$correspond to vectors $\{\mathbf{m_1}, \mathbf{m_2}\}$ in **Figures D.1**a,b.